Search for and Follow-up Imaging of Subparsec Accretion Disks in AGN

A dissertation presented

by

Paul Thomas Kondratko

to

The Department of Astronomy

in partial fulfillment of the requirements

for the degree of

Doctor of Philosophy

in the subject of

Astronomy

Harvard University

Cambridge, Massachusetts

March 2007

Search for and Follow-up Imaging of Subparsec Accretion Disks in AGN

Dissertation Advisor: Lincoln Jared Greenhill   Paul Thomas Kondratko

Abstract

We report results of several large surveys for water maser emission among Active Galactic Nuclei with the 100-m Green Bank Telescope and the two NASA Deep Space Network 70-m antennas at Tidbinbilla, Australia and at Robledo, Spain. We detected 23 new sources, which resulted in a 60% increase in the number of then known nuclear water maser sources. Eight new detections show the characteristic spectral signature of emission from an edge-on accretion disk and therefore constitute good candidates for the determination of black hole mass and geometric distance. This increase in the number of known sources has enabled us to reconsider statistical properties of the resulting sample. For the 30 water maser sources with available hard X-ray data, we found a possible correlation between unabsorbed X-ray luminosity $(2 - 10\,\mathrm{keV})$ and total isotropic water maser luminosity of the form $L_{2-10} \propto L_{\mathrm{H_2O}}^{0.5\pm0.1}$, consistent with the model proposed by Neufeld et al. (1994) in which X-ray irradiation of molecular accretion disk gas by the central engine excites the maser emission.

We mapped for the first time with Very Long Baseline Interferomatey (VLBI) the full extent of the pc-scale accretion disk in NGC 3079 as traced by water maser emission. Positions and line-of-sight velocities of maser emission are consistent with a nearly edge-on pc-scale disk and a central mass of $\sim 2 \times 10^6\,M_\odot$ enclosed within $\sim 0.4\,\mathrm{pc}$. Based on the kinematics of the system, we propose that the disk

is geometrically-thick, massive, subject to gravitational instabilities, and hence most likely clumpy and star-forming. The accretion disk in NGC 3079 is thus markedly different from the compact, thin, warped, differentially rotating disk in the archetypal maser galaxy NGC 4258. We also detect maser emission at high latitudes above the disk and suggest that it traces an inward extension of the kpc-scale bipolar wide-angle outflow previously observed along the galactic minor axis.

We also report the first VLBI map of the pc-scale accretion disk in NGC 3393. Water maser emission in this source appears to follow Keplerian rotation and traces a linear structure between disk radii of 0.36 and ~ 1 pc. Assuming an edge-on disk and Keplerian rotation, the inferred central mass is $(3.1 \pm 0.2) \times 10^7\, M_\odot$ enclosed within 0.36 ± 0.02 pc, which corresponds to a mean mass density of $\sim 10^{8.2}\, M_\odot\, \mathrm{pc}^{-3}$. We also measured with the Green Bank Telescope centripetal acceleration within the disk, from which we infer the disk radius of 0.17 ± 0.02 pc for the maser feature that is located along the line of sight to the dynamical center. This emission evidently occurs much closer to the center than the emission from the disk midline (0.17 vs. 0.36 pc), contrary to the situation in the two archetypal maser systems NGC 4258 and NGC 1068.

Contents

Acknowledgments

First and foremost, I would like to thank my advisor Lincoln Greenhill for all he has given me throughout the past few years. He has provided me with a challenging thesis project — a unique educational experience in many respects — and with the invaluable and necessary guidance along the way. He has taught me both single-dish radio astronomy and interferometry. By attempting to meet his high editorial standards, I have learned to write better scientific papers. I am also forever indebted to Jim Moran for his assistance and support throughout this process. Lincoln and Jim have provided me with models of scientists with highest standards of integrity, honesty, and intellectual rigor.

This work would not have been possible without the assistance of the scientists and the scientific staff affiliated with the NASA Deep Space Network (DSN) stations, particularly Graham Baines, Leigh Cameron, Cristina García-Miró, Patxi Gómez, Itziar de Gregorio-Monsalvo, David Jauncey, E. Jiménez-Bailón, Tom Kuiper, Jim Lovell, Jamie McCallum, and Esther Moll. I am indebted to Carl Bignell for unprecedented flexibility in the scheduling of the Green Bank Telescope (GBT) and to the scientific staff at the GBT, particularly Jim Braatz and Ron Maddalena, for help with the observing and data calibration. I owe many thanks to Mark Reid for assistance in scheduling the NGC 3393 VLBI experiment and for providing me with codes that enabled Gaussian component decomposition and zenith path delay calibration. The members of my thesis advisory committee — Martin Elvis, Ramesh Narayan, and Mark Reid — have provided constructive criticism and invaluable recommendations and I thank them for their guidance and assistance. I am forever

indebted to Jean and Peggy for brightening my days, for kind words of support, and for assistance in so many different ways.

I would like to single out the operators at the DSN and the GBT stations not only for their invaluable assistance with the observing but also for making my trips unforgettable. I will always hold dear the memorable discussions of Spain and countless other topics with the operators of the DSN station in Robledo. Among their company, the long observing nights were transformed into pleasant leisure. Recollections of the unforgettable discussions with the GBT operators, particularly Kevin Gum, Greg Monk, and Donna Stricklin, will forever brighten my days. I would like to thank Maggie and the ladies at the Green Bank cafeteria for many laughs and chats — the most pleasant aspect of my stay at Green Bank. The company of Leigh and Karen Cameron, Jamie McCallum, and Jim Lovell made Canberra home away from home. I would like to thank Richard DeBritt for hosting me during one of my stays in Australia. Our wonderful dinners and forays into Canberra are among the most memorable moments from my stay there.

Most importantly, I would like to thank Ania, my parents, and my brother for their boundless love, support, and confidence. I feel that any verbal expression of my gratitude would fall short of the significance that they play in my life. *Soyons reconnaissants aux personnes qui nous donnent du bonheur; elles sont les charmants jardiniers par qui nos mes sont fleuries* — Marcel Proust

– PTK

To Ania and My Parents

Chapter 1

Introduction

1.1 Historical Note

The water emission at 22.23508 GHz is caused by a transition of ortho-water between two rotationally excited levels ($6_{16} \rightarrow 5_{23}$) that lie approximately 600 K above the ground state. The extremely high brightness temperatures of the emission from astrophysical sources are not consistent with the conditions of thermal equilibrium and have led Cheung et al. (1969) to suggest that maser action must play a role. The first water maser source in an external galaxy was discovered by Churchwell et al. (1977) in M33. The emission was associated in position with an HII region and its isotropic luminosity (i.e., assuming uniform emission of radiation into a solid angle of 4π str) was comparable to the luminosities of the then known water maser sources in our own galaxy, which by this time had been firmly established to be associated with star formation regions. It was thus immediately suggested that the M33 maser is related to star formation activity. However, Dos Santos & Lepine (1979) reported

a detection of a source in an edge-on spiral galaxy NGC 4945 with an apparent isotropic luminosity ~ 10 times greater than that of the strongest water maser source in our own galaxy (W49). Shortly after, additional very luminous ($> 10\,L_\odot$) maser sources were detected in Circinus (Gardner & Whiteoak 1982), NGC 1068, NGC 4258 (Claussen et al. 1984), and NGC 3079 (Henkel et al. 1984; Haschick & Baan 1985). Their large luminosities were not consistent with the established star formation paradigm. Very Large Array (VLA) observations of NGC 1068 and NGC 4258 also revealed that the maser emission is confined to very small regions of $1 - 4\,\mathrm{pc}$ in size within the nucleus (Claussen & Lo 1986). If the emission was powered by a nuclear starburst, then the inferred space density of young massive stars would be $> 20\,\mathrm{pc}^{-3}$, much larger than the stellar density of $< 3\,\mathrm{pc}^{-3}$ in prototypical starburst galaxies such as M82 and NGC 253. Thus, the newly detected highly luminous maser emission could not be explained by a very large collection of star-forming maser sources.

1.2   Hosts to Maser Emission

Extragalactic water maser emission has been detected by now from two distinct types of astrophysical objects: star-forming regions and active galactic nuclei (AGN). The distinction between these two classes appears to be largely based on apparent isotropic luminosity: the sources associated with AGN (thereafter, nuclear water masers) typically have luminosities $> L_\odot$ while those associated with star formation tend to have $< L_\odot$. The water maser luminosity function (i.e., the number density of objects per luminosity interval) compiled by Henkel et al. (2005) indeed shows

a tentative evidence of a transition at $\sim 1\,L_\odot$, which takes the form of a local minimum in the luminosity function in the $1 - 10\,L_\odot$ bin and which gives credence to this luminosity-based classification system. However, Henkel et al. (2005) result does not account for source variability and beaming effects (whereby the emission might be radiated into a solid angle other than the assumed $4\pi\,\mathrm{str}$) and relies on small number of sources. In fact, the majority of individual data points that constitute the luminosity function are computed from three or fewer number of sources. Nevertheless, evidence for this luminosity-based classification system also comes from the consideration of absorbing column densities. Zhang et al. (2006) find that water maser systems with $< 10\,L_\odot$ tend to be Compton-thin ($N_H < 10^{24}\,\mathrm{cm}^{-2}$) while those with $> 10\,L_\odot$ arise from heavily obscured sources ($N_H > 10^{23}\,\mathrm{cm}^{-2}$), and such large column densities are considered to be an unambiguous signature of nuclear activity. Although the existence of the two distinct types of astrophysical objects that give rise to extragalactic water maser emission is now widely accepted, the ability to differentiate between the two types on source-to-source basis using only spectroscopic data remains limited.

This work is concerned primarily with nuclear water maser systems and it is unlikely that these sources are associated with nuclear starbursts. The peak luminosities of nuclear masers are typically $> L_\odot$, much greater than the typical peak luminosity of $0.05\,L_\odot$ from W49N (Gwinn 1994), the most luminous maser in our galaxy associated with a region of intense star formation. For instance, the isotropic luminosity of the brightest, spatially unresolved spectral feature in NGC 3079 is at least two orders of magnitude greater than the isotropic luminosity corresponding to the total integrated maser flux from other starburst galaxies such as M82 and NGC

253 and from the W49N maser (Trotter et al. 1998; Ho et al. 1987; Baudry et al. 1994; Gwinn 1994). As already mentioned, the starburst hypothesis is also rejected based on the consideration of the inferred stellar space density.

1.3   AGNs and Maser Emission

Active Galactic Nuclei are compact central regions ($< 1\,\text{kpc}$) of galaxies characterized by very large luminosities (bolometric luminosities of $> 10^8\,L_\odot$) that are variable and non-thermal in origin. It is now widely believed that the ultimate source of these extreme luminosities is accretion onto supermassive black holes (e.g., Lynden-Bell 1969). As the material flows towards the central object, it assumes — due to conservation of angular momentum — a flattened geometry such as a torus or a disk. In addition to accretion structures, the active nuclei also host outflows such as jets and winds. Although their matter content and the underlying process that generates these outflows remain under investigation (e.g., Reynolds et al. 1996; Wardle et al. 1998; Hirotani 2005), most proposed formation mechanisms rely on the presence of the accretion geometry and result in an outflow axis perpendicular to this structure on some characteristic scale (e.g., Blandford & Payne 1982; Lynden-Bell 1996; De Villiers et al. 2003, and references therein).

A great majority of AGN that host maser emission are classified optically as Seyfert 2 or LINER. In the context of the unified model for AGN, Seyfert 1 and 2 systems contain a central engine, powered by accretion onto a supermassive black hole, and a pc-scale thick molecular torus or disk surrounding the central engine (Lawrence & Elvis 1982; Antonucci 1993). The observed difference between the

two types of AGN is primarily due to orientation effects: for Seyfert 1s, the central engines are viewed unobstructed and face-on while Seyfert 2 systems are edge-on AGN for which the observer's line-of-sight to the central engine passes through the obscuring structure. Although the unified model remains the most widely accepted paradigm today, it fails to explain the wide range of apparent AGN luminosities, the existence of two distinct AGN classes (i.e., radio-loud and radio-quiet systems), and the preference of radio loud AGN to occur in elliptical galaxies.

Maser emission is also associated with LINERs, which might be present in as many as 30% of local galaxies (e.g., Heckman 1980; Ho et al. 1997a). Although their luminosities are typically lower than that of Seyfert systems, there exists good evidence of a relationship between the LINER and the AGN phenomena. For instance, LINERs are variable at radio (Nagar et al. 2002a), optical (Totani et al. 2005), and UV wavelengths (Maoz et al. 2005), and variability is considered as one of the defining properties of nuclear activity. Approximately half of the LINERs mapped with interferometry show unresolved radio cores, an unambigous signature of a jet (Falcke & Biermann 1999; Falcke et al. 2000; Nagar et al. 2000, 2002a). The systems that contain a compact radio core also tend to display an unresolved X-ray nucleus (Terashima & Wilson 2003). Approximately 10% of LINERs show broad Hα wings in their spectra (Ho et al. 1997c), in analogy with Seyfert 1 systems, and several sources display broad permitted lines in polarized light (Barth et al. 1999a,b), as has also been observed in some Seyfert 2 galaxies (e.g., Antonucci & Miller 1985; Tran 1995).

Water maser emission currently provides the only means of mapping via Very Long Baseline Interferometry (VLBI) the morphology of warm dense molecular gas

in the inner parsec of Seyfert 2 and LINER AGN, and can therefore be used to study the nuclear region in theses sources. Such a tracer is of particular importance for Seyfert 2 and LINER 2 systems, since the presence of an edge-on obscuring geometry hinders the study at other wavelengths.

1.4   High-velocity Systems

Prior to this work, water maser emission had been mapped with VLBI in eight AGN: NGC 4258 (Miyoshi et al. 1995), NGC 1386 (Braatz et al. 1997a), NGC 4945 (Greenhill et al. 1997b), NGC 1068 (Greenhill & Gwinn 1997), NGC 3079 (Trotter et al. 1998), IC 2560 (Ishihara et al. 2001), IRAS F22265-1826 (Ball et al. 2005), and Circinus (Greenhill et al. 2003). In these systems, the maser emission — in the form of numerous unresolved spots — appears to trace a nearly edge-on disk of molecular material 0.1 to 3 pc from a central object. As a consequence of these studies, it is now believed that nuclear maser emission is detected preferentially from edge-on disks along the diameter perpendicular to the line-of-sight (i.e., disk midline) and along the line-of-sight to the dynamical center. These are locations within an edge-on disk where the gradient in line-of-sight velocity vanishes and the coherent paths for maser emission are maximized. It is possible to qualitatively describe a spectrum that emerges from these specific loci in an edge-on disk. Because its velocity vector is in the plane of the sky, emission that occurs along the line of sight to the dynamical center (thereafter, low-velocity or systemic emission) results in a spectral complex at the systemic velocity of the galaxy. The emission that occurs along the midline (thereafter, high-velocity emission) has a velocity vector

along the line of sight and yields a spectral complex offset from the systemic velocity by the orbital velocity of the accretion disk. In particular, if a high-velocity maser feature is located at a disk radius r, it would appear in a spectrum at velocities $v_{sys} + \sqrt{GM/r}$ and $v_{sys} - \sqrt{GM/r}$ for receding and approaching sides of the disk, respectively (where we assumed an edge-on disk and Keplerian rotation around a central object of mass M). If the maser emission traces a range of disk radii, then the detected emission will occupy the corresponding range of velocities in the spectrum. In particular, if the high-velocity emission occupies a fractional range of disk radii $\Delta r/r$, then it will extend over $\Delta v/v \approx \Delta r/2r$ in velocity (where we assumed Keplerian rotation law, $v \propto r^{-0.5}$, and differentiated it with respect to r). Water maser sources that display high-velocity spectral features are referred to here as high-velocity systems and constitute approximately 40% of known water maser sources. In practice, classification of water maser systems as high-velocity is often hindered by the asymmetry of and irregularities in the actual spectra.

The study of high-velocity systems has significantly contributed to our understanding of the inner-parsec of AGN. In three sources (e.g., Greenhill & Gwinn 1997; Greenhill et al. 2003; Herrnstein et al. 2005), maps and spectra obtained with VLBI have been used to infer geometrical shapes, sizes, and orientations of accretion disks as well as to determine masses of central black holes to better than 20%. Black hole masses in these three systems have been inferred to be $(3.9 \pm 0.1) \times 10^7 \, M_\odot$, and $(1.7 \pm 0.3) \times 10^6 \, M_\odot$, and $(8.0 \pm 0.3) \times 10^6 \, M_\odot$ for NGC 4258 (Herrnstein et al. 2005), Circinus (Greenhill et al. 2003), and NGC 1068 (Lodato & Bertin 2003, but $\sim 1.5 \times 10^7 \, M_\odot$ under an alternative model presented in Greenhill et al. 1997), respectively. In NGC 4258, maser emission closely follows the Keplerian rotation

($v \propto r^{-0.5}$) and appears to trace a geometrically-thin, warped, and nearly edge-on (82°) accretion disk between radii of 0.16 and 0.28 pc (Herrnstein et al. 2005). The rotation curve in NGC 1068 on the other hand is sub-Keplerian ($v \propto r^{-0.31}$), which is suggestive of a massive ($\sim 9 \times 10^6 \, M_\odot$) and hence self-gravitating accretion disk of size $0.6 - 1.3$ pc (Greenhill & Gwinn 1997; Lodato & Bertin 2003). Maser emission in Circinus follows the Keplerian rotation and traces not only a warped, edge-on disk between radii of 0.11 and 0.40 pc but also a pc-scale wide-angle outflow (Greenhill et al. 2003).

VLBI imaging experiments have been attempted on five additional high-velocity systems. Although these studies failed to constrain the black hole masses and disk geometries as precisely, they nevertheless provided an invaluable insight into the inner-parsec of these AGN. In NGC 3079, the maser emission traces predominantly the approaching side of the accretion disk and is consistent with a binding mass of $\sim 10^6 \, M_\odot$ (Trotter et al. 1998). In this system, the emission appears disorganized and is therefore not consistent with a thin differentially-rotating accretion disk. Although the emission is also not well ordered kinematically in the case of IRAS F22265-1826, it has been interpreted in the context of a geometrical structure of radius ~ 3 pc in rotation about a central object of mass $\sim 10^7 \, M_\odot$ (Ball et al. 2005). The maser emission in NGC 1386 traces a linear structure 1.2 pc in extent but does not show an unambiguous signature of rotation (Braatz et al. 1997a). The evidence for rotation is stronger in the case of NGC 4945, where the red- and blue-shifted emission is symmetric on the sky about the systemic emission and the position-velocity diagram indicates a central mass of $\sim 10^6 \, M_\odot$ (Greenhill et al. 1997b). Although only the systemic emission has been mapped with VLBI in IC 2560, the measured centripetal

acceleration and the total-power spectra are suggestive of a $3 \times 10^5\, M_\odot$ binding mass (Ishihara et al. 2001).

In addition to mapping pc-scale molecular disk structure and accurately weighing supermassive black holes, nuclear high-velocity water maser emission has also been used as a distance indicator. Distance determination is possible for systems where a detailed model of the accretion disk from VLBI is combined with a measurement of either maser proper motions or drifts in line-of-sight velocity of spectral features (i.e., centripetal acceleration). A distance to NGC 4258 obtained in this manner is completely independent of standard candles like Cepheids and SN Ia supernova, is the most precise distance ever measured (Herrnstein et al. 1999), has provided the most stringent test of the revised Key Project distance scale, and might establish a new primary step in the extragalactic distance ladder (Freedman et al. 2001; Newman et al. 2001; Macri et al. 2006).

1.5 Outstanding Questions

Although the causal relationship between accretion onto supermassive black holes and nuclear activity is widely accepted, several outstanding questions remain. For instance, recent work has suggested that nuclear starbursts might contribute significantly to AGN luminosity. Young massive stars with ages $\leq 10^7$ years have indeed been detected within $\sim 200\,\mathrm{pc}$ of 30% to 50% of nuclei surveyed (Mas-Hesse et al. 1994, 1995; Cid Fernandes et al. 2001, and references therein). Among the Seyfert galaxies studied with the Spitzer Space Telescope, approximately half display strong polycyclic aromatic hydrocarbon features (Buchanan et al. 2006), which are

considered to be an unambiguous signature of starburst activity (but see Krolik 2001). As a result, it has been suggested that star formation and nuclear activity are likely to coexist in galactic nuclei, either because they are coupled through evolutionary mechanisms, or simply because they both depend on gas inflow and accretion (Cid Fernandes et al. 2001, and references therein). The relationship between nuclear star-formation and the central black hole is one of the most notable questions within the field of AGN studies.

The relationship between the central supermassive black hole and its host galaxy is an issue that is currently most intensely investigated. The temporal evolution of the central black hole and of the host galaxy might be closely coupled. This is supported by the $M - \sigma$ relationship, the correlation between black hole mass and the central stellar velocity dispersion, reported for broad samples of galaxies (Gebhardt et al. 2000a, 2000b; Ferrarese & Merritt 2000; Ferrarese et al. 2001). In its present form, the correlation is based on black hole mass estimates that are imprecise and might be sensitive to systematic errors. VLBI study of water maser emission currently provides the most precise method of determining black hole masses in AGN. Such measurements conducted for a large sample of water maser systems can provide a stringent test of other techniques for the determination of black hole masses and yield an independent estimate for the slope of the $M - \sigma$ relationship and one with much lower uncertainty.

Another outstanding question concerns the line-of-sight obscuring column density inferred from X-ray studies. As originally proposed in the unified scheme of active galaxies, this obscuration is due to a dusty toroidal (i.e., doughnut-shaped) structure in a hydrostatic equilibrium with $H \sim R$ (Lawrence & Elvis 1982; Krolik &

Begelman 1988; Antonucci 1993). However, because water maser emission requires high densities, pc-scale accretion disks that host the maser emission might also provide the measured obscuration (Greenhill et al. 2003; Herrnstein et al. 2005; Fruscione et al. 2005; Madejski et al. 2006). The observed hydrogen column densities might also be due to a wind that consists of dusty and optically-thick clumps hydromagnetically uplifted from the surface of the pc-scale accretion disk (Emmering et al. 1992; Kartje et al. 1999; Elitzur & Shlosman 2006). In this context, it has been suggested that H/R of the resulting hydromagnetic disk wind decreases as the mass accretion rate diminishes (Elitzur & Shlosman 2006), which is consistent with the smaller obscuration observed in lower luminosity AGN, the LINER systems (Maoz et al. 2005).

The geometry and the orientation of the nuclear region remain poorly understood. Based on studies of water maser systems, the accretion structures occupy regions from sub-parsec to parsec in extent, while the obscuring torus, as imaged via interferometry in the infrared, appears only slightly larger ($\sim 4\,\text{pc}$ in NGC 1068; Jaffe et al. 2004). These dimensions and their dependence on central engine parameters (i.e., luminosity, accretion rate, central mass, etc.) are of great interest. For instance, if both tori and disks are present (as in the particular case of NGC 1068; Greenhill & Gwinn 1997; Lodato & Bertin 2003; Jaffe, W., et al. 2004), do they overlap at a range of radii as in the hydromagnetic wind scenario (Emmering et al. 1992; Kartje et al. 1999; Elitzur & Shlosman 2006) or is there a well-defined transition from one structure to the other (e.g., Gallimore et al. 2004)? In addition, is the pc-scale accretion structure typically in the form of a geometrically-thick massive disk as in NGC 3079 or a geometrically-thin differentially-rotating disk

as in NGC 4258? Are warps in the accretion geometry prevalent? What is the orientation of the pc-scale accretion geometry relative to the outflow axis and the much larger kpc-scale stellar disk? As a tracer of pc-scale structures surrounding the supermassive black holes — both outflows and accretion geometries — water maser emission can be used to address some of these questions.

1.6 Models for Nuclear Maser Emission

Because of the association of maser emission with nuclear activity, it has been suggested that the two phenomena are causally related. Irradiation of molecular gas by X-rays from the central engine is indeed a plausible means of exciting maser emission. Detailed modelling work by Neufeld et al. (1994) suggests that a slab directly illuminated by a central X-ray power-law source gives rise to a molecular layer in which physical conditions are conducive to maser action (i.e., temperatures of $250 - 1000\,\mathrm{K}$ and H_2 number densities of $10^{8-10}\,\mathrm{cm}^{-3}$). For a wide range of gas pressure and incident X-ray flux, Neufeld et al. (1994) compute luminosities of $10^{2\pm0.5}\,L_\odot$ per pc^2 of irradiated area. These luminosity surface densities are sufficient to explain the large apparent isotropic luminosities of nuclear water maser sources, which occupy regions roughly $1\,\mathrm{pc}$ in extent. For instance, assuming an inner disk radius of $0.1\,\mathrm{pc}$, the model yields apparent luminosities of $4 - 40\,L_\odot$, which is consistent with luminosities observed for most nuclear water maser systems. If absorption of infrared radiation by dust grains is included, the model can produce maser luminosities more than an order of magnitude larger ($3800\,L_\odot\,\mathrm{pc}^{-2}$; Collison & Watson 1995). These calculations assume small velocity dispersions ($1\,\mathrm{km\,s}^{-1}$,

consistent with NGC 4258) and X-ray irradiation of only the inner surface of the disk. A larger velocity dispersion in the gas and irradiation of the upper and lower surfaces of the disk (due to scattering or disk warp) would further increase the calculated luminosities, which might make the model consistent with brighter water maser sources such as IRAS F22265-1826 ($\sim 6000\,L_\odot$; Koekemoer et al. 1995).

The Neufeld et al. (1994) model and its extension by Collison & Watson (1995) explains the association of maser emission with nuclear activity. Maser emission might be associated with Seyfert 2 systems in particular perhaps because the long gain paths for maser emission provided by the edge-on obscuring geometry are necessary to generate emission bright enough for us to detect. The importance of the obscuring geometry is indeed supported by an empirical observation that nuclear water maser sources are found preferentially in AGN with large hydrogen column densities ($N_H > 10^{24}\,\mathrm{cm}^{-2}$; Braatz et al. 1997b; Madejski et al. 2006; Zhang et al. 2006). In particular, $\sim 50\%$ of nuclear water maser sources arise from Compton-thick AGN ($N_H > 10^{24}\,\mathrm{cm}^{-2}$) and $\sim 85\%$ from heavily obscured systems ($N_H > 10^{23}\,\mathrm{cm}^{-2}$; Zhang et al. 2006). Among 11 active nuclei that host high-velocity water maser emission and with available column density measurements, eight are Compton-thick (Madejski et al. 2006). The association of maser emission with LINER systems is more difficult to understand. As already mentioned, the LINER and AGN phenomena might be closely related and it is possible that a large fraction of LINERs correspond to low-luminosity analogues of Seyfert 2 systems (e.g., Ho et al. 1997b; Ho 1999a; Ho et al. 2003; Kewley et al. 2006). Thus, the distinction between these two types of activity in the context of maser emission might simply be one of luminosity.

Nuclear maser emission has also been associated with jets arising from central engines. For instance, the maser emission in MRK 348 displays variability correlated with the radio continuum flux and arises from a region also occupied by a radio continuum component that is believed to be a part of a receding jet (Peck et al. 2003). VLBI study of the water maser in NGC 1052 established that the emission lies along the radio jet (Claussen et al. 1998) and is therefore most likely associated with it. In both of these sources, the emission lines appear relatively broad ($> 90 \, \mathrm{km \, s^{-1}}$), which is in contrast to $\sim 1 \, \mathrm{km \, s^{-1}}$ spectral line widths found in most other nuclear water maser systems. It is possible that the radio continuum emission from the jet is amplified by foreground molecular clouds, which results in the observed maser emission. However, it is also likely that the maser emission actually arises in shocks created by a jet as it impacts the interstellar medium. In this context, numerical calculations by Elitzur et al. (1989) showed that water is indeed abundant in long filamentary structures behind dissociative, high-velocity ($\geq 50 \, \mathrm{km \, s^{-1}}$), interstellar shocks. The predicted water column densities in the resulting warm post-shock gas are high enough to account for luminosities of brightest galactic sources. The model might also explain the unusually high luminosities of jet masers but only if magnetic fields in these sources are enhanced ($\gtrsim 50 \, \mathrm{mG}$) or for extreme filament elongations (i.e., ratio of length to width of > 70).

Regardless of the actual model for maser emission, beaming effects most likely play an important role in the production of the observed radiation. For instance, the apparent luminosities in Neufeld et al. (1994) model are computed by integrating the luminosity surface density over the illuminated inner edge of the disk, which ignores the manifest spot-like nature of water maser emission. Taking under consideration

the clumpiness of the medium, it becomes difficult to explain with single isolated clumps the unusually large isotropic luminosities of nuclear maser sources. In particular, an isolated clump of size $0.005\,\mathrm{pc}$ (expected clump size in NGC 3079 and NGC 4258; Kondratko et al. 2005; Yamauchi et al. 2005) irradiated by X-ray emission from one side can produce an isotropic luminosity of $0.3\,L_\odot$ (Neufeld et al. 1994; Collison & Watson 1995). However, a maser whose emission is beamed into a solid angle Ω has a true luminosity less than the isotropic luminosity by a factor of $\Omega/4\pi$. The detection rates of water maser emission among active galaxies ($\sim 5\%$) have been interpreted as suggesting $4\pi/\Omega \sim 20$ (Braatz et al. 1994). The beam angle in NGC 4258 has been inferred to be $\sim 7°$ (Miyoshi et al. 1995) and, as a result, the actual luminosity in this system is a factor of $4\pi/\Omega = 4\pi/(2\pi \times 7°) \sim 16$ smaller than isotropic. Small beaming angles are a natural consequence of amplification of emission from compact background continuum sources or of overlap on the sky of two or more clumps or filaments (Deguchi & Watson 1989; Kartje, Königl, & Elitzur 1999).

1.7   Past Surveys in Search of Maser Emission

Before this work, nuclear water maser emission had been detected in approximately 40 sources (Fig. 1.1). The first large scale attempt to detect emission among AGN was the seminal survey by Braatz et al. (1996) using Parkes and Effelsberg radio antennas. That work with $1\sigma \sim 60\,\mathrm{mJy}$ sensitivity (in $\sim 1\,\mathrm{km\,s^{-1}}$ spectral channels) yielded a detection of ten new sources and an incidence rates of water maser emission among nearby ($v_{sys} < 7000\,\mathrm{km\,s^{-1}}$) Seyfert 2 and LINER systems of $\sim 7\%$. A search

for water emission among 29 AGN with the NASA Deep Space Network (DSN) 70-m antenna at Goldstone (Greenhill et al. 1997a) and a survey among 131 AGN and star-forming galaxies with the Parkes 64-m radio telescope at Parkes, Australia (Greenhill et al. 2002) each resulted in only one new detection. As these past results suggest, each maser discovery has been challenging and hard won. Because the extragalactic maser emission is weak, typically $\ll 1$ Jy, a successful detection has required long integration times (~ 1 hour per target) and most sensitive apertures like the DSN and Effelsberg telescopes. Moreover, because the velocity extent of emission is determined by the Keplerian velocity of the masing accretion disk ($\gg 100$ km s^{-1}) and the maser emission lines in AGN are typically very narrow (≤ 1 km s^{-1}), spectrometers capable of both wide bandwidth and high resolution are necessary to conduct the surveys. Until 2001, observing systems that combined large apertures, wide-bandwidth receivers, and wide-bandwidth, high resolution spectrometers were largely unavailable. Consequently, nearly all maser surveys to that point were biased against the detection of the high-velocity systems, which are the most astrophysically interesting sources. This bias is certainly plausible considering the statistics of currently known nuclear water maser sources: approximately half of high-velocity systems (10 out of 20) display high-velocity emission weaker than systemic emission, although the uncertainty due to counting statistics is large (11%).

To discover more high-velocity systems and in response to incompleteness of previous surveys, we assembled a custom-built spectrometer with $5300 \, \mathrm{km \, s^{-1}}$ bandwidth and began an all-sky survey with the two NASA DSN 70-m antennas at Tidbinbilla, Australia and at Robledo, Spain. We have also used the 100-m Green Bank Telescope (GBT), the most sensitive radio telescope currently in operation at
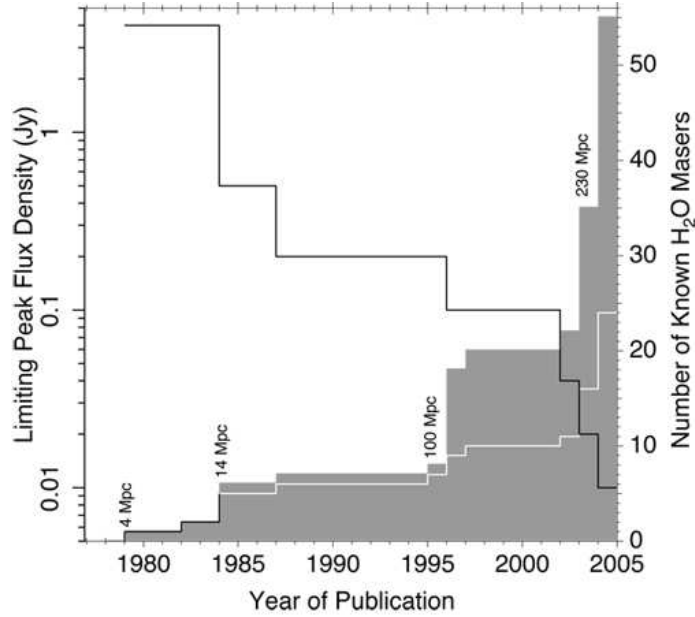
Figure 1.1.— Figure, reproduced from Greenhill (2004), shows the increase over time in the number of known nuclear water maser sources (shaded region) and of high-velocity systems (white line), the corresponding decrease in the peak flux density for the weakest source at each epoch (black line), and the increase in the maximum distance at which maser emission has been detected (text labels).

1.3 cm, to conduct a search for water maser emission in distant sources ($v_{sys} > 10^4$ km s^{-1}) and in edge-on systems (galaxy inclination $> 70°$), and to search for weak high-velocity emission in previously known sources. We have discovered a total of 23 new water maser sources, thereby increasing the number of known nuclear water masers by 60% to ~ 60. Among the new discoveries, eight are high-velocity systems and therefore constitute good candidates for the determination of black hole mass and geometric distance. We also detected with the GBT weak high-velocity emission from as many as four previously known water maser sources, which is consistent with the existence of the aforementioned bias.

1.8   Outline of Thesis

This work has been divided into two parts effectively by subject matter. The first part, chapters 1-3, contains the results obtained with single-dish telescopes. In particular, in chapter one, we present the discovery spectra of eight nuclear water maser sources obtained with the two NASA DSN antennas. The remaining seven DSN discoveries are reported in Greenhill et al. (2003). Chapter two presents the discovery of water maser emission in five active galactic nuclei (AGN) with the GBT and a possible correlation between water maser and nuclear $2 - 10\,\mathrm{keV}$ luminosities. Finally, in chapter three, we report the discovery of three nuclear water maser sources with the GBT, present sensitive maser spectra of nine previously known sources, and describe monitoring results of three others. In this chapter, we also report the lack of statistical evidence for the preference of maser emission to occur in edge-on galaxies.

The second part of the thesis, chapters four and five, contain follow-up VLBI imaging studies of two nuclear water maser systems. In these chapters, we use the position and line-of-sight velocity of nuclear water maser emission from VLBI to determine the masses of the central objects as well as the geometries and the orientations of the accreting structures. In particular, in chapter four, we report the evidence for a geometrically thick self-gravitating and possibly star-forming accretion disk in NGC 3079. In chapter five, we present the VLBI map of nuclear water maser in NGC 3393 and interpret the results in terms of a pc-scale differentially-rotating edge-on accretion disk. All five chapters are in a format appropriate for papers submitted to the Astrophysical Journal.

Chapter 2

Discovery of Water Maser Emission in Eight AGN with 70-m Antennas of NASA's Deep Space Network

P. T. Kondratko, L. J. Greenhill, J. M. Moran, J. E. J. Lovell, T. B. H. Kuiper, D. L. Jauncey, L. B. Cameron, J. F. Gómez, C. García-Miró, E. Moll, I. de Gregorio-Monsalvo, J. McCallum, and E. Jiménez-Bailón

Abstract

We report the discovery of water maser emission in eight active galactic nuclei (AGN) with the 70-m NASA Deep Space Network (DSN) antennas at Tidbinbilla, Australia and Robledo, Spain. The positions of the newly discovered masers, measured with the VLA, are consistent with the optical positions of the host nuclei to within 1σ ($0\rlap{.}''3$ radio and $1\rlap{.}''3$ optical) and most likely mark the locations of the embedded central engines. The spectra of two sources, NGC 3393 and NGC 5495, display the characteristic spectral signature of emission from an edge-on accretion disk, with orbital velocities of ~ 600 and $\sim 400\,\mathrm{km\,s^{-1}}$, respectively. In a survey with DSN facilities of 630 AGN selected from the NASA Extragalactic Database, we have discovered a total of 15 water maser sources. The resulting incidence rate of maser emission among nearby ($v_{sys} < 7000$ km s^{-1}) Seyfert $1.8 - 2.0$ and LINER systems is $\sim 10\%$ for a typical rms noise level of $\sim 14\,\mathrm{mJy}$ over $1.3\,\mathrm{km\,s^{-1}}$ spectral channels. As a result of this work, the number of nearby AGN ($v_{sys} < 7000$ km s^{-1}) observed with $< 20\,\mathrm{mJy}$ rms noise has increased from 130 to 449.

2.1 Introduction

Water maser emission ($\lambda = 1.3$ cm) is currently the only resolvable tracer of warm dense molecular gas in the inner parsec of active galactic nuclei (AGN) and has been detected to-date in approximately 60 nuclei. In eight water maser systems that have been studied with sub-milliarcsecond resolution using Very Long Baseline Interferometry (VLBI), the mapped emission appears to trace structure

and dynamics of molecular disks 0.1 to 1 pc from supermassive black holes: Circinus (Greenhill et al. 2003), NGC 1068 (Greenhill & Gwinn 1997), NGC 4258 (Miyoshi et al. 1995), NGC 3079 (Trotter et al. 1998), IC 2560 (Ishihara et al. 2001), NGC 5793 (Hagiwara et al. 2001a), NGC 4945 (Greenhill et al. 1997b), NGC 1386 (Braatz et al. 1997a). Due to spatial coherence in line-of-sight velocity within the rotating structures, maser emission is detected preferentially in edge-on disks along the midline (i.e., the diameter perpendicular to the line of sight) and close to the line of sight towards the center. A characteristic spectral signature of emission from an edge-on disk thus consists of a spectral-line complex in the vicinity of the systemic velocity (low-velocity emission) and two spectral-line complexes symmetrically offset from the systemic velocity by the orbital velocity of the disk (high-velocity emission). Sources that display such spectra are referred to here as high-velocity systems and constitute $\sim 40\%$ of the known nuclear water masers.

The study of high-velocity systems with VLBI has significantly contributed to our understanding of the immediate vicinity (i.e., $\lesssim 1\,\mathrm{pc}$) of supermassive black holes. In three of these systems — NGC 4258 (Miyoshi et al. 1995), NGC 1068 (Greenhill & Gwinn 1997), and the Circinus Galaxy (Greenhill et al. 2003) — resolved position and line-of-sight velocity data provided evidence for differential rotation and enabled accurate estimation of black hole mass and pc-scale molecular disk structure. Another system, NGC 3079, in which the rotation curve traced by the maser emission appears flat, was interpreted in the context of a pc-scale, thick, edge-on, self-gravitating, and possibly star forming molecular disk (Kondratko et al. 2005; Yamauchi et al. 2004). In addition to mapping pc-scale molecular disk structure and accurately weighing supermassive black holes, nuclear water maser

emission has also been used as a distance indicator. Distance determination is possible for systems where a robust pc-scale disk model from VLBI maps is combined with a measurement of either maser proper motions or drifts in line-of-sight velocity of spectral features (i.e., centripetal acceleration). The distance to NGC 4258 obtained in this manner is the most accurate extragalactic distance thus far, is independent of standard candle calibrators such as Cepheids (Herrnstein et al. 1999), and it has contributed to analysis of the Cepheid period-luminosity relation (Freedman et al. 2001; Newman et al. 2001).

The ~ 60 known nuclear water masers are in the great majority of cases associated with Seyfert $1.8 - 2.0$ or LINER nuclei; only five systems are exceptions: NGC 5506 (NLSy1 from Nagar et al. 2002b; Braatz et al. 1996), NGC 4051 (Sy1.5 from the NED; Hagiwara et al. 2003b), NGC 2782 (Sy1, starburst from the NED; Braatz et al. 2004), NGC 4151 (Sy1.5 from the NED; Braatz et al. 2004), and 3C 403 (FRII; Tarchi et al. 2003). In the context of the unified AGN model, Seyfert $1.8 - 2.0$ systems contain an active nucleus and an obscuring structure along the line of sight to the central engine (Lawrence & Elvis 1982; Antonucci 1993). Irradiation of molecular gas by X-rays from the central engine is a plausible means of exciting maser emission (e.g., Neufeld, Maloney, & Conger 1994), which might explain the association of maser emission with nuclear activity in general. Maser emission might be associated with Seyfert $1.8 - 2.0$ systems in particular because, over a range of AGN luminosity, the shielding column density that provides the obscuring geometry maintains not only a reservoir of molecular gas but also physical conditions conducive to maser action, which are temperatures of $250 - 1000\,\mathrm{K}$ and H_2 number densities of $10^{8-10}\,\mathrm{cm}^{-3}$ (e.g., Desch, Wallin, & Watson 1998). Since

there is good evidence for a physical relationship between LINER systems and the AGN phenomenon (e.g., Ho et al. 1997b; Ho 1999a; Ho et al. 2003), the distinction between these two types of activity in the context of maser emission might simply be one of luminosity, whereby a large fraction of LINERs correspond to low-luminosity analogues of Seyfert $1.8 - 2.0$ systems.

Since water maser emission is typically weak ($\ll 0.1$ Jy) and the velocity range of emission is determined by the orbital velocity of the molecular disk ($\gg 100$ km s^{-1}), surveys designed to detect new water maser sources require both large, sensitive apertures and wide bandwidth spectrometers. The detection rate of water maser emission among Seyfert 2 and LINER galaxies with $v_{sys} < 7000$ km s^{-1} is $\sim 4\%$ for surveys with a typical rms noise level on each source of ~ 60 mJy (thereafter, sensitivity; Braatz et al. 1996). This low detection rate, the weakness of the emission, and its potential wide velocity range make the discovery of new water maser sources challenging. Most past survey work has been characterized by limited sensitivity (~ 60 mJy) and narrow bandwidths (~ 700 km s^{-1}) and thus might have missed new maser sources because the emission was either too weak or outside the observing bands. These limitations of the previous surveys provide the major impetus for the present work. We note that a recent survey with ~ 3 mJy sensitivity (converted to 1.3 km s^{-1} spectral channels) using the Green Bank Telescope (GBT) has yielded a detection rate of $\sim 20\%$ among Seyfert 2 and LINER systems with $v_{sys} < 7500$ km s^{-1}, though it was limited to just 145 sources (Braatz et al. 2004).

In order to discover more high-velocity systems, we procured a custom-built 4096-channel spectrometer with 5300 km s^{-1} bandwidth and are conducting a survey with the 70-m NASA Deep Space Network (DSN) antennas at Tidbinbilla,

Australia and at Robledo, Spain. We selected our sample from among 1150 AGN with $v_{sys} < 14600\,\mathrm{km\,s^{-1}}$ listed in the NASA Extragalactic Database (NED), with preference for Seyfert $1.8 - 2.0$ and LINER systems at lower recessional velocities. Thus far, we have discovered water maser emission in 15 AGN. The first seven discoveries were reported in Greenhill et al. (2003); here, we present spectra of eight most recent detections.

2.2 Observations

The discoveries reported here were obtained during the 2004-2005 northern winter with the Robledo 70-m antenna and during the 2003 and 2005 southern winters with the Tidbinbilla 70-m antenna. The observing system at Tidbinbilla and its calibration was described in Greenhill et al. (2003). The observing system setup at Robledo was identical to that at Tidbinbilla. We estimated the gain curve and aperture efficiency of the Robledo antenna through measurement of opacity corrected antenna temperature of 3C 147, for which we adopted a flux density of 1.82 Jy at 22.175 GHz (Baars et al. 1977). The resulting peak efficiency was 0.43 ± 0.09 at $43° \pm 5°$ elevation, which yields a sensitivity of $1.7 \pm 0.3\,\mathrm{Jy\,K^{-1}}$.

To obtain single-polarization total-power spectra of each source, we moved the telescope every 30 or 45 s between the target source and a reference position on the sky $\sim 0.2°$ away. Antenna rms pointing errors were typically $7''$ and system temperatures ranged from 40 to 75 K depending on elevation and weather. Typical 1σ noise levels attained in an integration time (on+off source) of one hour were $\sim 8 - 17\,\mathrm{mJy}$ in a $1.3\,\mathrm{km\,s^{-1}}$ channel. The spectra reported here have been Hanning

smoothed to an effective resolution of $3.5\,\mathrm{km\,s^{-1}}$ and corrected for atmospheric opacity estimated from tipping scans.

2.3   Results

During the 2003 and 2005 southern winters, we detected maser emission in six AGN with the Tidbinbilla antenna: AM 2158-380 NED02, IC 0184, NGC 0235A, NGC 0613, NGC 3393, and NGC 5495 (Fig. 2.1 and Table 2.1). Maser emission from NGC 4293 and VII ZW 073 was detected during the 2004-2005 northern winter with the Robledo antenna. Each discovery was confirmed by at least one observation with another instrument (Table 2.1). Positions of the maser emission measured with the Very Large Array (VLA) of the NRAO[1] are consistent with optical positions of the AGN to within 1σ ($0\rlap{.}{''}3$ radio and $1\rlap{.}{''}3$ optical; Table 2.1), which confirms the association of the discovered emission with nuclear activity.

The nuclei that are host to the detected maser emission are spectroscopically classified as Seyfert 2 or LINER in all but two cases (Table 2.1). Ambiguity remains in the case of NGC 0613, which is listed as a possible Seyfert by Veron-Cetty & Veron (1986), and in the case of NGC 0235A, which is classified as Seyfert 2 by Monk et al. (1986) but as Seyfert 1 by Maia et al. (1987). There is some indication of a broad component in Hα in the optical spectrum presented by Maia et al. (1987) (the Monk et al. (1986) spectrum does not cover the wavelength of Hα). However,

---

[1]The National Radio Astronomy Observatory is operated by Associated Universities, Inc., under cooperative agreement with the National Science Foundation

Table 2.1.   Newly Discovered Nuclear Masers.

Galaxy	Type[a]	α_{2000}[b] (hhmmss)	δ_{2000}[b] (ddmmss)	v_{sys}[c] (km s^{-1})	$\log_{10} L_{H_2O}$[d] ($\log_{10} L_\odot$)	Date[e] (ddd-yy)	T[f] (s)	1σ[g] (mJy)	Misc[h]
NGC 0235A	Sy2	00 42 52.81	−23 32 27.7	6519	2.0	214-03	2280	15	TV
		00 42 52.81	−23 32 27.8						BnA
NGC 0613	Sy	01 34 18.23	−29 25 06.6	1468	1.2	174-03	1680	16	TV
		01 34 18.18	−29 25 06.5						BnA
IC 0184	Sy2	01 59 51.23	−06 50 25.4	5287	1.4	183-05	8760	7	GV
		01 59 51.23	−06 50 25.4						CnB
VII ZW 073	Sy2	06 30 25.57	+63 40 41.2	11899	2.2	337-04	19560	6	GRV
		06 30 25.54	+63 40 41.3			353-04			B
NGC 3393	Sy2	10 48 23.46	−25 09 43.4	3704	2.4	167-03	6120	8	GTV
		10 48 23.45	−25 09 43.6			174-03			BnA
NGC 4293	LINER	12 21 12.89	+18 22 56.6	890	0.1-0.7	056-04	15420	5	RV
		12 21 12.82	+18 22 57.4			063-04			B
NGC 5495	Sy2	14 12 23.35	−27 06 28.9	6589	2.3	215-03	2820	10	GV
		14 12 23.35	−27 06 29.2						BnA
AM 2158-380 NED02	Sy2	22 01 17.07	−37 46 24.0	9661	2.7	175-05	11460	7	GTV
		22 01 17.10	−37 46 23.0			178-05			CnB

[a] Activity type. NGC 5495 is classified as Seyfert 2 by Kirhakos & Steiner (1990b), NGC 3393, IC 0184, VII ZW 073, and AM 2158-380 NED02 are listed as Seyfert 2 in the Veron-Cetty catalogue (Véron-Cetty & Véron 2003), NGC 0613 is classified as a possible Seyfert by Veron-Cetty & Veron (1986), NGC 4293 is listed as LINER by Ho et al. (1997a), while NGC 0235A is classified as Seyfert 1 by Maia et al. (1987) but as Seyfert 2 by Monk et al. (1986). Refer to the text for the discussion of the ambiguity in NGC 0235A spectral classification.

[b] *First line:* optical positions from the NED with uncertainties of $\pm 1''3$. *Second line:* maser positions measured with a VLA snapshot with typical uncertainties of $\pm 0''3$. In an effort to test for systematic errors in the derived maser positions, we imaged disjoint segments of the VLA data and confirmed that they yield consistent maser positions (that is, within $0''3$).

[c] Heliocentric systemic velocity computed assuming the radio definition of Doppler shift.

[d] Total water maser luminosity assuming isotropic emission of radiation and distances based on $H_o = 75\,\mathrm{km\,s^{-1}\,Mpc^{-1}}$, except for for NGC 0613 and NGC 4293, whose distances were adopted to be 17.9 Mpc (Jungwiert et al. 1997) and 17 Mpc (Tully 1988), respectively.

[e] Data obtained at listed epochs were combined to form a single spectrum.

[f] Total integration time on+off source.

[g] Rms noise in a $1.3\,\mathrm{km\,s^{-1}}$ spectral channel, corrected for atmospheric opacity (typically ~ 0.07) and for the dependence of antenna gain on elevation.

[h] *First line:* Instruments used to confirm the initial detections: G=GBT, R=Robledo, T=Tidbinbilla, V=VLA. The velocities and flux densities of the narrow spectral peaks in AM 2158-380 NED02, NGC 0235A, NGC 3393, NGC 5495, and NGC 4293 detected with the VLA agree with those measured using the Tidbinbilla antenna to within $1.3\,\mathrm{km\,s^{-1}}$ and 30%, respectively. On the other hand, a $6\,\mathrm{km\,s^{-1}}$ discrepancy in the velocity centroid of the NGC 0613 spectral-line likely reflects uncertainty due to noise in the Tidbinbilla spectrum. Although the peak flux densities of the IC 0184 maser agree to within 20%, the velocity centroids are in disagreement by $5\,\mathrm{km\,s^{-1}}$, which is again most likely due to low signal-to-noise ratio in the Tidbinbilla spectrum. The strengths of the VII ZW 073 maser measured with the VLA and the Robledo antenna differ by a factor of 2.5 (time baseline of 5 months), which could be due to either maser variability or low signal-to-noise ratio in both spectra. We note that such variability is not unusual (e.g., Baan & Haschick 1996). The flux densities of AM 2158-380 NED02, IC 0184, NGC 3393, NGC 5495, and VII ZW 073 measured with the DSN and the GBT antennae agree to within 25%. (The GBT spectra will be presented in a follow-up article.) *Second line:* Configuration of the VLA. The VLA bandwidth was 6.25 MHz (channel spacing of $1.3\,\mathrm{km\,s^{-1}}$) for all imaged sources except NGC 0613, where a wider bandwidth of 25 MHz (channel spacing of $11\,\mathrm{km\,s^{-1}}$) was necessary in order to include all the emission.
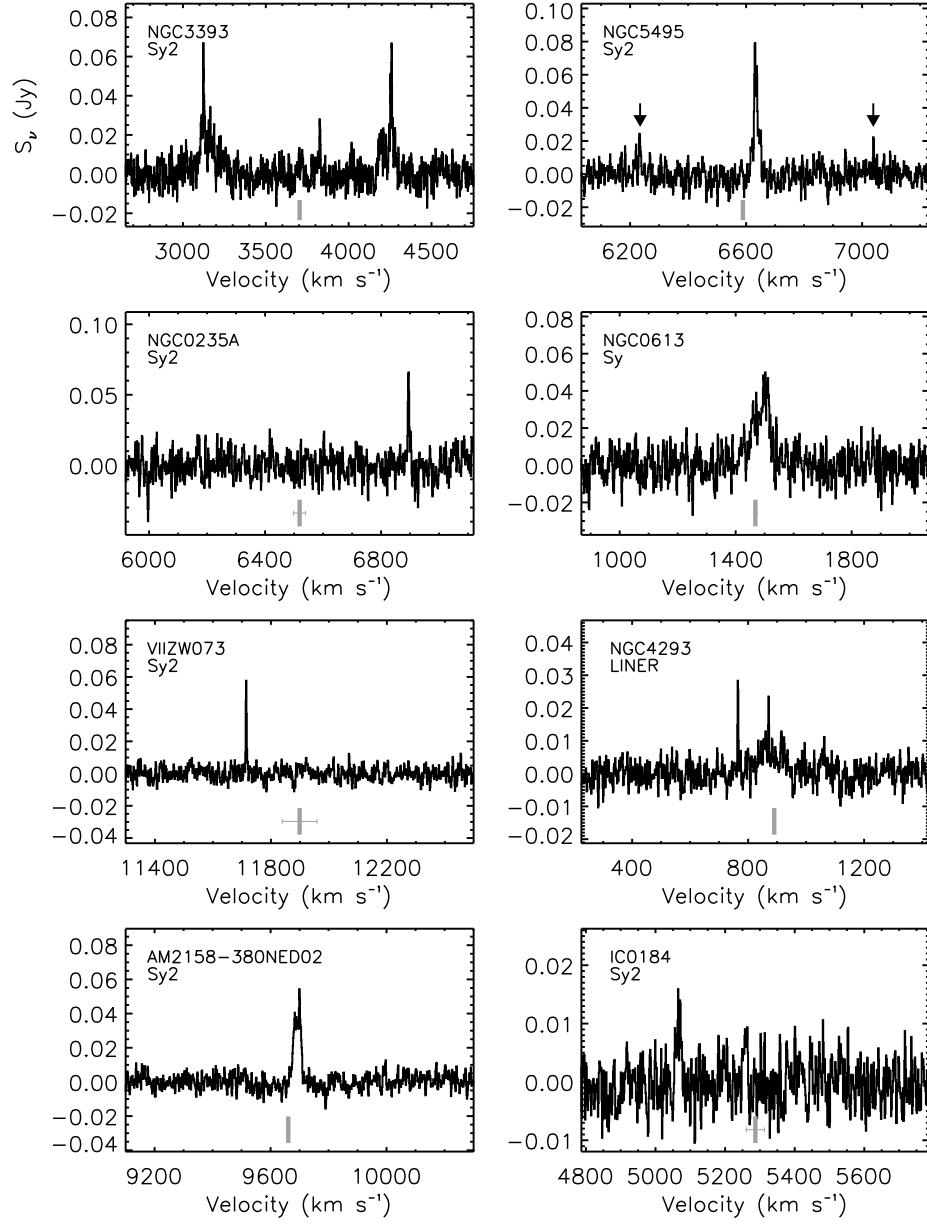
Figure 2.1.— Spectra of NGC 3393, NGC 5495, NGC 0235A, NGC 0613, VII ZW 073, NGC 4293, AM 2158-380 NED02, and IC 0184 obtained with the 70-m Deep Space Network antennas at Tidbinbilla, Australia and Robledo, Spain. The arrows indicate NGC 5495 high-velocity features confirmed with the GBT. The velocity was computed in accordance with the radio definition of Doppler Shift and in the heliocentric reference frame. Vertical bars depict systemic velocities of the host galaxies and respective uncertainties.

optical spectra presented by Monk et al. (1986) and Maia et al. (1987) exhibit a narrow Hβ line and a strong [O III]λ 5007 line relative to Hβ. According to the quantitative classification scheme of Winkler (1992) (see also Osterbrock 1977, 1981), NGC 0235A thus harbors either a Seyfert 1.9 or a Seyfert 2 nucleus. A spectrum obtained independently by J. Huchra (2004, private communication) confirms this classification. It is thus likely that NGC 0235A was misclassified based on the hint of broad Hα reported by Maia et al. (1987).

The maser spectrum of NGC 3393 shows a characteristic spectral signature of emission from an edge-on disk: two high-velocity complexes ($\sim$ 70 mJy) symmetrically offset by $\sim 600 \, \mathrm{km \, s^{-1}}$ from the systemic velocity and a single spectral complex ($\sim$ 28 mJy) within $120 \, \mathrm{km \, s^{-1}}$ of the systemic velocity. We have confirmed the weak systemic feature with the Tidbinbilla antenna ($1\sigma = 7 \, \mathrm{mJy}$) and with the GBT ($1\sigma = 2 \, \mathrm{mJy}$ in a $0.33 \, \mathrm{km \, s^{-1}}$ spectral channel). If the high-velocity emission indeed originates from the midline of an edge-on disk, then the orbital velocity of the disk as traced by the maser emission is $\sim 600 \, \mathrm{km \, s^{-1}}$, making NGC 3393 the third fastest known rotator after NGC 4258 ($\sim 1200 \, \mathrm{km \, s^{-1}}$; Miyoshi et al. 1995) and ESO269-G012 ($\sim 650 \, \mathrm{km \, s^{-1}}$; Greenhill et al. 2003). Because the high-velocity emission extends over $\Delta v \sim 200 \, \mathrm{km \, s^{-1}}$, it must occupy a fractional range of radii $\Delta r / R \approx 2\Delta v / v = 2/3$, which yields $\Delta r \sim 0.15 - 0.57 \, \mathrm{pc}$, assuming Keplerian rotation ($v \propto r^{-0.5}$) and a range in disk sizes from that of NGC 4258 ($0.16 - 0.28 \, \mathrm{pc}$) to NGC 1068 ($0.6 - 1.1 \, \mathrm{pc}$). The corresponding central mass would be on the order of $5 \times 10^7 \, M_\odot$ and the anticipated centripetal acceleration — that is the secular velocity drift of the systemic feature — would be on the order of $1 \, \mathrm{km \, s^{-1} \, yr^{-1}}$, which should be readily detectable within one year using single dish monitoring.

We confirmed the detection of high-velocity lines in NGC 5495 (refer to Fig. 2.1) with the GBT ($1\sigma = 5\,\mathrm{mJy}$ in a $0.33\,\mathrm{km\,s^{-1}}$ spectral channel). If we again assume that the high-velocity emission originates from the midline of an edge-on disk, then the orbital velocity of the accretion disk is $\sim 400\,\mathrm{km\,s^{-1}}$ while the corresponding central mass and centripetal acceleration are on the order of $10^7\,M_\odot$ and $0.5\,\mathrm{km\,s^{-1}\,yr^{-1}}$, respectively, assuming disk sizes as in NGC 4258 and NGC 1068.

Each of the remaining six detections — AM 2158-380 NED02, IC 0184, NGC 0235A, NGC 0613, NGC 4293, and VII ZW 073 — displays only a single complex of spectral features. In particular, the spectrum of NGC 0613 reveals a very broad emission feature (full width at half-maximum of ~ 87 km s^{-1}) and such broad lines have been typically associated with radio jets rather than molecular disks (e.g., Peck et al. 2003; Claussen et al. 1998). The spectral lines in NGC 0235A, VII ZW 073, and IC 0184 are significantly displaced from systemic velocities of the host galaxies (by ~ 380, ~ 180, and $\sim 220\,\mathrm{km\,s^{-1}}$, respectively) and thus might be either emission features associated with radio jets (e.g., Peck et al. 2003; Claussen et al. 1998) or high-velocity emission lines from only a single side of an edge-on accretion disk. NGC 0613, NGC 3393, NGC 4293, and IC 0184 have been targeted but not detected in previous surveys for maser emission. For NGC 0613, Braatz et al. (1996) and Henkel et al. (1984) report 1σ noise levels of $364\,\mathrm{mJy}$ and $70\,\mathrm{mJy}$ in 1.7 and $1.3\,\mathrm{km\,s^{-1}}$ spectral channels, respectively, corresponding to signal-to-noise ratios of $\lesssim 1$ at the current line strength (peak flux of $\sim 70\,\mathrm{mJy}$ in a 1.3 km s^{-1} spectral channel). Considering the large line-width, broader spectral averaging could have been applied to Henkel et al. (1984) data to achieve a marginal detection, and it is thus unclear whether this observation indicates line variability analogous to

that observed in other masers associated with jet activity (e.g., Peck et al. 2003). For NGC 3393, Braatz et al. (1996) report 1σ noise level of 11 mJy in 0.66 km s^{-1} channels, which should have been sufficient to detect the maser emission at its present strength of ~ 80 mJy (in a 1.3 km s^{-1} channel). In the case of NGC 4293, J. A. Braatz (private communication) obtained in 1998 a 1σ noise level in a 1.3 km s^{-1} channel of 35 mJy, which would not have been sufficient to detect the weak emission (peak of ~ 40 mJy in a 1.3 km s^{-1} channel). For IC 0184, Braatz et al. (1996) report 1σ noise level of 63 mJy in 0.66 km s^{-1} channels, again not sufficient to detect the maser at present line strength (peak of ~ 27 mJy in a 1.3 km s^{-1} channel).

In a survey with the Tidbinbilla and Robledo antennas of 630 AGN with $v_{sys} < 14600$ km s^{-1} selected from the NED (Table 2.2), we have detected to-date 15 new water maser sources (this paper and Greenhill et al. 2003). Since previous searches for water maser emission reported detections mostly in Seyfert $1.8 - 2.0$ or LINER systems (e.g., Braatz et al. 1996), we have focused our survey primarily on obscured nuclei (488 Seyfert $1.8 - 2.0$ or LINER systems, among which there are the 15 new maser sources, and 143 Seyfert $1.0 - 1.5$ systems, for which we report no new detections). Our survey includes 55% of known AGN with $v_{sys} < 14600$ km s^{-1} (630 out of 1150) and is nearly complete to 7000 km s^{-1} with 82% of Seyfert $1.8 - 2.0$ and LINER systems (325 out of 398) already observed, although AGN catalogs consolidated by the NED may themselves be incomplete. The detection rate among nearby ($v_{sys} < 7000$ km s^{-1}) Seyfert $1.8 - 2.0$ and LINER galaxies is 4%. The detection rate among nearby Seyfert $1.8 - 2.0$ and LINER galaxies that have been observed with absolute sensitivity (i.e., 1σ noise level in flux density units multiplied by the spectral channel width and converted to luminosity using

$H_o = 75\,\mathrm{km\,s^{-1}\,Mpc}$) of better than $2\,L_\odot$ is 4%, consistent with the analogous detection rate of 6% reported by Braatz et al. (1996). However, taking into account all known maser sources with peak flux densities above four times the typical rms achieved in this survey ($4\sigma = 56\,\mathrm{mJy}$ or $15\,L_\odot$ in a $1.3\,\mathrm{km\,s^{-1}}$ spectral channel at $v_{sys} = 7000\,\mathrm{km\,s^{-1}}$), the resulting incidence rate of maser emission among nearby Seyfert $1.8 - 2.0$ and LINER systems is $\sim 10\%$, which should be compared to the analogous incidence rates of $\sim 7\%$ and $\sim 20\%$ for surveys with $\sim 60\,\mathrm{mJy}$ ($\sim 1\,\mathrm{km\,s^{-1}}$ spectral channels; Braatz et al. 1996) and $\sim 3\,\mathrm{mJy}$ (converted to $1.3\,\mathrm{km\,s^{-1}}$ spectral channels; Braatz et al. 2004) sensitivities, respectively. Six of the detections obtained with DSN (NGC 0613, NGC 3393, NGC 4293, NGC 5643, NGC 6300, and IC 0184) lie in nuclei that had been targeted in previous surveys, which demonstrates the importance of either survey sensitivity or source variability. As a result of this work, the number of nearby AGN ($v_{sys} < 7000$ km s^{-1}) observed with $< 20\,\mathrm{mJy}$ sensitivity has increased from 130 to 449.

2.4   Future Prospects

Four of the fifteen detections obtained using the 70-m antennas of the DSN — NGC 3393, NGC 5495 (this study), ESO 269-G012, and possibly NGC 6926 (Greenhill et al. 2003) — display the archetypal spectral signature of emission from an edge-on disk. The remaining 11 sources appear to be non-high-velocity systems, but monitoring and deep integrations (as with the GBT, which is roughly an order of magnitude more sensitive than the DSN antennas) may result in detection of high-velocity features. All high-velocity systems stronger than few mJy are good

candidates for follow-up high angular resolution study with VLBI, where pc-scale molecular disk geometry and black hole mass may be inferred directly from resolved position and line-of-sight velocity data with high accuracy and relatively few sources of systematic uncertainty. Assuming disk sizes of 0.1 to 1 pc (i.e., comparable to NGC 4258 and NGC 1068, respectively) and a VLBI resolution element of ~ 0.3 mas, the source structure should be readily resolved because the AGN are relatively nearby ($3704 \, \mathrm{km \, s^{-1}} < v_{sys} < 6589 \, \mathrm{km \, s^{-1}}$). The additional detection with single dish spectroscopic monitoring of secular drift in the velocities of low-velocity Doppler components (i.e., centripetal acceleration) may also enable estimation of geometric distances, as has been done for NGC 4258 (Herrnstein et al. 1999). A geometric distance to any of these systems would be of considerable value since it might help in calibration of the Hubble relation independent of standard candles such as Cepheids.

(CSIRO) on behalf of JPL for NASA, with operations and maintenance undertaken by Raytheon, Australia. The Australia Telescope National Facility is funded by the Commonwealth Government for operation as a national facility by the CSIRO.

Table 2.2.   Sources Surveyed for Water Maser Emission with 70-m Deep Space Network Antennas at Tidbinbilla and Robledo.

Galaxy Name	Type[a]	α_{2000}[a] (hhmmss)	δ_{2000}[a] (ddmmss)	v_{sys}[a] (km s^{-1})	Date	T[b] (s)	1σ[c] (mJy)	Site[d]
KUG2358+330	SY2	00 00 58.14	+33 20 38.1	12387	2005-01-05	6240	9	R
UGC12914	LINER	00 01 38.32	+23 29 01.5	4308	2003-02-03	2910	18	R
UGC12915	LINER	00 01 41.94	+23 29 44.5	4274	2004-07-20	2460	12	T
CGCG517-014	SY2	00 01 58.46	+36 38 56.6	9311	2004-12-26	6060	9	R
NGC7814	LINER	00 03 14.89	+16 08 43.5	1046	2002-08-15	1980	14	T
UGC00013	LINER	00 03 29.23	+27 21 05.9	7498	2002-12-25	2100	23	R
UGC00050	LINER	00 06 40.15	+26 09 16.2	7366	2003-01-20	2100	28	R
UGC00085	LINER	00 09 28.64	+47 21 21.0	5066	2003-01-01	2340	28	R
NGC0019	LINER	00 10 40.88	+32 58 58.5	4713	2002-12-29	1980	19	R
NGC0017	SY2	00 11 06.55	-12 06 26.3	5816	2003-01-28	2070	16	R
NGC0041	LINER	00 12 47.97	+22 01 24.3	5833	2003-01-19	2340	17	R
NGC0051	LINER	00 14 34.91	+48 15 20.5	5257	2003-01-17	2700	18	R
2MASXIJ0018358-070255	SY2	00 18 35.90	-07 02 55.8	5301	2003-01-17	2760	14	R
UGC00215	SY2	00 22 26.22	+29 30 10.8	6927	2002-12-22	1080	29	R
LEDA087391	SY2	00 23 13.90	-53 58 22.0	8370	2002-06-01	2700	12	T
UGC00233	LINER	00 24 42.70	+14 49 28.0	5188	2002-09-09	1620	18	T
UGC00238	LINER	00 25 03.35	+31 20 42.6	6645	2003-01-12	1080	16	R
MRK0945	SY2	00 25 54.87	-03 25 14.9	4366	2003-01-17	2280	15	R
ESO540-G001	SY1.8	00 34 13.82	-21 26 20.6	7825	2004-06-29	1560	14	T
MRK0955	SY2	00 37 35.81	+00 16 50.5	10105	2003-01-18	2760	23	R
NGC0185	SY2	00 38 57.68	+48 20 11.6	-202	2005-02-01	4980	13	R
ESO540-G014	SY2	00 41 11.73	-21 07 53.5	1645	2002-08-05	1500	15	T
NGC0237	LINER	00 43 27.82	-00 07 30.3	4118	2002-09-06	1890	15	T
ESO540-G017NED01	SY2	00 44 21.80	-17 21 04.0	9025	2004-06-15	1800	14	T
NGC0266	LINER	00 49 47.89	+32 16 39.7	4590	2004-12-20	6780	8	R
NGC0291	SY2	00 53 29.80	-08 46 03.6	5589	2002-08-05	1530	15	T
UGC00556	LINER	00 54 50.27	+29 14 47.7	4559	2003-01-01	1140	44	R
NGC0315	SY1	00 57 48.89	+30 21 08.8	4862	2003-01-19	2610	18	R
ESO351-G025	LINER	00 58 22.23	-36 39 37.1	10029	2005-06-24	9000	7	T
IC0064	AGN	00 59 24.46	+27 03 32.0	13165	2005-02-09	5700	12	R
IRASF01010-1232	SY2	01 03 31.04	-12 16 06.4	7026	2002-08-13	1980	12	T
ESO079-G016	SY	01 04 27.10	-64 07 10.0	5917	2004-05-09	2460	10	T
ESO113-G010	SY1.8	01 05 16.98	-58 26 13.1	7512	2003-05-30	1950	15	T

Table 2.2—Continued

Galaxy Name	Type[a]	α_{2000}[a] (hhmmss)	δ_{2000}[a] (ddmmss)	v_{sys}[a] (km s^{-1})	Date	T[b] (s)	1σ[c] (mJy)	Site[d]
UM085	SY2	01 06 45.26	+06 38 02.0	11807	2003-01-29	2460	18	R
IC1631	SY2	01 08 44.80	-46 28 32.7	8969	2004-06-22	2700	13	T
CGCG551-008	SY	01 10 14.08	+50 10 32.1	6917	2003-01-30	1470	20	R
NGC0424	SY2	01 11 27.51	-38 05 01.1	3456	2002-06-01	2430	12	T
APMUKS(BJ)B010	SY2?	01 11 53.49	-45 58 46.5	7599	2002-08-17	2160	14	T
UGC00768	SY1.9	01 13 09.59	+02 17 16.0	13228	2005-02-23	7620	14	R
IC1657	SY2	01 14 06.98	-32 39 03.2	3541	2003-05-29	2580	11	T
NGC0454NED02	SY2	01 14 25.22	-55 23 47.3	3588	2003-05-08	3120	14	T
ESO195-G035	SY2	01 15 55.38	-50 11 22.2	7126	2002-09-09	1380	16	T
NGC0446	SY?	01 16 03.60	+04 17 38.0	5349	2003-06-23	1980	15	T
UGC00861	SY2	01 19 59.61	+14 47 10.5	4082	2002-08-10	1800	16	T
ESO244-G017	SY1.5	01 20 19.70	-44 07 41.6	6883	2003-05-31	1560	19	T
UM319	SY2	01 23 21.18	-01 58 36.0	4758	2003-01-17	2070	16	R
IC1689	LINER	01 23 47.90	+33 03 20.0	4498	2003-01-01	1980	27	R
NGC0526A	SY1.5	01 23 54.39	-35 03 55.7	5618	2003-06-23	1620	14	T
IRAS01217+0122	SY2	01 24 24.00	+01 38 35.0	5057	2004-06-19	1920	13	T
NGC0513	SY2	01 24 26.85	+33 47 58.0	5747	2004-12-15	4680	15	R
UM103	SY2	01 25 27.77	+03 00 11.7	12910	2003-01-22	2280	24	R
NGC0536	AGN	01 26 21.61	+34 42 14.0	5101	2002-03-02	2880	13	R
IC0123	SY2	01 28 51.46	+02 26 47.2	8906	2002-12-29	1920	21	R
ESO413-G008	LINER	01 30 49.12	-27 21 50.9	5509	2002-08-05	2400	12	T
UGC01093	LINER	01 31 49.01	+17 34 32.9	7710	2002-12-25	1920	22	R
ESO353-G009	SY2	01 31 50.42	-33 07 09.5	4877	2003-06-15	1680	12	T
UGC01098	LINER	01 32 16.10	+21 24 39.5	9548	2005-01-05	4380	12	R
MCG-03-05-007	SY	01 34 25.19	-15 49 08.3	5857	2002-12-29	1800	25	R
KUG0135-131	SY2	01 38 05.39	-12 52 11.1	11642	2004-06-22	2970	12	T
ESO297-G018	SY2	01 38 37.17	-40 00 41.2	7369	2004-06-27	1260	16	T
IIIZW035NOTES01	LINER	01 44 30.34	+17 06 00.0	8209	2004-07-21	900	22	T
MCG-01-05-031	SY2	01 45 25.46	-03 49 37.5	5358	2002-08-05	2160	11	T
ESO080-G005	SY1.8	01 47 39.24	-66 09 49.1	7868	2003-08-06	1920	13	T
NGC0676	SY2	01 48 57.30	+05 54 24.0	1498	2004-06-27	1560	13	T
UGC01282	SY2	01 49 29.87	+12 30 32.6	5132	2002-08-13	1620	13	T
IRAS01475-0740	SY2	01 50 02.70	-07 25 48.5	5204	2002-08-04	1080	16	T

Table 2.2—Continued

Galaxy Name	Type[a]	α_{2000}[a] (hhmmss)	δ_{2000}[a] (ddmmss)	v_{sys}[a] (km s^{-1})	Date	T[b] (s)	1σ[c] (mJy)	Site[d]
NGC0708	SY2	01 52 46.47	+36 09 06.6	4778	2002-12-29	2100	19	R
SBS0153+366	SY2	01 56 45.35	+36 52 41.0	5532	2003-02-06	2040	20	R
NGC0777	SY2	02 00 14.90	+31 25 46.0	4903	2002-12-29	1920	20	R
UGC01479	SY2	02 00 19.06	+24 28 25.3	4847	2002-08-15	1980	16	T
ESO153-G020	SY2	02 06 03.57	-55 11 35.0	5802	2003-05-05	2850	14	T
NGC0833	LINER	02 09 20.88	-10 08 00.3	3815	2002-09-06	1890	15	T
NGC0835	LINER	02 09 24.69	-10 08 10.5	4018	2002-09-11	2070	15	T
NGC0839	SY2	02 09 42.93	-10 11 02.7	3883	2003-02-02	3330	17	R
KUG0207-092	SY2	02 10 11.40	-09 03 36.2	11992	2003-01-29	3090	15	R
NGC0841	LINER	02 11 17.35	+37 29 49.8	4472	2005-01-02	4980	10	R
NGC0931	SY1.5	02 28 14.47	+31 18 42.0	4910	2005-02-08	3900	16	R
IC1816	SY1	02 31 50.99	-36 40 16.2	4995	2003-06-23	1680	15	T
UGC02024	SY2	02 33 01.24	+00 25 15.0	6567	2002-08-13	1530	13	T
MRK1179	SY1.9	02 33 22.33	+27 56 12.9	10864	2003-01-30	3180	15	R
NGC0985	SY1	02 34 37.77	-08 47 15.4	12399	2004-06-25	1260	16	T
MRK0595	SY1.5	02 41 34.89	+07 11 14.1	7876	2003-08-01	1860	16	T
NGC1056	SY	02 42 48.34	+28 34 26.9	1537	2002-12-15	2070	21	R
NGC1058	SY2	02 43 29.88	+37 20 27.1	517	2004-11-26	2280	30	R
ESO479-G031	LINER	02 44 47.68	-24 30 50.0	6891	2002-09-30	2258	13	T
NGC1097	SY1	02 46 18.99	-30 16 28.7	1270	2003-08-13	1680	15	T
ESO479-G039	LINER	02 46 37.64	-26 58 19.0	6964	2002-09-09	1440	16	T
2MASXIJ0246391+213510	LINER	02 46 39.15	+21 35 10.3	6828	2003-02-06	2280	18	R
IC1859	SY2	02 49 03.92	-31 10 21.0	5751	2002-08-15	3060	10	T
NGC1106	SY2	02 50 40.50	+41 40 18.0	4275	2004-12-15	6600	13	R
NGC1125	SY2	02 51 40.27	-16 39 03.7	3242	2003-01-17	2550	18	R
NGC1140	SY2	02 54 33.58	-10 01 39.9	1494	2002-08-13	1530	14	T
NGC1142	SY2	02 55 12.19	-00 11 00.8	8406	2003-08-02	2040	15	T
IRAS02530+0211	LINER	02 55 34.43	+02 23 41.4	8052	2002-12-22	1878	26	R
IC1867	SY2	02 55 52.23	+09 18 42.6	7488	2003-01-28	2430	16	R
ESO417-G006	SY2	02 56 21.52	-32 11 05.6	4806	2004-07-21	1860	13	T
IRAS03031-8335	AGN?	02 58 44.20	-83 23 14.0	10975	2004-06-24	2220	11	T
2MASXIJ0259304-242253	SY1	02 59 30.50	-24 22 53.6	10138	2003-06-02	3240	17	T
MCG-02-08-039	SY2	03 00 30.66	-11 24 55.1	8727	2003-08-02	1620	19	T

Table 2.2—Continued

Galaxy Name	Type[a]	α_{2000}[a] (hhmmss)	δ_{2000}[a] (ddmmss)	v_{sys}[a] (km s^{-1})	Date	T[b] (s)	1σ[c] (mJy)	Site[d]
2MASXJ03023999-7242231	SY2	03 02 40.16	-72 42 21.3	12387	2003-09-12	3180	9	T
NGC1204	LINER	03 04 40.01	-12 20 29.5	4222	2002-09-06	2070	14	T
NGC1217	LINER	03 06 05.87	-39 02 10.4	6159	2004-07-21	1860	14	T
NGC1241	SY2	03 11 14.71	-08 55 19.9	3998	2003-05-09	2160	17	T
2MASXJ03130881-0243191	SY2	03 13 08.80	-02 43 19.2	7938	2003-07-27	2010	11	T
KUG0312+013	SY2	03 15 05.33	+01 30 30.2	7031	2003-07-26	1500	11	T
NGC1266	LINER	03 16 00.74	-02 25 38.5	2178	2002-09-09	1500	16	T
UGC02638	LINER	03 17 02.21	+01 15 17.9	6958	2002-09-12	1910	13	T
NGC1316	LINER	03 22 41.72	-37 12 29.6	1750	2003-06-09	1530	18	T
NGC1326	LINER	03 23 56.38	-36 27 51.6	1354	2003-06-15	2280	12	T
NGC1320	SY2	03 24 48.72	-03 02 32.0	2692	2003-02-01	2610	19	R
ESO116-G018	SY2	03 24 53.16	-60 44 20.0	5445	2003-05-08	3240	11	T
MCG-02-09-040	SY2	03 25 04.94	-12 18 27.8	4429	2003-02-02	3330	17	R
MRK0609	SY1.8	03 25 25.34	-06 08 38.7	9898	2005-01-02	5460	8	R
UGC02724	SY2	03 25 25.58	+40 46 23.4	13656	2005-02-14	4560	10	R
NGC1350	SY	03 31 08.11	-33 37 42.1	1893	2003-05-29	1800	14	T
NGC1353	LINER	03 32 02.97	-20 49 07.0	1517	2002-09-12	1890	15	T
NGC1365	SY1.8	03 33 36.37	-36 08 25.4	1627	2003-06-09	1920	12	T
NGC1398	AB;SY	03 38 51.90	-26 20 14.2	1400	2003-05-29	1500	13	T
NGC1409	SY2	03 41 10.43	-01 18 09.2	7555	2003-02-03	2250	18	R
NGC1433	SY2	03 42 01.46	-47 13 19.6	1071	2003-05-30	1740	15	T
FCCB1658	SY2	03 43 26.52	-31 44 38.2	9222	2004-07-28	1920	14	T
IC0355	SY	03 53 46.26	+19 58 26.4	8406	2002-12-15	1260	27	R
MCG+00-11-002	AGN	03 57 58.66	-00 11 26.0	4139	2002-08-17	1800	14	T
3C098	SY2	03 58 54.46	+10 26 02.4	8860	2004-07-28	1860	16	T
ESO549-G049	LINER	04 02 25.67	-18 02 51.1	7680	2003-07-27	1440	13	T
MRK1193	SY2	04 07 01.05	-10 10 14.0	9627	2003-07-16	2220	19	T
ESO420-G013	SY2	04 13 49.69	-32 00 25.1	3528	2002-08-17	1980	13	T
LEDA094129	SY1.5	04 15 59.18	-08 21 38.2	11058	2005-02-24	7800	8	R
NGC1553	LINER	04 16 10.28	-55 46 51.0	1076	2002-06-02	2610	12	T
NGC1566	SY1	04 20 00.64	-54 56 17.0	1489	2003-08-06	1920	12	T
ESO550-IG025NED01	LINER	04 21 19.99	-18 48 39.0	9351	2005-05-23	7200	9	T
IRAS04210+0400	SY2	04 23 40.77	+04 08 02.4	12910	2003-01-22	2340	17	R

Table 2.2—Continued

Galaxy Name	Type[a]	α_{2000}[a] (hhmmss)	δ_{2000}[a] (ddmmss)	v_{sys}[a] (km s^{-1})	Date	T[b] (s)	1σ[c] (mJy)	Site[d]
MCG-01-12-006	SY2	04 25 55.56	-08 34 07.5	11309	2003-07-24	2010	14	T
ESO202-G023	SY2	04 28 00.03	-47 54 40.2	4867	2003-05-08	2880	13	T
2MASXIJ0428260-043348	SY2	04 28 26.05	-04 33 49.5	4576	2003-02-02	3690	14	R
NGC1598	LINER	04 28 33.45	-47 46 56.1	5046	2004-06-19	2040	12	T
NGC1614	SY2	04 33 59.85	-08 34 44.0	4703	2003-01-29	3240	12	R
IRAS04361-1430	SY2	04 38 28.33	-14 24 38.1	10290	2003-07-12	840	17	T
NGC1636	SY2	04 40 40.20	-08 36 27.9	4120	2002-09-12	1910	15	T
IRAS04385-0828	SY2	04 40 54.96	-08 22 22.2	4460	2003-01-17	2700	16	R
UGC03134	SY2	04 41 48.27	-01 18 06.5	8422	2003-01-17	1440	22	R
NGC1672	SY2	04 45 42.83	-59 14 51.6	1344	2004-06-27	900	19	T
2MASXIJ04472072-0508138	SY1	04 47 20.72	-05 08 14.1	12690	2003-07-24	1560	16	T
MCG-01-13-025	SY1.2	04 51 41.51	-03 48 33.7	4690	2003-06-26	2520	18	T
2MASXIJ0452445-031257	SY2	04 52 44.53	-03 12 57.8	4663	2003-02-01	2880	16	R
CGCG420-015	SY2	04 53 25.73	+04 03 41.5	8559	2003-06-01	3240	14	T
ESO033-G002	SY2	04 55 58.99	-75 32 28.1	5330	2003-07-19	1530	15	T
ESO552-G039	SY1.2	04 58 40.31	-21 59 30.8	11418	2003-06-02	3720	14	T
PMNJ0505+0416	SY1	05 05 34.78	+04 15 54.7	7938	2003-08-14	2760	8	T
NGC1808	SY2	05 07 42.32	-37 30 45.7	997	2003-05-05	3120	15	T
CGCG468-002	SY2	05 08 19.69	+17 21 48.4	5158	2003-01-17	2280	19	R
ESO362-G008	SY2	05 11 09.09	-34 23 35.8	4710	2003-05-09	1860	18	T
[HB91]0510+031	SY1	05 12 40.35	+03 11 44.1	4838	2003-08-14	1740	9	T
MCG-02-14-009	SY1	05 16 21.18	-10 33 41.4	8294	2003-06-29	2100	20	T
CGCG258-006	SY1.8	05 16 53.80	+53 11 30.4	8249	2004-12-25	4080	13	R
ESO362-G018	SY1.5	05 19 35.82	-32 39 27.9	3743	2003-05-30	1440	14	T
PICTORA	SY1	05 19 49.69	-45 46 44.5	10154	2003-09-12	1358	14	T
IRAS05187-1017	LINER	05 21 06.54	-10 14 46.7	8241	2003-06-07	1360	15	T
1RXSJ052135.1+671808	SY1.5	05 21 34.60	+67 18 07.9	4343	2005-01-12	4680	15	R
NGC1875	AGN?	05 21 45.80	+06 41 20.0	8732	2003-06-14	1800	14	T
ESO253-G003	SY2	05 25 18.30	-46 00 19.6	12219	2003-08-06	1740	12	T
NGC1961	LINER	05 42 04.80	+69 22 43.3	3883	2004-12-25	3840	12	R
UGC03351	SY?	05 45 47.80	+58 42 03.0	4390	2004-11-26	1740	30	R
ESO306-G025	SY2	05 45 50.86	-39 29 37.6	7312	2002-08-15	1170	15	T
2MASXIJ05465630-3337413	SY1	05 46 56.31	-33 37 41.5	8732	2003-06-28	1680	19	T

Table 2.2—Continued

Galaxy Name	Type[a]	α_{2000}[a] (hhmmss)	δ_{2000}[a] (ddmmss)	v_{sys}[a] (km s^{-1})	Date	T[b] (s)	1σ[c] (mJy)	Site[d]
UGC03374	SY1.5	05 54 53.61	+46 26 21.6	6018	2005-02-11	6960	12	R
2MASXJ05580206-3820043	SY1	05 58 02.00	-38 20 04.7	9821	2003-09-12	2476	12	T
AM0602-575	SY2	06 00 21.27	-57 56 20.6	11058	2003-05-11	3300	11	T
ESO254-G017	SY2	06 06 35.80	-47 29 56.0	8667	2003-07-16	2760	15	T
MCG+08-12-003	SY1.8	06 12 43.37	+47 30 51.1	11104	2005-01-12	21180	8	R
2MASXIJ0623053	SY2	06 23 05.31	-06 07 13.3	5923	2002-08-15	1530	14	T
ESO366-G002	LINER	06 37 57.13	-32 52 40.9	10769	2003-06-02	1860	26	T
ESO490-IG026	SY1.2	06 40 11.74	-25 53 41.8	7269	2003-05-29	1320	13	T
IRAS06483-1955	SY1.8	06 50 30.84	-19 59 15.5	7475	2003-05-29	940	16	T
CGCG145-017	SY2	06 52 02.52	+27 27 38.9	11926	2005-01-11	6000	12	R
IC0450	SY1.5	06 52 12.25	+74 25 37.5	5536	2005-02-01	7440	10	R
UGC03601	SY1.5	06 55 49.52	+40 00 00.8	5047	2005-01-13	4980	19	R
FAIRALL0265	SY1	06 56 29.80	-65 33 37.7	8591	2003-09-12	2880	9	T
AM0702-601	SY2	07 03 24.12	-60 15 23.3	9105	2003-05-11	3000	13	T
ESO428-G014	SY2	07 16 31.21	-29 19 28.8	1621	2003-05-08	3060	12	T
MRK0378	SY2	07 17 08.20	+49 41 36.4	12056	2004-12-28	2460	20	R
MRK1200	LINER	07 25 01.50	+27 19 27.5	7587	2003-01-21	2040	20	R
MRK0009	SY1.5	07 36 56.98	+58 46 13.4	11496	2005-02-15	7740	9	R
MRK0078	SY2	07 42 41.73	+65 10 37.5	10738	2005-01-05	7440	9	R
UGC03995NOTES01	SY2	07 44 07.11	+29 14 57.4	4666	2004-12-18	6780	12	R
2MASXIJ07554738-0157419	SY1	07 55 47.39	-01 57 41.9	11531	2003-06-01	2400	15	T
IC0486	SY1	08 00 20.98	+26 36 48.2	7846	2004-12-01	4500	19	R
IRAS07577+1021	SY1.5	08 00 26.89	+10 13 09.0	13676	2005-02-23	9420	12	R
UGC04211	SY2	08 04 46.30	+10 46 37.0	9979	2003-07-05	1440	16	T
UGC04248	SY1	08 08 55.35	+00 18 05.0	5335	2003-09-17	3120	11	T
SBS0805+607	LINER	08 09 31.77	+60 36 47.1	9099	2004-12-12	4320	19	R
ATZ98J081211.7+571746	SY2	08 12 11.70	+57 17 46.0	7824	2004-12-10	6660	18	R
SBS0808+587	SY2	08 12 17.10	+58 33 51.6	7938	2004-11-28	7380	17	R
KUG0811+462	SY1.5	08 15 16.87	+46 04 30.6	11800	2005-03-10	6360	9	R
SBS0811+584	SY2	08 16 01.30	+58 20 01.0	7397	2004-11-27	2580	18	R
SBS0814+579C	AGN	08 18 12.93	+57 46 39.1	7881	2004-12-05	4440	22	R
ESO018-G008	SY2	08 23 16.61	-77 49 10.8	5156	2002-06-11	2640	12	T
ESO018-G009	SY2	08 24 07.43	-77 46 52.5	5248	2003-05-07	1890	17	T

Table 2.2—Continued

Galaxy Name	Type[a]	α_{2000}[a] (hhmmss)	δ_{2000}[a] (ddmmss)	v$_{sys}$[a] (km s^{-1})	Date	T[b] (s)	1σ[c] (mJy)	Site[d]
IRASF08216+3009	SY2	08 24 43.28	+29 59 23.2	7312	2003-01-20	2460	26	R
KUG0826+225	AGN	08 29 44.33	+22 25 27.5	7312	2003-01-21	1920	19	R
CGCG004-040	SY2	08 30 14.41	-02 52 50.3	11684	2003-01-29	3330	12	R
NGC2617	SY1.8	08 35 38.79	-04 05 17.6	4227	2003-02-01	3150	17	R
MRK0093	SY2	08 36 42.34	+66 13 58.6	5200	2002-12-29	3960	17	R
UGC04498	AGN	08 37 26.60	+40 02 07.8	6982	2004-11-26	960	30	R
NGC2622	SY1.8	08 38 10.94	+24 53 43.0	8342	2004-12-12	6360	16	R
FAIRALL1146	SY1.5	08 38 30.50	-35 59 35.0	9177	2003-06-05	1500	16	T
2MASXJ08440647-1402130	SY1.5	08 44 06.37	-14 02 03.0	8109	2003-07-24	1290	21	T
2MASXIJ0846093-152125	AGN	08 46 09.33	-15 21 25.2	5327	2002-06-01	2600	13	T
NGC2683	SY2	08 52 41.42	+33 25 13.7	410	2003-02-03	2790	18	R
IC0520	LINER	08 53 42.20	+73 29 27.0	3446	2004-12-23	7020	9	R
ESO497-G003	SY2	09 01 38.06	-24 47 26.4	421	2002-05-31	2610	12	T
IC0526	SY2	09 02 40.78	+10 50 29.9	5681	2003-02-02	3150	16	R
NGC2783B	AGN	09 13 32.87	+29 59 59.4	6609	2003-01-19	2160	19	R
NGC2783	AGN	09 13 39.46	+29 59 34.7	6597	2003-01-21	1740	24	R
NGC2845	SY2	09 18 36.88	-38 00 41.1	2509	2002-07-02	2700	10	T
NGC2787	LINER	09 19 18.57	+69 12 11.9	694	2005-03-06	7440	7	R
MCG-01-24-012	SY2	09 20 46.31	-08 03 21.9	5821	2003-06-05	1500	14	T
ESO565-G019	SY2	09 34 43.53	-21 55 40.0	4588	2002-05-31	2700	16	T
UGC05101	SY1.5	09 35 51.65	+61 21 11.3	11361	2005-02-11	7740	11	R
CGCG181-077	SY1.5	09 39 17.22	+36 33 43.6	5867	2005-03-07	6780	9	R
UGC05165NOTES03	SY2	09 40 44.51	+21 14 03.7	7037	2003-07-26	2340	12	T
NGC2965	AGN	09 43 19.16	+36 14 52.3	6585	2002-12-29	2820	24	R
ESO434-G040	SY2	09 47 40.24	-30 56 54.2	2462	2003-05-09	3240	12	T
IC2510	SY2	09 47 43.24	-32 50 15.4	2776	2002-05-18	2190	20	T
NGC2985	LINER	09 50 21.61	+72 16 44.1	1316	2004-12-23	4620	11	R
NGC3035	SY1	09 51 55.29	-06 49 29.3	4292	2003-06-01	2340	19	T
CGCG035-090	SY2	09 55 40.50	+05 02 37.0	10007	2003-07-05	1480	16	T
NGC3081	SY2	09 59 29.54	-22 49 34.6	2366	2003-06-15	1740	12	T
NGC3080	SY1	09 59 55.83	+13 02 37.8	10258	2003-06-07	1820	16	T
NGC3094	SY2	10 01 25.97	+15 46 13.7	2385	2002-03-25	3150	15	R
WN1	SY1	10 02 00.05	-08 09 41.6	4500	2003-06-28	1350	20	T

Table 2.2—Continued

Galaxy Name	Type[a]	α_{2000}[a] (hhmmss)	δ_{2000}[a] (ddmmss)	v_{sys}[a] (km s^{-1})	Date	T[b] (s)	1σ[c] (mJy)	Site[d]
ESO263-G013	SY2	10 09 48.99	-42 48 46.7	9658	2003-05-07	3060	11	T
ESO374-G044	SY2	10 13 19.86	-35 58 59.6	8294	2003-07-12	1200	15	T
NGC3166	LINER	10 13 45.60	+03 25 32.0	1339	2003-06-16	1680	16	T
NGC3169	LINER	10 14 15.03	+03 27 57.1	1228	2003-06-07	1560	15	T
NGC3185	SY2	10 17 38.53	+21 41 17.9	1212	2003-06-16	2880	18	T
NGC3190	LINER	10 18 05.77	+21 49 55.8	1266	2003-07-26	1140	18	T
NGC3226	LINER	10 23 27.00	+19 53 54.4	1147	2003-07-27	2340	13	T
NGC3227	SY1.5	10 23 30.59	+19 51 54.0	1153	2003-08-02	2460	13	T
KUG1021+675	SY2	10 25 13.03	+67 17 49.6	11142	2004-12-28	6780	10	R
IC0614	SY2	10 26 51.88	-03 27 51.9	9919	2003-07-12	1230	15	T
NGC3245	LINER	10 27 18.39	+28 30 26.6	1352	2004-12-19	5040	11	R
ESO436-G029	SY2	10 30 23.70	-30 23 42.8	4024	2002-05-23	2700	19	T
CGCG009-070	SY2	10 30 50.85	-02 43 15.7	8654	2003-07-08	1740	19	T
NGC3281	SY2	10 31 52.06	-34 51 13.3	3166	2002-07-02	1080	16	T
IRAS10295-1831	SY1	10 31 57.29	-18 46 33.9	11604	2003-06-05	1800	13	T
MCG-02-27-009	SY2	10 35 27.26	-14 07 46.9	4462	2003-06-09	1920	12	T
CGCG037-092	SY2	10 36 35.80	+05 54 37.8	3464	2003-07-13	2178	13	T
NGC3312	AGN	10 37 02.59	-27 33 54.6	2858	2003-05-09	1020	22	T
GSC549500478	SY1	10 38 20.59	-10 07 00.4	8464	2003-06-14	1620	14	T
MCG-01-27-031	SY1	10 39 46.27	-05 28 59.6	6069	2003-06-14	1980	13	T
KUG1037+393A	AGN	10 40 00.59	+39 07 20.1	8990	2005-01-13	4860	15	R
MCG-03-27-026	SY2	10 42 18.73	-17 38 55.5	6067	2002-06-01	2700	12	T
CGCG333-049	SY2	10 44 08.51	+70 24 19.5	9739	2004-12-14	7560	12	R
NGC3362	SY2	10 44 51.71	+06 35 48.2	8067	2003-08-01	1800	14	T
NGC3367	SY	10 46 34.80	+13 45 02.0	3007	2003-06-16	2220	21	T
M96	LINER	10 46 45.74	+11 49 11.8	894	2002-02-15	2760	19	R
NGC3379	LINER	10 47 49.60	+12 34 54.8	908	2005-01-02	6840	8	R
MRK0152	LINER	10 48 52.53	+50 02 11.9	6748	2003-01-20	1160	20	R
MRK0417	SY2	10 49 30.93	+22 57 51.9	9509	2005-02-24	8880	8	R
ESO215-G014	SY1	10 59 18.52	-51 26 30.3	5479	2003-09-13	2636	11	T
NGC3486	SY2	11 00 23.88	+28 58 30.2	679	2004-12-15	3540	21	R
NGC3511	SY1	11 03 23.68	-23 05 10.6	1102	2003-08-14	180	33	T
NGC3507	LINER	11 03 25.39	+18 08 12.2	976	2004-12-20	3120	12	R

Table 2.2—Continued

Galaxy Name	Type[a]	α_{2000}[a] (hhmmss)	δ_{2000}[a] (ddmmss)	v_{sys}[a] (km s^{-1})	Date	T[b] (s)	1σ[c] (mJy)	Site[d]
NGC3521	LINER	11 05 48.58	-00 02 09.1	803	2003-08-02	2820	11	T
NGC3516	SY1.5	11 06 47.49	+72 34 06.9	2626	2005-02-09	3060	15	R
MCG-01-28-026	SY2	11 06 57.06	-05 36 19.4	10314	2003-06-05	1380	14	T
ESO438-G009	SY1.5	11 10 47.97	-28 30 04.2	7174	2003-07-30	1860	12	T
NGC3593	SY2	11 14 37.00	+12 49 04.0	627	2003-02-01	3330	17	R
CGCG156-051	SY2	11 17 52.66	+29 18 16.1	6711	2002-12-29	2760	22	R
M65	LINER	11 18 55.90	+13 05 37.0	805	2002-02-17	1980	18	R
ESO319-IG012NED02	SY2	11 19 01.24	-40 00 31.5	10334	2003-05-08	540	31	T
NGC3627	SY2	11 20 15.02	+12 59 29.5	725	2004-12-23	4740	10	R
CGCG011-076	SY2	11 21 12.26	-02 59 03.5	7283	2003-07-26	2400	9	T
KUG1120-073	LINER	11 22 51.08	-07 35 19.4	6485	2005-05-23	9480	8	T
NGC3656	LINER	11 23 38.43	+53 50 30.9	2842	2003-01-22	2070	18	R
IRAS11215-2806	SY2	11 24 01.24	-28 23 08.2	3993	2003-06-16	1500	20	T
NGC3675	LINER	11 26 07.90	+43 35 10.0	768	2004-12-18	1800	19	R
NGC3681	LINER	11 26 29.79	+16 51 48.4	1234	2005-03-07	3420	11	R
SBS1124+610	LINER	11 27 22.00	+60 44 53.8	9998	2005-01-09	13320	5	R
ESO439-G009	SY2	11 27 23.40	-29 15 27.0	6995	2003-07-30	2280	10	T
NGC3697	AGN	11 28 50.40	+20 47 43.0	6133	2003-01-17	2460	20	R
SBS1127+575	SY2	11 30 03.35	+57 18 30.3	10418	2005-01-15	6780	9	R
2MASXJ11322058+8223433	SY2	11 32 20.32	+82 23 42.9	8165	2004-12-06	6780	12	R
MRK0738	SY?	11 35 57.10	+28 11 48.6	11253	2003-01-30	1800	20	R
ESO216-G024	SY1.9	11 37 44.88	-49 10 43.2	4986	2003-05-07	3060	12	T
NGC3783	SY1	11 39 01.77	-37 44 18.7	2889	2003-10-03	1440	18	T
MRK0745	SY2?	11 39 56.31	+16 57 17.9	3175	2002-03-05	4050	15	R
NGC3822	SY2	11 42 11.20	+10 16 40.0	6015	2005-03-17	9660	9	T
[HB91]1143-185	SY1	11 45 44.23	-18 46 40.0	5878	2003-09-13	3116	10	T
MRK1457	SY2	11 47 21.61	+52 26 58.3	13922	2005-02-15	5460	8	R
MCG-01-30-041	SY1.8	11 52 38.18	-05 12 25.5	5641	2003-08-01	2280	12	T
NGC3941	SY2	11 52 55.27	+36 59 10.6	925	2002-04-12	2700	22	R
NGC3945	LINER	11 53 13.60	+60 40 32.0	1254	2003-01-21	1560	23	R
NGC3953	LINER	11 53 48.92	+52 19 36.4	1048	2003-01-19	2100	18	R
IC0745	SY2	11 54 12.27	+00 08 11.7	1141	2004-06-22	2340	14	T
NGC3976	SY2	11 55 57.32	+06 44 55.5	2476	2002-03-23	2808	16	R

Table 2.2—Continued

Galaxy Name	Type[a]	α_{2000}[a] (hhmmss)	δ_{2000}[a] (ddmmss)	v_{sys}[a] (km s^{-1})	Date	T[b] (s)	1σ[c] (mJy)	Site[d]
NGC3982	SY2	11 56 28.10	+55 07 30.6	1105	2002-02-26	3240	11	R
CGCG127-135	SY2	12 01 44.90	+20 19 44.0	6888	2003-07-27	2400	13	T
PGC038055	SY2	12 02 56.87	-20 56 03.3	6285	2003-09-17	2040	14	T
NGC4102	LINER	12 06 23.11	+52 42 39.5	844	2005-01-05	5520	9	R
NGC4111	LINER	12 07 03.11	+43 03 56.3	805	2002-02-17	2380	16	R
NGC4125	LINER	12 08 05.86	+65 10 26.8	1350	2003-02-03	2610	19	R
NGC4138	SY1.9	12 09 29.79	+43 41 06.9	885	2005-03-10	7740	8	R
NGC4143	LINER	12 09 36.10	+42 32 03.0	982	2005-01-11	6960	9	R
NGC4145	LINER	12 10 01.51	+39 53 01.1	1013	2003-01-19	2160	18	R
NGC4156	LINER	12 10 49.61	+39 28 21.8	6601	2005-03-06	5340	9	R
NGC4168	SY1.9	12 12 17.30	+13 12 18.0	2267	2002-02-24	3420	15	R
NGC4169	SY2	12 12 18.81	+29 10 46.3	3737	2002-03-02	3690	13	R
NGC4175	AGN	12 12 31.05	+29 10 06.4	3959	2002-03-05	3690	14	R
NGC4203	LINER	12 15 05.03	+33 11 50.0	1082	2005-03-07	6900	8	R
NGC4216	LINER	12 15 54.39	+13 08 58.3	131	2003-01-22	1620	19	R
ESO505-IG030	SY2	12 16 57.14	-26 12 33.5	11451	2003-07-12	1350	15	T
NGC4261	LINER	12 19 23.22	+05 49 30.8	2221	2002-03-01	3120	28	R
NGC4278	SY1	12 20 06.82	+29 16 50.7	648	2002-02-28	450	91	R
M61	SY2	12 21 54.89	+04 28 25.1	1558	2002-02-24	2520	17	R
NGC4314	LINER	12 22 32.01	+29 53 43.6	960	2002-02-28	3330	27	R
NGC4378	SY2	12 25 17.96	+04 55 29.8	2537	2002-03-31	3150	15	R
NGC4395	SY1.8	12 25 48.92	+33 32 48.4	319	2005-03-17	9540	10	R
NGC4394	LINER	12 25 55.63	+18 12 50.2	919	2003-01-22	1260	20	R
NGC4414	LINER	12 26 27.11	+31 13 24.3	714	2003-02-01	2790	19	R
NGC4412	LINER	12 26 35.92	+03 57 53.7	2277	2003-05-11	648	32	T
NGC4355	SY2	12 26 54.62	-00 52 39.2	2163	2004-06-22	2940	13	T
NGC4438	LINER	12 27 45.59	+13 00 31.8	71	2002-02-28	3300	29	R
NGC4457	LINER	12 28 59.10	+03 34 14.0	879	2003-05-28	1500	14	T
M49	SY2	12 29 46.79	+08 00 01.5	994	2002-03-31	3240	17	R
NGC4477	SY2	12 30 02.22	+13 38 11.2	1347	2002-03-23	2754	16	R
M87	SY	12 30 49.42	+12 23 28.0	1301	2002-02-28	2340	34	R
NGC4494	LINER	12 31 24.11	+25 46 28.1	1345	2003-02-02	2700	18	R
M88	SY2	12 31 59.16	+14 25 13.6	2264	2003-02-03	2160	19	R

Table 2.2—Continued

Galaxy Name	Type[a]	α_{2000}[a] (hhmmss)	δ_{2000}[a] (ddmmss)	v_{sys}[a] (km s^{-1})	Date	T[b] (s)	1σ[c] (mJy)	Site[d]
2MASXJ12335145-2103448	SY1	12 33 51.50	-21 03 45.0	6750	2003-09-13	2088	13	T
NGC4527	LINER	12 34 08.50	+02 39 10.0	1726	2004-07-01	1980	12	T
NGC4540	SY1	12 34 50.85	+15 33 05.3	1281	2003-05-28	1080	18	T
AM1232-365NED01	SY2	12 35 03.60	-37 15 32.0	8789	2003-05-22	2040	14	T
M91	SY	12 35 26.42	+14 29 46.9	485	2003-02-02	1980	21	R
NGC4550	LINER	12 35 30.61	+12 13 15.4	381	2003-01-22	1170	22	R
NGC4507	SY2	12 35 36.54	-39 54 33.3	3497	2003-06-23	1680	15	T
NGC4589	LINER	12 37 25.00	+74 11 31.0	1967	2004-12-20	3660	12	R
M104	SY1.9	12 39 59.43	-11 37 23.0	1021	2003-06-05	900	21	T
NGC4602	SY1.9	12 40 36.62	-05 07 57.0	2518	2002-03-31	3150	14	R
IC3639	SY2	12 40 52.88	-36 45 21.5	3240	2003-07-16	2520	18	T
WKK1263	SY2	12 41 25.80	-57 50 03.3	7149	2002-06-18	2820	10	T
NGC4628	SY2	12 42 25.26	-06 58 15.6	2802	2002-06-02	2520	12	T
IRAS12409+7823	SY1.9	12 42 36.03	+78 07 20.3	6482	2003-01-27	2340	19	R
NGC4636	LINER	12 42 50.00	+02 41 17.0	935	2004-04-25	3690	13	T
NGC4639	SY1.8	12 42 52.39	+13 15 27.1	1007	2003-07-13	1632	16	T
NGC4643	LINER	12 43 20.10	+01 58 42.0	1313	2003-05-28	900	17	T
NGC4651	LINER	12 43 42.62	+16 23 36.0	803	2004-06-12	4380	14	T
NGC4666	LINER	12 45 08.76	-00 27 40.9	1512	2004-06-17	1440	21	T
NGC4698	SY2	12 48 22.97	+08 29 14.3	999	2002-02-24	3060	16	R
NGC4699	SY	12 49 02.23	-08 39 53.5	1388	2003-07-19	2190	12	T
NGC4713	LINER	12 49 57.86	+05 18 39.0	651	2004-06-17	1860	14	T
NGC4750	LINER	12 50 07.12	+72 52 29.7	1614	2004-11-27	4920	16	R
NGC4725	SY2	12 50 26.60	+25 30 05.8	1201	2002-02-24	3240	12	R
NGC4736	LINER	12 50 53.06	+41 07 13.6	308	2005-02-11	8520	13	R
NGC4762	LINER	12 52 56.00	+11 13 53.0	981	2002-02-16	2700	16	T
ESO323-G032	SY2	12 53 20.35	-41 38 13.8	4720	2003-05-07	2790	13	T
NGC4785	SY2	12 53 26.82	-48 44 58.8	3689	2003-06-23	1740	16	T
NGC4772	LINER	12 53 29.04	+02 10 02.4	1036	2004-06-17	2280	14	T
NGC4813	LINER	12 56 36.34	-06 49 03.2	1367	2004-04-25	2430	15	T
NGC4826	SY2	12 56 43.76	+21 40 51.9	407	2005-01-15	4320	12	R
NGC4866	LINER	12 59 27.20	+14 10 18.0	1975	2004-07-07	2280	14	T
NGC4897	SY	13 00 52.87	-13 26 58.9	2539	2003-08-02	1800	14	T

Table 2.2—Continued

Galaxy Name	Type[a]	α_{2000}[a] (hhmmss)	δ_{2000}[a] (ddmmss)	v_{sys}[a] (km s^{-1})	Date	T[b] (s)	1σ[c] (mJy)	Site[d]
NGC4903	SY2	13 01 23.07	-30 56 02.2	4855	2003-05-07	3150	12	T
NGC4939	SY2	13 04 14.33	-10 20 22.7	3079	2002-03-02	3300	14	R
IC4180	SY2	13 06 56.53	-23 55 01.4	2943	2003-05-06	2520	13	T
NGC4968	SY2	13 07 05.89	-23 40 39.4	2928	2003-06-05	1320	16	T
2MASXJ13084201-2422581	SY2	13 08 42.10	-24 22 59.5	4118	2003-07-30	2460	12	T
NGC4981	LINER	13 08 48.86	-06 46 44.5	1677	2003-07-19	1770	12	T
NGC4995	SY	13 09 40.62	-07 50 01.0	1757	2003-06-05	1800	14	T
UGCA330	SY2	13 09 47.50	-10 19 12.0	1208	2002-03-31	3150	14	R
MCG-01-34-008	SY2	13 10 17.31	-07 27 15.2	6566	2002-07-31	1800	15	T
IISZ010	SY1	13 13 05.77	-11 07 41.5	9858	2003-06-07	1320	15	T
NGC5038	LINER	13 15 02.14	-15 57 06.3	2206	2002-09-06	1620	27	T
ESO508-G033	AGN	13 16 23.25	-26 33 41.5	3293	2002-06-01	2700	14	T
NGC5064	LINER	13 19 00.20	-47 54 39.7	2951	2002-05-31	2610	15	T
SBS1317+548	SY2	13 19 15.90	+54 36 06.1	9633	2004-12-14	5640	15	R
NGC5077	SY1.9	13 19 31.65	-12 39 25.9	2791	2003-07-30	1560	14	T
TOLOLO0081	SY2	13 19 38.53	-33 22 54.6	8483	2002-08-10	1800	17	T
NGC5104	LINER	13 21 23.08	+00 20 32.7	5476	2004-07-01	1560	13	T
CTS0022	SY1	13 21 58.15	-31 04 26.1	12855	2004-07-05	2160	12	T
LEDA169714	AGN?	13 22 27.60	-20 35 45.0	6064	2002-09-11	2250	11	T
PGC046808	SY2	13 23 45.01	-27 39 33.4	2319	2002-05-23	1160	19	T
NPM1G-19.0448	AGN	13 23 50.01	-19 41 48.3	5213	2002-09-09	2430	12	T
NGC5122	LINER	13 24 14.96	-10 39 16.4	2792	2002-08-05	2070	14	T
IRAS13218-1929	SY1.9	13 24 35.23	-19 45 11.0	5192	2002-06-01	2700	12	T
NGC5135	SY2	13 25 43.97	-29 50 02.3	4056	2003-07-30	1680	12	T
ESO576-G069	LINER	13 30 05.30	-20 55 58.7	5246	2002-06-02	2520	13	T
NGC5218	LINER	13 32 10.51	+62 46 03.9	2853	2004-11-27	5400	18	R
ESO383-G018	SY2	13 33 26.00	-34 00 55.7	3675	2002-09-09	1980	14	T
ESO509-IG064	SY2	13 34 39.19	-23 40 46.5	2555	2002-06-02	2610	13	T
ESO383-G035	SY1.2	13 35 53.73	-34 17 45.5	2305	2004-07-09	2760	17	T
NGC5258	LINER	13 39 57.95	+00 49 58.4	6608	2004-07-07	1380	15	T
NGC5283	SY2	13 41 05.76	+67 40 20.3	3087	2002-03-04	3060	30	R
2MASXIJ13411287-1438407	SY1	13 41 12.90	-14 38 40.6	12025	2003-07-08	7350	10	T
NGC5266	LINER	13 43 01.61	-48 10 11.8	3043	2002-05-17	2040	13	T

Table 2.2—Continued

Galaxy Name	Type[a]	α_{2000} [a] (hhmmss)	δ_{2000} [a] (ddmmss)	v_{sys} [a] (km s^{-1})	Date	T [b] (s)	1σ [c] (mJy)	Site[d]
MRK0796	SY2	13 46 49.43	+14 24 00.9	6333	2002-07-31	1530	20	T
MRK1361	SY2	13 47 04.38	+11 06 22.9	6625	2004-07-15	1980	12	T
CGCG045-099	SY2	13 47 09.23	+03 38 37.8	6711	2003-07-30	1140	14	T
MRK0461	SY2	13 47 17.74	+34 08 55.3	4779	2002-03-05	3150	15	R
MCG-01-35-013	AGN	13 48 59.59	-07 11 43.8	7401	2002-08-17	1620	17	T
IC4329	SY1	13 49 05.30	-30 17 47.0	4471	2003-05-22	2700	13	T
NGC5322	LINER	13 49 15.19	+60 11 26.5	1770	2004-11-27	4800	24	R
IC4329A	SY1.2	13 49 19.29	-30 18 34.4	4737	2004-06-27	1920	12	T
APMUKS(BJ)B134	LINER	13 49 48.40	-06 58 23.2	6471	2004-06-19	1500	14	T
UM614	SY1	13 49 52.83	+02 04 44.8	9521	2004-07-05	1440	14	T
ESO221-G012	SY?	13 51 31.97	-48 04 55.3	2921	2003-05-11	3350	14	T
NGC5353	AGN	13 53 26.69	+40 16 58.9	2292	2002-02-26	3150	12	R
NGC5354	LINER	13 53 26.70	+40 18 09.9	2548	2002-02-24	2970	13	R
NGC5363	LINER	13 56 07.10	+05 15 20.0	1135	2002-08-05	2070	14	T
ESO578-G009	SY1	13 56 36.70	-19 31 45.1	10040	2004-06-19	1020	16	T
NGC5395	SY2	13 58 38.13	+37 25 29.9	3451	2003-01-19	2100	18	R
UM625	SY2	14 00 40.59	-01 55 18.1	7309	2002-07-31	1530	15	T
ESO510-G046	SY2	14 01 58.45	-25 32 19.8	6219	2002-08-04	1980	11	T
MRK1370	SY2	14 08 04.02	+07 19 39.3	7193	2004-06-29	1320	15	T
PGC050427	SY1.4	14 08 06.78	-30 23 53.9	6936	2004-04-25	1170	19	T
CGCG074-129	SY2	14 10 41.38	+13 33 28.6	4759	2003-07-30	780	20	T
CGCG074-145	SY2	14 13 27.42	+08 58 52.3	7029	2003-08-02	960	16	T
IC4397	SY2	14 17 58.72	+26 24 45.2	4355	2004-11-27	3900	20	R
NGC5566	LINER	14 20 20.00	+03 56 02.0	1499	2002-03-31	3150	17	R
IRAS14167-723	SY2	14 21 21.30	-72 50 20.0	7654	2002-06-11	1800	13	T
NGC5631	SY2	14 26 33.20	+56 34 58.0	1966	2005-02-14	2820	12	R
NGC5678	LINER	14 32 05.80	+57 55 17.0	1910	2005-03-18	9180	13	R
NGC5664	SY2	14 33 43.54	-14 37 10.9	4469	2002-06-02	2160	17	T
IRAS14317-3237	SY2	14 34 44.89	-32 50 27.5	7426	2002-05-31	1890	16	T
WKK3262	SY2	14 35 14.84	-69 43 59.2	7556	2004-05-09	3360	9	T
NGC5701	LINER	14 39 11.03	+05 21 46.6	1497	2002-08-04	1530	15	T
ESO512-G020	SY1	14 44 56.92	-23 47 39.7	3154	2004-06-29	1740	14	T
IRAS14484-3613	SY	14 51 33.20	-36 25 57.0	8534	2004-07-01	1380	13	T

Table 2.2—Continued

Galaxy Name	Type[a]	α_{2000}[a] (hhmmss)	δ_{2000}[a] (ddmmss)	v_{sys}[a] (km s^{-1})	Date	T[b] (s)	1σ[c] (mJy)	Site[d]
WKK3646	SY2	15 04 39.45	-68 00 07.4	4422	2002-05-17	2550	11	T
NGC5838	LINER	15 05 26.20	+02 05 58.0	1357	2002-03-26	3870	15	R
NGC5866	LINER	15 06 29.81	+55 45 48.1	670	2002-04-12	3870	15	R
NGC5879	LINER	15 09 46.82	+57 00 02.6	770	2002-03-26	3780	16	R
2MASXJ15115979-2119015	NLSY1	15 11 59.80	-21 19 01.7	12802	2004-07-05	1380	14	T
ESO328-IG036NED01	SY1	15 14 48.80	-40 21 55.0	6941	2003-05-22	3120	11	T
NGC5921	LINER	15 21 56.50	+05 04 14.0	1473	2002-09-06	2040	21	T
MCG-01-40-001	SY2	15 33 20.70	-08 42 02.3	6733	2002-08-05	1710	13	T
NGC5953	SY2	15 34 32.40	+15 11 38.7	1952	2002-02-22	3240	22	R
NGC5954	SY2	15 34 35.06	+15 12 00.2	1946	2002-03-23	2862	16	R
UGC09944	SY2	15 35 47.86	+73 27 02.5	7178	2002-12-31	2340	22	R
IRAS15335-051	LINER	15 36 11.68	-05 23 52.0	7968	2002-08-02	1350	21	T
NGC5970	LINER	15 38 30.15	+12 11 12.2	1944	2002-03-31	3510	16	R
CGCG194-013	AGN	15 38 38.50	+36 57 29.9	5486	2002-12-31	1650	28	R
CGCG022-021	SY1.9	15 38 44.74	-03 22 48.2	6971	2002-08-17	1980	16	T
NGC5995	SY2	15 48 24.95	-13 45 28.0	7367	2002-08-02	2250	16	T
NGC6027A	AGN	15 59 11.22	+20 45 16.5	4178	2002-03-02	3960	12	R
MRK0885	SY1.5	16 29 48.25	+67 22 41.8	7405	2005-03-20	9120	14	R
NGC6217	SY2	16 32 39.29	+78 11 54.3	1356	2002-02-26	3600	11	R
ESO137-G034	SY2	16 35 13.73	-58 04 46.1	2722	2002-09-14	1890	13	T
IRAS16382-0613	SY2?	16 40 52.24	-06 18 52.3	8092	2002-07-27	1800	12	T
NGC6211	SY2	16 41 27.64	+57 47 00.9	5850	2003-02-02	3780	16	R
ESO138-G001	SY2	16 51 20.12	-59 14 05.2	2715	2002-09-14	2160	13	T
UGC10578	SY	16 51 23.46	-02 27 15.7	7342	2004-06-27	1920	11	T
NGC6221	SY2	16 52 46.08	-59 13 07.0	1475	2002-09-14	2430	11	T
NGC6240	SY2	16 52 58.89	+02 24 03.4	7164	2004-06-19	1560	14	T
NGC6286	LINER	16 58 31.65	+58 56 14.3	5402	2003-02-03	2610	17	R
UGC10639	SY2	16 59 08.57	+28 59 31.0	9456	2003-01-15	1380	19	R
NGC6340	LINER	17 10 24.90	+72 18 16.0	1193	2002-03-26	3780	13	R
NGC6328	LINER	17 23 41.03	-65 00 36.6	4200	2004-05-09	1560	20	T
NGC6394	SY2	17 30 21.43	+59 38 23.7	8252	2005-01-07	5400	9	R
NGC6384	LINER	17 32 24.30	+07 03 38.0	1656	2002-02-22	3420	16	R
CGCG321-020NED01	SY2	17 34 31.64	+67 02 29.2	7767	2004-12-03	4200	15	R

Table 2.2—Continued

Galaxy Name	Type[a]	α_{2000}[a] (hhmmss)	δ_{2000}[a] (ddmmss)	v_{sys}[a] (km s^{-1})	Date	T[b] (s)	1σ[c] (mJy)	Site[d]
CGCG112-010NE	SY2	17 35 33.78	+20 47 46.6	7090	2002-08-04	1710	16	T
NVSSJ173728-290802	SY1	17 37 28.35	-29 08 02.5	6282	2004-06-29	1440	14	T
ESO139-G012	SY2	17 37 39.20	-59 56 26.0	5111	2002-05-19	1710	17	T
[HB91]1739-126	SY1	17 41 48.75	-12 41 00.6	10696	2004-07-05	960	17	T
CGCG300-062	SY2	17 43 17.37	+62 50 20.8	9577	2005-01-09	6660	6	R
NGC6482	LINER	17 51 48.90	+23 04 19.0	3885	2004-07-15	2280	14	T
MRK1119	SY?	17 52 36.86	+37 44 53.2	3163	2003-01-27	1980	26	R
NGC6521	SY1.9	17 55 48.44	+62 36 44.1	8013	2005-01-04	5820	8	R
NGC6552	SY2	18 00 07.29	+66 36 54.3	7737	2003-01-23	2970	13	R
AM1754-634NED03	SY?	18 00 10.96	-63 43 33.9	4627	2004-06-27	2340	10	T
NGC6574	SY	18 11 51.24	+14 58 55.0	2265	2002-02-15	360	47	R
CGCG142-019	SY	18 12 14.07	+21 53 05.4	5367	2003-01-15	1920	15	R
UGC11185NED01	SY2	18 16 09.26	+42 39 18.7	11931	2005-01-11	5700	9	R
NGC6636	SY2	18 22 02.70	+66 36 58.0	4330	2002-12-31	2760	19	R
FAIRALL0049	SY2	18 36 58.29	-59 24 08.6	5945	2002-09-14	2520	11	T
IC4729	SY2	18 39 56.50	-67 25 32.0	4355	2004-05-08	3600	13	T
ESO103-G056	SY2?	18 43 33.37	-64 06 23.0	3293	2002-09-19	2880	13	T
IC4769	SY2	18 47 43.90	-63 09 22.6	4466	2002-05-16	2700	13	T
AM1843-602	LINER	18 47 45.40	-60 20 53.0	10371	2005-06-27	7020	9	T
IC4777	SY2	18 48 11.23	-53 08 51.4	5454	2002-07-04	1080	19	T
IRAS18491-2940	SY1	18 52 22.43	-29 36 20.7	12182	2004-06-25	2340	14	T
ESO025-G002	SY1	18 54 39.77	-78 53 51.2	8303	2003-05-22	2520	16	T
IRASF18492-7832	SY1	18 57 06.80	-78 28 20.0	12084	2003-05-22	1260	20	T
NGC6744	LINER	19 09 46.23	-63 51 25.1	839	2002-05-17	1440	15	T
UGC11415	SY2	19 11 04.50	+73 25 36.0	7369	2002-12-31	1740	25	R
WNB1927+6527	SY2	19 27 20.20	+65 33 51.2	5011	2002-12-31	1380	26	R
IRAS19348-0619	SY1	19 37 33.19	-06 13 05.5	3141	2004-06-29	1740	14	T
IC4870	SY2	19 37 38.00	-65 48 42.0	886	2002-06-05	1260	17	T
NGC6814	SY1.5	19 42 40.64	-10 19 24.6	1555	2004-04-25	3690	11	T
NGC6810	SY2	19 43 34.16	-58 39 20.6	2017	2002-09-21	2340	13	T
IC4889	SY2	19 45 15.82	-54 20 37.4	2552	2004-07-21	1980	13	T
HCG086-07	SY2	19 51 12.06	-30 59 12.9	6339	2002-05-20	1860	16	T
ESO339-G011	SY2	19 57 37.54	-37 56 08.5	5648	2002-05-16	2400	13	T

Table 2.2—Continued

Galaxy Name	Type[a]	α_{2000}[a] (hhmmss)	δ_{2000}[a] (ddmmss)	v$_{sys}$[a] (km s^{-1})	Date	T[b] (s)	1σ[c] (mJy)	Site[d]
IRAS19580-1818	SY1	20 00 55.71	-18 10 27.4	10780	2004-06-25	2220	13	T
CGMW5-11302	AGN	20 02 48.48	+22 28 27.8	8449	2002-08-17	2340	16	T
NGC6890	SY2	20 18 18.07	-44 48 23.4	2400	2004-04-29	1980	21	T
IC4995	SY2	20 19 59.06	-52 37 19.8	4749	2002-07-02	2880	11	T
ESO462-G009	SY2	20 21 51.12	-31 17 18.0	5670	2002-07-02	2610	13	T
ESO234-IG056	SY2	20 37 02.24	-50 05 37.7	2684	2002-06-09	2400	16	T
NGC6967	SY2	20 47 34.20	+00 24 45.0	3721	2002-09-06	2220	14	T
ESO597-G036	AGN	20 48 15.00	-19 50 57.9	8212	2002-08-17	1620	17	T
IC5063	SY2	20 52 02.02	-57 04 09.1	3364	2002-09-19	2976	12	T
NGC6977	AGN	20 52 29.70	-05 44 46.3	6067	2002-08-10	1620	15	T
NGC6978	AGN	20 52 35.59	-05 42 41.6	5914	2002-08-10	1620	14	T
APMUKS(BJ)B204	SY2	20 53 10.42	-52 54 53.2	12725	2004-06-24	1860	12	T
ESO286-G017	SY2	20 57 49.39	-43 21 05.2	9469	2004-06-15	1980	13	T
ESO187-G042	SY2	20 59 31.21	-52 39 51.3	7012	2004-05-09	1800	12	T
CGCG425-034	SY1.5	21 02 21.62	+10 58 16.0	8422	2005-06-16	4020	11	T
NGC7013	LINER	21 03 33.31	+29 53 49.3	777	2003-01-23	1620	17	R
ESO235-G059	SY1.8	21 06 33.65	-49 13 10.3	7284	2004-06-27	1980	11	T
UGC11680NED01	SY2	21 07 41.48	+03 52 19.6	7594	2002-08-10	2610	12	T
UGC11680NED02	SY2	21 07 45.82	+03 52 40.4	7694	2003-01-27	1710	19	R
MRK0510	SY?	21 09 23.06	-01 50 16.7	5735	2003-01-28	1440	18	R
IC1368	SY2	21 14 12.60	+02 10 41.0	3862	2005-02-11	5640	13	R
NGC7083	LINER	21 35 45.42	-63 54 16.6	3077	2002-06-05	2340	14	T
ESO343-IG013NED01	LINER	21 36 10.83	-38 32 40.9	5575	2002-08-05	1890	13	T
2MASXJ21391374-2646315	SY2	21 39 13.70	-26 46 31.3	8920	2004-06-15	1560	14	T
UGC11804	LINER	21 44 09.83	+46 14 45.8	5362	2003-01-23	1170	24	R
NGC7130	SY2	21 48 19.50	-34 57 06.0	4765	2002-09-11	1530	16	T
NGC7135	AGN	21 49 45.56	-34 52 32.7	2617	2002-07-02	1710	14	T
IRAS21497-0824	SY2	21 52 26.00	-08 10 25.0	9986	2004-06-25	2940	11	T
ESO075-G041	SY2	21 57 05.98	-69 41 23.7	8243	2002-06-02	2790	12	T
IC1417	SY2	22 00 21.61	-13 08 49.1	5251	2003-01-28	1890	17	R
NGC7177	LINER	22 00 41.20	+17 44 16.0	1146	2003-02-03	2640	20	R
UGC11871	SY1.9	22 00 41.37	+10 33 08.7	7771	2002-08-17	2520	13	T
NGC7172	SY2	22 02 01.68	-31 52 18.1	2581	2004-06-19	1500	13	T

Table 2.2—Continued

Galaxy Name	Type[a]	α_{2000}[a] (hhmmss)	δ_{2000}[a] (ddmmss)	v$_{sys}$[a] (km s^{-1})	Date	T[b] (s)	1σ[c] (mJy)	Site[d]
NGC7189	LINER	22 03 16.00	+00 34 17.0	8930	2003-01-21	2100	20	R
IC5154	SY2	22 04 29.79	-66 06 51.0	3086	2002-09-21	2610	16	T
UGC11897	LINER	22 04 30.73	+41 24 36.3	4351	2003-01-24	1890	19	R
NGC7212NED02	SY2	22 07 01.98	+10 14 00.3	7786	2002-08-04	1800	12	T
NGC7205	LINER	22 08 34.40	-57 26 33.1	1681	2004-04-29	2940	16	T
NGC7213	SY1.5	22 09 16.25	-47 10 00.0	1781	2004-04-29	3300	14	T
IC5169	SY2	22 10 09.98	-36 05 19.0	2986	2002-06-01	2700	14	T
ESO108-IG017	SY2	22 10 47.40	-66 52 11.5	2175	2002-09-19	1500	14	T
UGC11974	LINER	22 17 15.81	+33 30 13.9	6253	2003-02-03	2340	19	R
IC5201	SY2	22 20 57.43	-46 02 06.1	912	2004-06-19	1260	15	T
MCG+02-57-002	SY1.5	22 23 45.02	+11 50 09.0	8449	2004-07-28	2400	14	T
CGCG429-005	SY1	22 25 35.06	+11 40 11.3	10138	2004-06-25	2400	12	T
NGC7282	SY2	22 25 53.84	+40 18 53.5	4474	2003-01-23	2070	15	R
UGC12040	SY2	22 27 05.74	+36 21 41.9	6260	2003-01-24	1620	18	R
FAIRALL0357	SY2	22 27 31.03	-70 23 18.3	8407	2002-08-13	1890	12	T
ESO602-G025	LINER	22 31 25.49	-19 02 03.1	7324	2002-09-09	1380	16	T
NGC7303	LINER	22 31 32.80	+30 57 22.0	3652	2003-01-21	2280	20	R
ARK557	SY1.5	22 32 30.80	+08 12 26.0	7367	2004-07-15	1680	13	T
CTS0065	SY1	22 34 41.00	-37 06 45.0	12360	2004-06-25	2220	12	T
NGC7314	SY1.9	22 35 45.89	-26 03 01.3	1415	2002-09-11	1440	17	T
NGC7319	SY2	22 36 03.54	+33 58 32.6	6598	2004-12-20	4020	10	R
2DFGRSS180Z007	LINER	22 36 07.20	-27 43 29.4	7898	2002-06-23	2520	14	T
NGC7343	LINER	22 38 37.86	+34 04 17.2	7287	2004-11-27	4800	13	R
ESO534-G009	LINER	22 38 41.64	-25 51 00.5	3348	2002-08-05	2340	12	T
UGC12138	SY1.8	22 40 17.05	+08 03 14.1	7305	2004-06-27	1380	14	T
UGC12150	LINER	22 41 12.26	+34 14 57.0	6279	2004-11-26	2460	17	R
UGC12163	SY1.8	22 42 39.34	+29 43 31.3	7222	2005-01-01	7500	9	R
ESO345-IG045NED01	LINER	22 43 14.23	-40 02 55.5	8845	2003-07-08	2640	15	T
NGC7369	LINER	22 44 12.31	+34 21 04.4	6437	2003-02-04	2640	19	R
NGC7378	SY2	22 47 47.63	-11 48 58.8	2558	2004-06-27	1860	13	T
UGC12199	LINER	22 49 04.01	+40 00 04.2	6582	2004-11-26	2340	18	R
UGC12201	LINER	22 49 09.55	+34 59 30.5	4971	2003-02-02	2160	23	R
2MASXJ22493210+3455098	LINER	22 49 32.10	+34 55 09.8	6861	2004-12-06	5820	14	R

Table 2.2—Continued

Galaxy Name	Type[a]	α_{2000}[a] (hhmmss)	δ_{2000}[a] (ddmmss)	v_{sys}[a] (km s^{-1})	Date	T[b] (s)	1σ[c] (mJy)	Site[d]
MCG-03-58-007	SY2	22 49 37.14	-19 16 26.4	9144	2004-06-15	1418	17	T
NGC7410	SY2	22 55 00.95	-39 39 40.8	1741	2002-06-02	2610	14	T
IC1459	AGN	22 57 10.60	-36 27 44.0	1682	2002-09-21	2340	16	T
ESO027-G019	SY2	22 59 01.62	-80 01 55.3	10975	2004-06-24	2280	11	T
IRAS22570-2601	SY2	22 59 41.84	-25 45 06.3	7796	2002-08-05	1800	12	T
MRK0522	SY2	23 00 19.09	+16 22 57.9	9338	2004-07-28	2220	14	T
NGC7450	SY1.5	23 00 47.82	-12 55 06.7	3157	2002-09-09	1140	15	T
NGC7465	SY2	23 02 00.96	+15 57 53.4	1955	2003-01-21	3420	20	R
NGC7466	SY2	23 02 03.42	+27 03 09.5	7310	2003-01-27	990	24	R
NGC7469	SY1.2	23 03 15.62	+08 52 26.4	4813	2004-07-27	2340	14	T
IC5283	SY?	23 03 17.70	+08 53 37.0	4728	2003-01-27	1170	22	R
MRK0315	SY1.5	23 04 02.62	+22 37 27.5	11217	2005-02-04	5760	13	R
CGCG453-062	LINER	23 04 56.59	+19 33 08.1	7340	2002-08-13	2250	13	T
NGC7479	SY2	23 04 56.65	+12 19 22.4	2362	2003-02-01	2250	19	R
UGC12348	SY2	23 05 18.80	+00 11 21.0	7442	2002-08-15	1800	12	T
ESO469-G011	SY2	23 05 48.90	-30 36 41.8	8269	2004-06-22	2610	14	T
2MASXIJ2305539+171813	SY2	23 05 53.98	+17 18 13.9	12084	2003-01-30	2610	16	R
PG2304+042	SY1	23 07 02.91	+04 32 57.2	12084	2004-06-25	2220	12	T
NGC7496	SY2	23 09 47.26	-43 25 39.8	1640	2002-09-19	1530	15	T
NGC7550	AGN	23 15 16.01	+18 57 42.5	4988	2002-08-13	2340	13	T
NGC7549	AGN	23 15 17.23	+19 02 30.1	4662	2002-03-02	3120	14	R
IC5298	SY2	23 16 00.69	+25 33 24.2	7979	2004-12-21	6480	12	R
NGC7552	LINER	23 16 11.00	-42 34 59.0	1577	2004-06-19	1680	13	T
NGC7591	LINER	23 18 16.24	+06 35 09.3	4875	2002-08-17	1620	16	T
NGC7592A	SY2	23 18 21.16	-04 24 55.3	7203	2003-02-02	3600	14	R
NGC7582	SY2	23 18 23.50	-42 22 14.0	1567	2004-06-27	1560	13	T
UGC12492	SY2	23 18 53.79	-01 03 36.9	8659	2003-01-12	1230	17	R
NGC7590	SY2	23 18 54.60	-42 14 21.0	1588	2002-09-19	1680	15	T
NGC7603	SY1.5	23 18 56.62	+00 14 38.2	8597	2005-02-01	5520	10	R
UGC12519	SY2	23 20 02.75	+15 57 10.6	4315	2002-08-10	2070	16	T
UGC12591	LINER	23 25 21.85	+28 29 42.3	6792	2004-12-05	7500	16	R
KUG2323+226	LINER	23 25 42.71	+22 54 17.8	7190	2003-02-06	2160	19	R
NGC7672	SY2	23 27 31.44	+12 23 06.4	3957	2004-06-19	2280	13	T

Table 2.2—Continued

Galaxy Name	Type[a]	α_{2000}[a] (hhmmss)	δ_{2000}[a] (ddmmss)	v_{sys}[a] (km s^{-1})	Date	T[b] (s)	1σ[c] (mJy)	Site[d]
NPM1G+08.0558	SY2	23 27 42.57	+08 45 30.2	8562	2003-01-12	960	19	R
NGC7678	SY2	23 28 27.91	+22 25 16.2	3449	2003-01-28	2250	16	R
NGC7679	SY1	23 28 46.70	+03 30 42.0	5051	2004-07-27	1740	13	T
NGC7682	SY2	23 29 03.93	+03 32 00.0	5048	2003-02-01	2520	18	R
IC1495	SY2	23 30 47.72	-13 29 07.5	6251	2002-09-11	2250	12	T
UGC12646	SY2	23 31 39.06	+25 56 44.1	7824	2004-12-05	5220	21	R
2MASXIJ23315772-1846203	SY2	23 31 57.76	-18 46 20.7	9126	2003-07-08	1440	20	T
NGC7714	LINER	23 36 14.10	+02 09 18.6	2772	2002-09-11	2070	14	T
UGC12711	LINER	23 37 59.23	+31 59 42.6	4902	2003-02-01	2700	17	R
NGC7733	SY2	23 42 32.98	-65 57 22.7	9834	2004-05-09	3480	8	T
NGC7743	SY2	23 44 21.20	+09 56 03.0	1700	2002-12-08	1260	23	R
UGC12776	LINER	23 46 12.17	+33 22 12.4	4857	2003-01-24	2250	16	R
CGCG432-031	SY2	23 47 09.16	+15 35 45.8	7576	2002-08-17	1890	16	T
CGCG381-051	SY2	23 48 41.70	+02 14 23.0	8920	2004-06-22	2610	13	T
KUG2348+270A	LINER	23 50 47.48	+27 17 16.9	7791	2004-12-05	8340	11	R
NGC7769	LINER	23 51 03.97	+20 09 01.5	4153	2002-09-06	1890	18	T
UGC12812	SY2	23 51 26.80	+20 35 09.9	5440	2002-08-13	1980	14	T
CGCG407-065	SY2	23 51 32.87	+08 44 16.5	12107	2003-01-30	2220	20	R
CGCG498-038	SY2	23 55 44.26	+30 12 44.4	8964	2004-12-10	4950	14	R
IC1515	SY2	23 56 03.92	-00 59 18.6	6520	2003-02-01	2700	16	R
IC1524	SY1	23 59 10.73	-04 07 37.0	5678	2004-07-27	1740	13	T

[a]Type, position, and heliocentric systemic velocity obtained from the NED at the outset of the survey in 2002. Velocities are computed assuming the radio definition of Doppler shift.

[b]Total integration time on+off source.

[c]Rms noise in a 1.3 km s^{-1} spectral channel, corrected for atmospheric opacity (typically ~ 0.07) and for the dependence of antenna gain on elevation.

[d]R=Robledo, T=Tidbinbilla.

Chapter 3

Discovery of Water Maser Emission in Five AGN and a Possible Correlation Between Water Maser and Nuclear $2-10\,\mathrm{keV}$ Luminosities

Paul T. Kondratko, Lincoln J. Greenhill, & James M. Moran

Abstract

We report the discovery of water maser emission in five active galactic nuclei (AGN) with the 100-m Green Bank Telescope (GBT). The positions of the newly discovered masers, measured with the VLA, are consistent with the optical positions of the host nuclei to within 1σ ($0\overset{''}{.}3$ radio and $1\overset{''}{.}3$ optical) and most likely mark the locations of the embedded central engines. The spectra of three sources, 2MASX J08362280+3327383, NGC 6264, and UGC 09618 NED02, display the characteristic spectral signature of emission from an edge-on accretion disk with maximum orbital velocity of $\sim 700\,\mathrm{km\,s^{-1}}$, $\sim 800\,\mathrm{km\,s^{-1}}$, and $\sim 1300\,\mathrm{km\,s^{-1}}$, respectively. We also present a GBT spectrum of a previously known source MRK 0034 and interpret the narrow Doppler components reported here as indirect evidence that the emission originates in an edge-on accretion disk with orbital velocity of $\sim 500\,\mathrm{km\,s^{-1}}$. We obtained a detection rate of 12% (5 out of 41) among Seyfert 2 and LINER systems with $10000\,\mathrm{km\,s^{-1}} < v_{sys} < 15000\,\mathrm{km\,s^{-1}}$. For the 30 nuclear water masers with available hard X-ray data, we report a possible relationship between unabsorbed X-ray luminosity $(2 - 10\,\mathrm{keV})$ and total isotropic water maser luminosity, $L_{2-10} \propto L_{\mathrm{H_2O}}^{0.5\pm0.1}$, consistent with the model proposed by Neufeld and Maloney in which X-ray irradiation and heating of molecular accretion disk gas by the central engine excites the maser emission.

3.1   Introduction

Water maser emission ($\lambda = 1.3$ cm) is currently the only resolvable tracer of warm dense molecular gas in the inner parsec of active galactic nuclei (AGN) and has been detected to date in approximately 60 nuclei, the great majority of which are classified optically as Seyfert 2 or LINER (e.g., Braatz et al. 1996, 2004; Greenhill et al. 2003; Henkel et al. 2005; Kondratko et al. 2006; Zhang et al. 2006). Because of the association of maser emission with nuclear activity, X-ray irradiation of molecular gas by the central engine provides the most likely model for exciting the maser emission (e.g., Neufeld, Maloney, & Conger 1994). Maser emission might be associated with Seyfert 2 systems in particular because, over a range of AGN luminosity, the shielding column density that provides the obscuring geometry in type 2 AGN (e.g., Lawrence & Elvis 1982; Antonucci 1993) maintains not only a reservoir of molecular gas but also physical conditions conducive to maser action, which are temperatures of $250 - 1000 \, \mathrm{K}$ and H_2 number densities of $10^{8-10} \, \mathrm{cm}^{-3}$ (e.g., Desch, Wallin, & Watson 1998). The importance of the obscuring geometry in this context is supported by an empirical observation that water maser sources are found preferentially in nuclei with large hydrogen column densities ($N_H > 10^{24} \, \mathrm{cm}^{-2}$; Braatz et al. 1997b; Madejski et al. 2006; Zhang et al. 2006). There is good evidence that LINERs are low-luminosity analogues of Seyfert 2 systems (e.g., Ho et al. 1997b; Ho 1999a; Ho et al. 2003), which might explain the association of maser emission with the former. If X-ray irradiation indeed excites the maser emission (e.g., Neufeld et al. 1994), then a relationship between X-ray and water maser luminosities might reflect this dependance. Braatz et al. (1997b) observed no correlation between the

two, but that study was based on only seven water maser systems and relied on the relatively coarse X-ray data from EXOSAT, GINGA, and ASCA telescopes, with which luminosities can be difficult to estimate accurately when column densities are large. On the other hand, Henkel et al. (2005) reported a correlation between infrared and total isotropic water maser luminosities (i.e., assuming the isotropic emission of maser radiation), and this might be indirectly indicative of a physical relationship between X-ray and maser luminosities, mediated by dust reprocessing (e.g., Franceschini et al. 2005). The substantial increase in the number of known water maser sources over the past few years (e.g., Greenhill et al. 2003; Braatz et al. 2004; Kondratko et al. 2006) combined with the recent growth in the number of AGN for which high-quality X-ray spectra have been obtained (with angular apertures that isolate the central engines reasonably well), have enabled a new look at the possibility of a relationship between X-ray and water maser luminosities.

Very Long Baseline Interferometry (VLBI) maps of seven water maser sources have been interpreted in a context of a model in which the maser emission traces a nearly edge-on disk of molecular material 0.1 to 1 pc from a supermassive black hole: NGC 4258 (Miyoshi et al. 1995), NGC 1386 (Braatz et al. 1997a), NGC 4945 (Greenhill et al. 1997b), NGC 1068 (Greenhill & Gwinn 1997), NGC 3079 (Trotter et al. 1998), IC 2560 (Ishihara et al. 2001), and Circinus (Greenhill et al. 2003). As a consequence of these studies, it is believed that maser emission is detected preferentially in edge-on parsec-scale disks along the diameter perpendicular to the line of sight (a.k.a. the midline) and close to the line-of-sight towards the center. These are the loci within disks where the gradient in line-of-sight velocity is zero and, as a result, the coherent paths for maser emission are maximized. Thereby,

a characteristic spectral signature of emission from an edge-on disk consists of a spectral complex in the vicinity of the systemic velocity (low-velocity emission) and two spectral complexes (high-velocity emission) more or less symmetrically offset from the systemic velocity by the orbital velocity ($> 100 \, \mathrm{km \, s^{-1}}$, based on aforementioned VLBI studies). Sources that display such spectra constitute approximately 40% of the known nuclear water masers and are referred to here as high-velocity systems.

Discovery of new high-velocity water maser systems is important because VLBI maps of these sources can be used to determine pc-scale accretion disk structures, to estimate accurately black hole masses (e.g., Greenhill & Gwinn 1997; Greenhill et al. 2003; Herrnstein et al. 2005), and to obtain distances to the host galaxies independent of standard candles (Herrnstein et al. 1999), the latter in cases where a robust disk model is combined with a measurement of either maser proper motions or drifts in the line-of-sight velocities of spectral features (i.e., centripetal acceleration). However, surveys for water maser emission are challenging and require high sensitivity, wide bandwidth, and high spectral resolution because 1) the water maser emission is weak ($\ll 1$ Jy), 2) its velocity extent is determined by the rotational velocity of the accretion disk, which can exceed $1000 \, \mathrm{km \, s^{-1}}$ and is not known in advance, and 3) the maser lines are typically narrow (≤ 1 km s^{-1}). The Green Bank Telescope (GBT) of the NRAO[1] and its wide-bandwidth spectrometer together constitute the most sensitive observing system currently in operation at $\lambda = 1.3 \, \mathrm{cm}$; as a result, detection rates for samples with comparable distributions of

[1]The National Radio Astronomy Observatory is operated by Associated Universities, Inc., under cooperative agreement with the National Science Foundation

distance are highest for surveys conducted with the GBT. For instance, the seminal survey of AGN with $1\sigma \sim 60\,\mathrm{mJy}$ sensitivity (in $\sim 1\,\mathrm{km\,s^{-1}}$ spectral channels) by Braatz et al. (1996) and a search with $1\sigma \sim 14\,\mathrm{mJy}$ sensitivity (in $1.3\,\mathrm{km\,s^{-1}}$ spectral channels) with the 70-m NASA Deep Space Network (DSN) antennas (Greenhill et al. 2003; Kondratko et al. 2006) yielded incidence rates of water maser emission among nearby ($v_{sys} < 7000\,\mathrm{km\,s^{-1}}$) Seyfert 2 and LINER systems of $\sim 7\%$ and $\sim 10\%$, respectively. However, a GBT survey conducted with $1 \sim 3\,\mathrm{mJy}$ sensitivity (converted to $1.3\,\mathrm{km\,s^{-1}}$ spectral channels) resulted in an incidence rate of $\sim 20\%$ among Seyfert 2 and LINER systems with $v_{sys} < 7500\,\mathrm{km\,s^{-1}}$ (Braatz et al. 2004).

We used the GBT to survey 56 AGN with $10000 < v_{sys} < 30000\,\mathrm{km\,s^{-1}}$ selected from the NASA Extragalactic Database (NED). Previous surveys have concentrated on detection of water maser emission mostly among nearby sources (cf. Henkel et al. 1998; Barvainis & Antonucci 2005). In particular, galaxies with $v_{sys} > 10000\,\mathrm{km\,s^{-1}}$ constitute only $\sim 7\%$ and 14% of AGN in the two largest surveys to date (Braatz et al. 1996 and Kondratko et al. 2006, respectively) and, as a result, only 4 out of ~ 60 known maser sources lie beyond $10000\,\mathrm{km\,s^{-1}}$ (Tarchi et al. 2003; Henkel et al. 2005; Kondratko et al. 2006, Zhang et al. 2006). We have discovered water maser emission in five AGN between 10000 and $15000\,\mathrm{km\,s^{-1}}$. In this paper, Section 3.3, we present spectra and sub-arcsecond positions for the detected emission and address survey statistics. In Section 3.4, we discuss a possible correlation between X-ray and water maser luminosities.

3.2 Observations

The survey was conducted during the 2003-2004 northern winter with the GBT using the observing system and correlator setup identical to that described in Braatz et al. (2004). The channel spacing was 24.4 kHz and the instantaneous bandwidth was 380 MHz ($\approx 5600\,\mathrm{km\,s^{-1}}$ for a representative recessional velocity of $12500\,\mathrm{km\,s^{-1}}$, assuming the optical definition of Doppler shift). To obtain total-power spectra of each source, we nodded the telescope by $3'$ every 2 min between two positions on the sky so that each target was always present in one of the two GBT beams for each polarization. System temperatures were measured against a calibrated noise source injected at the receiver and ranged from 28 to 59 K depending on elevation and weather conditions. By comparing maser line amplitudes among beams and polarizations, we estimate that the calibration of the system temperature is accurate to within 30%. This uncertainty dominates the error budget for the flux density scale in the survey. Antenna pointing corrections — obtained every ~ 30 minutes using sources from the VLA Calibrator Manual — were typically $< 6''$, which corresponds to a $< 8\%$ loss in source flux density for a $36''$ beamwidth (FWHM) at 1.3 cm. For the observations reported here, the wind speed at the GBT site was generally < 13 mph, which corresponds to a one-dimensional rms tracking error of $< 5''$ and a signal loss of $< 6\%$ (with the exception of CGCG 482-008 and MRK 0948, which were observed with wind gusts up to 20 mph, corresponding to a one-dimensional rms tracking error of $< 13''$ and a signal loss of $< 29\%$; Condon 2003). Data were reduced using scripts written in the Interactive Data Language. We subtracted a running boxcar average of width 6.25 MHz to remove systematic baseline structure

from the total-power spectra. To convert the spectra to flux density units, we used the gain curve obtained by the GBT staff based on measurements of opacity corrected antenna temperature for NGC 7027 at $\sim 1.4\,$cm (R. Maddalena 2003, private communication). The resulting $1\,\sigma$ noise levels attained in an integration of $\sim 30\,$minutes total and corrected for atmospheric opacity estimated from tipping scans (typically ~ 0.06) were $3 - 6\,$mJy in a $24.4\,$kHz channel. The spectra presented here have been iteratively Hanning smoothed to an effective resolution of $108\,$kHz.

3.3   Results

In a survey with the GBT of $56\,$AGN with $10000\,\mathrm{km\,s^{-1}} < v_{sys} < 30000\,\mathrm{km\,s^{-1}}$ selected from the NED (Table 3.1), we have detected five new water maser sources: UGC 09618 NED02, 2MASX J08362280+3327383, NGC 6264, IRAS 03355+0104, SBS 0927+493 (Fig. 3.1 and Table 3.2). The five discoveries were subsequently confirmed with the Very Large Array (VLA) using narrow observing bandwidths ($6.25 - 12.5\,$MHz). In addition, the UGC 09618 NED02, 2MASX J08362280+3327383, NGC 6264, and SBS 0927+493 broadband (i.e., $350\,$MHz) maser spectra were confirmed by at least one observation on a different day with the GBT. The nuclei that are host to the detected maser emission are spectroscopically classified as Seyfert 2 or LINER (Table 3.2). Positions of the maser emission measured with the VLA are consistent with optical positions of the AGN to within 1σ (typically $0\rlap{.}''3$ radio and $1\rlap{.}''3$ optical, or of order $1\,$kpc at a recessional velocity of $15000\,\mathrm{km\,s^{-1}}$), which is suggestive of an association of the detected emission with nuclear activity.

Table 3.1.   Galaxies Surveyed for Water Maser Emission with the Green Bank Telescope.

Galaxy	Type[a]	α_{2000} (hh mm ss)	δ_{2000}[a] (dd mm ss)	v_{sys}[a] (km s^{-1})	Date	T_{sys}[b] (K)	1σ[c] (mJy)
UM213	LINER	00 12 17.83	−00 06 10.6	12149	11-10-2003	30	4.6
MRK0948	SY2	00 28 14.34	+07 07 45.4	12022	11-08-2003	42	4.8
UM254	SY2	00 31 34.27	−02 09 16.8	13311	11-10-2003	32	5.9
FGC0061	SY2	00 34 43.51	−00 02 26.7	12610	11-10-2003	28	3.7
LEDA093200	SY2	00 41 35.07	−09 21 52.2	14234	11-10-2003	29	4.0
MRK1143	SY2?	00 42 33.91	+03 15 25.0	11047	11-10-2003	28	3.2
3C033	SY2	01 08 52.86	+13 20 13.8	17898	11-03-2003	48	5.2
UGC00849	AGN	01 19 24.16	+12 26 48.7	14265	11-03-2003	57	6.0
IRAS01364-1042	LINER	01 38 52.87	−10 27 11.7	14520	11-10-2003	29	4.3
CGCG482-008	SY2	01 44 50.08	+21 52 56.7	10508	11-08-2003	37	4.1
IRAS02096-0526	SY2	02 12 04.96	−05 12 34.0	12291	11-10-2003	30	4.4
VV588	SY2	02 42 52.12	+07 35 51.7	11476	11-08-2003	37	4.2
IRAS03362-1641	SY2	03 38 34.54	−16 32 15.8	11062	11-10-2003	32	4.4
[ZHG90]0410+1021A	AGN	04 13 26.40	+10 28 27.0	27598	11-03-2003	36	4.0
IRAS04281-0944	LINER	04 30 33.22	−09 37 44.8	14060	11-10-2003	30	3.8
3C192	SY2	08 05 35.00	+24 09 50.0	17928	11-03-2003	38	4.2
MRK1212	SY2	08 07 05.53	+27 07 33.8	12409	11-08-2003	30	3.3
MCG+05-23-016	SY2	09 34 06.37	+27 20 59.5	13251	11-08-2003	31	3.2
WAS02	SY2	09 46 00.35	+22 22 48.5	10343	11-08-2003	32	3.4
RXJ0953.5+2539	AGN	09 53 31.30	+25 39 42.0	13221	11-03-2003	43	4.8

Table 3.1—Continued

Galaxy	Type[a]	α_{2000} (hh mm ss)	δ_{2000}[a] (dd mm ss)	v_{sys}[a] (km s^{-1})	Date	T_{sys}[b] (K)	1σ[c] (mJy)
CGCG182-038	SY2	09 55 52.54	+35 57 56.4	12651	11-09-2003	40	4.1
IRASF09581+3126	SY2	10 01 01.90	+31 12 16.9	12735	11-10-2003	32	4.2
UGC05984NED01	SY2	10 52 14.95	+30 03 28.8	10372	11-08-2003	33	3.8
ABELL1142:[GBB84]059	SY2	11 00 57.29	+11 02 47.4	10697	11-08-2003	34	4.0
2MASXJ11165338+2758219	SY2	11 16 53.39	+27 58 22.3	10408	11-10-2003	35	5.0
IC3078	SY1.9	12 16 00.03	+12 41 14.0	19814	11-03-2003	42	4.8
UGC07342NOTES01	SY2	12 18 12.20	+29 15 06.3	13834	11-03-2003	45	4.6
[HB89]1219+047	SY1	12 21 37.91	+04 30 26.3	28180	11-03-2003	38	4.8
IRAS13293+0216	SY2	13 31 52.85	+02 00 59.7	25875	11-03-2003	40	4.4
MRK0661	SY2	13 32 13.68	+26 56 59.3	10603	11-10-2003	40	5.1
MRK0268	SY2	13 41 11.14	+30 22 41.2	11950	11-10-2003	38	5.2
FBQSJ143444.9+231743	SY1	14 34 44.94	+23 17 43.0	29979	11-03-2003	37	3.9
CGCG077-021	SY2	15 09 08.78	+09 02 21.5	13275	11-08-2003	39	4.2
UGC09756NED01	AGN	15 11 24.27	+06 20 38.7	11938	11-08-2003	46	5.0
CGCG049-106	AGN	15 17 51.80	+05 06 26.0	11603	11-08-2003	38	4.5
CGCG077-117	SY2	15 24 12.58	+08 32 41.1	11120	11-08-2003	38	4.5
IC1191	SY2	16 06 28.75	+18 16 04.4	11632	11-08-2003	43	4.7
[GCD2000]J161710.5+063843.0	AGN	16 17 10.50	+06 38 43.0	27581	11-03-2003	37	4.2
IRAS16184+0651	LINER	16 20 56.66	+06 44 44.4	17988	11-03-2003	44	4.7
IRAS16319+4725	SY1	16 33 23.50	+47 19 00.1	34866	11-02-2003	50	5.2

Table 3.1—Continued

Galaxy	Type[a]	α_{2000} (hh mm ss)	δ_{2000} [a] (dd mm ss)	v_{sys} [a] (km s^{-1})	Date	T_{sys} [b] (K)	1σ [c] (mJy)
IRAS16388+4634	SY2	16 40 20.80	+46 28 43.0	17688	11-03-2003	45	4.1
FBQSJ172527.2+372631	AGN	17 25 27.27	+37 26 31.0	11692	11-08-2003	57	6.5
IRAS17348+4920	SY2	17 36 09.84	+49 18 28.1	22424	11-03-2003	49	5.4
IRASF17418+7042	SY2	17 41 14.87	+70 41 26.1	17988	11-02-2003	51	5.3
[MHH96]J181353+570456	SY2	18 13 53.00	+57 04 56.0	17628	11-03-2003	55	6.1
2MASXJ21234458+2504272	SY2	21 23 44.58	+25 04 27.1	30579	11-03-2003	45	5.1
MRK0309	SY2	22 52 34.70	+24 43 49.8	12636	11-08-2003	39	4.2
2MASXJ22593337+0237355	SY2	22 59 33.39	+02 37 35.2	14390	11-03-2003	55	5.9
UGC12551	SY2	23 22 09.20	+09 16 11.0	11782	11-08-2003	44	4.7
IRAS23201+0805	SY2	23 22 43.82	+08 21 36.9	11330	11-03-2003	59	6.1
CGCG455-055	SY2	23 51 13.93	+20 13 46.3	13049	11-08-2003	44	4.8

[a]Type, position, and heliocentric optical systemic velocity obtained from the NED at the outset of the survey in 2002.

[b]Average system temperature.

[c]Rms noise in a 24.4 kHz spectral channel, corrected for atmospheric opacity (typically from 0.02 to 0.07) and for the dependence of antenna gain on elevation.
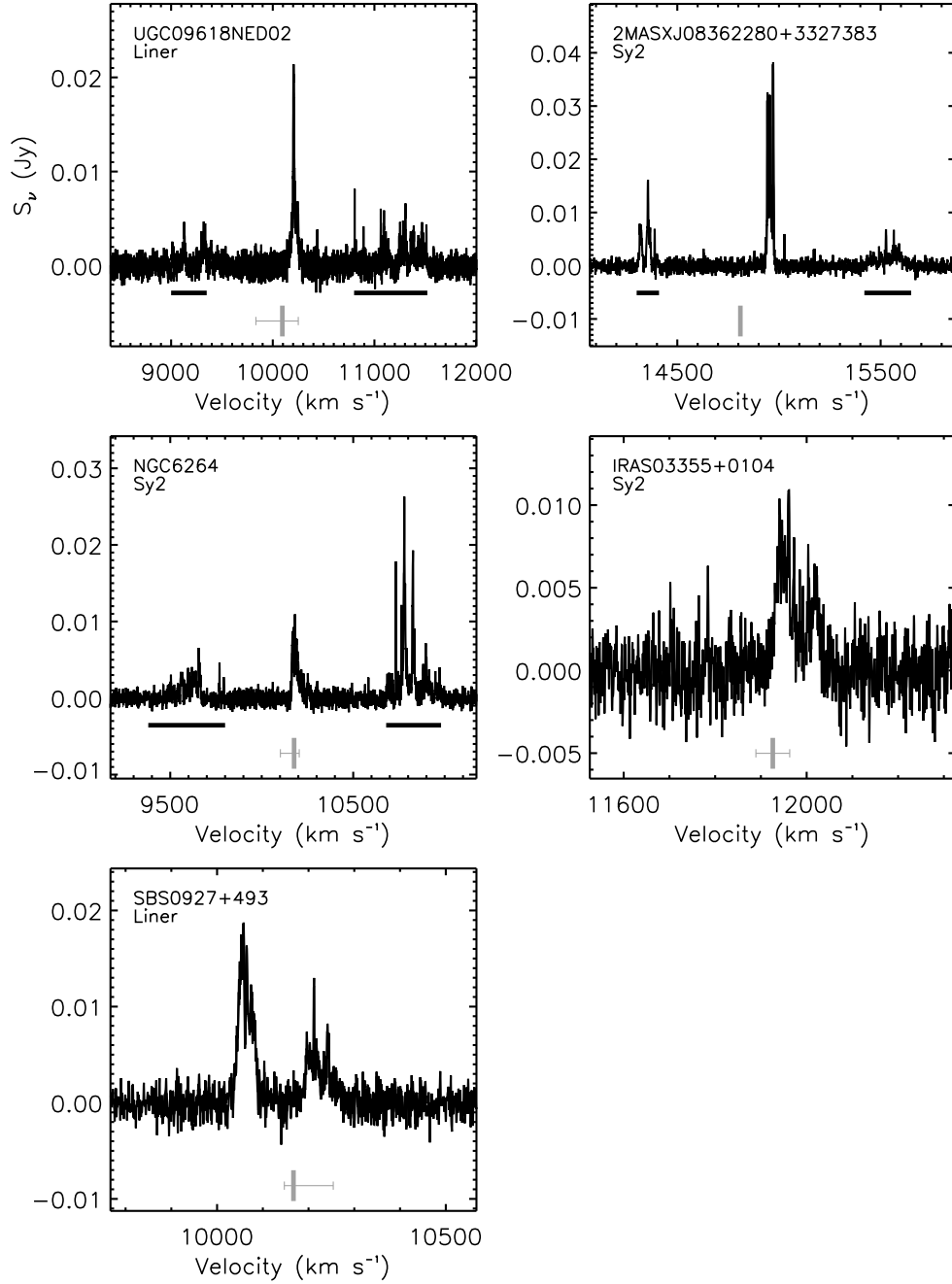
Figure 3.1.— Spectra of UGC 09618 NED02, 2MASX J08362280+3327383, NGC 6264, IRAS 03355+0104, SBS 0927+493 obtained with the Green Bank Telescope. Vertical bars mark the optical heliocentric systemic velocities of the host galaxies listed in the NED, while the associated error bars show the range of listed systemic velocity estimates. Horizontal bars indicate approximate velocity ranges of high-velocity emission. To illustrate the difference in the velocity scale among spectra, the tick marks are placed every $100\,\mathrm{km\,s^{-1}}$ for each x-axis.

The maser spectra of UGC 09618 NED02, 2MASX J08362280+3327383, and NGC 6264 show a characteristic spectral signature of emission from an edge-on disk: two high-velocity complexes approximately symmetrically offset from the systemic velocity and a third spectral complex in the vicinity of the systemic velocity. If the highly red- and blue-shifted emission in these systems indeed represents high-velocity emission, then the maximum orbital velocities of the disks as traced by the maser emission are $\sim 1300\,\mathrm{km\,s^{-1}}$, $\sim 700\,\mathrm{km\,s^{-1}}$, and $\sim 800\,\mathrm{km\,s^{-1}}$, respectively, making UGC 09618 NED02 the fastest known rotator. (The previously fastest rotator was NGC 4258 at $\sim 1200\,\mathrm{km\,s^{-1}}$; Modjaz et al. 2005.) Because the high-velocity emission extends over $\Delta v \sim 750\,\mathrm{km\,s^{-1}}$ for UGC 09618 NED02, it must occupy a fractional range of radii $\Delta r/R \approx 2\Delta v/v \sim 1.6$ assuming Keplerian rotation (where we have differentiated the Keplerian rotation law, $v \propto r^{-0.5}$, with respect to r). For a range in disk sizes from that of NGC 4258 ($0.16 - 0.28\,\mathrm{pc}$) to NGC 1068 ($0.6 - 1.1\,\mathrm{pc}$), the maser emission in this source traces a disk of radial extent $\Delta r \sim 0.36 - 1.4\,\mathrm{pc}$. The corresponding central mass would be $(6 - 24) \times 10^7\,M_\odot$, which is larger than black hole masses measured with VLBI to date (the highest is NGC 4258 at $3.9 \times 10^7\,M_\odot$ Herrnstein et al. 2005). The anticipated centripetal acceleration — that is the secular velocity drift of the systemic feature — would be $0.3 - 11\,\mathrm{km\,s^{-1}\,yr^{-1}}$, which should be readily detectable within one year using single dish monitoring. The remaining two detections — IRAS 03355+0104 and SBS 0927+493 — display spectral feature(s) only in the vicinity of the systemic velocity of the host galaxy, which makes physical interpretation difficult.

Table 3.2.   Newly Discovered Nuclear Water Maser Sources.

Galaxy Name	Type[a]	α_{2000}[b] (hh mm ss)	δ_{2000}[b] (dd mm ss)	v_{sys}[c] (km s^{-1})	Date	T_{sys}[d] (K)	1σ[e] (mJy)	$\Delta\nu$[f] (kHz)	BW[g] (MHz)
IRAS 03355+0104	Sy2	03 38 10.38	+01 14 18.2	11926	11-08-2003	38	3.2	195	12.5
		03 38 10.38	+01 14 18.3						
2MASX J08362280+3327383	Sy2	08 36 22.80	+33 27 38.6	14810	01-15-2005	25	1.5	97.7	6.25
		08 36 22.80	+33 27 38.8						
SBS 0927+493	LINER	09 31 06.76	+49 04 47.5	10167	02-01-2006	37	2.3	195	12.5
		09 31 06.77	+49 04 47.2						
UGC 09618 NED02	LINER	14 57 00.68	+24 37 02.7	10094	01-15-2005	26	1.4	195	12.5
		14 57 00.67	+24 37 02.9						
NGC 6264	Sy2	16 57 16.12	+27 50 58.7	10177	01-27-2005	23	1.3	195	12.5
		16 57 16.13	+27 50 58.6						

[a] Activity type from the NED.

[b] *First line:* optical positions from the NED with uncertainties of ±0″5 (SBS 0927+493) or ±1″3. *Second line:* maser positions measured with a VLA snapshot, providing typical uncertainties of ±0″3. To establish the magnitude of systematic uncertainties in position, we imaged disjoint segments of the VLA data and confirmed that they yield consistent maser positions (that is, within 0″3).

[c] Optical heliocentric systemic velocity from the NED.

[d] Average system temperature.

[e] Rms noise in a 24.4 kHz spectral channel, corrected for atmospheric opacity (typically from 0.02 to 0.07) and for the dependence of antenna gain on elevation.

[f] VLA channel width.

[g] VLA bandwidth; the VLA band was in each case centered on the strongest maser line.
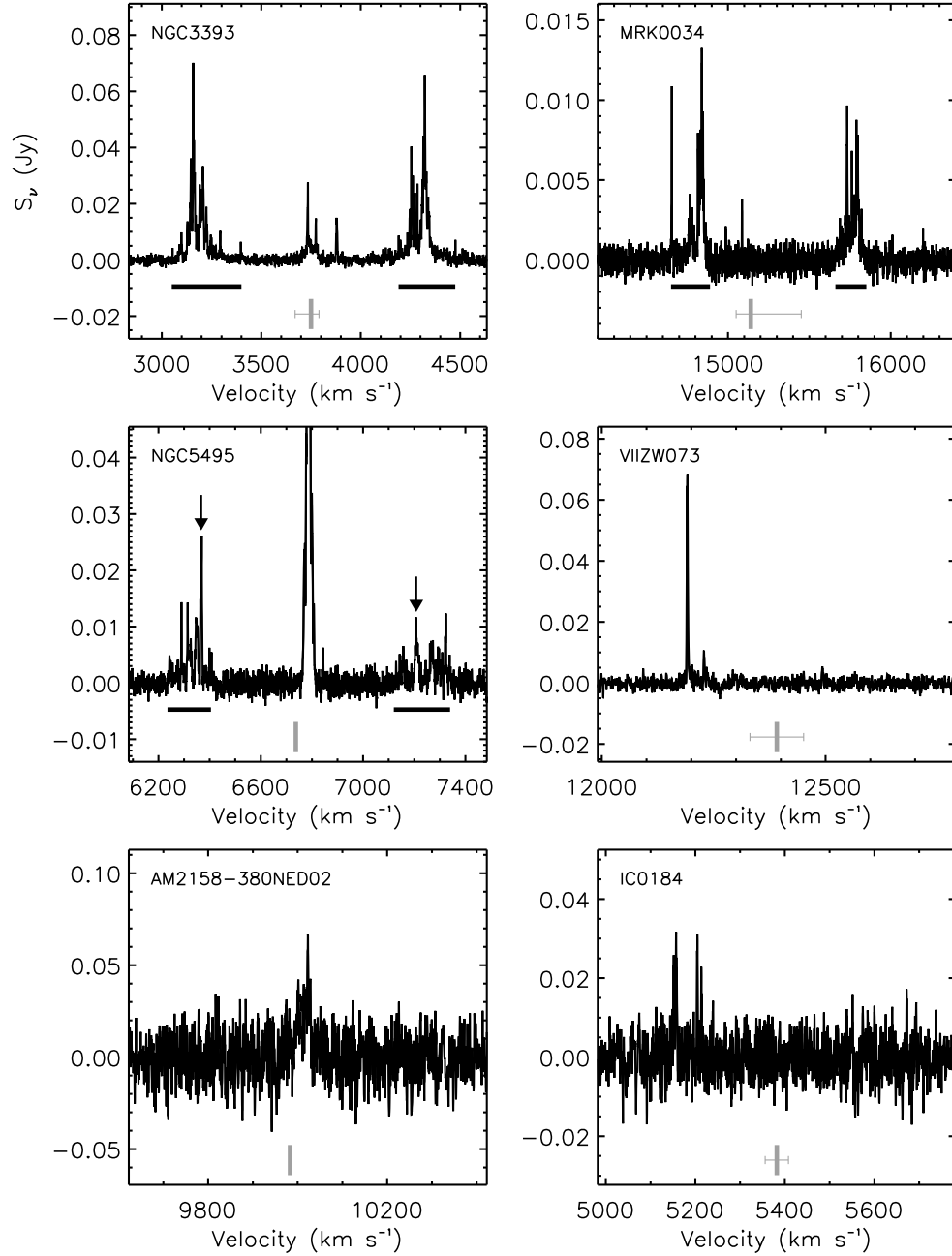
Figure 3.2.— Spectra of previously known masers in NGC 3393, MRK 0034, NGC 5495, VII ZW 073, AM 2158-380 NED02, and IC 0184 obtained with the Green Bank Telescope. The arrows indicate NGC 5495 high-velocity features marginally detected with the DSN (Kondratko, P. T., et al. 2006). Vertical bars mark the optical heliocentric systemic velocities of the host galaxies listed in the NED, while the associated error bars show the range of listed systemic velocity estimates. Horizontal bars indicate approximate velocity ranges of high-velocity emission. To illustrate the difference in the velocity scale among spectra, the tick marks are placed every $100\,\mathrm{km\,s^{-1}}$ for each x-axis.

We also used the GBT to obtain high signal-to-noise-ratio (SNR) spectra of known sources, including those recently discovered with the DSN (cf. Henkel et al. 2005; Kondratko et al. 2006; Fig. 3.2 and Table 3.3). Spectra of MRK 0034, NGC 3393, NGC 5495, VII ZW 073, and IC 0184 presented here are the most sensitive obtained to date (cf. Henkel et al. 2005; Kondratko et al. 2006). The narrow Doppler components in the spectrum of MRK 0034 reported here were not evident in the previous spectra of the source obtained with $4.65 \, \mathrm{km \, s^{-1}}$ channels. Absent narrow lines, Henkel et al. (2005) suggested the possibility that the maser emission in MRK 0034 might be excited by jet activity, which has been associated with broad spectral features in other AGN (e.g., Claussen et al. 1998; Gallimore et al. 2001; Peck et al. 2003). However, the new spectrum adds support for the hypothesis that MRK 0034 is a high-velocity system. In this context and considering the large uncertainty on the recessional velocity of the galaxy (see Fig. 3.2), the two spectral complexes are consistent with blue- and red-shifted high-velocity emission that is symmetrically displaced from the systemic velocity by $\sim 500 \, \mathrm{km \, s^{-1}}$. The GBT spectrum of NGC 3393 shows a new systemic complex at $\sim 3750 \, \mathrm{km \, s^{-1}}$ as well as weak ($\sim 5 \, \mathrm{mJy}$) high-velocity lines at ~ 3098, ~ 3293, ~ 3396, ~ 4190, and $\sim 4475 \, \mathrm{km \, s^{-1}}$ (Fig. 3.2). We also confirmed the low-velocity line at $\sim 3878 \, \mathrm{km \, s^{-1}}$ in the NGC 3393 spectrum and the high-velocity lines in the NGC 5495 spectrum, which were all marginally detected with the DSN (Kondratko et al. 2006).

Our detection rate is consistent with the survey being sensitivity limited. Among Seyfert 2 and LINER systems with $10000 \, \mathrm{km \, s^{-1}} < v_{sys} < 15000 \, \mathrm{km \, s^{-1}}$, we obtain a detection rate of 5 out of 41 or $12\% \pm 5\%$, which should be compared to the incidence rates of $20\% \pm 5\%$ (15 out of 75) and $14\% \pm 5\%$ (7 out of 49) in

Table 3.3. Known Water Maser Sources Reobserved with the Green Bank Telescope.

Galaxy	Type[a]	α_{2000}[b] (hh mm ss)	δ_{2000}[b] (dd mm ss)	v_{sys}[c] (km s^{-1})	Date	T_{sys}[d] (K)	1σ[e] (mJy)
IC 0184	Sy2	01 59 51.23	−06 50 25.4	5382	07-03-2005	71	8.9
VII ZW 073	Sy2	06 30 25.54	+63 40 41.3	12391	01-01-2005	35	2.6
MRK 0034	Sy2	10 34 08.592	+60 01 52.01	15140	01-18-2005	21	0.98
NGC 3393	Sy2	10 48 23.45	−25 09 43.6	3750	01-15-2005	37	1.9
NGC 5495	Sy2	14 12 23.35	−27 06 29.2	6737	02-09-2006	40	2.4
AM 2158-380 NED02	Sy2	22 01 17.10	−37 46 23.0	9983	07-03-2005	99	22

[a]Activity type from the NED.

[b]Positions from Kondratko et al. 2006 ($\sigma = 0\rlap{.}''3$) except for MRK 0034, which is from the NED ($\sigma = 0\rlap{.}''3$).

[c]Optical heliocentric systemic velocity from the NED.

[d]Average system temperature.

[e]Rms noise in a 24.4 kHz spectral channel, corrected for atmospheric opacity (typically from 0.02 to 0.07) and for the dependence of antenna gain on elevation.

velocity bins $0 - 5000$ and $5000 - 12000 \, \mathrm{km \, s^{-1}}$, respectively, from a GBT survey of the same sensitivity (Braatz et al. 2004; to estimate the errors, we used the unbiased maximum likelihood estimator for the variance of the Binomial parameter p). The detection rate decreases with distance because the spectral rms noise level was approximately the same for each source in both surveys. The detection rate of high-velocity emission is $60\% \pm 24\%$ (3 out of 5) in this survey or $44\% \pm 13\%$ (7 out of 16) if we include the GBT detections reported in Braatz et al. (2004; where we excluded the starburst galaxy NGC 2782). These rates should be compared to the analogous rate of $27\% \pm 12\%$ (4 out of 15) in the DSN survey (Greenhill et al. 2003; Kondratko et al. 2006). Although the uncertainties due to counting statistics are large, the higher detection rates for high-velocity emission in the GBT surveys may have been a consequence of higher sensitivity, and perhaps finer spectral resolution as well.

3.4   Discussion

Using the sample of known nuclear masers with available $> 2 \, \mathrm{keV}$ X-ray data, we have identified a possible relationship between unabsorbed X-ray luminosity $(2 - 10 \, \mathrm{keV})$ and integrated water maser luminosity, assuming isotropic emission of radiation. In log-log space (Fig. 3.3 and Table 3.4), we obtain a slope of $m = 0.4 \pm 0.1$ and a Spearman correlation coefficient of $\rho = 0.4 \pm 0.1$ (Table 3.5). The probability that a random data set of the same size would yield a larger magnitude of the correlation coefficient (hereafter referred to as the significance level) is 0.07 ± 0.07.
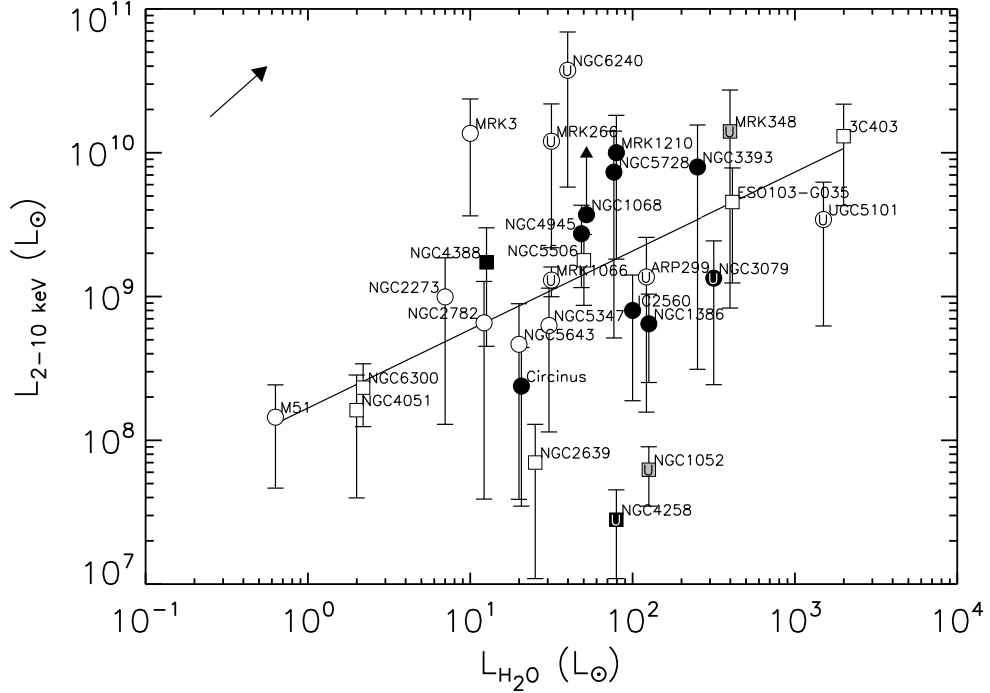
Figure 3.3.— Unabsorbed X-ray luminosity $(2 - 10\,\text{keV})$ versus total isotropic water maser luminosity where the data points are from Table 3.4. Symbol shading discriminates among maser types: *(black)* high-velocity systems (see definition in Section 3.1), *(open)* sources that are not known to be high-velocity systems, and *(grey)* maser sources known to be associated with radio jets rather than disks. Symbol shape differentiates between Compton-thick *(round)* and Compton-thin *(square)* objects. Galaxies with multiple nuclei, AGN with maser emission tied to jet activity, and LINER systems (see the text) are labelled by a letter U. Vertical error bars indicate the range of luminosity estimates given in the literature for independent data sets (Table 3.4), and the symbols are placed at the midpoints. The arrow in the top left corner illustrates the effect of a hypothetical factor of 1.5 increase in distance (i.e., points move up and to the right by this amount). For the full sample with no LINERs, systems with multiple nuclei, and "jet masers," we obtain a correlation coefficient of 0.5 ± 0.1 and a slope of 0.5 ± 0.1 (black line shows the results of a linear fit), where the asymmetric uncertainties in ordinate values have been taken into account (see Table 3.5). The lower limit on X-ray luminosity of NGC 1068 was not used in the fit.

Table 3.4. Water Maser and Unabsorbed $2 - 10\,$keV Luminosities.

Galaxy	D[a] (Mpc)	$\log L_{H_2O}$[b] $(L_\odot)$	$\log L_{2\text{-}10}$[c] $(L_\odot)$	Telescopes[d]	Ref[e]	Type[f]	Ref[g]
NGC 1068	14	1.7	>9.6	ABR	1	D C	A
Circinus	4.0	1.3	7.5-8.6	B	2-4	D C	B
NGC 4945	4.0	1.7	9.1-9.6	BCR	5,6	D C	C
M 51	10	-0.2	7.7-8.4	BG	7,8	X C	D
NGC 3079	16	2.5	8.4-9.4	B	9	D C	E
NGC 1386	17	2.1	8.4-9.0	BCX	10,11	D C	F
NGC 3393	50	2.4	8.5-10.2	BX	10,12,13	d C	G
IC 2560	35	2.0	8.3-9.2	AC	14,15	D C	H
NGC 4051	10	0.3	7.6-8.5	CBRX	16-20	X c	I
NGC 4388	34	1.1	8.7-9.5	ABCRSX	21	d c	J
3C 403	235	3.3	9.6-10.3	C	22	X c	K
NGC 4258	7.2	1.9	7.0-7.7	ABCX	23	D c	L
NGC 6240	98	1.6	9.8-10.8	ABR	24,25	X C	M
MRK 266	110	1.5	9.3-10.3	B	26	X C	J
MRK 3	54	1.0	9.6-10.4	BCGR	27-32	X C	J
NGC 5643	16	1.3	7.6-9.0	BX	13,33	X C?	G
NGC 5347	31	1.5	8.1-9.1	A	14	X C	N
MRK 1066	48	1.5	9.0-9.2	A	34	X C	J
ESO 103-G 035	53	2.6	9.1-9.9	ABEGR	35-38	X c	N
NGC 6300	15	0.34	8.1-8.5	BRX	35,39-41,67	X c	G
NGC 5506	25	1.7	8.9-9.4	ABCGRX	35,42-48	X c	N
NGC 1052	17	2.1	7.5-8.0	ABC	49-55	J c	O
MRK 348	62	2.6	8.9-10.4	AG	32,56,57	J c	P
MRK 1210	54	1.9	9.3-10.3	AB	58,59	d C?	T

Table 3.4—Continued

Galaxy	$D^{(a)}$ (Mpc)	$\log L_{H_2O}^{(b)}$ $(L_\odot)$	$\log L_{2\text{-}10}^{(c)}$ $(L_\odot)$	Telescopes[d]	Ref[e]	Type[f]	Ref[g]
NGC 2639	44	1.4	7.0-8.1	A	52,59-61	X c	N
UGC 5101	157	3.2	8.8-9.8	C	62	X C	R
NGC 2273	25	0.8	8.1-9.3	BX	10,13	X C	R
NGC 2782	34	1.1	7.6-9.1	C	63	X C	J
ARP 299	42	2.1	8.2-9.4	BCX	64-66	X C	S
NGC 5728	37	1.9	8.7-10.2	C	63	d C?	J

[a] Distances adopted from Henkel et al. (2005).

[b] Total isotropic water maser luminosities from Henkel et al. (2005) except for NGC 3393, NGC 5643, NGC 6300, NGC 1068 (Kondratko et al. 2006), NGC 3079 (Kondratko et al. 2005), UGC 5101, and NGC 2273 (Zhang et al. 2006).

[c] Unabsorbed $2-10$ keV luminosity. In cases where this is not described in the literature, the unabsorbed $2-10$ keV luminosity has been inferred from other reported parameters (flux, photon index, and the neutral hydrogen column density) using WebPIMMS. The ranges quoted here reflect results from multiple observations, alternative source models, and/or the uncertainty in the reflection efficiency (in case of Compton-thick sources only; see †. To account for source variability in case of 3C 403, where multiple observations and alternative models were not available, we adopted the fractional uncertainty averaged over all Compton-thin systems in our sample. Only observations sensitive to energies above 10 keV were considered for Compton-thick sources, with the exception of NGC 1386, IC 2560, NGC 5347, MRK 1066, UGC 5101, NGC 2782, and NGC 5728 for which hard X-ray data were not available.

[d] X-ray telescopes used in luminosity measurements: A=ASCA, B=BeppoSAX, C=CXO, E=EXOSAT, G=GINGA, R=RXTE, S=SL2-XRT, X=XMM.

[e] References for the $2-10$ keV luminosity: [1] Colbert et al. (2002) but also see Comastri (2004) and references therein, [2] Guainazzi et al. (1999), [3] Matt et al. (1999), [4] Smith & Wilson (2001), [5] Guainazzi et al. (2000a), [6] Done et al. (2003), [7] Fukazawa et al. (2001), [8] Makishima et al. (1990), [9] Iyomoto et al. (2001), [10] Guainazzi et al. (2005), [11] Comastri (2004), [12] Salvati et al. (1997), [13] Maiolino et al. (1998b),† [14] Risaliti et al. (1999),† [15] Iwasawa et al. (2002), [16] Pounds et al. (2004), [17] Uttley et al. (2004), [18] McHardy et al. (2004), [19] Uttley et al. (2003), [20] Uttley et al. (1999), [21] Elvis et al. (2004), [22] Kraft et al. (2005), [23] Fruscione et al. (2005), [24] Ikebe et al. (2000), [25] Vignati et al. (1999), [26] Risaliti et al. (2000),† [27] Lutz et al. (2004), [28] Matt et al. (2000), [29] Sako et al. (2000), [30] Capi et al. (1999), [31] Georgantopoulos et al. (1999), [32] Smith & Done (1996), [33] Guainazzi et al. (2004), [34] Levenson et al. (2001), [35] Risaliti (2002), [36] Wilkes et al. (2001), [37] Akylas et al. (2001), [38] Georgantopoulos & Papadakis (2001), [39] Maddox et al. (2002), [40] Guainazzi (2002), [41] Leighly et al. (1999), [42] O'Neill et al. (2005), [43] Bianchi et al. (2005), [44] Perola et al. (2002), [45] Matt et al. (2001), [46] Lamer et al. (2000), [47] Wang et al. (1999), [48] Nandra & Pounds (1994), [49] Kadler et al. (2004), [50] Satyapal et al. (2004), [51] Ueda et al. (2001), [52] Terashima et al. (2000), [53] Guainazzi et al. (2000b), [54] Weaver et al. (1999), [55] Guainazzi & Antonelli (1999), [56] Akylas et al. (2002), [57] Warwick et al. (1989), [58] Ohno et al. (2004), [59] Bassani et al. (1999),† [60] Terashima et al. (2002), [61] Wilson et al. (1998), [62] Assuming that the source is Compton-thick based on Armus et al. (2004) and using the measured flux from Ptak et al. (2003),† [63] Zhang et al. (2006),† [64] Della Ceca, R., et al. (2002), [65] Ballo et al. (2004),† [66] Zezas et al. (2003),† [67] Matsumoto et al. (2004).

[f] Two letter code describing (1) maser type and (2) magnitude of X-ray absorption column. Maser type: d=high-velocity water maser system, i.e., a source where origin of emission in an edge-on disk is suggested by spectral data only; D=high-velocity water maser systems, where hypothesized disk origin has been reinforced by an analysis of VLBI data; J=maser source associated with a radio jet; X=non-high-velocity system. Obscuration: C=Compton-thick; c=Compton-thin. A question mark after obscuration type indicates controversy in analysis of X-ray data reported in the literature.

[g] References for the maser type: [A] Greenhill & Gwinn (1997), [B] Greenhill, L. J., et al. (2003), [C] Greenhill et al. (1997b), [D] Hagiwara et al. (2001b), [E] Kondratko et al. (2005), [F] Braatz et al. (1997a), [G] Kondratko et al. 2006, [H] Ishihara et al. (2001), [I] Hagiwara et al. (2003b), [J] Braatz et al. (2004), [K] Tarchi et al. (2003), [L] Miyoshi et al. (1995), [M] Hagiwara et al. (2003a), [N] Braatz et al. (1996), [O] Claussen et al. (1998), [P] Peck et al. (2003), [R] Zhang et al. (2006), [S] Henkel et al. (2005) [T] Kondratko et al., in preparation.

†Following Comastri (2004), we assumed in case of Compton-thick models for NGC 5347, NGC 5643, NGC 3393, MRK 266, MRK 1210, UGC 5101, NGC 2273, NGC 2782, ARP 299, and NGC 5728 that the observed $2-10$ keV luminosity is $1-10\%$ of the unabsorbed $2-10$ keV luminosity due to reflection and scattering.

Table 3.5. Correlation Coefficients and Power Law Indices for L_{2-10} vs. L_{H_2O}.

Population	$m^{(a)}$	$\rho^{(b)}$	Significance$^{(c)}$	N$^{(d)}$
all systems	0.4 ± 0.1 (0.4 ± 0.1)	0.4 ± 0.1 (0.3 ± 0.1)	7 ± 7 (20 ± 10)	29
all systems†	0.5 ± 0.1 (0.5 ± 0.1)	0.5 ± 0.1 (0.4 ± 0.1)	3 ± 4 (10 ± 10)	20
unclassified and jet masers	0.5 ± 0.1 (0.4 ± 0.1)	0.5 ± 0.1 (0.4 ± 0.1)	5 ± 6 (20 ± 10)	19
high-velocity	0.4 ± 0.3 (1.0 ± 0.5)	0.1 ± 0.2 (0.2 ± 0.2)	70 ± 20 (60 ± 20)	10
Compton-thick	0.3 ± 0.1 (0.2 ± 0.2)	0.3 ± 0.1 (0.1 ± 0.1)	30 ± 20 (60 ± 20)	19
Compton-thin	0.6 ± 0.1 (0.5 ± 0.2)	0.5 ± 0.1 (0.3 ± 0.1)	20 ± 10 (40 ± 20)	10

$^{(a)}$Index $(L_{2-10} \propto L_{H_2O}^m)$ obtained from a Monte Carlo simulation where the probability distribution function for each data point in Fig. 3.3 is modelled in linear luminosity space by a Gaussian with mean and standard deviation corresponding to the plotted symbols and the error bars in Fig. 3.3, respectively. The parentheses enclose the result for the same population but with the leftmost and the rightmost data points in Fig. 3.3 removed.

$^{(b)}$Spearman correlation coefficient and uncertainty from the Monte Carlo simulation described in (a). Alternative use of a Pearson correlation coefficient changes the results negligibly but assumes in the calculation of the significance level that the two variables are normally distributed, which is most likely not the case here. Quantities in parentheses are as in (a).

$^{(c)}$Two-sided significance level (expressed as a percentage), i.e., probability that a random data set of the same size would yield a larger magnitude of the correlation coefficient. Quantities in parentheses are as in (a). We have confirmed the reported significance levels with numerous ($\sim 10^5$) realizations of the permutation test, whereas the null hypothesis of no correlation is assumed and the water luminosity data points are permuted among the x-ray luminosity data points (e.g., Wall & Jenkins 2003).

$^{(d)}$Number of sources. The lower limit on the X-ray luminosity of NGC 1068 was not used in the fit.

†Galaxies with multiple nuclei (NGC 6240, MRK 266, MRK 1066, ARP 299), jet masers (MRK 348, NGC 1052), and LINER systems (NGC 3079, NGC 4258, NGC 6240, NGC 1052, UGC 5101) have been removed from the sample. See the text for details.

Under the assumption of a thin viscous accretion disk obliquely illuminated at an angle $\cos^{-1} \mu$ by a central X-ray source, the outer radius at which the disk becomes atomic and the maser emission ceases is given by $R_{cr} \propto L_{2-10}^{-0.43} (\dot{m}/\alpha)^{0.81} \mu^{-0.38} M_{BH}^{0.62}$ (Neufeld & Maloney 1995), where L_{2-10} is the $2 - 10$ keV luminosity, M_{BH} is the mass of the central black hole, $\dot{m}$ is the mass accretion rate, and α is the standard dimensionless viscosity parameter (Shakura & Sunyaev 1973). If we assume that X-ray heated accretion disks emit water maser radiation with a surface luminosity of $\sim 10^{2\pm0.5} L_{\odot} \, \mathrm{pc}^{-2}$ (and hence $L_{\mathrm{H_2O}} \propto R_{cr}^2$; Neufeld et al. 1994), that $2 - 10$ keV luminosity is a fraction γ of AGN bolometric luminosity ($L_{2-10} = \gamma L_{Bol}$), that central engines radiate with an Eddington ratio η ($L_{Bol} = \eta L_{Edd} \propto \eta M_{BH}$), and that they convert rest mass to energy with an accretion efficiency $\epsilon = L_{Bol}/\dot{m}c^2$ ($\epsilon \sim 0.1$; Frank, King, & Raine 2002), then we obtain $L_{2-10} \propto L_{\mathrm{H_2O}}^{0.5} [(\epsilon\alpha)^{0.81} \gamma^{1.4} \mu^{0.38} \eta^{0.62}]$, in agreement with the observed trend.

The scatter about the linear relationship in Fig. 3.3 in excess of the reported uncertainties could be attributed to differences in the parameters α, ϵ, γ, μ, and η from source to source. For instance, although $0.01 \lesssim \gamma \lesssim 0.03$ based on an average quasar spectral energy distribution (SED; Fabian & Iwasawa 1999; Elvis et al. 2002), the actual variation in γ among individual Seyfert systems is more than an order of magnitude (e.g., $0.01 < \gamma < 0.6$; Kuraszkiewicz et al. 2003). Furthermore, although η is relatively constrained for Seyfert nuclei (e.g., $0.01 \lesssim \eta \lesssim 1$; Padovani 1989; Wandel et al. 1999; Satyapal et al. 2005), it might be as low as $10^{-6.7}$ for LINER systems (e.g., Satyapal et al. 2005). For the LINER in NGC 4258 where black hole mass is well constrained with VLBI, we obtain $10^{-3.6} < \eta < 10^{-2.9}$, where we adopted $M_{BH} = 3.9 \times 10^7 \, M_{\odot}$ (Herrnstein et al. 1999), $L_{2-10} = 10^{40.6-41.2} \, \mathrm{erg \, s^{-1}}$

(Table 3.4), and $\gamma = 0.03$ as determined from SEDs of 7 low-luminosity AGNs (Ho 1999b). Because of the broader range of Eddington ratio specific to LINERs, we have considered a Seyfert-only sub-sample. Furthermore, we have also removed galaxies in which the maser sources are associated with jets (for which the Neufeld & Maloney model does not apply), and galaxies with multiple nuclei (wherein it may be uncertain which nucleus is responsible for the maser emission or the production of maser luminosity may in some way be affected by processes specific to mergers). The active galaxies with multiple nuclei are MRK 266 (e.g., Wang et al. 1997), ARP 299 (e.g., Ballo et al. 2004), NGC 6240 (e.g., Lira et al. 2002), and MRK 1066 (e.g., Gimeno et al. 2004). If these mergers, known "jet masers" (NGC 1052 and MRK 348; Claussen et al. 1998; Peck et al. 2003), and LINERs (NGC 3079, NGC 4258, NGC 6240, NGC 1052, UGC 5101) are omitted from the sample, then we obtain a slope of $m = 0.5 \pm 0.1$ and a Spearman correlation coefficient of $\rho = 0.5 \pm 0.1$, the latter with a significance level of 0.03 ± 0.04 (Table 3.5). To test for the robustness of this strongest correlation, we removed the data points with lowest *and* highest maser luminosity and obtained $m = 0.5 \pm 0.1$ and $\rho = 0.4 \pm 0.1$, the latter with a significance level of 0.1 ± 0.1 (Table 3.5).

The appearance of a correlation may be surprising given large uncertainties in X-ray and maser luminosities. Both are time variable, and it is easy to imagine some independence in that variability. As well, measured X-ray luminosities for heavily absorbed sources depend sensitively on the details of instrumentation and subsequent data modelling, although we have accounted for this to some extent with the adopted uncertainties. Moreover, isotropic maser luminosities should be regarded with some caution because maser beam angles are often poorly constrained and

may be quite small due to source geometry and propagation effects (e.g., Deguchi & Watson 1989; Kartje, Königl, & Elitzur 1999). For instance, the beam angle for NGC 4258 is on the order of $7°$ (Miyoshi et al. 1995) and, as a result, the actual luminosity is a factor of $4\pi/\Omega = 4\pi/(2\pi \times 7°) \sim 16$ smaller than isotropic. Accretion disk warping may also bias maser brightness, as beamed radiation may be directed away from the observer. However, one might argue conversely based on the putative correlation that beam angles among water maser systems are relatively similar and variability is a second order effect on average. Furthermore, since the estimated power law index of 0.5 ± 0.1 is consistent with the value (0.5) predicted by the Neufeld & Maloney (1995) model — notwithstanding the large uncertainties that enter through the Eddington ratio, bolometric correction, viscosity, and accretion efficiency — one might venture to propose that these parameters are similar among sources, at least to within factors of a few.

The full sample presented here is inhomogeneous in that it contains AGN that are Compton-thin and Compton-thick, as well as water maser sources for which there is evidence of an origin in accretion disk material and those for which available data do not enable any particular physical classification. We have computed m and ρ for various sub-samples and find ranges of $0.3 - 0.6$ and $0.1 - 0.5$, respectively (Table 3.5). The correlation coefficient is largest (0.5 ± 0.1) and most statistically significant (0.03 ± 0.04) for the sample absent LINERs, multiple-nuclei systems, and "jet masers." No correlation is apparent for high-velocity systems due to the small sub-sample size. We have also considered Compton-thick and Compton-thin sub-samples. Since a minimum H_2 density of $\sim 10^8\,\mathrm{cm}^{-3}$ is required by the presence of water maser emission (e.g., Desch et al. 1998), the column within a disk becomes

Compton-thick for lengths greater than $\sim 0.002\,\mathrm{pc}$ and, consequently, it has been suggested that the pc-scale accretion disks that host the maser emission also provide the Compton obscuration (Greenhill et al. 2003; Herrnstein et al. 2005; Fruscione et al. 2005). We note however that there is no theoretical reason why maser emission should not originate in a Compton-thin environment. Investigation into properties of astrophysical gas by Maloney, Hollenbach, & Tielens (1996) suggests that fractional water abundances of $10^{-6} - 10^{-4}$ and temperatures of $250 - 1000\,\mathrm{K}$ — both conditions necessary for maser action — are possible for column densities of $\sim 10^{23}\,\mathrm{cm}^{-2}$ (their Fig. 10). Assuming that the edge-on pc-scale accretion disks also provide the line-of-sight X-ray obscuration, the fact that Compton-thin environments are conducive to maser action is also supported by an empirical observation that approximately 33% of the known nuclear masers lie in Compton-thin systems (Table 3.4) and that several of these are also high-velocity systems (such as NGC 4388, NGC 4258, and NGC 5728). If pc-scale accretion disks indeed provide the line-of-sight obscuring column density, factors such as the disk inclination, warping, and filling factor might affect the X-ray absorption column and it is thus possible that the intrinsic relationship between water maser and X-ray luminosities is different for Compton-thick and -thin sources. However, the two sub-samples are too small to assess any difference (Table 3.5).

3.5   Conclusion

In a survey with the GBT of 56 AGN with $10000\,\mathrm{km\,s}^{-1} < v_{sys} < 30000\,\mathrm{km\,s}^{-1}$, we have detected five new water maser sources. The spectra of three sources display the

characteristic spectral signature of emission from an edge-on accretion disk. For the 30 nuclear water masers with available hard X-ray data, we have found evidence of a possible relationship between unabsorbed X-ray luminosity $(2 - 10 \, \text{keV})$ and total isotropic water maser luminosity. The power law index of 0.5 ± 0.1 is consistent with the Neufeld & Maloney (1995) model in which X-ray irradiation of molecular accretion disk gas by a central engine excites maser emission that is most intense in the disk plane. The appearance of a correlation may be surprising considering the large uncertainties in X-ray and maser luminosities, at least in part due to source variability and assumption of isotropic emission of maser radiation. However, one might interpret the correlation as indirectly supporting the proposition that Eddington ratios, bolometric corrections, viscosities, accretion efficiencies, and maser beaming angles are similar among water maser systems, and variability is a second order effect on average. Evaluation of the putative correlation would be greatly helped by an increase in the number of known maser systems and reduction in measurement and systematic uncertainties in the luminosity data. This will require measurement of X-ray spectra above $10 \, \text{keV}$, new radio surveys of AGN (in search of maser emission), and VLBI mapping to quantify accretion disk structure. If verified and strengthened, the proposed relation between luminosities would be valuable in the modelling of maser excitation, identification of maser-rich samples of AGN using hard X-ray sky surveys, and perhaps modelling of the hard X-ray background in the era of the Square Kilometer Array, which will enable detection of many thousands of maser galaxies (Morganti et al. 2004).

3.6   Acknowledgements

Chapter 4

Discovery of   ater Maser Emission in Three Edge-on AGN with the GBT

Paul T. Kondratko, Lincoln J. Greenhill, James M. Moran, James A. Braatz, Mark J. Reid

Abstract

In this work, we report the discovery of three nuclear water maser sources with the 100-m Green Bank Telescope (GBT), present sensitive maser spectra of nine previously known sources, and describe monitoring results of three others. Emission from one of the discoveries, NGC 1320, most likely originates in a pc-scale accretion

disk; the spectra of the other two detections do not enable any particular physical interpretation. In the survey among edge-on Seyfert 2 and LINER systems with $v_{sys} < 10000\,\mathrm{km\,s^{-1}}$, we obtained a detection rate of $9 \pm 5\%$ (3 out of 33). Based on this detection rate and the distribution of galactic plane inclinations for known water maser systems, we find no evidence for the preference of maser emission to occur in edge-on galaxies, which is consistent with recent studies that have shown lack of correlation between galactic plane orientation and nuclear jet or narrow line region direction. We also used the GBT to obtain sensitive ($1\sigma \sim 2 - 4\,\mathrm{mJy}$) spectra of nine known maser sources and detect disk emission from as many as four sources. In NGC 2979 and NGC 3735, we report detection of weak emission offset by more than $200\,\mathrm{km\,s^{-1}}$ from the systemic velocities of the host galaxies. The spectra of these sources are consistent with emission from edge-on accretion disks with orbital velocities of ~ 500 and $\sim 250\,\mathrm{km\,s^{-1}}$, respectively, although the classification remains ambiguous in the case of NGC 2979. The maser spectrum of NGC 0449 shows a characteristic spectral signature of emission from an edge-on accretion disk with orbital velocity of $\sim 130\,\mathrm{km\,s^{-1}}$. In UGC 04203, we detect with high signal-to-noise ratio spectral features that were marginally detected in previous studies and interpret the spectrum as emission from an edge-on accretion disk with maximum orbital velocity of $\sim 300\,\mathrm{km\,s^{-1}}$. We have also monitored with the GBT emission in the vicinity of the systemic velocity in three water maser sources (2MASX J08362280+3327383, NGC 6264, UGC 09618 NED02). We have decomposed the detected emission into Gaussian components and, for multiple spectral features, report the measurement of velocity drifts, which are a manifestation of centripetal acceleration due to accretion disk rotation. These measurements, when combined

in the future with robust models of accretion disks, might yield distances to these sources, which would be of considerable value since all three systems are deep within Hubble flow ($v_{\mathrm{sys}} > 10000$ km s^{-1}) and thus might be used to establish a Hubble relation independent of standard candle calibrators such as Cepheids and SN Ia supernovae.

4.1   Introduction

Water maser emission ($\lambda = 1.3$ cm) is currently the only resolvable tracer of warm dense molecular gas in the inner parsec of active galactic nuclei (AGN) and therefore can be used to investigate properties of AGN on pc-scales. Very Long Baseline Interferometry (VLBI) maps of water maser sources have been interpreted in the context of a model in which the maser emission traces a nearly edge-on disk of molecular material 0.1 to 1 pc from a supermassive black hole: e.g., NGC 4258 (Miyoshi et al. 1995), NGC 4945 (Greenhill et al. 1997b), NGC 1068 (Greenhill & Gwinn 1997), NGC 3079 (Trotter et al. 1998; Yamauchi et al. 2004; Kondratko et al. 2005), IC 2560 (Ishihara et al. 2001), Circinus (Greenhill et al. 2003). As a consequence of these VLBI studies, it is believed that maser emission is detected preferentially from edge-on parsec-scale disks at locations where the gradient in line-of-sight velocity is zero and hence the coherent paths for maser emission are maximized. These occur close to a midline (i.e., diameter perpendicular to the line of sight) and close to the line of sight towards a dynamical center. A characteristic spectral signature of emission from an edge-on disk thus consists of a spectral complex in the vicinity of the systemic velocity (low-velocity emission) and two

spectral complexes (high-velocity emission) symmetrically offset from the systemic velocity by the orbital velocity ($> 100\,\mathrm{km\,s^{-1}}$, based on aforementioned VLBI studies). Sources that display such spectra are referred to here as high-velocity systems.

In addition to determination of pc-scale accretion disk structures and of black hole masses (e.g., Greenhill & Gwinn 1997; Greenhill et al. 2003; Herrnstein et al. 2005), high-velocity systems can also be used for estimation of distances based solely on geometry and dynamics of the pc-scale accretion disk and independent of standard candles like Cepheids and SN Ia supernovae. Analysis of water maser emission in NGC 4258 yielded the first geometric distance to an extragalactic object and the most precise extragalactic distance ever measured (Herrnstein et al. 1999). Distance estimation depends on two crucial components: a robust disk model from VLBI observations and a measurement of secular velocity drift in the low-velocity lines, which is a manifestation of centripetal acceleration in the disk (the velocity drift is largest for low velocity features, as the centripetal acceleration vector points along the line of sight). In Section 4.3, we report the measurement with the Green Bank Telescope (GBT) of centripetal acceleration in three high-velocity systems.

As a tracer of edge-on pc-scale geometries in AGN, water maser emission can also be used to investigate the relationship between the orientations of the galactic plane and the pc-scale accretion disk. In particular, an open question remains whether the pc-scale disks are preferentially aligned with the galactic disks. In what follows, we review available evidence from literature for and against such an alignment. An alignment between the stellar disk and the pc-scale accretion disk might be anticipated from simplistic angular momentum considerations if the

accreting gas originates from a kpc-scale disk and dynamical effects such as warps are not important. There is indeed tentative evidence that the nuclear obscuring geometry is aligned with the galactic plane. Correlation between disk axial ratio and Hβ luminosity to X-ray luminosity ratio has been interpreted as evidence that the obscuring geometries are flattened and parallel to the galactic disks (Lawrence & Elvis 1982). The dearth of edge-on optically-selected (Kirhakos & Steiner 1990a) or soft-X-ray-selected (Simcoe et al. 1997) active galaxies has led to a suggestion that the nuclear obscuring material is aligned with the kpc-scale stellar disk. Correlation between orientations of the galactic plane and the scattering geometry is also suggested by the alignment between the galactic major axis and the polarization vector for scattered radiation (Thompson & Martin 1988; Brindle et al. 1990; Webb et al. 1993; Corbett et al. 1998). There is evidence that the sub-kpc-scale molecular disks seen in CO (e.g., Curran 2000) or the kpc-scale dust disks seen in optical light (Martel et al. 2000) are aligned with the galactic planes. It is important to note however that the aforementioned studies are sensitive to dust obscuration or probe structures at larger scales, and thus infer orientation of the pc-scale nuclear structure with respect to the galactic plane indirectly.

Studies have nonetheless shown lack of correlation between galactic plane orientation and either neutral hydrogen column density (Malizia et al. 1997), nuclear jet direction (Ulvestad & Wilson 1984; Schmitt et al. 1997, 2001, 2002; Clarke et al. 1998; Nagar & Wilson 1999; Kinney et al. 2000; Middelberg et al. 2004), or narrow line region orientation (Schmitt et al. 2003). However, these studies are not unambiguous indicators of pc-scale disk inclination, as they infer orientation of the innermost nuclear structure indirectly from either X-ray absorption or orientations of

outflow and illumination axes that are presumed to be orthogonal. It is possible that the pc-scale accretion disks and the geometries that provide X-ray absorption are either not the same physical entities or themselves misaligned. Furthermore, pc-scale accretion disks and outflow or illumination axes may be misaligned or may appear misaligned for a variety of reasons. First, as reviewed by Kinney et al. (2000), a jet might not be launched perpendicular to the pc-scale accretion disk due to either radiative instability (Pringle 1996, 1997), relativistic frame dragging (Bardeen & Petterson 1975), or a nuclear star cluster. Second, jet direction as determined with respect to the accretion disk may change with time or be affected by interaction with the ISM, as is well illustrated by two active systems on kpc-scales — NGC 4258 (e.g., Cecil et al. 2000) and NGC 1068 (e.g., Gallimore et al. 2004; Muxlow et al. 1996) — and possibly also by NGC 3079 (Kondratko et al. 2005) and NGC 5793 (Hagiwara et al. 2001a) on pc-scales. Third, radio or optical features might correspond to interaction regions that appear in projection significantly offset from the principle outflow axis; for instance, the anomalous optical and radio arms in NGC 4258 have been interpreted as galactic disk gas that has been shocked by the out-of-plane radio jets (Wilson et al. 2001). Fourth, narrow line regions might be delimited by shadows cast by warped structures at smaller radii, in which case misalignments between the two are expected; in the Circinus galaxy, for example, the outer edges of the warped pc-scale molecular disk traced by the maser emission have position angles very similar to those of the narrow line region (Greenhill et al. 2003).

If the orientation of a pc-scale accretion disk and the galactic stellar disk are correlated, then the detection rate for water maser emission among edge-on active galaxies might reflect the preference for water maser emission to occur in edge-on

pc-scale molecular disks. Based on 14 water maser systems known at the time, Braatz et al. (1997b) found a marginal predisposition for water maser emission to occur in edge-on active galaxies. In principal, an apparent excess of maser sources in inclined active galaxies should result in a relatively high detection rate among inclined seemingly normal (i.e., not active) systems, in light of the conclusion by Ho et al. (1997b) that $\sim 43\%$ of nearby and seemingly-normal galaxies exhibit some evidence for nuclear activity. However, a search by Braatz et al. (2003) for water maser emission among 58 highly inclined ($i > 80°$), nearby ($v_{sys} < 3000 \, \mathrm{km \, s^{-1}}$), seemingly normal galaxies yielded no detections, either because the AGN X-ray luminosity of these systems is insufficient to excite maser emission bright enough for us to detect or because the excess reported by Braatz et al. (1997b) was a result of small number statistics. To test for this preference, we surveyed with the Green Bank Telescope (GBT) 41 edge-on AGN with $v_{sys} < 18000 \, \mathrm{km \, s^{-1}}$ selected from NASA Extragalactic Database (NED). We have discovered water maser emission in three edge-on AGN at about the expected, not elevated, rate. In Section 4.3, we present spectra and positions for the detected emission. In Section 4.4, we discuss the survey detection rate and the distribution of galactic plane inclinations for all known water maser systems.

4.2 Observations

The survey was conducted during 2004-2005 with the GBT of the NRAO[1] with channel spacing of 24.4 kHz and two 200 MHz IFs configured to overlap by 50 MHz. We tuned the center of the resulting 350 MHz instantaneous bandwidth to the systemic velocity of each target source (350 MHz $\approx 4880\,\mathrm{km\,s^{-1}}$ for a representative recessional velocity of $5000\,\mathrm{km\,s^{-1}}$, assuming the optical definition of Doppler shift). The observations of known water maser sources were conducted between 2003 and 2006 with the same setup with the exception of the 2003 December 8 epoch on 2MASX J08362280+3327383, for which the two IFs were configured to overlap by 20 MHz and the IF at lower velocity was centered on the systemic velocity of the galaxy.

To obtain total-power spectra of each source, we moved the telescope by $3'$ every 2 min between two positions on the sky so that each target was always present in one of the two GBT beams for each polarization. System temperatures were measured against a calibrated noise source injected at the receiver and ranged from 23 to 75 K depending on elevation and weather conditions. To convert the spectra to flux density units, we used the gain curve obtained by the GBT staff based on measurements of opacity-corrected antenna temperature for NGC 7027 at $\sim 1.4\,\mathrm{cm}$ (R. Maddalena 2003, private communication). By comparing maser line amplitudes among beams and polarizations, we estimate that the calibration of the system temperature is accurate to within 30%, an uncertainty that dominates the error

[1]The National Radio Astronomy Observatory is operated by Associated Universities, Inc., under cooperative agreement with the National Science Foundation

budget for the flux density scale. Antenna pointing corrections were obtained every ~ 30 minutes and were typically $< 6''$, which corresponds to a $< 8\%$ loss in source flux density for a $36''$ beamwidth (FWHM) at $1.3\,\mathrm{cm}$. For the observations reported here, the wind speed at the GBT site was typically $< 22\,\mathrm{mph}$, which corresponds to a one-dimensional rms (1σ) tracking error of $< 15''$ and a signal loss of at most 38% . Data were reduced using custom scripts written in the Interactive Data Language. We subtracted a running boxcar average of width $6.25\,\mathrm{MHz}$ to remove systematic baseline structure from the total-power spectra. The resulting 1σ noise levels attained in an integration of $\sim 30\,\mathrm{minutes}$ total and corrected for atmospheric opacity estimated from tipping scans (from 0.03 to 0.2) were $3.8 - 14\,\mathrm{mJy}$ in a $24.4\,\mathrm{kHz}$ channel. The spectra presented here have been Hanning smoothed to a resolution of $108\,\mathrm{kHz}$, though channel spacing of $24.4\,\mathrm{kHz}$ has been maintained throughout.

4.3   Results

4.3.1   Survey

In a survey with the GBT of 41 edge-on ($i > 70^{\circ}$) AGN with $v_{sys} < 18000\,\mathrm{km\,s^{-1}}$ selected from the NED (Table 4.1), we have detected three new water maser sources: NGC 0017, NGC 1320, and IRAS 16288+3929 (Fig. 4.1 and Table 4.1). All three discoveries were subsequently confirmed either or both with the Very Large Array (VLA) using a narrow observing bandwidth of $6.25\,\mathrm{MHz}$ (NGC 1320, IRAS 16288+3929) or with the GBT on a different day but using the same

spectrometer configuration (NGC 0017, IRAS 16288+3929). The nuclei that host the detected maser emission are spectroscopically classified as Seyfert 2 (Table 4.1). Positions of the maser emission in NGC 1320 and IRAS 16288+3929 measured with the VLA are consistent with optical positions of the AGNs to within 1σ (typically $0\rlap{.}''3$ radio and $0\rlap{.}''4 - 1\rlap{.}''3$ optical), which suggests association of the detected emission with nuclear activity. The peak luminosities of the discovered emission ($\sim 0.5 - 4\,L_\odot$) are consistent with those of other AGN related masers (e.g., Kondratko et al. 2006) but greater than the typical peak luminosity from W49N ($0.05\,L_\odot$; Gwinn 1994), the most luminous maser in our galaxy associated with a region of intense star formation, and from an H II region in a spiral galaxy M33 ($\sim 0.02\,L_\odot$; Greenhill et al. 1990). Because of the high luminosities, we consider nuclear star-formation as a less likely explanation for the discovered emission.

Table 4.1. Active Galaxies with Inclinations $> 70°$ Surveyed for Water Maser Emission with the Green Bank Telescope.

Galaxy	Type[a]	α_{2000}[b] (hh mm ss)	δ_{2000}[b] (dd mm ss)	v_{sys}[c] (km s^{-1})	Date	T_{sys}[d] (K)	1σ[e] (mJy)
UGC 12915	LINER	00 01 41.94	+23 29 44.5	4336	02-02-2005	27	4.3
UGC 00050	LINER	00 06 40.15	+26 09 16.2	7552	02-01-2005	26	4.7
NGC 0017★	Sy2	00 11 06.55	−12 06 26.3	5931^{+11}_{-235}	04-18-2006	47	3.2
		. . .	. . .				
UGC 00238	LINER	00 25 03.35	+31 20 42.6	6796	02-01-2005	27	4.3
M31	LINER	00 42 44.32	+41 16 08.5	-300	02-01-2005	33	6.1
IRAS 01189+2156	Sy2	01 21 44.27	+22 12 35.1	17478	02-01-2005	27	4.1
UM 319	Sy2	01 23 21.18	−01 58 36.0	4835	09-21-2005	56	9.2
UGC 00987	Sy2	01 25 31.46	+32 08 11.4	4658	01-28-2005	24	4.0
NGC 0660	LINER	01 43 01.70	+13 38 34.0	850	02-02-2005	33	6.7
UGC 01282	Sy2	01 49 29.87	+12 30 32.6	5221	02-02-2005	29	5.0
UGC 01479	Sy2	02 00 19.06	+24 28 25.3	4927	02-02-2005	28	4.4
UGC 01757	Sy2	02 17 23.05	+38 24 49.9	5254	01-28-2005	23	4.2
UGC 02456	Sy2	02 59 58.59	+36 49 14.3	3605	02-01-2005	32	4.5
UGC 02638	LINER	03 17 02.21	+01 15 17.9	7123	09-21-2005	54	10
NGC 1320★	Sy2	03 24 48.70	−03 02 32.2	2663^{+360}_{-16}	09-30-2005	47	5.9
		03 24 48.70	−03 02 32.3				
MCG -02-09-040	Sy2	03 25 04.94	−12 18 27.8	4495	09-30-2005	48	6.0
SBS 0811+584	Sy2	08 16 01.30	+58 20 01.0	7584	09-30-2005	43	5.6
NGC 2683	Sy2	08 52 41.42	+33 25 13.7	411	09-30-2005	44	6.5

Table 4.1—Continued

Galaxy	Type[a]	α_{2000}[b] (hh mm ss)	δ_{2000}[b] (dd mm ss)	v_{sys}[c] (km s^{-1})	Date	T_{sys}[d] (K)	1σ[e] (mJy)
NGC 3190	LINER	10 18 05.77	+21 49 55.8	1271	10-01-2005	46	5.9
UGC 05613	LINER	10 23 32.50	+52 20 30.0	9620	02-01-2005	26	4.6
NGC 3593	Sy2	11 14 37.00	+12 49 04.0	628	10-01-2005	47	6.5
NGC 3628	LINER	11 20 16.95	+13 35 20.1	843	02-01-2005	40	6.2
NGC 3753	AGN	11 37 53.90	+21 58 53.0	8727	02-01-2005	31	4.2
UGC 09532 NED01	AGN	14 47 53.39	+19 04 37.1	12506	02-01-2005	27	4.6
IRASF 15033+2617	Sy2	15 05 27.93	+26 05 29.3	16579	02-01-2005	27	4.5
2MASXi J1559189+651357	AGN	15 59 18.95	+65 13 57.8	8975	02-01-2005	26	4.6
IRAS 16288+3929★	Sy2	16 30 32.66	+39 23 03.2	9161^{+21}_{-21}	04-10-2006	39	2.8
		16 30 32.68	+39 23 03.1				
UGC 10593	Sy2	16 52 18.87	+55 54 19.8	8739	09-21-2005	70	14
UGC 10695	LINER	17 05 05.56	+43 02 35.1	8328	09-28-2005	51	6.6
NGC 6503	LINER	17 49 27.11	+70 08 39.6	60	09-28-2005	56	6.5
NGC 6636 NED01	Sy2	18 22 02.20	+66 36 37.7	4393	09-28-2005	57	7.0
CGCG 341-006	Sy2	18 45 26.23	+72 11 01.7	13880	02-01-2005	27	4.6
NGC 7013	LINER	21 03 33.31	+29 53 49.3	779	02-02-2005	29	4.5
IC 1417	Sy2	22 00 21.61	−13 08 49.1	5345	09-30-2005	53	6.4
NGC 7331	LINER	22 37 04.09	+34 24 56.3	816	02-01-2005	32	5.5
UGC 12201	LINER	22 49 09.55	+34 59 30.5	5055	02-02-2005	26	3.8
NGC 7466	Sy2	23 02 03.42	+27 03 09.5	7493	02-01-2005	25	3.9

Table 4.1—Continued

Galaxy	Type[a]	α_{2000}[b] (hh mm ss)	δ_{2000}[b] (dd mm ss)	v$_{sys}$[c] (km s^{-1})	Date	T_{sys}[d] (K)	1σ[e] (mJy)
UGC 12318	Sy2	23 02 08.01	+25 40 13.7	9533	02-01-2005	26	4.2
NGC 7549	AGN	23 15 17.23	+19 02 30.1	4736	02-02-2005	27	4.2
UGC 12519	Sy2	23 20 02.75	+15 57 10.6	4378	02-01-2005	29	4.3

[a]Activity type from the NED.

[b]Optical positions from the NED with typical uncertainties of $\pm1\rlap{.}''3$ used for GBT pointing. For newly discovered nuclear water maser sources, *first line:* optical positions from the NED with uncertainties of $\pm0\rlap{.}''5$ (NGC 0017), $\pm1\rlap{.}''3$ (NGC 1320), or $\pm0\rlap{.}''4$ (IRAS 16288+3929); *second line:* maser positions measured with a VLA snapshot with typical uncertainties of $\pm0\rlap{.}''3$. To establish the magnitude of systematic uncertainties in position, we imaged disjoint segments of the VLA data and confirmed that they yield consistent maser positions (that is, within $0\rlap{.}''3$).

[c]Optical heliocentric systemic velocity. For each source, the listed value represents the systemic velocity measurement with the smallest uncertainty. For the three discoveries, we also list in the form of upper and lower limits the range of optical heliocentric systemic velocity estimates. The measurements (km s^{-1}) are: NGC 1320: 2663 ± 16 (HI; Davoust & Contini 2004), 2716 ± 29 (optical; Huchra et al. 1993), 3023 (optical; Bottinelli et al. 1993); NGC 0017: 5881 ± 2 (optical; Rothberg & Joseph 2006), 5931 ± 11 (HI; de Vaucouleurs et al. 1991), 5772 ± 25 (optical; de Vaucouleurs et al. 1991), 5726 ± 30 (optical; Bottinelli et al. 1993), 5821 ± 38 (optical; Huchra et al. 1993), 5821 ± 44 (optical; da Costa et al. 1998); IRAS 16288+3929: 9161 ± 21 (optical; Rines et al. 2002).

[d]Average system temperature (not-corrected for opacity).

[e]Rms noise in a 24.4 kHz spectral channel corrected for atmospheric opacity (typically from 0.03 to 0.2) and for the dependence of antenna gain on elevation.

★Newly discovered water maser sources.
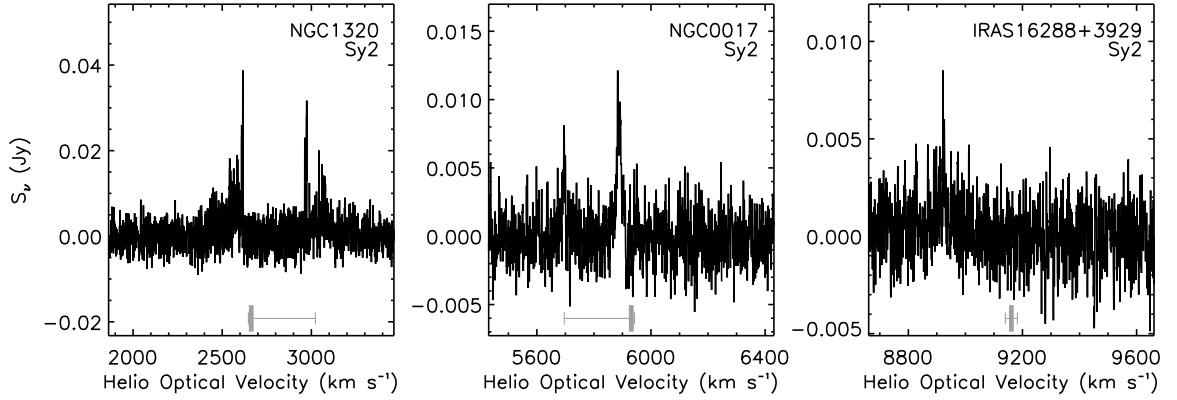
Figure 4.1.— Spectra of newly discovered emission in NGC 1320, NGC 0017, and IRAS 16288+3929 obtained with the Green Bank Telescope. For each source, the horizontal error bar shows the range of optical heliocentric systemic velocity estimates while the vertical bar marks the systemic velocity measurement with the smallest uncertainty.

The maser emission in NGC 1320 either is related to jet activity or arises in an edge-on pc-scale accretion disk. We favor the latter hypothesis, since there is no evidence in the maser spectrum of broad (i.e., $\gg 5\,\mathrm{km\,s^{-1}}$) spectral features, which have been associated circumstantially with jet activity in other AGN (e.g., Claussen et al. 1998; Gallimore et al. 2001; Peck et al. 2003; Kameno et al. 2005). Considering the large uncertainty on the systemic velocity of the host galaxy, the two emission complexes at ~ 2600 and $\sim 3000\,\mathrm{km\,s^{-1}}$ (Fig. 4.1) might be either low- and high-velocity emission or two high-velocity complexes. Thus, we infer from the separation of $\sim 400\,\mathrm{km\,s^{-1}}$ between the two emission complexes, a maximum orbital velocity of the disk as traced by the maser emission of either ~ 200 or $\sim 400\,\mathrm{km\,s^{-1}}$. In NGC 0017, we detected two spectral lines (at ~ 5880 and $\sim 5695\,\mathrm{km\,s^{-1}}$) separated by $190\,\mathrm{km\,s^{-1}}$. Physical classification in this case is uncertain due to the spectral character and since the position of the maser with respect to the nucleus has

not been determined. We note that optical and near-infrared images of NGC 0017

(a.k.a, NGC 0034) show evidence of extreme tidal distortions and it is thus likely that

the galaxy hosts a multiple nucleus (e.g., Vorontsov-Vel'Yaminov 1977; Hunt et al.

1999; Mazzarella & Boroson 1993). The spectrum of IRAS 16288+3929 exhibits a

single line at $\sim 8920\,\mathrm{km\,s^{-1}}$ that is significantly displaced (by $\sim 240\,\mathrm{km\,s^{-1}}$) from the

systemic velocity of the host galaxy ($v_{sys} = 9161\,\mathrm{km\,s^{-1}}$) and that might be either

emission associated with a radio jet (e.g., Peck et al. 2003; Claussen et al. 1998) or

high-velocity emission from the approaching side of an edge-on accretion disk.

NGC 1320 and NGC 0017 were targeted but not detected in previous surveys

for maser emission. For NGC 0017, Braatz et al. (1996) and Kondratko et al. (2006)

report 1σ noise levels of 73 and 16 mJy in 0.66 and $1.3\,\mathrm{km\,s^{-1}}$ spectral channels,

respectively, corresponding to signal to noise ratios (SNR) of $\lesssim 1$ at the current line

strength (peak flux of ~ 11 mJy and noise level of $1\sigma = 1.5$ mJy, both in a $1.5\,\mathrm{km\,s^{-1}}$

spectral channel). In the case of NGC 1320, Braatz et al. (1996) and Kondratko et

al. (2006) obtained 1σ noise levels of 61 and 19 mJy in 0.84 and $1.3\,\mathrm{km\,s^{-1}}$ spectral

channels, respectively, again not sufficient to detect the maser with SNR of at least

4 at present line strength (peak flux of ~ 37 mJy and noise level of $1\sigma = 2.7$ mJy,

both in a $1.5\,\mathrm{km\,s^{-1}}$ channel). We note that no emission is evident in the Kondratko

et al. (2006) spectrum of NGC 1320 even when smoothed to an effective resolution

of $3.5\,\mathrm{km\,s^{-1}}$.

Table 4.2.   Known Water Maser Sources Observed with the Green Bank Telescope.

Galaxy	Type[a]	α_{2000}[b] (hh mm ss)	δ_{2000}[b] (dd mm ss)	v_{sys}[c] (km s^{-1})	Date	T_{sys}[d] (K)	1σ[e] (mJy)
NGC 0235A	Sy2	00 42 52.81	−23 32 27.8	6664^{+108}_{-21}	02-01-2006	58	3.8
NGC 0449 (MRK 1)	Sy2	01 16 07.25	+33 05 22.4	4780^{+51}_{-46}	04-19-2006	48	2.4
UGC 04203 (MRK 1210)	Sy2	08 04 05.86	+05 06 49.8	4046^{+114}_{-156}	04-24-2006	44	3.3
NGC 2824	Sy?	09 19 02.22	+26 16 12.0	2760^{+39}_{-49}	01-27-2006	35	2.5
NGC 2979	Sy2	09 43 08.65	−10 23 00.0	2720^{+15}_{-15}	02-09-2006	37	2.0
ARP 299 (NGC 3690)	AGN	11 28 32.20	+58 33 44.0	3121^{+3}_{-253}	04-27-2006	46	2.9
NGC 3735	Sy2	11 35 57.30	+70 32 08.1	2696^{+81}_{-141}	02-09-2006	37	3.9
NGC 4293	LINER	12 21 12.82	+18 22 57.4	893^{+63}_{-318}	04-10-2006	38	2.8
2MASXi J1939388-012433	Sy2	19 39 38.91	−01 24 33.2	6188^{+36}_{-36}	04-19-2006	48	3.7

[a] Activity type from the NED, except for NGC 0235A, which is from Kondratko et al. 2006.

[b] GBT pointing positions adopted from Kondratko et al. 2006 for NGC 0235A, NGC 4293 ($\sigma = 0.''3$), from Greenhill et al. 2003 for NGC 2824, NGC 2979, 2MASXi J1939388-012433 ($\sigma = 0.''2$), and from the NED for NGC 0449 ($\sigma = 0.''28$), UGC 04203 ($\sigma = 0.''75$), NGC 3556 ($\sigma = 1.''3$), ARP 299 (NGC 3690, $\sigma = 10''$), NGC 3735 ($\sigma = 1.''3$).

[c] Optical heliocentric systemic velocity. For each source, we list the systemic velocity measurement with the smallest uncertainty (main value) and the range of optical heliocentric systemic velocity estimates available in literature (upper and lower limits). The measurements (km s^{-1}) are: UGC 04203 (MRK 1210): 4046 ± 10 (HI; de Vaucouleurs et al. 1991), 4035 ± 60 (optical; de Vaucouleurs et al. 1991), 4065 ± 42 (optical; Falco et al. 1999), 4090 ± 70, 3890 (optical; Bottinelli et al. 1993); NGC 2979: 2720 ± 15 (optical; Fisher et al. 1995); NGC 3735: 2696 ± 7 (HI; de Vaucouleurs et al. 1991), 2671 ± 46 (optical; de Vaucouleurs et al. 1991), 2684 ± 39 (optical; Falco et al. 1999), 2738 ± 39, 2597 ± 42 (optical; Bottinelli et al. 1993); ARP 299 (NGC 3690): 3121 ± 3 (HI; Nordgren et al. 1997), 2996 ± 14, 3051 ± 22, 2948 ± 80 (optical; Bottinelli et al. 1993); NGC 0449 (MRK 1): 4780 ± 2 (optical; Keel 1996), 4823 ± 6 (optical; Huchra et al. 1999), 4824 ± 7 (HI; de Vaucouleurs et al. 1991), 4795 ± 22 (optical; de Vaucouleurs et al. 1991), 4750 ± 16 (optical; Falco et al. 1999), $4793 - 4830$ (optical; Bottinelli et al. 1993); NGC 4293: 893 ± 8 (optical; di Nella et al. 1995), 948 ± 8 (HI; de Vaucouleurs et al. 1991), 883 ± 54 (optical; Falco et al. 1999), 717 ± 58 (optical; de Vaucouleurs et al. 1991), 750 ± 175 (optical; Humason et al. 1956); NGC 2824: 2760 ± 23 (optical; Fisher et al. 1995), 2759 ± 31 (optical; de Vaucouleurs et al. 1991), 2755 ± 44 (optical; Falco et al. 1999), 2759 (optical; Bottinelli et al. 1993); NGC 0235A: 6664 ± 21 (optical; de Vaucouleurs et al. 1991), 6692 ± 28 (optical; da Costa et al. 1991), 6692 ± 37 (optical; da Costa et al. 1998), 6772 (optical; Bottinelli et al. 1993); 2MASXi J1939388-012433: 6188 ± 36 (optical; Strauss et al. 1992).

[d] Average system temperature (not-corrected for opacity).

[e] Rms noise in a 24.4 kHz spectral channel corrected for atmospheric opacity (typically from 0.02 to 0.04) and for the dependence of antenna gain on elevation.
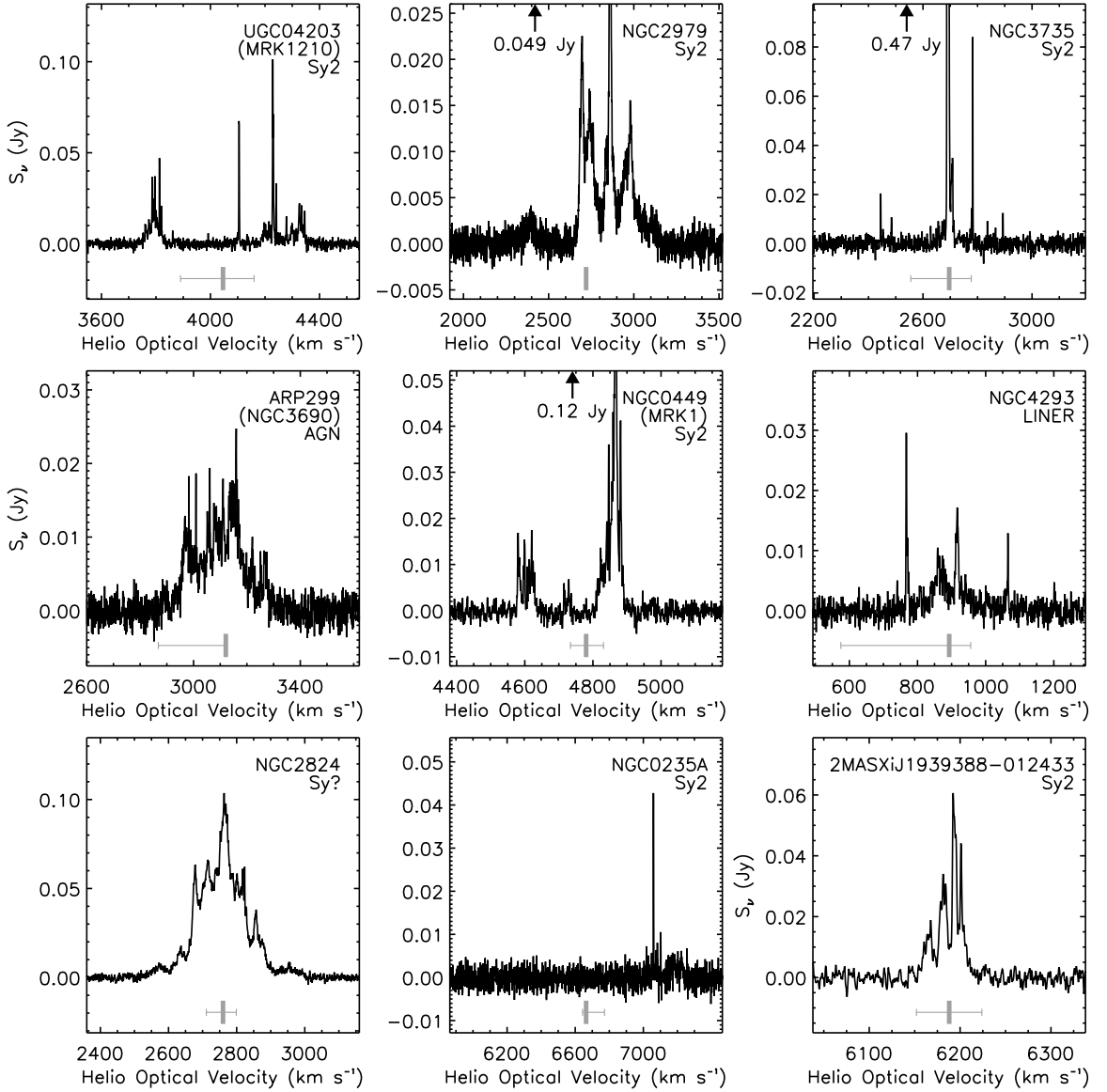
Figure 4.2.— Spectra of known masers in UGC 04203 (MRK 1210), NGC 2979, NGC 3735, ARP 299 (NGC 3690), NGC 0449 (MRK 1), NGC 4293, NGC 2824, NGC 0235A, and 2MASXi J1939388-012433 obtained with the Green Bank Telescope. For each source, the horizontal error bar shows the range of optical heliocentric systemic velocity estimates while the vertical bar marks the systemic velocity measurement with the smallest uncertainty. For NGC 2979, NGC 3735, and NGC 0449, the vertical scale was expanded to make apparent weak emission. In these three cases, the peak flux densities are 0.049, 0.47, and 0.12 Jy, respectively.

4.3.2 Monitoring of Known Sources

We also used the GBT to obtain sensitive ($1\sigma \sim 2-4\,\mathrm{mJy}$) spectra of known non-high-velocity sources (Fig.4.2 and Table 4.2) in an effort to detect weak high-velocity emission that was not detected in previous studies. In what follows, we comment on selected systems:

- *UGC 04203 (MRK 1210).* We detected with high SNR (> 15) emission in the velocity range $4200 - 4350\,\mathrm{km\,s^{-1}}$, a line at $\sim 4100\,\mathrm{km\,s^{-1}}$, and a complex at $\sim 3775\,\mathrm{km\,s^{-1}}$. The latter two were detected only marginally in previous spectra of the source (Braatz et al. 1996, 2003). The resulting spectrum reveals unambiguously a characteristic spectral signature of emission from an edge-on disk: a spectral line ($\sim 70\,\mathrm{mJy}$ at $\sim 4100\,\mathrm{km\,s^{-1}}$) in the vicinity of the systemic velocity of $4046 \pm 10\,\mathrm{km\,s^{-1}}$ (HI; de Vaucouleurs et al. 1991) and two high-velocity complexes (at $3740 - 3830\,\mathrm{km\,s^{-1}}$ and $4190 - 4350\,\mathrm{km\,s^{-1}}$) symmetrically offset by approximately $250\,\mathrm{km\,s^{-1}}$ from the systemic velocity. If the red- and blue-shifted emission in this system indeed represents high-velocity emission, then the maximum orbital velocity of the disk as traced by the maser emission is $\sim 300\,\mathrm{km\,s^{-1}}$.

- *NGC 3735.* We detected weak narrow lines at ~ 2440, ~ 2480, ~ 2840, $\sim 2890\,\mathrm{km\,s^{-1}}$ not evident in previous spectra of the source (Greenhill et al. 1997a; Braatz et al. 2003) and blue-shifted and red-shifted from the systemic emission at $\sim 2700\,\mathrm{km\,s^{-1}}$ ($v_{sys} = 2696 \pm 7\,\mathrm{km\,s^{-1}}$ from HI; de Vaucouleurs et al. 1991) by $210 - 250$ and $150 - 200\,\mathrm{km\,s^{-1}}$, respectively. As in the case of NGC 1320, we infer from the presence of narrow (i.e., $< 5\,\mathrm{km\,s^{-1}}$) line widths

and the association of emission with the nucleus (Greenhill et al. 1997a) that NGC 3735 is likely a high-velocity system. The maximum orbital velocity of the disk as traced by the maser emission in this case is $\sim 250\,\mathrm{km\,s^{-1}}$.

- *NGC 2979.* The GBT spectrum shows weak emission ($\sim 3\,\mathrm{mJy}$ at $2390\,\mathrm{km\,s^{-1}}$) that was not evident in the previous spectrum of this source (Greenhill et al. 2003) and that is blue-shifted by $325\,\mathrm{km\,s^{-1}}$ from the systemic velocity of the host galaxy. The maser emission originates in the active nucleus (Greenhill et al. 2003) but, absent narrow lines, the excitation of the maser emission by jet activity cannot be excluded. For water maser systems with multiple systemic velocity measurements, estimates of systemic velocity from optical data are often offset (irrespective of the quoted formal uncertainties) by as much as $\sim 100\,\mathrm{km\,s^{-1}}$ from either the average or the systemic velocity measurement based on HI data (refer to Fig.4.2). Hence, if we assumed that emission originates in an edge-on accretion disk and that the single optical systemic velocity measurement is highly uncertain (2720 ± 15; Fisher, K. B., et al. 1995), then we would identify the broad complex at $2700 - 3000\,\mathrm{km\,s^{-1}}$ and the newly detected feature at $2390\,\mathrm{km\,s^{-1}}$ with systemic and blue-shifted high-velocity emission, respectively. Under this scenario, the orbital velocity of the disk would be $\sim 500\,\mathrm{km\,s^{-1}}$, and we would expect red-shifted high-velocity emission to occur approximately at $3300\,\mathrm{km\,s^{-1}}$. We note however that no emission is apparent in the GBT spectrum at this velocity. It is also possible that the complex at $2700 - 3000\,\mathrm{km\,s^{-1}}$ represents emission from an entire quadrant of the accretion disk, i.e., it arises at azimuthal angles intermediate to the midline and the line of sight towards the central engine. Emission

that arises from locations within the disk other than the midline and the line-of-sight towards the center has been observed from NGC 1068 (Greenhill & Gwinn 1997; Gallimore et al. 2001). If this speculation is correct, then the orbital velocity of the disk in NGC 2979 would be $\sim 350\,\mathrm{km\,s^{-1}}$.

- *NGC 0449 (Mrk 1).* We detected an emission complex at $\sim 4860\,\mathrm{km\,s^{-1}}$, a $\sim 20\,\mathrm{mJy}$ component at $\sim 4600\,\mathrm{km\,s^{-1}}$, and a weak line (peak of $7\,\mathrm{mJy}$ in a $1.5\,\mathrm{km\,s^{-1}}$ spectral channel) at $\sim 4725\,\mathrm{km\,s^{-1}}$. The complex at $\sim 4860\,\mathrm{km\,s^{-1}}$ has been present in the spectrum of the source since its discovery (Braatz et al. 1996, 2003) while the component at $\sim 4600\,\mathrm{km\,s^{-1}}$ was marginally detected by Braatz et al. (2003). The newly detected emission is approximately halfway in velocity between the two previously known spectral components. Although the position of the maser emission with respect to the nucleus has not been determined, the spectrum shows an archetypical spectral signature of emission from an edge-on accretion disk. In particular, considering the uncertainty on the systemic velocity of the galaxy ($4780^{+51}_{-46}\,\mathrm{km\,s^{-1}}$ from various optical studies; see Fig.4.2), we identify the complex at $\sim 4860\,\mathrm{km\,s^{-1}}$, the component at $\sim 4600\,\mathrm{km\,s^{-1}}$, and the newly detected emission at $\sim 4725\,\mathrm{km\,s^{-1}}$ with red-shifted high-velocity, blue-shifted high-velocity, and low-velocity emission, respectively. Under this scenario, the spectrum is consistent with emission from an edge-on disk with orbital velocity of $\sim 130\,\mathrm{km\,s^{-1}}$.

- *ARP 299 (NGC 3690).* The spectrum contains a feature with FWHM $\sim 250\,\mathrm{km\,s^{-1}}$ and narrow Doppler components that were not evident in the previous spectra of the source obtained with $4.3\,\mathrm{km\,s^{-1}}$ channels (Henkel et al. 2005). Broad spectral components such as the one in ARP 299 have

been associated circumstantially with jet activity in three other AGN (e.g., Claussen et al. 1998; Gallimore et al. 2001; Peck et al. 2003; Kameno et al. 2005). Furthermore, there is tentative evidence from single-dish mapping that emission arises from multiple regions separated by kpc's in this merging system (Henkel et al. 2005). This and the presence of both narrow and broad spectral features complicate the physical classification of this source.

- *NGC 2824.* The GBT spectrum shows relatively narrow Doppler components on top of a broad ($\sim 150\,\mathrm{km\,s^{-1}}$) line profile, which is consistent with the discovery spectrum of the maser (Greenhill et al. 2003). Although the maser emission is associated in position with the AGN (Greenhill et al. 2003), the presence of both narrow and broad spectral components hinders physical interpretation in this case.

4.3.3   Centripetal Acceleration

We also monitored with the GBT low-velocity emission in three high-velocity systems that were initially detected with the GBT (2MASX J08362280+3327383, NGC 6264, and UGC 09618 NED02; Kondratko et al. 2006) in an effort to detect velocity drifts, which are a manifestation of centripetal acceleration due to disk rotation (Table 4.3, Figs.4.3 and 4.4). For each source, we used an iterative least squares technique adopted from Humphreys et al. (2007) to solve for amplitudes, peak centroids, widths, and velocity drifts of all Gaussian components at all epochs simultaneously. We constrained the widths of most Gaussian components to $< 5\,\mathrm{km\,s^{-1}}$, since we believe that properly decomposed spectra of high-velocity systems should consist of

Table 4.3. Velocity drifts of Gaussian components that comprise low-velocity emission.

Source	Epoch[a]	χ_R^2 [b]	Velocity[c] (km s^{-1})	Drift[d] (km s^{-1} yr^{-1})	Epochs[e]
2MASX J08362280+3327383[f]	12-08-2003	1.7	14940.92 ± 0.06	0.405 ± 0.005	4
			14943.2 ± 0.4	0.9 ± 0.1	
			14951.9 ± 0.1	0.93 ± 0.03	
			14954.70 ± 0.06	0.58 ± 0.03	
			14963.9 ± 0.1	0.85 ± 0.07	
			14967.7 ± 0.1	1.55 ± 0.04	
			14969.9 ± 0.1	1.88 ± 0.07	
			14976.0 ± 0.2	0.11 ± 0.05	
			14949.2 ± 0.9	1.45 ± 0.09	
	12-08-2003	1.0	15025.5 ± 0.1	0.65 ± 0.04	
NGC 6264	10-17-2005	1.2	10164.0 ± 0.2	1.9 ± 0.2	3
			10164.4 ± 0.3	1.7 ± 0.5	
			10168.2 ± 0.3	2.1 ± 0.3	
			10174.7 ± 0.3	1.7 ± 0.6	
			10181.9 ± 0.3	2.1 ± 0.6	
			10184.7 ± 0.4	2.0 ± 0.4	
			10186.0 ± 0.1	2.1 ± 0.1	
			10188.7 ± 0.2	2.0 ± 0.2	
			10191.0 ± 0.2	1.2 ± 0.4	
UGC 09618 NED02[f]	12-13-2003	1.4	10199.6 ± 0.1	3.8 ± 0.1	5

[a] Reference epoch for component velocities.

[b] Reduced chi-squared for a least squares solution that determines velocities, velocity drifts, widths, and amplitudes of all Gaussian components at all epochs simultaneously. Only components for which the amplitudes were obtained with signal-to-noise ratio of > 3 over at least two epochs are reported.

[c] Velocity of a Gaussian component at the reference epoch.

[d] Velocity drift of a Gaussian component.

[e] Total number of epochs.

[f] A first-order polynomial and a wide ($\sim 25\,\mathrm{km\,s^{-1}}$) stationary Gaussian component — models for the broad low-velocity plateaus in UGC 09618 NED02 and 2MASX J08362280+3327383, respectively — are not reported here.

narrow Doppler widths. However, a first-order polynomial and a wide ($\sim 25 \, \mathrm{km \, s^{-1}}$) stationary Gaussian component were used to model the broad low-velocity plateaus in UGC 09618 NED02 and 2MASX J08362280+3327383, respectively. We note that these two models affect our velocity drift results insignificantly (i.e., within the reported uncertainties). In case of 2MASX J08362280+3327383 and NGC 6264, we report the detection of centripetal acceleration in multiple features. We obtain ~ 0.5, $1.2 - 2.1$, and $3.8 \pm 0.1 \, \mathrm{km \, s^{-1} \, yr^{-1}}$ for 2MASX J08362280+3327383, NGC 6264, and UGC 09618 NED02, respectively (Table 4.3).
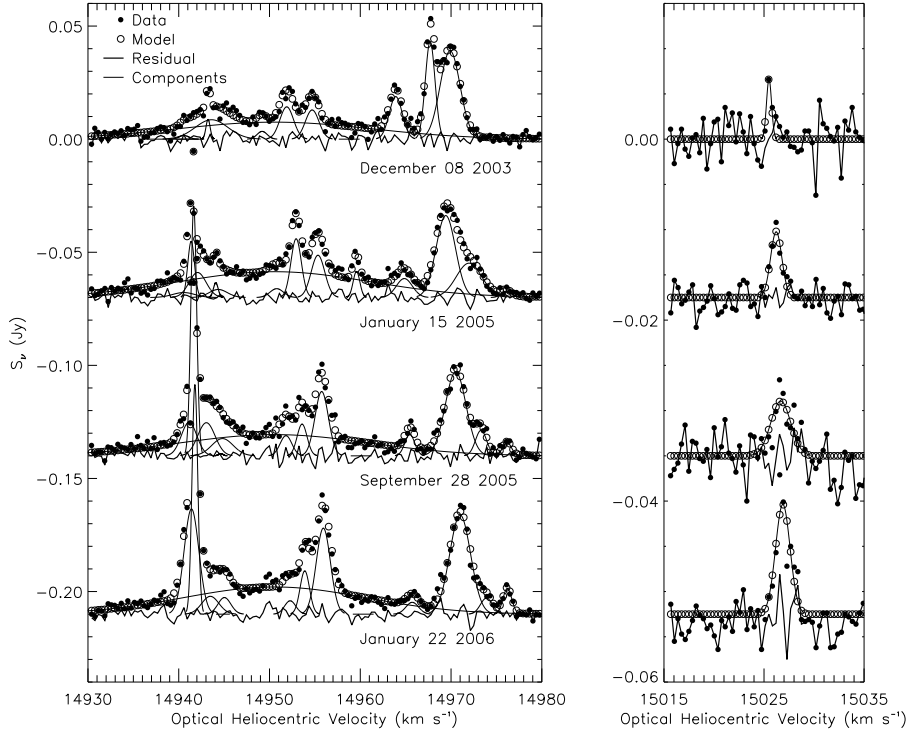
Figure 4.3.— Spectra of low-velocity features in 2MASX J08362280+3327383 obtained with the Green Bank Telescope and the results of Gaussian component decomposition (also see Table 4.3). A wide ($\sim 25 \, \mathrm{km \, s^{-1}}$) stationary Gaussian component at $\sim 14951 \, \mathrm{km \, s^{-1}}$ represents a broad low-velocity plateau present at each epoch.
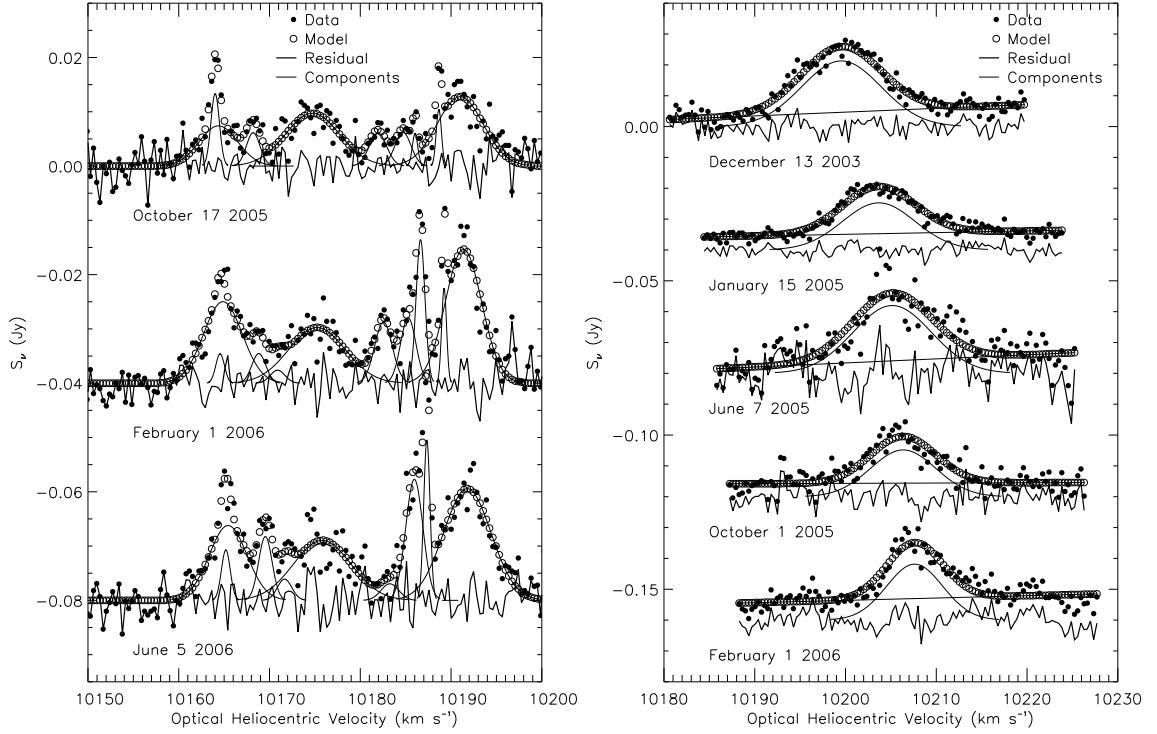
Figure 4.4.— Spectra of low-velocity features in NGC 6264 *(left)* and UGC 09618 NED02 *(right)* obtained with the Green Bank Telescope and the results of Gaussian component decomposition (also see Table 4.3). An overplotted line shows a model for the broad low-velocity plateau in UGC 09618 NED02 present at each epoch.

4.4 Discussion

4.4.1 Black Hole Masses and Disk Radii

The measured centripetal accelerations, when combined with the orbital velocities as inferred from single-dish spectra, can be used to estimate black hole masses and accretion disk radial extents. If we combine equations for centripetal acceleration, $a = v^2/r$, and orbital velocity, $v^2 = GM/r$, we obtain $M_{BH} = v_{\rm rot}^4/Ga$ and $r = GM_{BH}/v_{\rm rot}^2$, where M_{BH} is the black hole mass, r is the radius, $v_{\rm rot}$ is the orbital

velocity, and a is the centripetal acceleration. If we assume that the orbital velocity of the low-velocity emission is represented by the orbital velocity of the high-velocity emission as inferred from the spectra (i.e., low-velocity emission arises within the accretion disk at the mean radius of the high-velocity features), then we obtain black hole masses of $\sim 6 \times 10^7$, 2×10^7, and $6 \times 10^7 \, M_\odot$ and accretion disk radial extents of $\sim 0.5 - 1$, $0.1 - 0.5$, and $0.2 - 0.8$ pc for 2MASX J08362280+3327383, NGC 6264, and UGC 09618 NED02, respectively.

We note that for 2MASX J08362280+3327383, the scatter in the velocity drift measurements is larger than the individual formal uncertainties. Since $a = GM_{BH}/r^2$ and hence $\Delta a/\langle a \rangle = -2 \, \Delta r/\langle r \rangle$, the scatter in the measured accelerations of $\Delta a/\langle a \rangle \sim 1.3$ might be due to low-velocity emission that populates a wide range of radii within the accretion disk, i.e., $\Delta r/\langle r \rangle \sim 0.6$. Such radial spread has been observed in the case of NGC 4258, for which robust de-projection has been achieved (Humphreys et al. 2007). Furthermore, the measured centripetal accelerations might vary with spectral component velocity if the disk radius of the low-velocity features changes with the azimuth angle due to a disk warp for instance (e.g., Herrnstein et al. 2005). However, we find no evidence for a dependence of velocity drift on component velocity for any of the sources.

Moreover, we detect only spectral components that drift towards larger velocities with time (i.e., components with positive centripetal acceleration), as is expected for low-velocity emission that arises along the line of sight to and in front of the dynamical center. Low-velocity emission from behind the dynamical center, which would manifest itself as spectral components with negative centripetal acceleration, have not been detected to date from known nuclear water maser

systems. Seed photons from a nuclear continuum source might be necessary to generate low-velocity emission luminous enough for us to detect; it is likely that amplification of background continuum emission indeed plays a role in the case of the systemic emission in NGC 4258 (e.g., Herrnstein et al. 1997). Alternatively, free free absorption by ionized gas in close proximity to the central engine may significantly weaken the emission from behind the dynamical center (e.g., Herrnstein et al. 1996). The environment outside of the disk is expected to be ionized and hence differential attenuation of the maser emission is readily achieved for free-free absorption with a relatively small difference in emission measure (e.g., Mezger & Henderson 1967). In particular, difference in optical depth of $\Delta\tau > 3$ between the front side and the back side of the disk would be sufficient to attenuate a low-velocity line with a typical strength of $\sim 150\,\mathrm{mJy}$ to below 4σ detection threshold in our GBT spectra.

4.4.2 Disk Orientations

We now consider evidence for the preference of water maser emission to occur in edge-on galaxies from survey detection rates and from the distribution of galactic plane inclinations. In what follows, we computed the inclination i using $\sin^2 i = (1 - 10^{-2\log_{10} r_{25}})/(1 - 10^{-2\log_{10} r_o})$, where $\log_{10} r_{25}$ is the logarithm of the ratio of major to minor isophotal diameters, both measured at the surface brightness level of $m_B = 25\,\mathrm{mag}^{-2}$, $\log_{10} r_o = 0.43 + 0.053\,t$ for $-5 \leq t \leq 7$, $\log_{10} r_o = 0.38$ for $t > 7$, and t is the morphological type code, $t = -5$ to 10 (Hubble 1926). The morphological type code and its uncertainty were culled from the Third Reference Catalogue of Bright Galaxies (RC3; de Vaucouleurs et al. 1991) while the axial ratios

were taken from two independent sources: the RC3 and the 2MASS Extended Source Catalog (2MASS XSC; Skrutskie et al. 2006). The axial ratios and the resulting inclinations from the RC3 correlate (Spearman ρ of 0.75 and 0.74, respectively) at a very high significance level ($\ll 1\%$) with the corresponding 2MASS XSC parameters. The two inclination data sets differ by more than $0.5\,\mathrm{rad}$ for only 6% of the sources with the largest discrepancy of 60°. Standard deviation about the linear fit to the the RC3 and the 2MASS inclination data sets is 10°, which is comparable to the average uncertainty (8°) in the RC3 inclinations (2MASS XSC provides no errors on the axial ratios) and which we adopt as the representative uncertainty on inclination.

Among Seyfert 2 and LINER systems with $v_{sys} < 10000\,\mathrm{km\,s^{-1}}$ and $i > 70^{\circ}$, we obtain a detection rate of 3 out of 33 or $9 \pm 5\%$ (to estimate the uncertainty, we used the unbiased maximum likelihood estimator for the variance of the Binomial parameter p). If we include the inclined systems from a GBT survey reported by Kondratko et al. (2006), we obtain a detection rate of 5 out of 41 or $12 \pm 5\%$ among Seyfert 2 and LINER systems with $v_{sys} < 15000\,\mathrm{km\,s^{-1}}$ and $i > 70^{\circ}$. These rates are consistent within errors with an incidence rate of $18 \pm 3\%$ (22 out of 124) from a survey by Braatz et al. (2004) of comparable sensitivity among Seyfert 2 and LINER systems with $v_{sys} < 12000\,\mathrm{km\,s^{-1}}$ but not selected by inclination. Based on survey detection rates, we therefore find no evidence for a preference of maser emission to occur in inclined active galaxies, in contrast to the marginal predisposition reported by Braatz et al. (1997b).

We also find no evidence for the preference of maser emission to occur in inclined active systems from a distribution of galactic plane inclinations for water maser sources and for all Seyfert 2 and LINER systems with $v_{sys} < 20000\,\mathrm{km\,s^{-1}}$

Table 4.4. Results of the Kolmogorov-Smirnov (K-S) test applied to the inclination and morphological type data.

Population A	Population B	Inclination (RC3)		Inclination (2MASS XSC)		Morphology (RC3)	
		$D^{(a)}$	$\%^{(b)}$	$D^{(a)}$	$\%^{(b)}$	$D^{(a)}$	$\%^{(b)}$
all masers	Sy2/LINER$^{(c)}$	0.15 ± 0.03	40 ± 20	0.22 ± 0.07	20 ± 20	0.13 ± 0.03	60 ± 20

$^{(a)}$The K-S statistic — the maximum deviation between the cumulative distributions of population A and population B. The mean and its error for the RC3 inclination data are from a Monte Carlo simulation where the probability distribution function for each inclination data point is modelled by a Gaussian, the standard deviation of which is computed using error propagation from uncertainties on morphological type code t and on logarithm of axial ratio $\log_{10} r_{25}$, both from the RC3. Since the 2MASS XSC provides no errors on the axial ratios, the uncertainties on the K-S statistic for the 2MASS XSC inclination data were computed using the Bootstrap technique.

$^{(b)}$Significance level of the K-S statistic — probability (expressed as a percentage) that two samples drawn from the same parent distributions could differ by as much as the two samples considered. Small values of the significance level indicate that the difference between cumulative distribution functions of populations A and B is statistically significant. Mean and its uncertainty are from the simulation described in (a).

$^{(c)}$All Sy2/LINER systems with $v_{sys} < 20000 \, \text{km} \, \text{s}^{-1}$ selected from the NED.
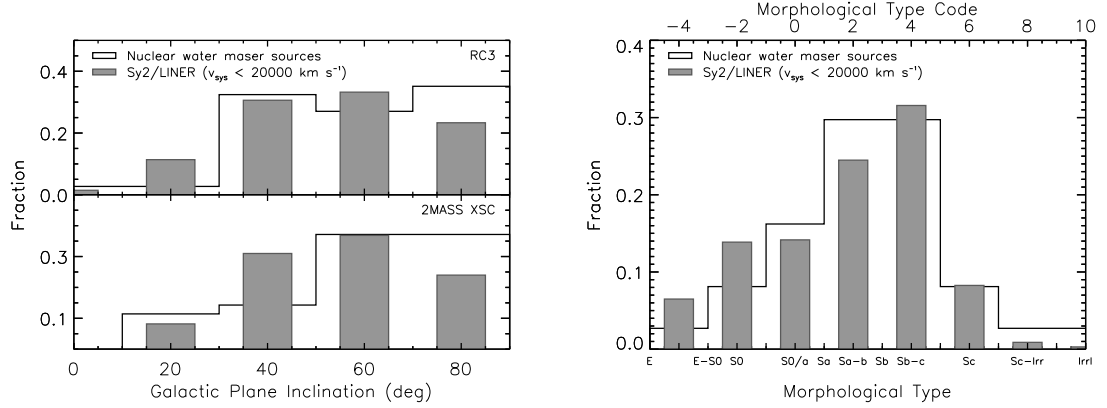
Figure 4.5.— Histograms of galactic plane inclination *(left)* and morphological type *(right)* for all published water maser sources (37 and 35 from RC3 and 2MASS XSC, respectively) and for Seyfert 2 or LINER systems with $v_{sys} < 20000\,\mathrm{km\,s^{-1}}$ for which inclination data were available (343 and 342 from RC3 and 2MASS XSC, respectively). The upper and lower panels in the figure on the left show the histograms of galactic plane inclination computed using the axial ratios from the RC3 and the 2MASS XSC, respectively. Inclination of 90° represents an edge-on galactic plane.

(Fig.4.5). The inclination excess is apparent from Fig.4.5: $23 \pm 2\%$ $(24 \pm 2\%)$ of Seyfert 2 and LINER systems with $v_{sys} < 20000\,\mathrm{km\,s^{-1}}$ but $35 \pm 8\%$ $(37 \pm 8\%)$ of all water maser systems have galactic plane inclinations from RC3 (2MASS XSC) greater than 70°. However, this apparent excess is not statistically significant if we consider the distributions in their entirety. A Kolmogorov-Smirnov test yields a $40 \pm 20\%$ $(20 \pm 20\%)$ probability that two samples drawn from the same parent distribution would differ by as much as RC3 (2MASS XSC) inclination data for all water maser systems and for Seyfert 2 and LINER nuclei (Table 4.4). The results of the Kolmogorov-Smirnov test that compares Seyfert 2 and LINER nuclei with either all maser sources, high-velocity systems, or unclassified and jet masers are all consistent within the uncertainties (results available upon request). Consequently, there is no statistical evidence for the preference of water maser systems to occur in

edge-on galaxies.

Our null result is contrary to the previously reported marginal predisposition for water maser emission to occur in edge-on active galaxies (Braatz et al. 1997b) but consistent with recent studies that have shown lack of correlation between galactic plane orientation and nuclear jet or narrow line region direction (Ulvestad & Wilson 1984; Schmitt et al. 1997, 2001, 2002, 2003; Clarke et al. 1998; Nagar & Wilson 1999; Kinney et al. 2000; Middelberg et al. 2004). We also find no statistical difference between distributions of Hubble morphological type for water maser sources and for Seyfert 2 and LINER systems (Fig.4.5). In this case, a Kolmogorov-Smirnov test yields a $60 \pm 20\%$ probability that two samples drawn from the same parent distribution would differ by as much as the morphological type data for all water maser systems and for Seyfert 2 and LINER nuclei (Table 4.4). We note that the distribution of Hubble morphological type for Seyfert 2 and LINER systems clearly reflects the established fact that nuclear activity occurs more frequently in spiral galaxies (e.g., Kirhakos & Steiner 1990a; Malkan et al. 1998).

4.5   Conclusions

In a survey with the GBT of 41 edge-on AGN, we have detected three new water maser sources. Emission in NGC 1320 most likely originates in an edge-on pc-scale accretion disk. Based on the survey detection rates and the distribution of galactic plane inclinations for known water maser systems, we find no evidence for a preference of maser emission to occur in edge-on galaxies. We also used the GBT to obtain sensitive ($1\sigma \sim 2 - 4\,\mathrm{mJy}$) spectra of known sources. Maser spectra of

UGC 04203 and NGC 0449 display characteristic spectral signatures of emission from an edge-on accretion disk, while in NGC 2979 and NGC 3735 we detect weak emission offset by more that $200\,\mathrm{km\,s^{-1}}$ from the systemic velocities of the host galaxies. For three high-velocity water maser sources, we have detected secular drift in multiple low-velocity features — a manifestation of centripetal acceleration due to accretion disk rotation. These centripetal acceleration results when combined with robust models of accretion disks from VLBI might yield distances to these sources based solely on geometry and dynamics of the pc-scale accretion disks and independent of standard candles like Cepheids and SN Ia supernovae. Since all three sources are at large distances ($> 10000\,\mathrm{km\,s^{-1}}$) and peculiar velocities are typically $\lesssim 500\,\mathrm{km\,s^{-1}}$ (e.g., Dale et al. 1999), a determination of distance to any of these systems would be of significant value since it might provide an independent estimate of the Hubble constant.

4.6 Acknowledgements

Chapter 5

Evidence for a Geometrically Thick Self-Gravitating Accretion Disk in NGC 3079

Paul T. Kondratko, Lincoln J. Greenhill, & James M. Moran

Abstract

We have mapped, for the first time, the full velocity extent of the water maser emission in NGC 3079. The largely north-south distribution of emission, aligned with a kpc-scale molecular disk, and the segregation of blue- and red-shifted emission on the sky are suggestive of a nearly edge-on molecular disk on pc-scales. Positions and line-of-sight velocities of blue- and red-shifted maser emission are consistent

with a central mass of $\sim 2 \times 10^6 \, M_\odot$ enclosed within a radius of $\sim 0.4\,\mathrm{pc}$. The corresponding mean mass density of $10^{6.8} \, M_\odot \, \mathrm{pc}^{-3}$ is suggestive of a central black hole, which is consistent with the detection of hard X-ray excess $(20 - 100\,\mathrm{keV})$ and an Fe Kα line from the nucleus. Because the rotation curve traced by the maser emission is flat, the mass of the pc-scale disk is significant with respect to the central mass. Since the velocity dispersion of the maser features does not decrease with radius and constitutes a large fraction of the orbital velocity, the disk is probably thick and flared. The rotation curve and the physical conditions necessary to support maser emission imply a Toomre Q-parameter that is $\ll 1$. Thus, the disk is most likely clumpy, and we argue it is probably forming stars. Overall, the accretion disk in NGC 3079 stands in contrast to the compact, thin, warped, differentially rotating disk in the archetypal maser galaxy NGC 4258.

We have also mapped radio continuum emission in the vicinity of the disk and identify a new, time-variable, non-thermal component (E) that is not collinear with the previously imaged putative jet. Based on the large luminosity and the unusually steep spectrum $(\alpha < -2.1)$, we exclude a radio supernova as the progenitor of E. However, because its spectrum is consistent with an aging electron energy distribution, E might be a rapidly cooling remnant, which may indicate that the jet axis wobbles. Alternatively, considering its location, the component might mark a shock in a wide-angle outflow that is interacting with a dense ambient medium. In this context, masers at high latitudes above the disk, mapped in this and previous studies, may be tracing an inward extension of the kpc-scale bipolar wide-angle outflow previously observed along the galactic minor axis.

5.1   Introduction

NGC 3079 is a relatively nearby ($v_{sys} = 1125 \pm 6 \, \mathrm{km \, s^{-1}}$), edge-on spiral galaxy classified as Seyfert 2 (Ford et al. 1986; Ho, Filippenko, & Sargent 1997a) or a LINER (Heckman 1980). Observations of large-scale structure in this galaxy indicate the presence of a powerful outflow that appears to originate within the nucleus. Along the minor axis of the galaxy, at a position angle (P.A.) of $\sim 80°$, a bipolar super-wind inflates a kpc-scale superbubble visible in radio continuum emission (Duric & Seaquist 1988; Baan & Irwin 1995; Irwin & Saikia 2003), [NII]+Hα emission (Veilleux et al. 1994), and soft X-ray continuum emission (Cecil, Bland-Hawthorn, & Veilleux 2002). The apex of the superbubble is embedded in a dense molecular kpc-scale disk traced by CO (Koda et al. 2002), HCN, and HCO$^+$ emission (Kohno et al. 2001). The circumnuclear molecular disk is aligned with, and rotates in the same sense as, the much larger galaxy disk such that the north side is approaching and the near side is projected to the west of its major axis.

There is compelling evidence that NGC 3079 contains an AGN. The X-ray spectrum exhibits a continuum excess in the $20 - 100 \, \mathrm{keV}$ band and a $6.4 \, \mathrm{keV}$ Fe Kα line, which are both believed to be unambiguous indicators of nuclear activity (Iyomoto et al. 2001; Cecil et al. 2002). Both soft and hard X-ray data are suggestive of unusually high hydrogen column density towards the nucleus, $N_H \sim 10^{25} \, \mathrm{cm^{-2}}$ (Iyomoto et al. 2001), which, in the context of the AGN unified model, is indicative of an almost edge-on obscuring structure along the line of sight to the nucleus (Lawrence & Elvis 1982; Antonucci 1993). The existence of nuclear activity is also indirectly supported by radio observations of the nucleus. Continuum images of the

inner-pc region obtained with Very Long Baseline Interferometry (VLBI) reveal a linear distribution of compact knots consistent with a jet (Irwin & Seaquist 1988). Furthermore, the galaxy harbors one of the most luminous (i.e., assuming isotropic emission of radiation) water masers known (Henkel et al. 1984; Haschick & Baan 1985), and such maser emission generally is associated with AGN activity (Braatz, Wilson, & Henkel 1997b). In fact, the isotropic luminosity of the brightest, spatially unresolved spectral feature in NGC 3079 ($\sim 130\,L_\odot$) is comparable to luminosities of other AGN related masers such as NGC 4258 and NGC 1068 but at least two orders of magnitude greater than the isotropic luminosity corresponding to the total integrated maser flux from starburst galaxies such as M82 (Baudry, Brouillet, & Henkel 1994) and NGC 253 (Ho et al. 1987) and from the W49N maser, the most luminous maser in our galaxy associated with a region of intense star formation (Gwinn 1994).

The nucleus of NGC 3079 may also host a starburst; the most convincing evidence comes from infrared (IR) and far-infrared (FIR) observations. Lawrence et al. (1985) found color excess and an extended 10μm nuclear source indicative of large amounts of dust in the nuclear region. The IRAS 60 to $100\,\mu$m flux ratio is ~ 0.5, which is suggestive of warm dust on kpc scales and qualifies NGC 3079 as a starburst galaxy (Soifer et al. 1989; Braine et al. 1997). FIR observations of the galaxy with ISOPHOT reveal a powerful $\sim 3.0 \times 10^{10}\,L_\odot$ point source of FWHM ≤ 4.5 kpc coincident with the nucleus (Klaas & Walker 2002). The SED of this point source is indicative of $20 - 32\,\mathrm{K}$ dust temperature. The luminosity of $3.5 \times 10^{10}\,L_\odot$ from IRAS (Soifer et al. 1987) or $\sim 3.0 \times 10^{10}\,L_\odot$ from ISOPHOT (Klaas & Walker 2002) yields a star formation rate of $\sim 10\,M_\odot\,\mathrm{yr}^{-1}$ on kpc scales

(Veilleux et al. 1994), under the assumption that star formation alone contributes to the infrared flux. The presence of nuclear star formation may also be inferred from large quantities of molecular gas associated with the nucleus. The observations of CO emission indicate a dynamical mass of $7 \times 10^8 \, M_\odot$ enclosed within a radius of 76 pc (Koda et al. 2002) as well as an unusually large molecular surface gas density relative to other normal, starburst, or active galaxies of $\sim 7200 \, M_\odot \, \mathrm{pc}^{-2}$ (Planesas, Colina, & Perez-Olea 1997; Sakamoto et al. 1999; Koda et al. 2002). Although sufficient to fuel a starburst, such a high concentration of gas does not necessarily imply intense nuclear star formation (Jogee 2001). However, the dynamical and gas masses deduced from CO observations by Koda et al. (2002) are suggestive of a Toomre-Q parameter that is less than unity within 150 pc of the nucleus and for isothermal sound speeds $< 50 \, \mathrm{km \, s^{-1}}$, consistent with the presence of molecular gas. Thus, the unusually high concentration of gas in the nucleus of NGC 3079 is subject to gravitational instabilities and might be actively forming stars. Detailed studies of the kpc-scale superbubble are also indicative of the nuclear starburst. The inferred starburst age ($> 10^7$ years) and gas depletion time ($\gtrsim 10^9$ years) are longer than the dynamical age of the superbubble ($\sim 10^6$ years), which is consistent with a starburst driving the bubble expansion (Veilleux et al. 1994). Furthermore, based on 1) the similarity of the superwind in NGC 3079 to that in prominent starburst galaxies like M82 and NGC 253, and 2) the general lack of correlation between the properties of outflow and nuclear activity in a sample of galaxies, Strickland et al. (2004b) argue that supernova feedback is responsible for the superbubble in NGC 3079. The correlation between diffuse halo X-ray luminosity per unit stellar mass and the infrared luminosity per unit mass in a sample of seven starburst and three

"normal" galaxies (see Fig.4 in Strickland et al. 2004b) is supportive of the starburst hypothesis, although that correlation does not imply causation particularly in the context of an alleged starburst-AGN connection.

Arguments have been made against the existence of a nuclear starburst in NGC 3079. The ratio of FIR luminosity to the molecular gas mass (i.e., the star formation efficiency) computed on kpc scales is $L_{FIR}/M_{H_2} \approx 13$, which is greater than the value of ~ 4 for the Milky Way and $1 < L_{FIR}/M_{H_2} < 7$ for Giant Molecular Clouds, but below the average value of ~ 25 observed for starburst galaxies (Young et al. 1986; Planesas et al. 1997). In fact, small-beam ($6''$) $10\,\mu$m flux of NGC 3079 measured by Lawrence et al. (1985) yields L_{FIR}/M_{H_2} of only 4.7 on smaller scales, which is suggestive of low star formation efficiency in the nuclear region (Hawarden et al. 1995). Furthermore, since the $10\,\mu$m flux in a $5.5''$ aperture is only 4% of the larger beam color corrected IRAS flux, the infrared emission is not centrally concentrated, contrary to expectation for a nuclear starburst (Devereux 1987). The nuclear region of NGC 3079 ($< 500\,$pc) is characterized by a flat spectrum between 10 and $20\,\mu$m in contrast to what is observed for starburst galaxies (Lawrence et al. 1985; Hawarden et al. 1986; Klaas & Walker 2002). According to Hawarden et al. (1995), low extinction towards the parts of the nucleus not obscured by the molecular disk, the lack of a $10\,\mu$m compact source coincident with the relatively well-defined apex of the superbubble, as well as the unusually high $H_2/Br\gamma$ ratio all argue against the starburst hypothesis. However, the validity of these arguments may be in doubt because of extremely heavy obscuration in the nuclear region due to dust lanes and the massive kpc-scale molecular disk. Indeed, asymmetry in the K-band image of the nucleus implies considerable extinction even at $2.2\,\mu$m (Israel et al. 1998).

If the nuclear starburst hypothesis is accepted, then it is not unreasonable to suppose the coexistence of star formation and nuclear activity in the inner parsec of NGC 3079, although the particular relationship between the two remains uncertain. It has been suggested that star formation and nuclear activity are likely to coexist in galactic nuclei, either because they are coupled through evolutionary mechanisms, or simply because they both depend on gas inflow and accretion (Cid Fernandes et al. 2001, and references therein). The existence of star formation and of young stellar populations with ages of $(7 - 20) \times 10^6$ years in the circumnuclear tori of radii $\lesssim 1\,\mathrm{pc}$ has been proposed to explain the UV excess of many Seyfert 2 galaxies (Terlevich 1996). Our galaxy contains a population of young, hot, bright, and massive stars within the inner-pc of the central black hole (Genzel et al. 1996, 2003), which might have formed in-situ in a preexisting accretion disk (Milosavljević & Loeb 2004). A young stellar population with an age of $\sim 7 \times 10^7$ years has been found in the central $12\,\mathrm{pc}$ of the Circinus active galaxy (Maiolino et al. 1998a), and young massive stars with ages $\leq 10^7$ years have been unambiguously detected within $\sim 200\,\mathrm{pc}$ of 30% to 50% of Seyfert 2 nuclei surveyed (Mas-Hesse et al. 1994, 1995; Cid Fernandes et al. 2001, and references therein). Because of the likely coexistence of star formation and nuclear activity in NGC 3079, the proximity of the galaxy, the presence of maser emission, and apparent jet activity, NGC 3079 is an important case to study with regard to understanding connections between star formation and nuclear activity.

5.1.1 Previous Imaging Studies of the Nucleus

Continuum

VLBI continuum images of NGC 3079 (refer to Fig.5.1 for a schematic) reveal several collinear components, A, B, C, and D, extending over $\sim 2.1\,\mathrm{pc}$ ($\sim 25\,\mathrm{mas}$) at P.A.$\sim 125°$ (Irwin & Seaquist 1988; Trotter et al. 1998; Sawada-Satoh et al. 2000, 2002). A line connecting the continuum components is significantly misaligned with respect to the superbubble axis but approximately aligned with the southern edge of the bubble (Cecil et al. 2001). Components A and B are separating at about $0.13\,c$, which strongly indicates the presence of a jet (Trotter et al. 1998; Sawada-Satoh et al. 2000, 2002), while the dominant component B is relatively stationary with respect to the molecular gas supporting the maser emission to within a transverse speed of $0.02\,c$ (Sawada-Satoh et al. 2000). These observations led Sawada-Satoh et al. (2000) to identify component B with the central engine. However, this interpretation is not unique since, even if component B were a radio jet core, an offset of the core from the central engine could be significant (e.g., NGC 4258; Herrnstein et al. 1997). Component B would also remain stationary with respect to the maser if B were shock excited emission, as would occur where a hot ionized supersonic flow encounters a dense ambient medium (e.g., Phillips & Mutel 1982; O'Dea, Baum, & Stanghellini 1991; Aurass, Vršnak, & Mann 2002, Kellermann et al. 2004). In support of the latter hypothesis, Trotter et al. (1998) found that components A and B have similar spectra, exhibit spectral turnovers between 5 and 22 GHz, and consist of multiple components or extensions. Since its spectrum is not flat, B is most likely not a jet core. Instead, Trotter et al. (1998) suggested that both components

are lower redshift and lower luminosity counterparts of compact symmetric objects whose flux densities have been observed to peak at gigahertz frequencies, and which are ascribed to the interaction between jets and associated high-density nuclear gas.

The putative jet coexists with additional non-thermal sources of continuum emission, whose nature remains ambiguous. Component E, identified by Kondratko, Greenhill, & Moran (2000), and component F, identified by Middelberg et al. (2003), both lie ~ 1.5 and $\sim 3.7\,\mathrm{pc}$ approximately east of component B, respectively. Middelberg et al. (2003) found that the separation of components E and B at 5 GHz systematically decreases at a rate of $0.07 \pm 0.01\,c$ (i.e., roughly one beam width over $\sim 3\,\mathrm{years}$). These authors suggested that E is stationary, and that component B is moving towards E. However, this proposition seems unlikely since B appears to be stationary with respect to the extended molecular gas structure underlying the maser emission. A more realistic scenario is that component E is a pattern in a flow that only appears to move in the direction of B as its physical characteristics change. Such apparently inward motions have been observed in several quasar and AGN jets (Kellermann et al. 2004).

Maser

In previous observations (Fig. 5.1), the water maser in NGC 3079 was found to be distributed in a disordered linear structure along P.A.$\sim -10°$ and aligned with the larger circumnuclear CO disk at P.A.$\sim -11°$ (Trotter et al. 1998; Koda et al. 2002). Unlike the archetypal water megamaser NGC 4258, the maser in NGC 3079 displays significant structure orthogonal to the general elongation and large velocity dispersion

($\sim 30\,\mathrm{km\,s^{-1}}$) in relatively compact areas on the sky ($\sim 0.1\,\mathrm{pc}$). Although no simple rotation law fits the data well, the velocity distribution of the maser emission is consistent with a binding mass of $\sim 10^6\,M_\odot$ and indicates that the pc-scale accretion disk rotates in the same sense as the kpc-scale molecular disk. The maser predominantly traces the approaching side of the disk and thus reveals considerable asymmetry with the blue-shifted emission thereby significantly dominating the detected flux density. In particular, the maser emission extends roughly from 890 to 1190 $\mathrm{km\,s^{-1}}$ with most emission lying between 930 and 1060 $\mathrm{km\,s^{-1}}$. In addition to the main distribution of the maser emission at P.A.$\sim -10°$, Trotter et al. (1998) found two maser features that define a second axis at P.A.$\sim 128°$. Since one of these two maser features coincides on the sky with component C and the other is in close proximity to component B, they may constitute a second population of water masers in which amplification of the continuum components might play a role.

The difficulty in interpreting the maser data has resulted in two very different models for the nuclear region in NGC 3079 (Fig. 5.1). Relying on the apparent alignment of the distribution of the maser emission with the kpc-scale molecular structure, Trotter et al. (1998) proposed a largely north-south, relatively thin, turbulent, and highly-inclined accretion disk for the geometry of the nuclear region (Fig. 5.1). In this model, the dynamical center is located between components A and B, while the maser emission occurs on the surface of the disk in shocks stimulated by the interaction of a nuclear wind with the disk. The asymmetry in blue- and red-shifted flux density is attributed to free-free absorption in the ionized wind, related to the off-axis outflow as traced by components A, B, and C.

The model proposed by Trotter et al. (1998) differs significantly from that

proposed by Sawada-Satoh et al. (2000). According to these authors, the observed velocity drift of the maser feature at $1190\,\mathrm{km\,s^{-1}}$ is much larger than the velocity drift of the other maser features and is due to centripetal acceleration. In a rotating system, only the maser features nearest in projection to the rotation axis are expected to show large velocity drifts. Consequently, the rotation axis would have to pass close to the $1190\,\mathrm{km\,s^{-1}}$ feature and through component B, the proposed location of the dynamical center. In this model (Fig. 5.1), the masers are embedded in a torus of parsec thickness misaligned with respect to the kpc-scale molecular disk by $\sim 110°$. It is not clear why the embedded maser emission should be distributed along the observed locus. However, the outflow axis is misaligned with respect to the minor axis of the pc-scale rotating structure significantly more in the Trotter et al. (1998) model than in the Sawada-Satoh et al. (2000) model.

5.1.2   Motivation

The Trotter et al. (1998) and Sawada-Satoh et al. (2000) models for the nuclear region of NGC 3079 differ primarily in the location of the dynamical center as well as in the thickness and orientation of the rotating structure. It is thus not clear what is the correct geometric model for the inner parsec, what stimulates the maser emission, and why it predominantly traces the regions of the molecular disk approaching the observer. Ambiguity also remains about the connection of the continuum components and the disk and the central engine, about the relationship, if any, between the nuclear activity and the starburst, and about the connection between the pc and kpc-scale outflows in this galaxy. Our study of NGC 3079 is
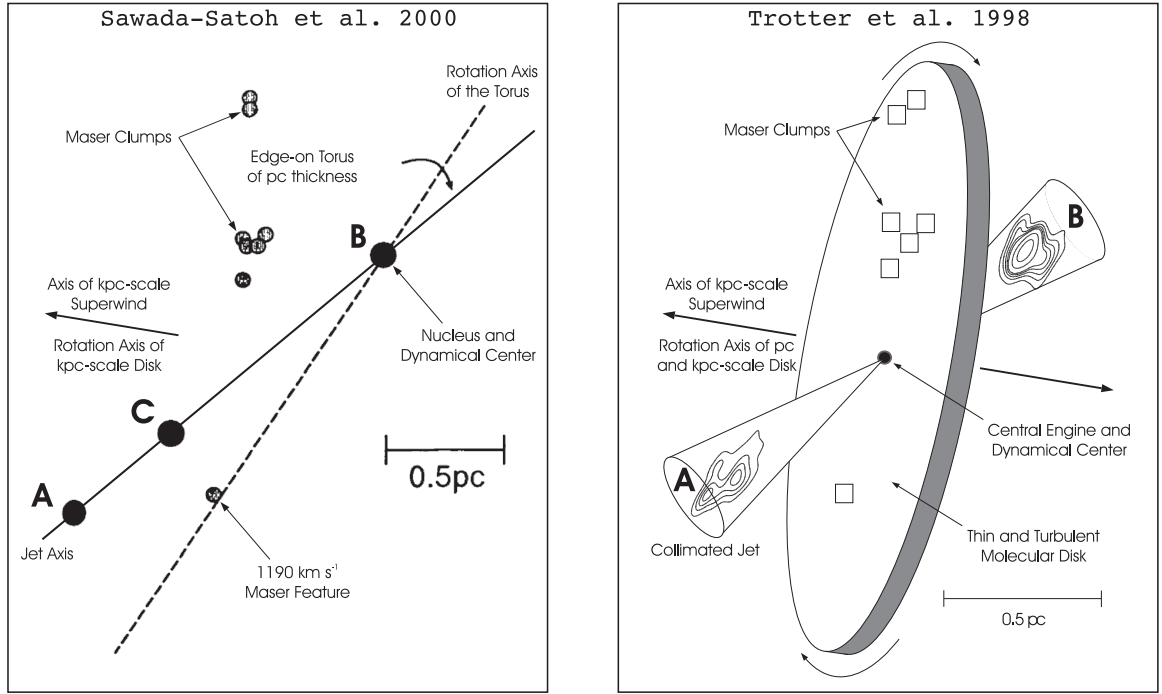
Figure 5.1.— Previously proposed models for the nuclear region of NGC 3079. In the model on the right, reproduced from Trotter et al. (1998), the maser emission occurs in a thin, almost edge-on, and turbulent disk aligned with, and rotating in the same sense as, the kpc-scale molecular disk. In the model shown on the left, adapted from Sawada-Satoh et al. (2000), the maser emission takes place in a very thick, edge-on torus misaligned significantly with respect to the kpc-scale molecular disk. In both models, the outflow takes the form of a collimated jet not well aligned with the axis of the rotating structure.

motivated by these outstanding questions and by the disagreements between the two existing models.

In an effort to better understand the nuclear region in NGC 3079, we attempted to fit a geometric and dynamical model of an inclined, thick, turbulent disk to the maser positions and velocities reported by Trotter et al. (1998). The model not only reproduced the known emission at velocities $930 - 1060 \, \mathrm{km \, s^{-1}}$ but also predicted the existence of emission at velocities $1190 - 1320 \, \mathrm{km \, s^{-1}}$ located roughly south

from the known blue-shifted emission. No previous VLBI observation had explored the velocities above $1222 \, \mathrm{km \, s^{-1}}$. However, Nakai et al. (1995) marginally detected a 0.08 Jy peak at $1267 \, \mathrm{km \, s^{-1}}$ using the 45-m telescope of the Nobeyama Radio Observatory (Fig. 5.2). Motivated by this detection, we imaged with VLBI the water maser emission in NGC 3079 in order to determine whether the red-shifted emission lay south of the blue-shifted emission as predicted by our model. Recently, more red-shifted features have been detected with the Effelsberg 100-m antenna (Hagiwara et al. 2002). In this study, we present the first VLBI map of the red-shifted side of the accretion disk in NGC 3079, and thereby hope to clarify the geometry of the inner-pc.
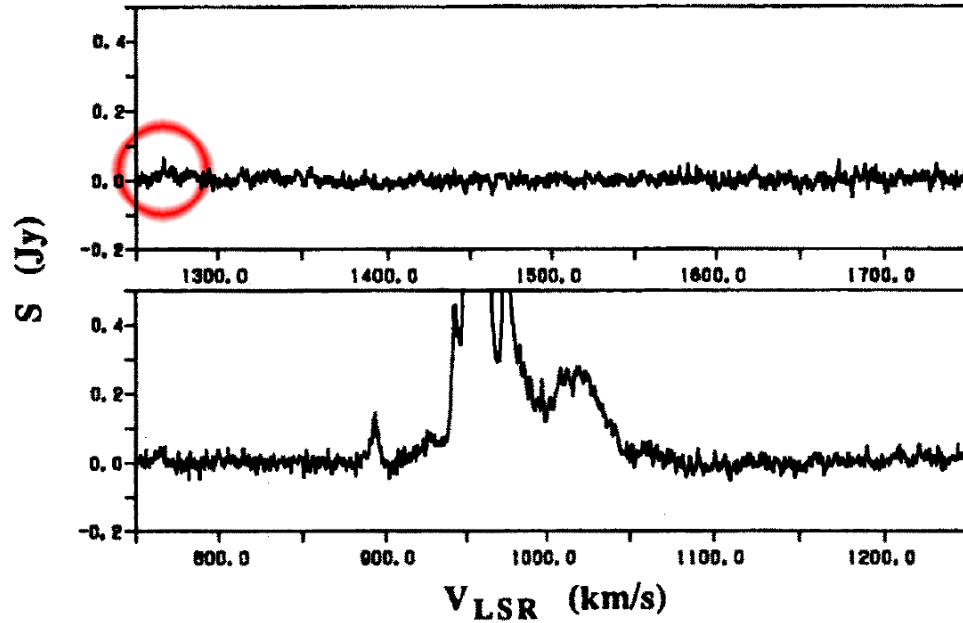
Figure 5.2.— First possible detection of red-shifted water maser emission in NGC 3079. Spectra reproduced from Nakai et al. (1995).

Data calibration and reduction techniques are discussed in Section 5.2. Spectral-line and continuum images of the inner-pc region are presented in Section

5.3. In Section 5.4, we interpret the observed kinematics of the maser in terms of a thick, flared, disordered, self-gravitating, and clumpy pc-scale disk, which orbits a central mass of $\sim 2 \times 10^6 \, M_\odot$ enclosed within 0.4 pc. In this work, we assume that NGC 3079 is at a distance of 17.3 ± 1.5 Mpc (Tully, Shaya, & Pierce 1992), so that 1 mas corresponds to 0.084 pc. All velocities have been computed in accordance with the radio definition of Doppler shift and in the Local Standard of Rest (LSR) frame.

5.2   Observations and Calibration

NGC 3079 was observed in spectral-line mode with the VLBA, augmented by the phased VLA and the Effelsberg (EB) 100-m antenna, for approximately 12 hours on 2001 March 23. The source was observed with 4×16 MHz IF bands, which covered a velocity range of 726 to 1491 km s^{-1}. The 5, 8, and 15 GHz radio continuum observations were made on 1996 December 2 with the VLBA and the VLA phased array. The source was observed with a 32 MHz bandwidth in each polarization and for approximately three hours at each frequency. Both spectral and continuum data were processed with the VLBA correlator at the NRAO[1].

The data were reduced and calibrated with standard continuum and spectral-line VLBI techniques in AIPS[2]. The amplitude calibration for the two experiments included corrections for atmospheric opacity. Antenna gain curves and measurements

---

[1] The National Radio Astronomy Observatory is operated by Associated Universities, Inc., under cooperative agreement with the National Science Foundation

[2] Astronomical Image Processing System

of system temperature were used to calibrate amplitude data for each of the VLBA stations. Amplitude calibration for the VLA was based on VLA scans of 3C286, for which we adopted a 22 GHz flux density of 2.55 Jy, and on bootstrapping of flux densities for VLBI calibrators. To minimize systematic errors due to atmospheric opacity effects, only the VLA scans of VLBI calibrators obtained near the elevation of 3C286 were used in bootstrapping. The data in each polarization were corrected for the effect of time variable source parallactic angle, and the station positions were corrected for motions due to plate tectonics by utilizing the US Naval Reference Frame solutions 9810 and 9513.

In the 5, 8, and 15 GHz data, the residual delays and fringe rates due to the troposphere and clock uncertainties were removed via observations of calibrators 4C39.25, 3C273, OJ287, and OQ208. The final images of the nuclear region of NGC 3079 were obtained through application of self-calibration. In the spectral data, the complex bandpass shape and any electronic phase difference between the IF bands were removed by observation of calibrators 4C39.25, 1150+812, 1308+326, and 3C345. The position of the maser was corrected by a fringe rate analysis of 10 spectral channels including the brightest spectral feature at $956 \, \mathrm{km \, s^{-1}}$ with the result: $\alpha_{2000} = 10^h 01^m 57\overset{s}{.}802 \pm 0.001$, $\delta_{2000} = 55°40'47\overset{''}{.}26 \pm 0.01$. Phase and amplitude fluctuations due to troposphere and clock uncertainties were removed by self-calibration of the brightest maser feature at $956 \, \mathrm{km \, s^{-1}}$ and application of the resulting solution to all spectral channels in all IF bands. After calibrating and imaging the spectral-line data set, the relative positions of the maser features were obtained by fitting two-dimensional elliptical Gaussians to the distribution of the maser emission in each spectral channel. We obtained a continuum image at 22 GHz

by averaging all line-free frequency channels. Table 5.1 lists beam dimensions and noise levels at each frequency. Table 5.2 lists the properties of all spectral-line observations of the water maser with the VLBA. The experiment presented in this study images the widest velocity range of emission among all VLBA observations made to-date.

Table 5.1: Half-power beam dimensions and noise levels.

Frequency (GHz)	Major (mas)	Minor (mas)	P.A. (°)	RMS (mJy beam^{-1})
5	3.6	2.4	14	0.060
8	2.0	1.3	29	0.055
15	2.0	1.3	−89	0.11
22	0.30	0.26	−43	0.14[a], ~ 2.3[b]

[a] continuum

[b] spectral-line for a channel width of $0.42\,\mathrm{km\,s^{-1}}$.

Table 5.2: VLBA studies of the water maser in NGC 3079.

	Trotter et al. 1998	Sawada-Satoh et al. 2000, 2002			This study
Date	1995 Jan 9	1996 Oct 20	1997 Mar 7	1997 Oct 2	2001 Mar 23
V Range[a]	$880 - 1204$	$590 - 1008$	$832 - 1222$	$832 - 1222$	$726 - 1491$
ΔV[b]	0.21	0.42	0.42	0.42	0.42
σ[c]	0.22	0.54	0.24	0.49	0.14
σ[d]	2.8	6.6	5.8	7.9	2.3

[a] Total velocity coverage in $\mathrm{km\,s^{-1}}$

[b] Channel spacing in $\mathrm{km\,s^{-1}}$

[c] RMS noise level in the pseudo continuum image in Janskys

[d] RMS noise level in the spectral-line image in Janskys

To estimate the fraction of the power imaged by the interferometer, we acquired a single-dish spectrum of NGC 3079 (see Fig.5.3) by position-switching in a single

polarization mode with the NASA Deep Space Network 70-m antenna in Robledo, Spain, on 2003 February 4, using an observing setup similar to that described in Greenhill et al. (2003). After integrating for a total of 2.5 hours, we achieved an RMS noise level in the spectrum of 11 mJy for 1.3 $\mathrm{km\,s^{-1}}$ channel spacing. The antenna gain curve was obtained in a single track by measurement of the elevation dependence of 1308+326 antenna temperature, corrected for atmospheric opacity estimated from a tipping scan. The antenna efficiency was estimated to be 0.43 ± 0.01 based on several measurements of antenna temperature for 3C286. From the RMS deviation of our gain measurements about the best fit polynomial and the formal uncertainty in the efficiency, we estimate that the gain calibration of the antenna is accurate to within 10%.

5.3   Results

5.3.1   Maser

In agreement with previous observations of NGC 3079, we found that the maser exhibits a conspicuous asymmetry whereby the blue-shifted emission significantly dominates the detected flux density (Fig. 5.3). The spectrum of the imaged power agrees satisfactorily with the spectrum detected with the Effelsberg 100-m antenna 10 days prior to the VLBI observation (see Fig.2c in Hagiwara et al. 2002). The observation with the NASA Deep Space Network 70-m antenna in Robledo, Spain, conducted 1.9 years later showed significant flux variability throughout the spectrum except for the strongest feature (Fig. 5.3). Such variations, however, are not unusual
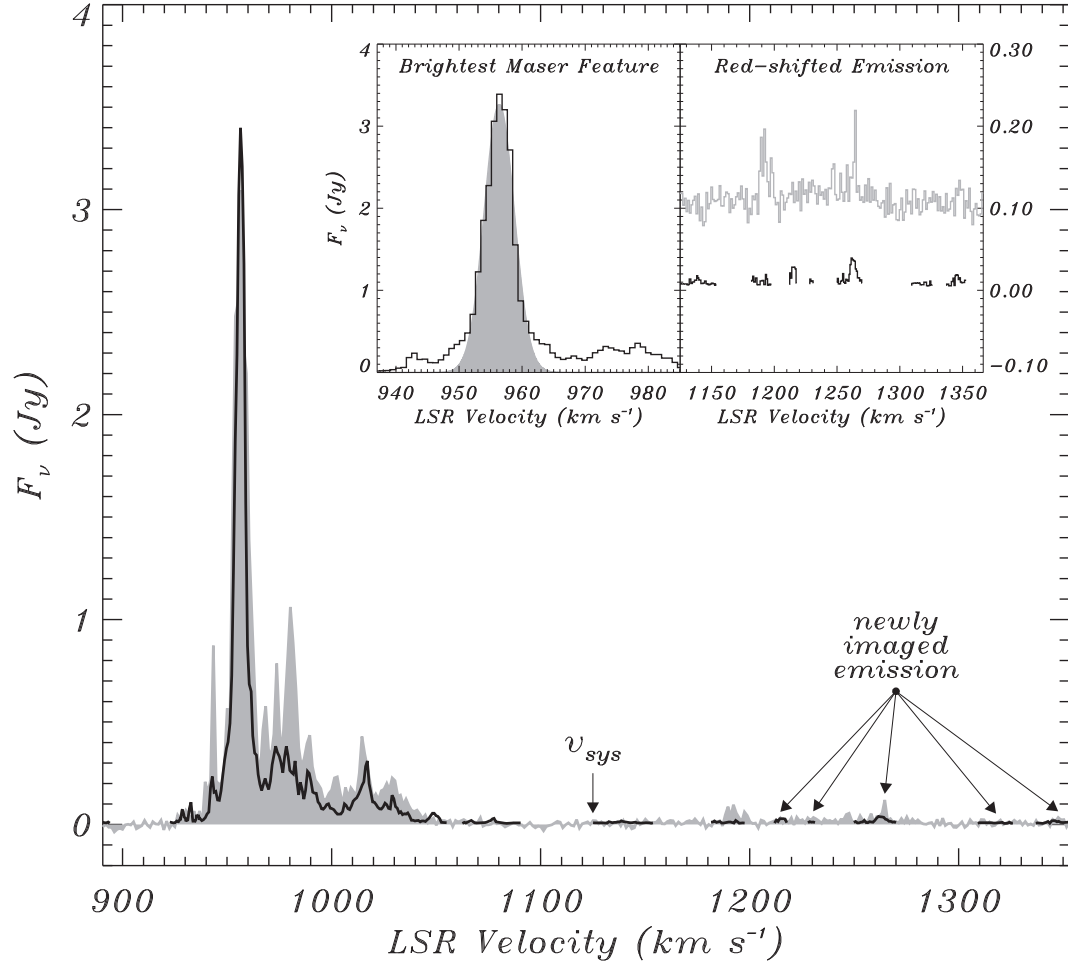
Figure 5.3.— Imaged-power and total-power spectra of the maser in NGC 3079. The total power spectrum (gray) was obtained by position-switching with a 70-m Deep Space Network antenna in Robledo, Spain on 2003 February 4. The spectrum of the imaged power (black line) is based on the VLBI observation conducted on 2001 March 23 and was computed by summing the flux densities of the individual maser spots. *(left inset)* Imaged power spectrum (black) of the brightest maser feature at $\sim 956\,\mathrm{km\,s^{-1}}$ and a Gaussian fit to the main peak (gray) corresponding to an isotropic luminosity of $131\,L_{\odot}$. *(right inset)* Total and imaged power spectra of the red-shifted emission with the vertical scale expanded and the total power spectrum shifted upward to facilitate comparison. The vertical arrow indicates the systemic velocity of the galaxy ($1125\,\mathrm{km\,s^{-1}}$).

since single-dish monitoring of the maser has revealed substantial flux variability on timescales of years (Nakai et al. 1995; Baan & Haschick 1996; Hagiwara et al. 2002).
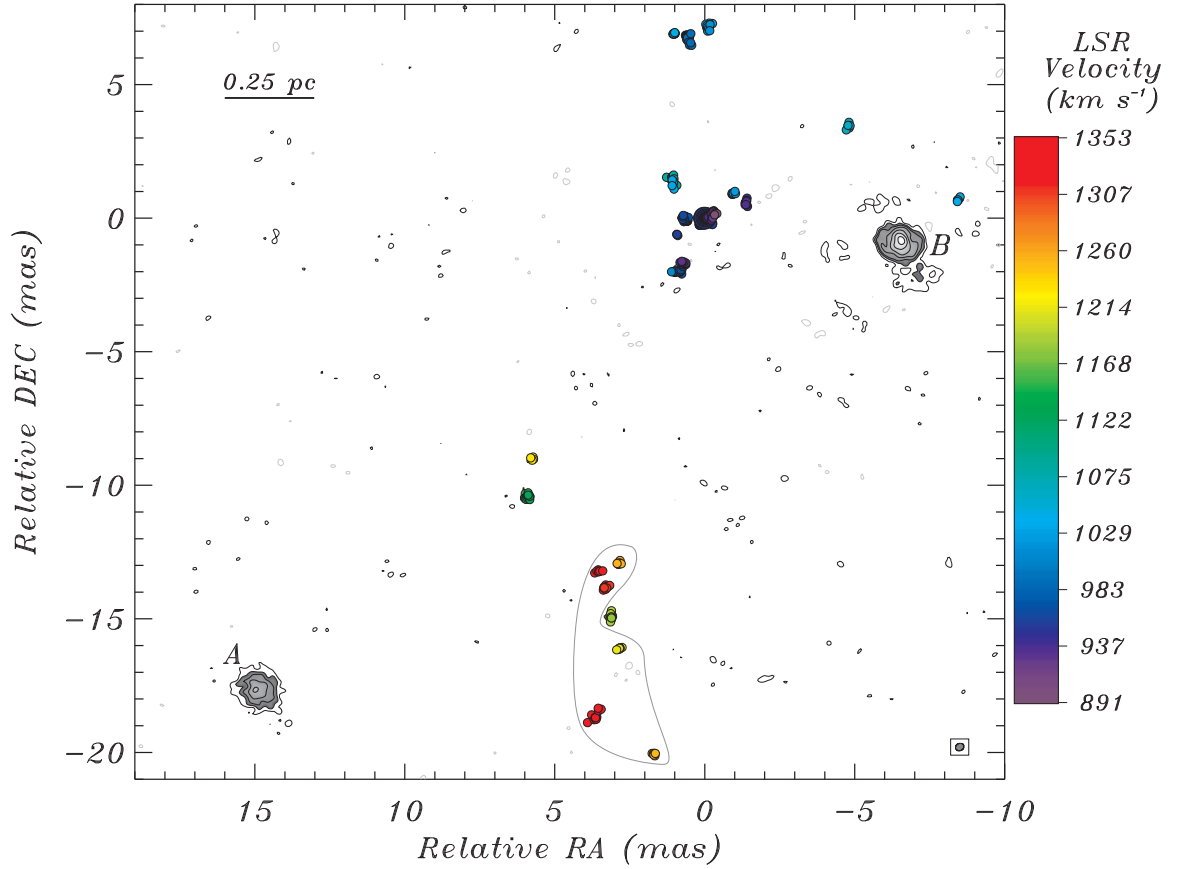
Figure 5.4.— Distribution of maser emission (colored spots) and of the 22 GHz continuum (gray contours) in the nuclear region of NGC 3079. The color of the maser spots indicates line-of-sight velocity in accordance with the bar on the right. The continuum contour levels are $-3\sigma, 3\sigma, 5\sigma \times 2^{k/2}$ where $\sigma = 0.14\,\mathrm{mJy\,beam^{-1}}$ and $k = 0, 1, 2, 3, \ldots$. Contours above 5σ are shaded. The gray curve encloses the newly imaged emission while the ellipse in the bottom right corner of the figure illustrates the resolution beam.

As with the previous investigations (Trotter et al. 1998; Sawada-Satoh et al. 2000), we found that the maser emission is distributed in a disordered linear structure at P.A.$\sim -10°$ (Fig. 5.4). Furthermore, the distribution of emission on the sky is clearly segregated by velocity with emission blue- and red-shifted with respect to the systemic velocity located in the northern and southern section of the image, respectively. To determine temporal changes in the maser distribution,
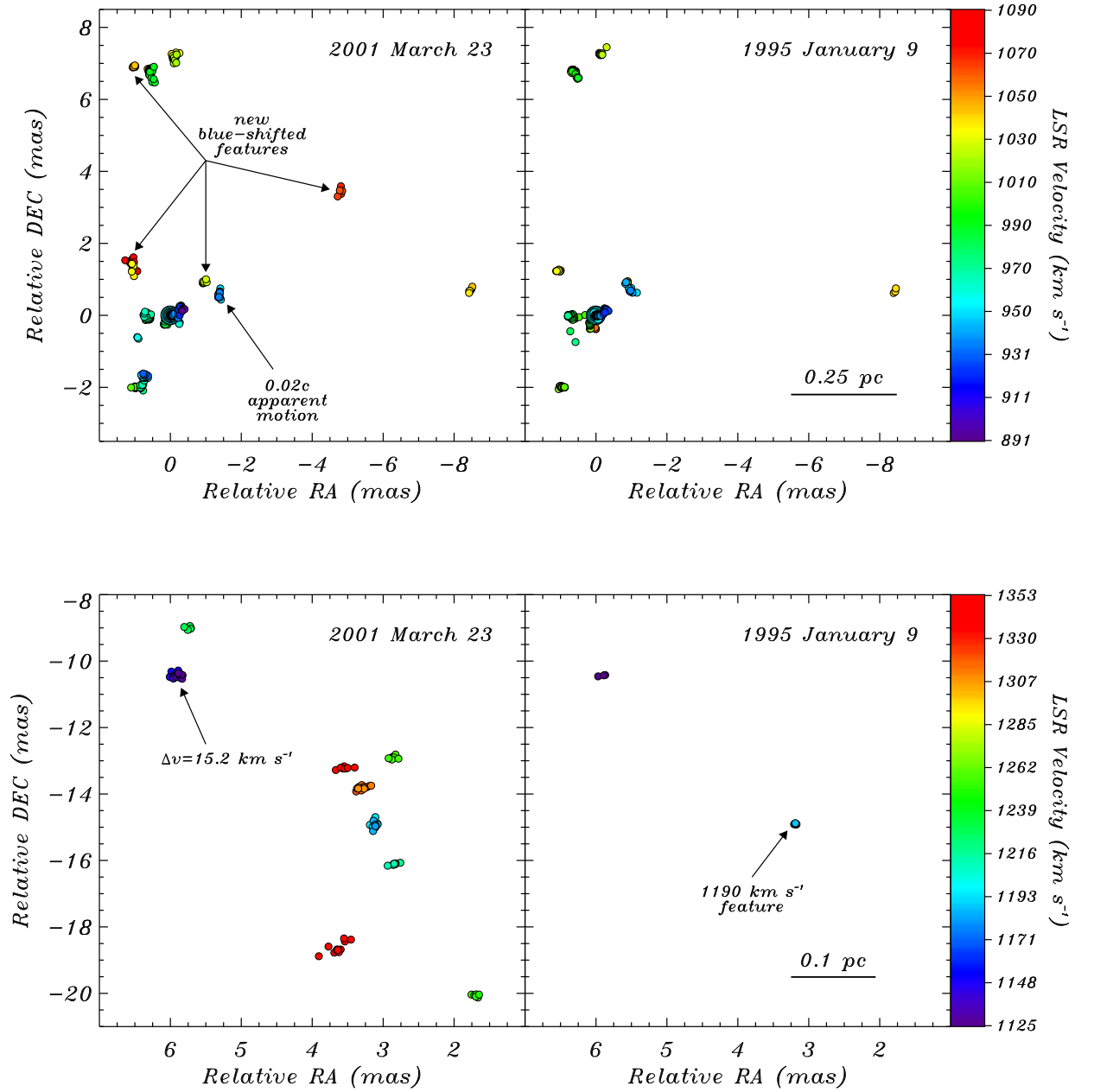
Figure 5.5.— Angular distribution of the water maser emission in NGC 3079 obtained on 1995 January 9 (Trotter et al. 1998) and on 2001 March 23 (this study). The upper and lower two panels show emission blue- and red-shifted with respect to the systemic velocity, $1125\,\mathrm{km\,s^{-1}}$, respectively. The velocity and angular scales are expanded to facilitate comparison between the two epochs.

we compared the maser positions obtained here with those of Trotter et al. (1998).
Both the 1995 January 9 (Trotter et al. 1998) and the 2001 March 23 (this study)
epochs were calibrated by referencing the phases of all spectral channels to the
brightest maser feature at $\sim 956\,\mathrm{km\,s^{-1}}$ and thereby are most likely registered to
the same volume of masing gas. Indeed, three-dimensional flux density-weighted
correlation of the distribution of the maser emission presented in this study with
that presented in Trotter et al. (1998) indicates that the two epochs are aligned to
within $\sigma = 3.2\,\mathrm{km\,s^{-1}}$ in velocity and are registered by the self-calibration technique
to within $\sigma = 0.5\,\mathrm{mas}$ on the sky (0.5 mas corresponds to a transverse speed of
$0.02\,c$ over 6.25 years and is not an intrinsic measurement limit on the maser proper
motions). In fact, spectra of nearly half of the maser emission clumps imaged in
both Trotter et al. (1998) and this study peak within $3.2\,\mathrm{km\,s^{-1}}$ of each other, which
is comparable to the $\sigma = 2.4\,\mathrm{km\,s^{-1}}$ half width of the brightest maser feature (Fig.
5.3). The comparison of the two epochs (Fig. 5.5) indicates that 1) the newly imaged
red-shifted emission is confined to a region south to south-west from the previously
known blue-shifted features, 2) several new blue-shifted features have appeared, 3)
the maser feature located at $(5.9, -10.5)\,\mathrm{mas}$ appears to have drifted in velocity from
$1123\,\mathrm{km\,s^{-1}}$ to $1139\,\mathrm{km\,s^{-1}}$, a change of $\sim 16\,\mathrm{km\,s^{-1}}$ in 6.25 years, and 4) the maser
feature located at velocity $\sim 940\,\mathrm{km\,s^{-1}}$ and at position $(-1.4, 0.7)\,\mathrm{mas}$ appears to
have moved westward with velocity of $\sim 0.02\,c$ ($\sim 6000\,\mathrm{km\,s^{-1}}$). The latter two cases
might each be due to variability of separate and distinct gas clumps rather than
physical motions. Note that the maser feature that has drifted in velocity between
Trotter et al. (1998) and this study is significantly displaced on the sky from the
$\sim 1190\,\mathrm{km\,s^{-1}}$ maser feature (located at $3.1, -14.9\,\mathrm{mas}$), on whose velocity drift the

model of Sawada-Satoh et al. (2000) depends. Based on the Trotter et al. (1998) and Hagiwara et al. (2002) studies, we place an upper limit of $0.5\,\mathrm{km\,s^{-1}\,yr^{-1}}$ on the velocity drift of the $\sim 1190\,\mathrm{km\,s^{-1}}$ feature.
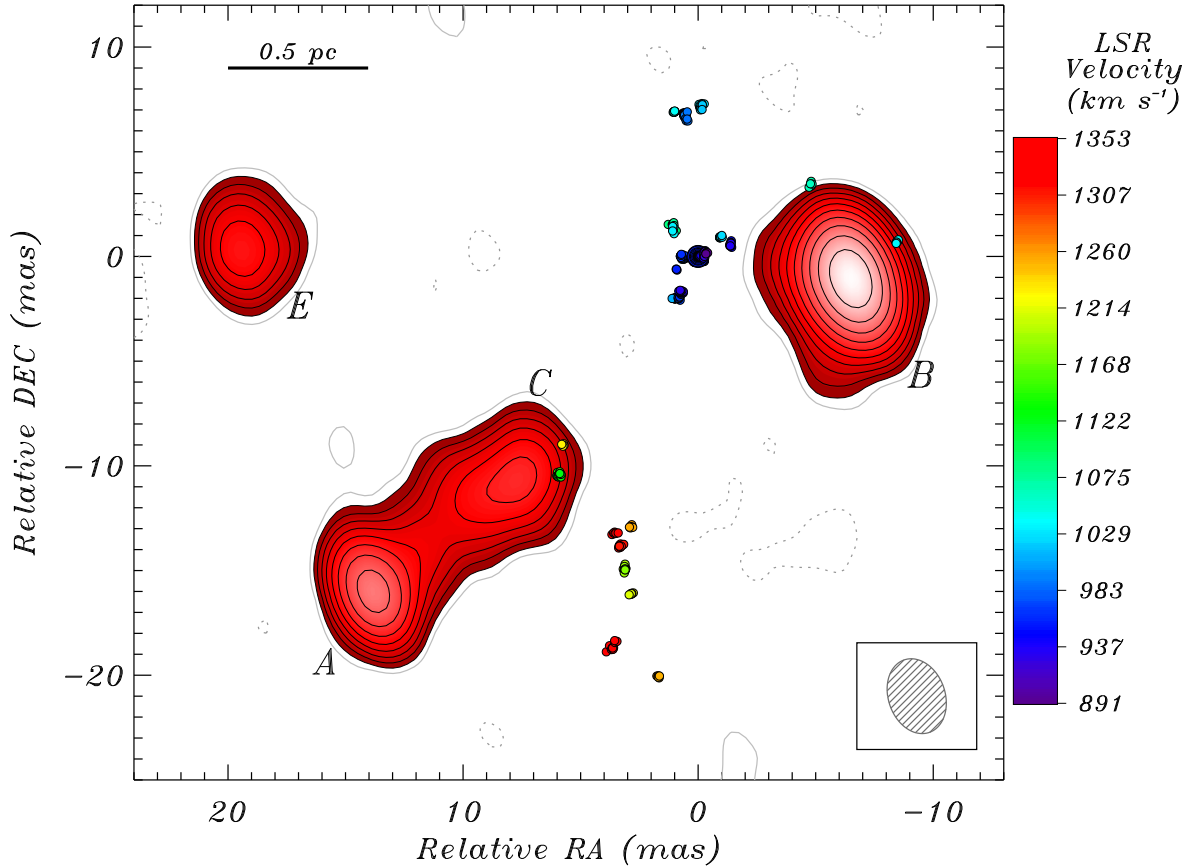
Figure 5.6.— Contours of the 5 GHz continuum drawn at levels -2σ, 4σ, $6\sigma \times 2^{k/2}$ where $\sigma = 0.060\,\mathrm{mJy\,beam^{-1}}$ and $k = 0, 1, 2, 3, \ldots$. Contours above 6σ are shaded. Compact component D detected by Trotter et al. (1998) at 5 GHz with flux density of $4.3 \pm 0.5\,\mathrm{mJy}$ would be located at $(38.3, -31.9)\,\mathrm{mas}$ in the above plot but was not detected at a level of $6\sigma = 0.36\,\mathrm{mJy}$. The maser features shown here as small filled circles were registered to the 5 GHz continuum by aligning the positions of component B at 5 and 22 GHz. The uncertainties in this registration are 0.02 mas and 0.03 mas in RA and DEC, respectively. The conversion from the color of the maser spots to their line-of-sight velocity is given by the bar on the right. Beam dimensions are shown in the bottom right corner.
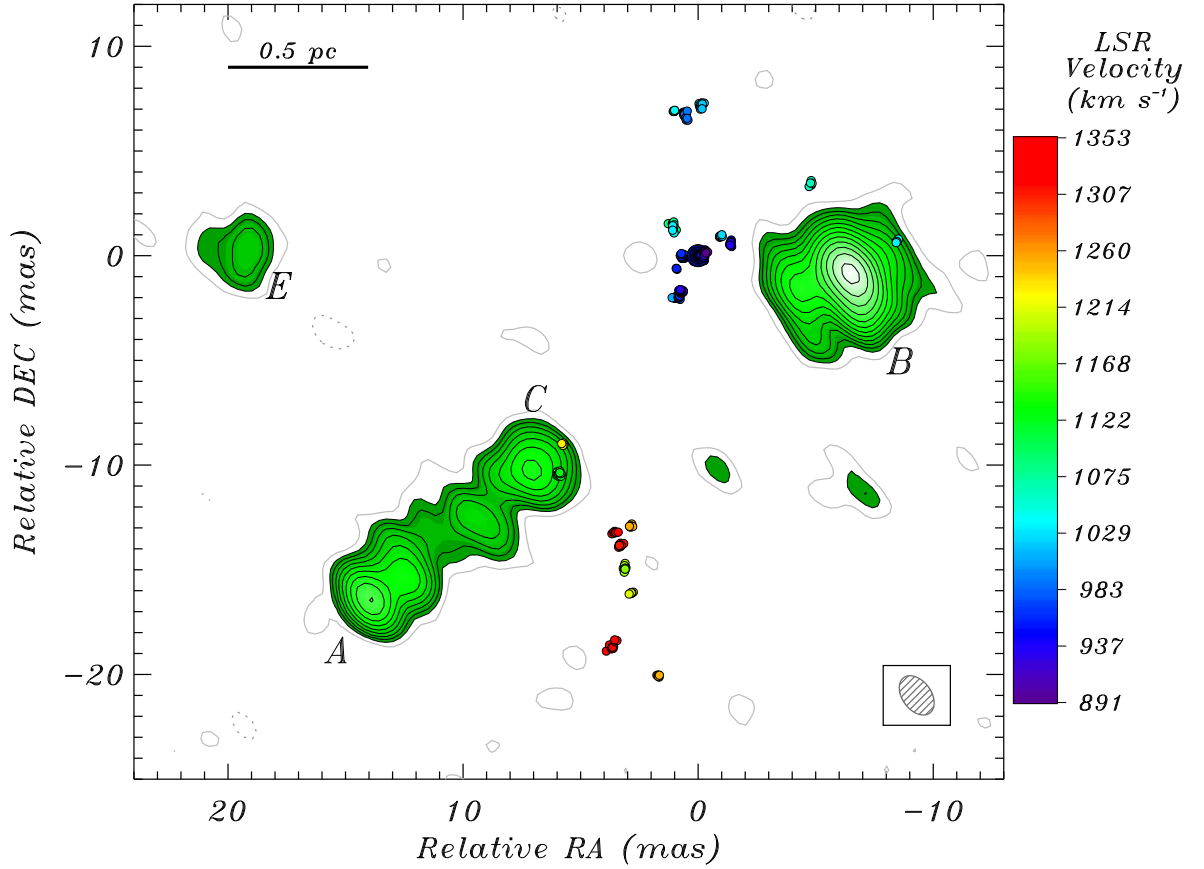
Figure 5.7.— Contours of the 8 GHz continuum drawn at levels -3σ, 3σ, $6\sigma \times 2^{k/2}$ where $\sigma = 0.055\,\text{mJy beam}^{-1}$ and $k = 0, 1, 2, 3, \ldots$. Contours above 6σ are shaded. The maser features are shown using small filled circles color coded by velocity in accordance with the bar on the right. The registration of the maser to the 8 GHz continuum was achieved by aligning the positions of component B at 8 and 22 GHz. The uncertainty in this registration is 0.01 mas in both RA and DEC. The ellipse in the bottom right corner of the figure illustrates beam dimensions.

5.3.2   Continuum

Components A and B were detected at all frequencies while component C was detected at 5, 8, and 15 GHz, but not at 22 GHz (Fig. 5.6, 5.7, 5.8, and 5.4). In agreement with previous reports, components A, B, and C are collinear along the position angle of $\sim 126°$. To estimate the flux density, position, and position
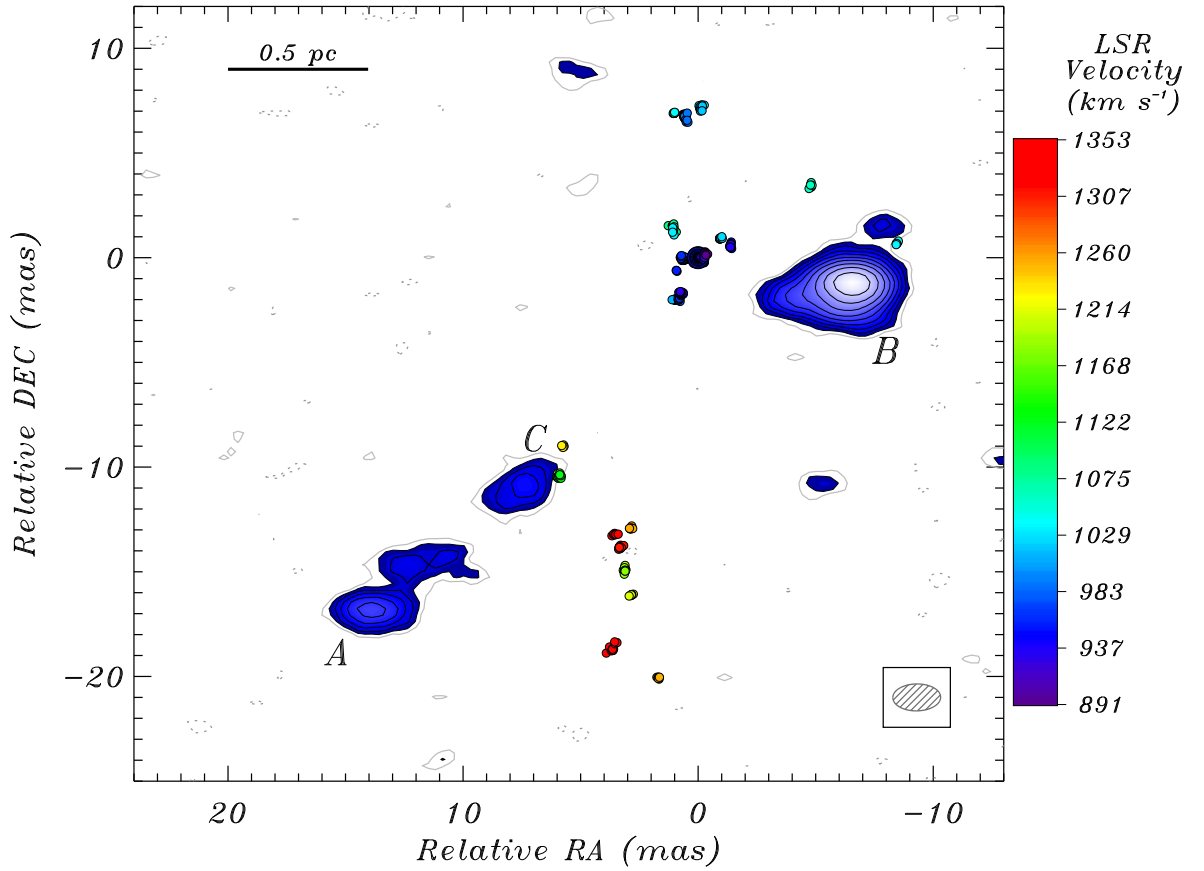
Figure 5.8.— Contours of the 15 GHz continuum drawn at levels -2σ, 4σ, $6\sigma \times 2^{k/2}$ where $\sigma = 0.11\,\mathrm{mJy\,beam}^{-1}$ and $k = 0, 1, 2, 3, \ldots$. Contours above 6σ are shaded. Superposed on top of the continuum are the maser features registered to the 15 GHz continuum by aligning the positions of component B at 15 and 22 GHz. The uncertainty in this registration is 0.01 mas in both RA and DEC directions. The bar on the right indicates the relationship between the color and the velocity of the maser features. Beam dimensions are shown in the bottom right corner of the figure.

uncertainty of each continuum component, we fitted multiple two-dimensional Gaussian model components to the emission peaks at each frequency (Table 5.3). In agreement with previous reports (e.g., Sawada-Satoh et al. 2000) and supplementing our data with published positions, we found that the systematic motion of component A at 22 GHz is consistent with a transverse speed of $0.12 \pm 0.02\,c$ along P.A. of $\sim 126° \pm 5°$, which is approximately away from component B (Fig.5.9). Note that

the change (typical magnitude of $\sim 0.35\,\text{mas}$) from epoch to epoch in the position

of component B with respect to the reference maser feature does not appear to be

systematic and is inconsistent with formal measurement uncertainties (Fig. 5.9).

This observed scatter might be due to the change in morphology or position of either

component B or the reference maser feature. However, the time average position of

component B is approximately stationary with respect to the maser emission. We

emphasize that the jitter of component B, like the motion of E in the direction of B

reported by Middelberg et al. (2003), might not be a real but an apparent motion

due to changing source characteristics in a flow or across shocks (e.g., Kellermann et

al. 2004).

Table 5.3: Characteristics of continuum components at 5, 8, 15, and 22 GHz obtained
by two-dimensional multiple component Gaussian fits to emission features.

Frequency (GHz)	Component	S_ν (mJy)	R (mas)	ϕ (°)	Major (mas)	Minor (mas)	P.A. (°)
5	B	13.4 ± 0.4	—	—	3.63 ± 0.07	1.62 ± 0.03	19 ± 1
	A	4.7 ± 0.3	25.25 ± 0.05	126.5 ± 0.1	3.0 ± 0.1	1.60 ± 0.07	20 ± 3
	C	3.6 ± 0.5	17.8 ± 0.1	123.5 ± 0.4	3.4 ± 0.4	2.7 ± 0.3	109 ± 19
	E	2.8 ± 0.6	25.9 ± 0.2	85.5 ± 0.5	4.0 ± 0.7	2.7 ± 0.4	32 ± 17
8	B	32.4 ± 0.2	—	—	2.89 ± 0.01	1.87 ± 0.01	24.2 ± 0.3
	A	11.5 ± 0.2	25.07 ± 0.02	126.94 ± 0.03	3.11 ± 0.04	2.31 ± 0.03	140 ± 2
	C	9.7 ± 0.3	16.81 ± 0.03	124.4 ± 0.1	4.5 ± 0.1	2.58 ± 0.06	135 ± 2
	E	2.5 ± 0.2	25.90 ± 0.06	87.4 ± 0.2	2.9 ± 0.2	2.5 ± 0.2	175 ± 20
15	B	27.3 ± 0.3	—	—	2.71 ± 0.02	1.95 ± 0.02	97.6 ± 0.6
	A	7.8 ± 0.5	24.84 ± 0.09	127.2 ± 0.2	4.6 ± 0.3	2.3 ± 0.1	128 ± 3
	C	3.7 ± 0.4	16.91 ± 0.09	124.6 ± 0.3	3.0 ± 0.2	2.0 ± 0.2	130 ± 7
22	B	40 ± 1	—	—	1.09 ± 0.03	0.88 ± 0.03	31 ± 6
	A	28 ± 2	27.14 ± 0.03	127.96 ± 0.06	1.24 ± 0.06	1.08 ± 0.05	24 ± 14

Note. — Angular separation R and position angle ϕ are measured with respect to component B at each frequency. The 5, 8, and 15 GHz data were acquired on 1996 February 12 while the 22 GHz data were obtained on 2001 March 23. Component D ($S_\nu = 4.3 \pm 0.5\,\text{mJy}$) at position $r = 54.5 \pm 0.4\,\text{mas}$ and $\phi = 124.7° \pm 0.4°$ and detected by Trotter et al. (1998) was not detected at a level of $6\sigma = 0.36\,\text{mJy}$ in this study. One mas corresponds to 0.084 pc.

We confirmed the spectral turnover reported by Trotter et al. (1998) of

components A and B and constrain the frequency of this turnover to the range
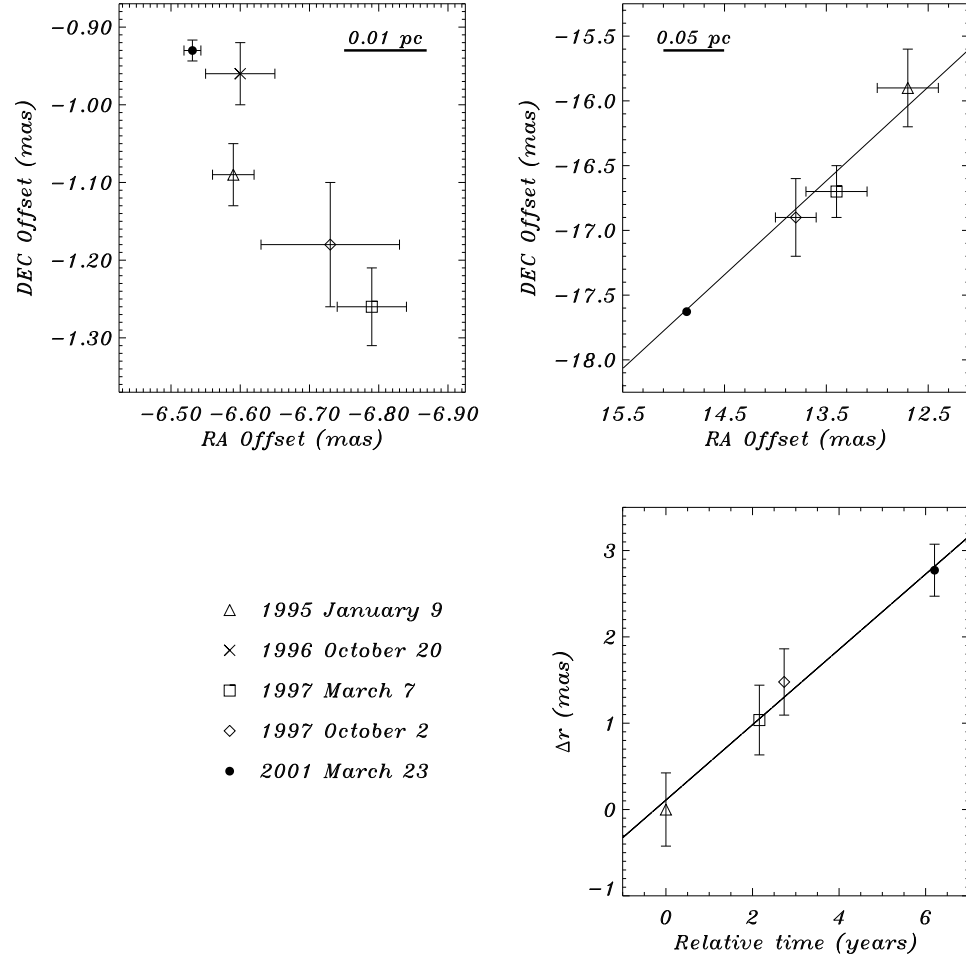
Figure 5.9.— *(left)* Position of component B with respect to the reference maser feature. The small scatter (typical magnitude of $\sim 0.35\,$mas) in the relative position of component B is not consistent with formal measurement uncertainties and might be due to morphological or positional changes in the reference maser feature or in component B itself. *(top right)* Position of A with respect to the reference maser feature. A fit to the four measured positions indicates that A is moving along P.A. $\sim 126° \pm 5°$, effectively away from component B. *(bottom right)* Temporal motion of A along the linear trajectory in the top right panel, consistent with a transverse speed of $0.12 \pm 0.02\,c$. The 1995 January 9 epoch was obtained from Trotter et al. (1998), epochs 1996 October 20, 1997 March 7, and 1997 October 2 are from Sawada-Satoh et al. (2002), while 2001 March 23 epoch is from this study. For points where error bars are not visible, the errors are smaller than the plotting symbol.

between 5 and 15 GHz (Fig. 5.10). To place more stringent constraints on the turnover frequencies, we considered two simple spectral models for each component. In the first model, we assumed that at lower frequencies the spectra are dominated by synchrotron self-absorption ($S_\nu \propto \nu^{5/2}$) intrinsic to the source, while at higher frequencies the spectra are determined by optically-thin synchrotron emission ($S_\nu \propto \nu^\alpha$) also internal to the source. Under these assumptions, the spectra of components A and B can be characterized by $S_\nu = a\nu^{5/2}(1 - e^{-b\nu^{\alpha-5/2}})$, where a, b, and α are parameters of the model. The flux densities measured at three frequencies for each component uniquely determine the three parameters of the model, which yielded $\alpha = -1.5$ and -1.1, and turnover frequencies (i.e., frequency of maximum flux density) of 9.0 and 9.6 GHz for components A and B, respectively. For the data reported by Trotter et al. (1998), we obtained $\alpha = -1.5$ and -1.3, and turnover frequencies of 9.1 and 9.0 GHz for components A and B, respectively. However, if free-free absorption ($\tau_\nu \propto \nu^{-2.1}$) extrinsic to the source dominates at lower frequencies instead of synchrotron self-absorption, then the spectra of components A and B can be modelled by $S_\nu = a\nu^\alpha e^{-\beta\nu^{-2.1}}$ (e.g., Bicknell, Dopita, & O'Dea 1997; Tingay & Murphy 2001). For this model, we obtained $\alpha = -1.8$ and -1.3 as well as turnover frequencies of 8.7 and 9.5 GHz for components A and B, respectively. Similarly, the flux densities reported by Trotter et al. (1998) yielded $\alpha = -1.8$ and -1.6 as well as peak locations of 8.8 and 8.7 GHz. Thus, for both models and for both data sets, spectral turnover frequencies lie in the range $8 - 10$ GHz.

The spectra of components A and B are reminiscent of spectra of gigahertz peaked spectrum (GPS) sources, as already noted by Trotter et al. (1998). These sources are thought to arise from regions where jets interact with the dense

ambient gas (e.g., Bicknell et al. 1997). Their spectra peak in the frequency range of $0.1 - 10$ GHz with high-frequency spectral indices of $-1.3 \lesssim \alpha \lesssim -0.5$ and low-frequency indices of $\alpha \sim 1$. Because of the similarity between the two components and the GPS sources, we suggest that components A and B arise in regions where a relativistic outflow is interacting with a dense ambient medium. Since components A and B consist of multiple components and do not exhibit a flat spectrum, neither A nor B is likely to be a jet core (cf. Sawada-Satoh et al. 2000).

Trotter et al. (1998) reported a detection at 5 GHz with SNR of 39 of a compact 4.3 ± 0.5 mJy component (D) located ~ 4 pc southeast of B and collinear with components A, B, and C. However, we found no evidence above 0.36 mJy (6σ) level of this component at 5 GHz. Since the 5 GHz beam area of Trotter et al. (1998) was $2.4\times$ larger than the 5 GHz beam area in our study, the non-detection of D could be due to either resolution effects or source variability. Component D was also not detected at 5 GHz by Middelberg et al. (2003).

The continuum images at 5 and 8 GHz revealed a new component (E) that is not collinear with previously known components A, B, C, and D (Fig. 5.6 and Fig. 5.7). We detected component E with signal-to-noise ratios (SNR) of 31 and 16 at 5 and 8 GHz, respectively (Kondratko et al. 2000). Middelberg et al. (2003) confirmed the detection of E and also reported identification at 1.7 and 2.3 GHz of a new component F located roughly 3.7 pc from component B along P.A. of $\sim 100°$. Since the beam size in the Trotter et al. (1998) study was larger than the beam size in our study, component E should have been detected by Trotter et al. (1998) with a SNR of at least 17 at 5 GHz if its flux density were constant. The failure of Trotter et al. (1998) to detect E indicates that the source is most likely time
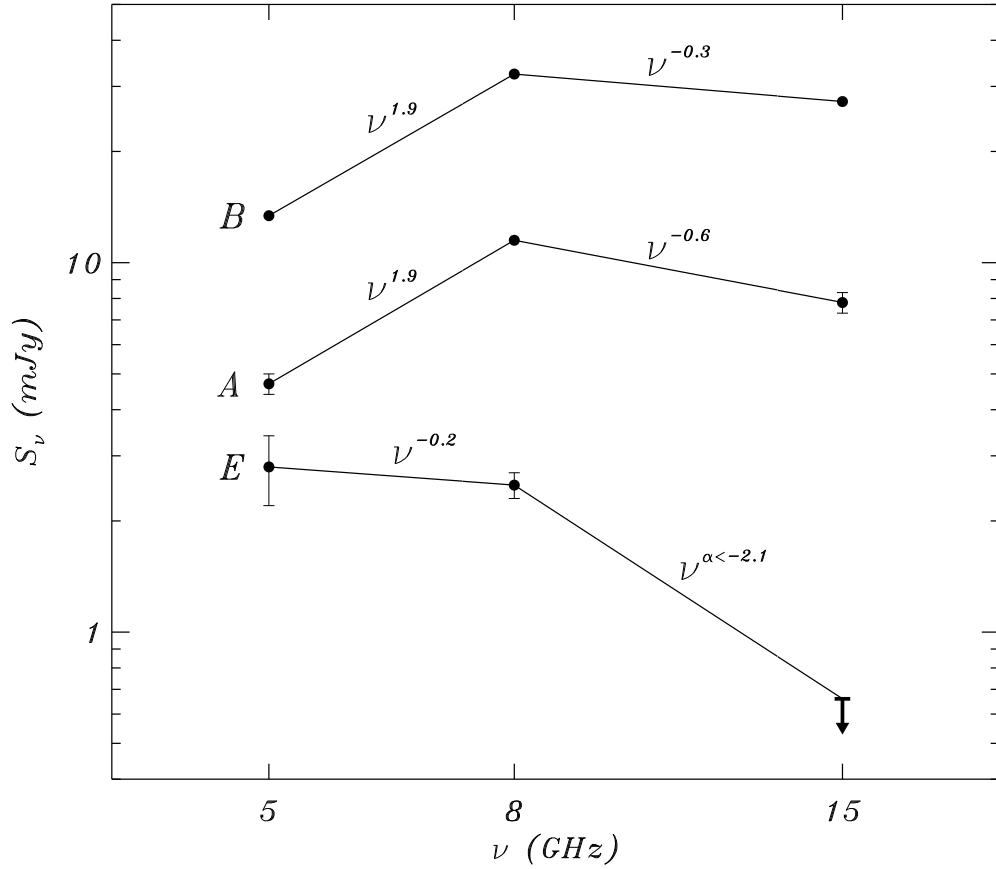
Figure 5.10.— Spectra of continuum components A, B, and E and corresponding spectral indices α, where $S_\nu \propto \nu^\alpha$. The arrow indicates an upper limit on the flux density of component E at 15 GHz. The effect of resolution on the spectral index is probably small because the beam dimensions at the three frequencies are comparable (Table 5.1). Flux densities of the continuum components at 22 GHz are not shown because they were obtained at a different epoch, and the emission is known to be time variable.

variable. Indeed, comparison of our results with those of Trotter et al. (1998) reveals variation in the flux density of continuum component A at 22 GHz by a factor of ~ 5 over 6.2 years. If we compare the results of Sawada-Satoh et al. (2000) and of this study, the variation in the flux density of component A at 22 GHz could have been as large as a factor ~ 52 over 4.4 years (we note that, although Sawada-Satoh et al. (2000) 22 GHz beam is larger, they fail to detect component A). In both cases, the

time-scale of variability is greater than the light travel time within the components

(< 2 yr).

Our flux density estimates for component E indicate a spectral index of $\alpha = -0.2$

between 5 and 8 GHz and a spectral index of $\alpha < -2.1$ between 8 and 15 GHz

(Fig.5.10). The high-frequency decline in the flux density of component E is too

steep to be consistent with optically-thin synchrotron emission ($\alpha = (1-p)/2$), since

it would require $p > 5.2$, much greater than the normally assumed value of $p \sim 2.4$,

where p is the power law index on the electron energy distribution ($N(E) \propto E^{-p}$).

However, for a situation where there is no continuous injection of electrons into the

synchrotron source and the pitch angle distribution remains conserved, the cooling

of high-energy electrons leads to a spectral index of $\alpha = -(2p+1)/3$ above a break

frequency $\nu_b = [B/(1 \text{ G})]^{-3}[t/(1 \text{ yr})]^{-2}$ GHz (Kardashev 1962). Hence, nominally,

a field of ~ 40 mG would give $\nu_b \sim 10$ GHz after a cooling time of ~ 40 years, the

travel time of component E at $0.12\,c$ from the central engine (refer to Section 5.4.1).

A value of $p > 2.6$ would be required to give a spectral index of $\alpha < -2.1$ above the

break frequency, consistent with our observations. Using the same magnetic field

and extending the cooling time by ~ 5.8 years (i.e., the time difference between the

two studies), we estimate a break frequency at the observing epoch of Middelberg

et al. (2003) to be ~ 8 GHz, consistent with their detection of E at 5 GHz and

non-detection of E at 15 GHz. We note that their spectrum appears to be shifted to

lower frequencies because it peaks between 1.7 and 5 GHz rather than between 5 and

8 GHz as in our study. This shift is consistent with an adiabatic expansion of the

rapidly cooling synchrotron source, for a source lifetime of ~ 40 years, $p \sim 2.6$, and

the ratio of the turnover frequencies of ~ 1.4 (corresponding to a shift of roughly

1.5 GHz; note that turnover frequency is different from ν_b; Eq. 13.27 of Kellermann & Verschuur 1988).

5.4   Discussion

In what follows, we propose that the inner parsec in NGC 3079 contains a nearly edge-on, massive, thick, and flared disk. The disk orbits a mass of $\sim 2 \times 10^6 \, M_\odot$ enclosed within 0.4 pc, most likely a supermassive black hole, and it is aligned with the kpc-scale molecular disk. The disk is most likely self-gravitating, clumpy, and forming stars. Accretion onto the black hole drives a jet that is misaligned with the disk rotation axis and is interacting with the dense ambient medium. The presence of off-axis aging synchrotron components may suggest the jet changes orientation. The jet may coexist with a pc-scale wide-angle outflow, which is inferred from the observation of masers at high latitudes above the disk and which might be related to the known kpc-scale superbubble.

5.4.1   Analysis of Maser Kinematics

The Disk Major Axis and the Dynamical Center

The largely north-south linear distribution of the maser emission, aligned with the kpc-scale molecular disk, as well as the segregation of the blue- and the red-shifted emission on the sky are suggestive of a nearly edge-on pc-scale molecular disk. A fit to the angular distribution of maser emission yields the following disk major axis: $\alpha(\mathrm{mas}) = (-0.17 \pm 0.06) \times \delta(\mathrm{mas}) + (0.5 \pm 0.7)\,\mathrm{mas}$, where α and δ are right
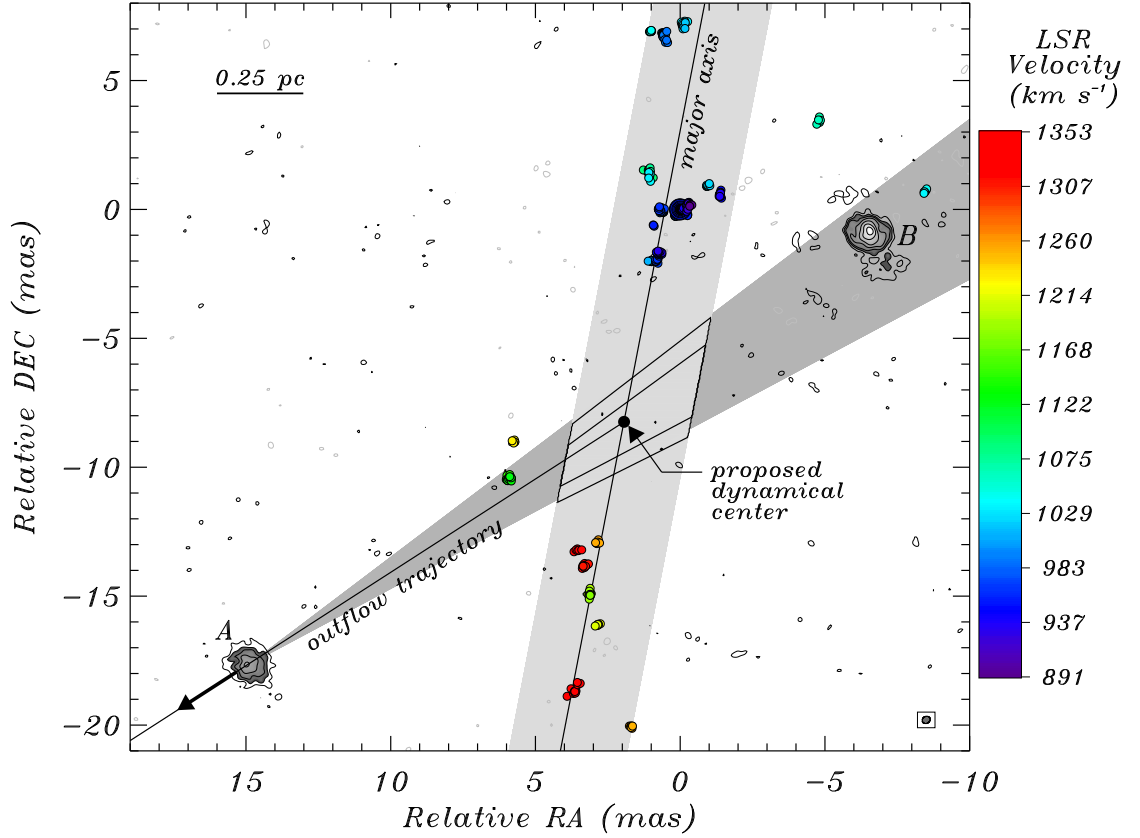
Figure 5.11.— Distribution of maser emission (colored spots) and of the 22 GHz continuum (gray contours) in the nuclear region of NGC 3079. The color of the maser spots indicates line-of-sight velocity in accordance with the bar on the right. The continuum contour levels are $-3\sigma, 3\sigma, 5\sigma \times 2^{k/2}$ where $\sigma = 0.14\,\mathrm{mJy\,beam^{-1}}$ and $k = 0, 1, 2, 3, \ldots$. The nearly vertical line is the proposed disk major axis while the gray nearly vertical region illustrates the uncertainty in the location and orientation of the axis. Also shown on the figure is the outflow trajectory of component A at P.A. of $126° \pm 5°$ (as in Fig. 5.9), where the cone shows the 1σ uncertainty in the orientation of this trajectory. The intersection of the outflow direction with the disk major yields the location for the dynamical center (filled symbol) where 70% and 45% confidence regions for its location are illustrated by the central contours. Note that the two easternmost and two westernmost maser features (outside the gray area depicting the maser disk) are most likely associated with the outflow. The ellipse in the bottom right corner of the figure illustrates beam dimensions.
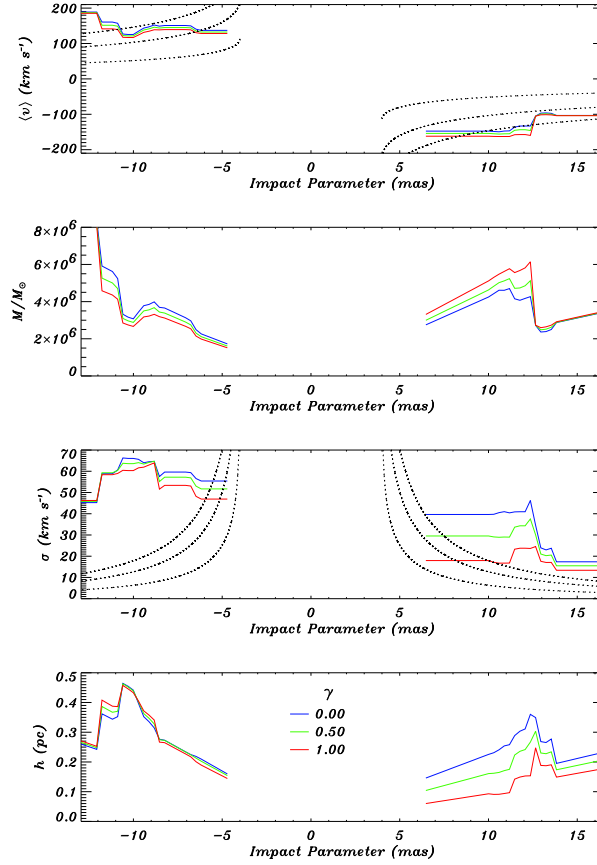
Figure 5.12.— Average velocity $\langle v \rangle$, enclosed total mass $M(r)$, velocity dispersion σ, and scale height h as a function of distance from the location of the dynamical center along the disk major axis, i.e., impact parameter. At each impact parameter, the four quantities under consideration were computed using an averaging aperture of radius 4 mas (0.34 pc) and weighting F^γ for various values of γ, where F is the maser flux density and γ is denoted by color. The average velocity, velocity dispersion, enclosed mass, and disk scale height were computed using $\langle v \rangle = [\sum_i F_i^\gamma]^{-1} \sum_i F_i^\gamma (v_i - v_{sys})$, $M(r) = \langle v \rangle^2 r / G$, $\sigma^2 = [\sum_i F_i^\gamma]^{-1} \sum_i F_i^\gamma (v_i - v_{sys} - \langle v \rangle)^2$, and $h \sim r\sigma/\langle v \rangle$, respectively, where the sums are over all maser features located within the averaging aperture, and r is the impact parameter. The curves were computed in a quasi-continuous fashion to emphasize the uncertainty in the computed parameters due to discreteness in velocity and spatial sampling. The dotted lines show the analytical results for a Keplerian edge-on disk of negligible mass around a $[0.5, 2, 4] \times 10^6 \, M_\odot$ point mass computed using an averaging aperture of 4 mas and under the assumption that the maser emission traces completely the midline of the putative disk.

ascension and declination measured with respect to the reference maser feature (Fig. 5.11). The position angle of the proposed major axis is $\sim -10°$, in close agreement with the position angle of the kpc-scale molecular disk (P.A.$\sim -11°$; Koda et al. 2002).

We use the estimated disk major axis and the systematic motion of component A to establish the location for the dynamical center. The uncertainty in the location and orientation of the disk major axis restricts the position of the dynamical center to lie within the gray nearly vertical band in Fig.5.11. The systematic motion of component A (Fig.5.9), on the other hand, limits the location of the dynamical center to P.A.$\sim -54° \pm 5°$ as measured with respect to A and illustrated as a cone in Fig.5.11. The intersection of these two loci yields $(\alpha, \delta) = (1.9 \pm 1, -8.2 \pm 2)$ for the mean position of the dynamical center (shown in Fig. 5.11). Note that the proposed position of the dynamical center lies in close proximity to the intersection of the disk major axis with the line joining components A and B, which was expected since the trajectory of A is nearly parallel to the line joining A and B. The position of the dynamical center proposed in this study is similar to that proposed in Trotter et al. (1998) but significantly different from that proposed by Sawada-Satoh et al. (2000) (Fig. 5.1).

Disk Structure

To study the disk structure traced by the maser emission, we computed the average velocity $\langle v \rangle$, the enclosed total mass $M(r)$, the velocity dispersion σ, and the disk scale height h as a function of distance r from the putative dynamical center

along the major axis of the disk, i.e., the impact parameter (Fig. 5.12). In this computation and the following analysis, we explicitly assume that the kinematics of the maser emission trace the kinematics of the underlying molecular material, as is indeed the case in the archetypal maser galaxy NGC 4258. To compute the four average quantities at each impact parameter, we used an averaging aperture of radius 4 mas (0.34 pc) and weighting function F^γ, where F is the maser flux density and $0 \le \gamma \le 1$. This particular weighting scheme was adopted to demonstrate that the general conclusions inferred from this analysis are relatively insensitive to the observed broad range of the maser flux density (Fig. 5.3). Moreover, at each impact parameter, the average velocity and velocity dispersion were computed in accordance with $\langle v \rangle = [\sum_i F_i^\gamma]^{-1} \sum_i F_i^\gamma (v_i - v_{sys})$ and $\sigma^2 = [\sum_i F_i^\gamma]^{-1} \sum_i F_i^\gamma (v_i - v_{sys} - \langle v \rangle)^2$, respectively, where the sums are over all maser features located within the averaging aperture. Assuming Keplerian rotation and spherical symmetry, we estimated the enclosed mass as $M(r) = \langle v \rangle^2 r / G$, where r is the impact parameter. Under the assumption of hydrostatic equilibrium and axisymmetric potential, the disk scale height is given by $h \sim r\sigma/\langle v \rangle$. Note that the two easternmost and two westernmost maser features have been omitted from this analysis because they do not appear to be associated with the disk (Fig. 5.11). Their inclusion would not change our conclusions significantly.

Rotation, the Enclosed Mass, and the Disk Mass

The computed average velocity displays a red-blue asymmetry about the adopted v_{sys} and estimated dynamical center and is thus consistent with rotation (Fig. 5.12). The Keplerian rotation law yields a mass of $\sim 2 \times 10^6 \, M_\odot$ enclosed within 0.4 pc

(5 mas). Trotter et al. (1998) reported a similar enclosed mass, $\sim 10^6\ M_\odot$, from consideration of the blue-shifted emission only. In our case, however, both the blue- and the red-shifted emission provide independent and consistent estimates of enclosed mass. We note that since the maser features may lie somewhat away from the disk midline or the disk might be somewhat tilted from edge-on, the computed enclosed mass is a lower limit, but is probably correct to within factors of order unity. For a central mass of $2 \times 10^6\ M_\odot$ and an inner radius of 0.4 pc, the maximum centripetal acceleration (i.e., velocity drift) and the maximum proper motion would be $0.05\ \mathrm{km\,s^{-1}\,yr^{-1}}$ and $2\ \mu\mathrm{as\,yr^{-1}}$, respectively. The much larger apparent velocity drifts and motions (Fig. 5.5) are most likely due to variability of separate gas clumps and macroscopic random motions among clumps rather than global kinematics, which makes a measurement of velocity drifts and proper motions due to the gravitational potential of a central mass difficult if not impossible.

Since the rotation curve of both blue- and red-shifted features is flat, i.e., $M(r) \propto r$, the mass of the circumnuclear pc-scale disk is significant with respect to the central mass. In fact, the disk mass within 0.7 pc, the distance from the dynamical center to the brightest maser feature, is roughly $M_d(0.7\ \mathrm{pc}) \sim M(0.7\ \mathrm{pc}) - M(0.4\ \mathrm{pc}) \sim 10^6\ M_\odot$. The mass of the entire disk traced by the maser emission (< 1.3 pc) might be as large as $7 \times 10^6\ M_\odot$ but this is uncertain by a factor of a few. Interestingly, if we extrapolate $M(r) \propto r$ to larger radii, we estimate a mass of $\sim 4 \times 10^8\ M_\odot$ enclosed within 76 pc, which is in surprisingly good agreement with the $7 \times 10^8\ M_\odot$ dynamical mass inferred from CO observations (Koda et al. 2002).

Mean Mass Density, Eddington Ratio, and Mass Accretion Rate

The mean mass density corresponding to $2 \times 10^6 \, M_\odot$ enclosed within $0.4 \, \mathrm{pc}$ is $10^{6.8} \, M_\odot \, \mathrm{pc}^{-3}$. The relatively high mean mass density for NGC 3079 is suggestive of a massive central black hole as opposed to a dense star cluster (e.g., Maoz 1995a), which is consistent with the X-ray observations of the nucleus. The estimated enclosed mass of $\sim 2 \times 10^6 \, M_\odot$ is in agreement with proposed correlations between bulge velocity dispersion and black hole mass (Gebhardt et al. 2000a, 2000b; Ferrarese & Merritt 2000; Ferrarese et al. 2001). If we adopt $M_{BH} = 1.2 \times 10^8 \, M_\odot \, [\sigma/(200 \ \mathrm{km \ s}^{-1})]^{3.75}$ (Gebhardt et al. 2000a, 2000b), then the velocity dispersion of the bulge, $40 \, \mathrm{km \, s}^{-1} < \sigma < 160 \, \mathrm{km \, s}^{-1}$ (Shaw, Wilkinson, & Carter 1993), is consistent with a black hole mass of $10^{5.5-7.7} \, M_\odot$, although the heavy dust obscuration might bias the measured dispersion.

To estimate the mass accretion rate as well as the accretion time-scale, we first approximate the luminosity of the nucleus. Since the $2 - 10 \, \mathrm{keV}$ luminosity is probably $\sim 5\%$ of the AGN bolometric luminosity (e.g., Kuraszkiewicz et al. 2003, Elvis et al. 1994), we obtain an AGN bolometric luminosity of $\sim 5 \times 10^{9-10} \, L_\odot$ from the X-ray data analysis reported by Iyomoto et al. (2001). The Eddington luminosity of a $2 \times 10^6 \, M_\odot$ object is $7 \times 10^{10} \, L_\odot$ and, assuming that all of the enclosed mass is concentrated in a supermassive black hole, the approximate luminosity of the central engine yields an Eddington ratio of $0.08 - 0.8$, which is consistent with the $0.01 - 1$ range obtained for Seyfert 1 galaxies, representative supermassive black hole systems (e.g., Padovani 1989; Wandel 1999). Assuming a standard accretion efficiency of ~ 0.1 (Frank, King, & Raine 2002), we obtain mass accretion rate

of $\dot{M} = 0.007\,L_{Bol,10}\,M_\odot\,\mathrm{year}^{-1}$, where $L_{Bol,10}$ is the AGN bolometric luminosity in units of $10^{10}\,L_\odot$. The disk mass computed above yields an average accretion time-scale of $t = M_d(r)/\dot{M} \sim 10^8\,L_{Bol,10}^{-1}$ years at a radius of $0.7\,\mathrm{pc}$ (Table 5.4).

Table 5.4: Parameters of the central engine and pc-scale disk in NGC 3079.

Quantity	Estimate
Central mass ($r < 0.4$ pc)	$\sim 2 \times 10^6\,M_\odot$
Mean mass density	$\sim 10^{6.8}\,M_\odot\,\mathrm{pc}^{-3}$
Disk mass (0.4 pc $< r < 0.7$ pc)	$\sim 10^6\,M_\odot$
Disk mass (0.4 pc $< r < 1.3$ pc)	$\lesssim 7 \times 10^6\,M_\odot$
Disk scale height	0.05 pc $< h < 0.5$ pc
AGN bolometric luminosity	$\sim 5 \times 10^{9-10}\,L_\odot$
Eddington ratio	$0.08 - 0.8$
Accretion rate[b]	$0.007\,L_{Bol,10}\,M_\odot\,\mathrm{year}^{-1}$
Accretion time-scale[a,b]	$10^8\,L_{Bol,10}^{-1}$ years
Toomre Q-parameter	$0.01 < Q < 0.02$
Clump size[a]	< 0.006 pc
Clump mass[a]	$< 5 \times 10^2\,M_\odot$
Jeans mass	$0.3 - 53\,M_\odot$
Rotation period[a]	4×10^3 years
Clump cooling time-scale[a]	< 60 years
Clump free-fall time-scale	$10^{2.5-4.0}$ years
Clump collision time-scale	10^{4-5} years
Roche limit[a]	$n > 5.3 \times 10^8\,\mathrm{cm}^{-3}$

[a] Computed at the location of the brightest maser feature, $r = 0.7\,\mathrm{pc}$.
[b] $L_{Bol,10}$ is the AGN bolometric luminosity in units of $10^{10}\,L_\odot$.

Disordered, Thick, and Flared Disk

The disk in NGC 3079 is different from the archetypal Keplerian disk in NGC 4258 in that the velocity structure of the former is much more disordered. The rotation traced by the maser emission in NGC 3079 is characterized by relatively large velocity differences across relatively small areas on the sky. For instance, the velocity dispersion (σ) as computed using an averaging radius of $4\,\mathrm{mas}$ ($0.34\,\mathrm{pc}$)

ranges from 20 to 80 km s^{-1} (Fig. 5.12). The maximum velocity difference between neighboring maser features is 144 km s^{-1} across a region as small as 0.1 pc. The large velocity dispersion is most likely indicative of macroscopic random motions among the molecular clumps responsible for the maser emission rather than turbulence within the clumps (Section 5.4.2). As already noted above, the variability in the angular distribution and in the spectrum of the maser (Figs. 5.3, 5.5) is a direct consequence of these macroscopic random motions. Although a significant fraction of the orbital velocity, the computed velocity dispersion is everywhere much smaller than the escape velocity of a $\sim 2 \times 10^6\, M_\odot$ central object ($v_{escape} > 110$ km s^{-1} in the region supporting maser emission) and thus has little impact on the stability of the underlying rotating structure. Although we favor the macroscopic random motions of clumps as the origin of the observed high dispersion, we note the small size of the dominant maser feature ($< 5 \times 10^{16}$ cm) for which $\sigma \sim 14$ km s^{-1}, and we speculate there may be some regions in which turbulence is significant but does not interfere with maser action (e.g., Wallin, Watson, & Wyld 1998).

The computed velocity dispersion can be used to infer the disk thickness. Because σ is a considerable fraction of the orbital velocity, the rotating structure is most likely geometrically thick (e.g., Alves & Nelson 2000; Wainscoat, Freeman, & Hyland 1989). Moreover, since σ does not decrease with the impact parameter, the disk scale height ought to increase with the distance from the center, i.e., the disk is probably flared. In particular, the scale height, computed using $h \sim r\sigma/\langle v \rangle$ appropriate in the case of hydrostatic equilibrium, is on the order of 0.05 pc at an impact parameter of 0.5 pc and might be as large as $h \sim 0.5$ pc at a radius of 0.9 pc (Fig. 5.12). The computed scale height is in reasonable agreement with the apparent

thickness of the disk inferred from the dispersion of the maser spots about the disk major axis, $h \sim 0.25\,\mathrm{pc}$ at $r \sim 0.7\,\mathrm{pc}$ (see Fig. 5.11).

5.4.2   Clumpy Star-Forming Disk

The Toomre-Q parameter characterizes the stability of the accretion disk and we can estimate it based on our measurements and an assumption about the temperature of the maser medium. The Q parameter is given by $Q = \Omega c_s/(\pi G \Sigma)$, where Ω is the angular rotation rate, Σ is the surface density, and c_s is the sound speed. If we assume that the mass distribution in the accretion disk has circular symmetry, then $\Sigma = (dM/dr)/(2\pi r)$ and we can write $Q = 2vc_s/(G\,dM/dr)$. Using $M(r) = v^2 r/G$ and the fact that the orbital velocity of $v \sim 150\,\mathrm{km\,s^{-1}}$ is approximately constant with radius (Fig. 5.12), we estimate a radius independent value of roughly $dM/dr = v^2/G \sim 3 \times 10^{21}\,\mathrm{g\,cm^{-2}}$. The sound speed in a neutral medium is given by $c_s = 0.04\,T^{1/2}\,\mathrm{km\,s^{-1}}$ (e.g., Maoz & McKee 1998) and most models of maser emission from water vapor require the gas temperature to lie in the range $300 - 1000\,\mathrm{K}$ (e.g., Desch et al. 1998). With these parameters we obtain $Q = 0.01 - 0.02$, where the range reflects only the uncertainty in temperature. Except for possible temperature variation, our estimate of Q is independent of radius since both the orbital velocity and dM/dr are to first order constant with radius. Since Q is significantly less than unity, the disk appears to be gravitationally unstable in the region supporting the maser emission. The flat rotation curve, which implies significant accretion disk mass with respect to the black hole mass, is fundamentally responsible for the low value of Q. The value of Q we estimate is rather robust if our fundamental assumption that

the velocities of the masers are due to the gravity of the enclosed mass holds true.

From our estimate of dM/dr, we parameterize the disk surface density as $\Sigma \sim 250 \, (r/0.7 \, \text{pc})^{-1} \, \text{g} \, \text{cm}^{-2}$, i.e., about 430 and 130 $\text{g} \, \text{cm}^{-2}$ at the inner and outer radii of 0.4 and 1.3 pc, respectively. (The empirically derived power law index of -1 is not unreasonable; for instance, $\Sigma \propto r^{-3/4}$ for a radiatively cooled gas pressure dominated α disk with a constant rate of accretion throughout the disk.) Using the scale height in Fig. 5.12, our estimate for disk surface density, and $\Sigma = 2h\langle\rho\rangle$, we compute mean density that varies from about $0.3 \times 10^8 \, m_H \, \text{cm}^{-3}$ to $3 \times 10^8 \, m_H \, \text{cm}^{-3}$ over the observed disk. The densities deduced here lie comfortably within the normally required range of H_2 number densities of 10^7 to $10^{10} \, \text{cm}^{-3}$ for maser emission (e.g., Desch et al. 1998). Our determination here of the average density of a maser medium is probably the first accurate determination of this quality for water in general.

The ultimate fate of an accretion disk characterized by $Q < 1$ depends on the balance between cooling and heating. It has been argued that the disk will maintain $Q \sim 1$ by rearrangement of surface density to reduce Σ or by heating through turbulence (Lin & Pringle 1987; Huré 2000; Gammie 2001). However, the energy required to maintain $Q \sim 1$ is prohibitive (Goodman 2003) and, in the case of NGC 3079, would require temperatures as high as $10^6 \, \text{K}$. Furthermore, cooling time scales might be sufficiently short that a $Q \sim 1$ criterion is unsupportable (Shlosman & Begelman 1989; Monaghan & Lattanzio 1991), in which case, the disk would fragment into clumps (e.g., Gammie 2001; Kumar 1999).

We consider the clumpy disk model in detail by computing clump size and

mass at a representative location within the disk, the distance from the dynamical center to the brightest maser feature, $0.7\,\text{pc}$. The gas number density required for gravitational collapse in a strong tidal field is given by the Roche limit, $n > 5.3 \times 10^8 \, (M(r)/2 \times 10^6 \, M_\odot) \, (0.7 \text{ pc}/r)^3 \text{ cm}^{-3}$, which is consistent with the H_2 number density required by the presence of the maser emission. Furthermore, as derived by Vollmer, Beckert, & Duschl (2004), an upper limit on the radius of a self-gravitating clump subject to tidal shear is $R_c < \pi c_s/\sqrt{8}\Omega$, from which we obtain $R_c < 0.006\,\text{pc}$ and an upper limit on the clump mass of $5 \times 10^2 \, M_\odot$. It is instructive to compare this upper limit to the Jeans mass, $m_J = (\pi c_s^2/G)^{3/2} \rho^{-1/2}$, which is $0.3 - 53 \, M_\odot$ given the conditions necessary to support maser emission. Since the Jeans mass and the Roche limit are consistent with the upper limit on cloud mass and with H_2 number density inferred from the presence of the maser emission, respectively, fragmentation and star formation is expected to occur within the clumps.

In addition to the Jeans mass analysis, straightforward considerations of energetics also suggest that individual clumps are susceptible to collapse. The time in which a clump will radiate its binding energy via black-body emission is given by $t_c \sim (GM_c^2/R_c)/(4\pi R_c^2 \sigma T_c^4) \approx 2.3 \times (GM_c m_H \langle n_{H_2}\rangle)/(3\sigma T_c^4)$ where M_c, R_c, T_c, $\langle n_{H_2}\rangle$ are the clump's mass, radius, effective temperature, and average H_2 number density, respectively (e.g., Goodman 2003). In our case, $M_c < 4 \times 10^2 \, M_\odot$, $T_c > 300\,\text{K}$, and $\langle n_{H_2}\rangle \leq 10^{10}\,\text{cm}^{-3}$, which yields $t_c < 60\,\text{years}$. However, if line emission is the dominant cooling mechanism then the time-scale becomes $t_c \sim (GM_c^2/R_c)/(4\pi R_c^3 \Lambda/3) \approx (2.3)^2 \times (4\pi G m_H^2 R_c^2 \langle n_{H_2}\rangle/3)(\Lambda/\langle n_{H_2}\rangle)^{-1}$ where $\Lambda/\langle n_{H_2}\rangle$ is the total cooling rate per H_2 molecule in erg s^{-1}. Using the cooling rates

in Neufeld et al. (1995) and $R_c < 0.006\,\mathrm{pc}$, the expression above is maximized for $\langle n_{\mathrm{H_2}} \rangle = 10^{10}\,\mathrm{cm}^{-3}$ and $T_c = 300\,\mathrm{K}$, which results in $t_c < 40\,\mathrm{years}$. If cooling of the gas by cold dust grains dominates, then, using $R_c < 0.006\,\mathrm{pc}$, dust temperature of $T_d \approx 200\,\mathrm{K}$ (Collison & Watson 1995), and the cooling rate per unit volume of Hollenbach & McKee (1989), we obtain a cooling time-scale of at most $5\,\mathrm{years}$. Thus, the time in which a clump will radiate all of its binding energy either via black-body radiation, line emission, or heating of cold dust is much less than the accretion time-scale and even the disk rotation period (Table 5.4) and, consequently, clumps collapse on their free-fall time-scale resulting in star formation. In our case, the free-fall time-scale is $\sqrt{R_c^3/GM} \approx (3\pi G m_H n_{\mathrm{H_2}})^{-0.5} = 10^{2.5-4.0}\,\mathrm{years}$, depends only on the hydrogen number density implied by the conditions necessary for maser amplification, and is four orders of magnitude smaller than the computed accretion time-scale.

Star formation can also be triggered by collisions among clumps. W49N, the most luminous water maser in our Galaxy, provides probably the best example of how clump-clump interaction can induce O-type star formation (Serabyn, Güsten, & Schulz 1993). To estimate the collision time-scale, we must obtain the mean clump separation. Using the scale height in Fig. 5.12, we estimate the volume of the entire disk as traced by the maser emission to be roughly $2\,\mathrm{pc}^3$. Mass of the entire maser disk of $\sim 7 \times 10^6\,M_\odot$ and a $5 \times 10^2\,M_\odot$ upper limit on clump mass yield $> 1.5 \times 10^4$ clumps in the disk and mean clump separation of $l_s < 0.03\,\mathrm{pc}$. Hence, the collision time-scale, $\sim \Omega^{-1}\,(l_s/R_c)^2$ (Kumar 1999), is $\sim 10^{4-5}\,\mathrm{years}$ and in fact depends only on disk size, disk mass, and $\mathrm{H_2}$ number density inferred from the presence of the maser emission. Since the collision time-scale is much less than

the accretion time-scale, collisions among clumps might also be a significant process in triggering star formation and overall evolution of the disk.

In summary, since $Q \ll 1$, the pc-scale circumnuclear disk in NGC 3079 is most likely gravitationally unstable and therefore clumpy. Furthermore, the Jeans mass, the Roche limit, as well as cooling and collision timescales are suggestive of star formation within the clumps through either clump collapse or clump collisions. Once a clump collapses, star formation proceeds via accretion of gas from the pc-scale accretion disk onto the Hill sphere of the stellar object, as considered in detail by Milosavljević & Loeb (2004). The star formation efficiency of giant molecular clouds ($M = 10^{1-3} \, M_\odot$) and dark molecular cores ($M = 1 \, M_\odot$) ranges from 0.1 to 5 % while the star formation timescale and the lifetime of hot massive stars is on the order of 10^6 years (e.g., Blitz & Thaddeus 1980; Larson 1982; Wilking & Lada 1983; Myers 1985; Silk 1985, 1987). Thus, the long accretion time-scale and the large potential clump mass computed above are consistent with the relatively slow and inefficient process of star formation (Table 4).

5.4.3 Pumping of Maser Emission by the Central Engine

Since the nucleus of NGC 3079 contains a compact hard X-ray source, irradiation of molecular gas is a plausible means of exciting maser emission (e.g., Neufeld, Maloney, & Conger 1994). In maser sources such as NGC 4258 and Circinus, irradiation over a wide range of radii is achievable because the disks are warped (Herrnstein, Greenhill, & Moran 1996; Greenhill et al. 2003). In NGC 3079, the disk in which the masers lie does not appear to be warped, in which case maser excitation

over the observed range of radii ($0.4 - 1.3$ pc) depends on penetration of X-rays in the disk plane. However, because maser action requires high densities, the disk must be inhomogeneous, which is consistent with our earlier stability arguments. For a minimum H_2 density of 10^8 cm^{-3}, a column within the disk becomes Compton thick for lengths greater than ~ 0.02 pc. However, for a line-of-sight filling factor of $\sim 2\%$, the column could pass X-rays to a radius of ~ 1.3 pc.

For an irradiated slab of gas, Collison & Watson (1995) estimate a maser emission rate of $\sim 4000\,L_\odot$ per pc^{-2} of surface area beamed in the plane of the slab. For a model spherical gas clump of radius ~ 0.005 pc that is irradiated on one side, the integrated output is on the order of $0.3\,L_\odot$, which is much less than the isotropic luminosity inferred from the strength of individual maser features (e.g., $131\,L_\odot$; Fig.5.3). We suggest instead that the emission from the observed masers is narrowly beamed along our line of sight by the overlap of clumps with similar Doppler velocities, whereby the integrated output of each is directed toward us (e.g., Deguchi & Watson 1989; Kartje et al. 1999). To support the peak observed isotropic luminosity, we require two clumps, each 0.005 pc in size, separated by on the order of 0.1 pc, which is reasonable in light of the ~ 1.3 pc radius of the disk. We note that amplification of background continuum emission by individual clumps can also generate strongly forward beamed maser emission, but we do not detect continuum emission in the vicinity of the disk above 0.84 mJy (6σ) at 22 GHz. On the other hand, the two easternmost and westernmost maser features do lie in close vicinity to continuum components B and C, and we speculate that maser emission observed away from the disk, where the density of clumps is probably greatly reduced, may be the result of continuum amplification.

Under the assumption that clumps are optically thick, irradiation of individual clumps by a central source creates a dissociation region on the inward facing side, which results in anisotropic emission of microwave photons preferentially along the length of the dissociation region. This pattern may be used to explain why we observe maser emission in the vicinity of the disk midline but not close to the line of sight to the central engine. Clumps on the front and back sides of the disk beam maser photons along axes that are substantially inclined to our line of sight. Furthermore, we speculate that the observed variability of maser spectrum (Nakai et al. 1995; Baan & Haschick 1996; Hagiwara et al. 2002) and the observed variation in angular structure (Fig. 5.5) may be the result of pairs of clumps moving in and out of alignment along the line of sight. The presence of the maser feature at ~ 956 km s^{-1} in the spectrum of NGC 3079 since the discovery of the maser (Henkel et al. 1984; Haschick & Baan 1985; Baan & Haschick 1996) and the $\sigma \sim 30\,\mathrm{km\,s^{-1}}$ dispersion due to bulk random motion (Fig.5.12) place a lower limit on the clump size of ~ 0.001 pc, consistent with the upper limit (Table 5.4). Year-to-year variation in the flux density of some maser features might be due to incomplete overlaps on the sky of the X-ray dissociation regions.

5.4.4   Outflow

Components E and F

Component E, identified by Kondratko et al. (2000), and component F, identified by Middelberg et al. (2003), might be remnants of jet emission along former axes of a wobbling jet, currently traced by components A, B, and C. The apparent decrease

in the break frequency of components E and F with distance from the central engine (Middelberg et al. 2003) and the shift of the spectrum of component E towards lower frequencies with time (Section 5.3.2) are indirectly supportive of the hypothesis that both components are rapidly cooling and adiabatically expanding remnants of jet emission. Although the structure of the continuum is difficult to understand in detail, we speculate that components A and B are regions where the jet, in its current orientation, interacts with a dense ambient medium, an inference supported by their GPS-like spectra (Section 5.3.2).

Alternatively, considering the location of E (Fig. 5.13) and of F (Middelberg et al. 2003) within the opening angle of the kpc-scale superbubble, these two components might provide evidence for a pc-scale wide-angle outflow, most likely an inward extension of the kpc-scale superbubble. In this interpretation, the two VLBI components could be moving knots or shocks as the ionized wide-angle wind interacts with the dense ambient medium along the edges of the flow as seen in projection. If this hypothesis is true, then new continuum components are expected to appear on both sides of the central engine but within the opening angle of the superbubble. However, it is currently not possible to distinguish between the two models proposed above and more sensitive images and proper motion studies of the continuum components extending over a longer time frame are necessary. Given the possible source lifetimes and transverse speeds (Section 5.3.2), time baselines on the order of a decade are necessary.
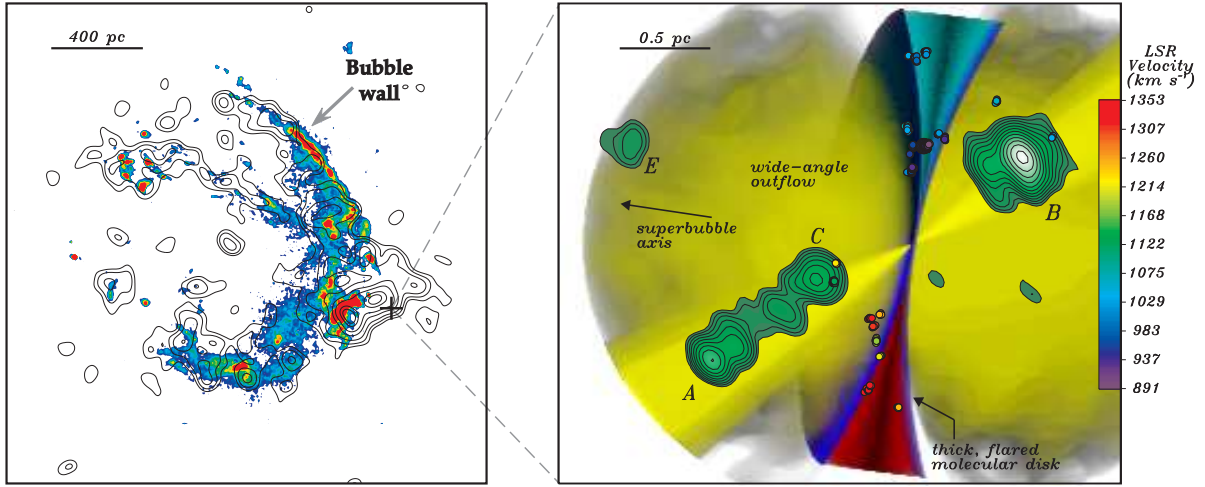
Figure 5.13.— *(left)* [NII] + Hα image of the superbubble (filled color contours) obtained with the HST (Cecil et al. 2001) and the soft X-ray image of the same (unfilled black contours) obtained with the Chandra X-ray Observatory (CXO). The X-ray image has been convolved with a Gaussian of $0.64''$ FWHM. The cross indicates both the VLBI-derived position of the maser source with respect to the X-ray emission as well as the $0.6''$ uncertainty in the CXO absolute astrometry (Chandra X-ray Center website: http://cxc.harvard.edu/cal/ASPECT/celmon/). Note that the position of a nearby soft X-ray emission peak: $\alpha_{2000} = 10^h 01^m 57\overset{s}{.}91 \pm 0.06$, $\delta_{2000} = 55°40'47\overset{''}{.}7 \pm 0.6$ is offset from the dynamical center of the maser disk by $\sim 1''$. The alignment of the two images has been accomplished by computing their two-dimensional cross-correlation. Although the uncertainty in the HST absolute positions might be as large as few arcseconds, Monte Carlo simulations of the 2D correlation, performed by repeatedly adding Gaussian or Poisson noise to the original images, indicate that the two images are registered to within $0.16''$. *(right)* Proposed model for the nuclear region of NGC 3079, a VLBI image of 8 GHz continuum (see Fig.5.7), and a map of 22 GHz maser emission (shown as spots color-coded by Doppler velocity). We propose a thick and flared disk (shown in a cross-section) that is slightly tilted with the west side being closer and that is aligned with both the kpc-scale molecular disk and the axis of the kpc-scale superbubble. The color coding indicates the Doppler shift of the disk material. The water maser emission traces the disk and may arise from X-ray irradiated clumps within the disk, which is unstable to fragmentation. An off-axis jet traced by the continuum components A, B, and C probably coexists with a wide-angle outflow (yellow), most likely an inward extension of the kpc-scale superbubble. The outflow may result in an uplift of clumps from the disk surface, which would explain the high latitude maser features and their association in velocity with the most proximate side of the disk.

On the other hand, it is unlikely that E and F are radio supernovae associated with the nuclear starburst. The spectral index of E, $\alpha < -2.1$ between 8 and 15 GHz (Fig. 5.10), is much steeper than what has been observed in radio supernovae ($\alpha \gtrsim -0.9$; Weiler et al. 1986; Weiler, Panagia, & Sramek 1990; Allen & Kronberg 1998; McDonald et al. 2001, 2002; Bartel et al. 2002) . The extremely steep spectrum of F, $\alpha \sim -6.1$ between 1.7 and 2.3 GHz, is also not compatible with a radio supernova. Furthermore, the radio supernovae in the prominent starburst galaxy M82 scaled to the distance of NGC 3079 would have flux densities ($\lesssim 0.1\,\mathrm{mJy}$) below our detection limits at 5 and 15 GHz (McDonald et al. 2002).

Wide-Angle Outflow on Parsec Scales

The existence of a wide-angle outflow in NGC 3079 was hypothesized in previous studies of the nucleus. Based on VLA data, Duric & Seaquist (1988) first suggested that a wide-angle wind is responsible for a bipolar "figure eight" structure along the minor axis of the galaxy in radio continuum. A wide-angle outflow on pc-scales has been suggested to explain a blue-shifted OH absorption component and two weak OH emission features detected from the nucleus (Baan & Irwin 1995; Hagiwara et al. 2004). By considering the energetics and morphology of the kpc-scale superbubble observed in Hα with the HST, Cecil et al. (2001) argued that the bubble is inflated by a wide-angle outflow rather than a precessing jet. Wide-angle outflows seem to be quite common among Seyfert galaxies (Colbert et al. 1996a,b, 1998) and one has been imaged on pc-scales in the Circinus galaxy, the nearest Seyfert 2 nucleus (Greenhill et al. 2003). Guided by this result, by the presence of molecular gas as dense as the disk gas at high latitudes above the disk, (i.e., the two easternmost and

two westernmost maser features in Fig. 5.11), and by the existence of a kpc-scale superwind, we suggest a wide angle outflow on pc-scales in NGC 3079.

It has been suggested that winds are driven by photoionized evaporation of matter from an inner surface of a torus (Krolik & Kriss 2001), by radiation and gas pressure acting on an accretion disk (Murray et al. 1995), or by the magneto-centrifugal uplift of gas and dust from an accretion disk (Emmering, Blandford, & Shlosman 1992; Königl & Kartje 1994, Kartje et al. 1999). In addition, ram pressure of a wide-angle outflow can entrain clumps at the surface of an accretion disk. If the wind is sufficiently dense to effectively shield the clumps from the central engine and the clumps can be confined, then they can potentially rise to high latitudes above the rotating structure (see Fig. 7 in Kartje et al. 1999) while still maintaining, to some degree, the rotational velocity imprinted by the parent disk. In light of this, the fact that the line-of-sight velocities of the two easternmost and the two westernmost features (Fig. 5.11) reflect the velocity of the most proximate side of the disk can be explained if these clumps were uplifted from the disk surface and carried to high latitudes by a dense wide-angle outflow. We thus consider the four maser features located significantly out of the plane of the disk as indirect evidence for a pc-scale wide-angle outflow, likely an inward extension of the kpc-scale superbubble. The fact that some clouds attain large latitudes above the disk surface while others remain within or in a close proximity to the thick disk might be due to a mixture of heavy and light clumps within the disk. We note that, due to beaming effects of maser emission, the actual number of the clumps uplifted might be much greater than the four clumps that are observed to be associated with the wind.

Although the origin of the putative pc-scale wide-angle outflow is unclear, we suggest that it is unlikely to be driven by star formation in the pc-scale accretion disk. The mechanical luminosity required to blow out a superbubble from the galactic disk in NGC 3079 is $\sim 3 \times 10^{41}\,\mathrm{erg\,s^{-1}}$ (Veilleux et al. 1994). Following Strickland et al. (2004b), such a luminosity would require $\sim 10^4\,(t/\mathrm{Myr})$ supernovae corresponding to a cluster of mass $5 \times 10^5\,(t/\mathrm{Myr})\,M_\odot$, assuming a thermalization efficiency of ~ 1, an energy release of $10^{51}\,\mathrm{ergs}$ per supernova, and a starburst lifetime t equal to the dynamical age of the superbubble, $\sim 10^6$ years (Veilleux et al. 1994). The predicted cluster mass is an order of magnitude greater than the $21,000 - 79,000\,M_\odot$ mass of one of the most massive star clusters known, R136 in 30 Doradus, with a half-mass radius of $0.5\,\mathrm{pc}$ (Campbell et al. 1992; Brandl et al. 1996; Massey & Hunter 1998). Such massive clusters are thus extremely rare, constituting only a fraction of $\sim 5 \times 10^{-5}$ of all star clusters (Strickland et al. 2004b). More reasonable values of the starburst lifetime ($\sim 40\,\mathrm{Myr}$) would require an even more extreme cluster mass and number of supernovae, effectively excluding a pc-scale cluster as a progenitor of the kpc-scale superbubble. Supernovae localized in multiple starburst regions and distributed over larger scales (e.g., kpc) might still contribute significantly to the wide-angle outflow, although the degree of this contribution is uncertain (Strickland et al. 2004a,b).

One consequence of the broad outflow that we hypothesize — or the canted jet marked by continuum components A, B, and C — may be the uniform weakness of maser emission south of the dynamical center. Since AGN outflows are ionized, differential attenuation of the maser emission is readily achieved for free-free absorption with a small difference in electron density and corresponding emission

measure. If the disk is tilted slightly from edge-on such that the lines of sight to the maser emission traverse outside of the disk (Fig.5.13), the observed two order of magnitude flux density difference between blue- and red-shifted features may be explained by a factor of at most ~ 2 difference in local electron number density (provided that $\tau > 1$ in the direction of the blue-shifted maser emission). In the case of a canted jet, an enhancement in density may be readily achieved given that the jet is inclined toward the apparently weaker masers (see also Trotter et al. 1998), but a density inhomogeneity in the wide-angle outflow might also be the cause of the differential attenuation. However, in either case, it is interesting to note that the balance of blue- and red-shifted emission can be readily governed by factors extrinsic to the maser emitting regions both in case of NGC 3079 and NGC 4258 (Herrnstein et al. 1996). This may be generalizable to other maser sources and contrasts with the models of Maoz (1995b) and Maoz & McKee (1998).

5.5 Summary

Water maser emission in the active nucleus of NGC 3079 has recently been recognized to cover a $\sim 450\,\mathrm{km\,s^{-1}}$ range centered on the systemic velocity of the galaxy. We have mapped for the first time maser emission over this entire velocity interval. We have also imaged non-thermal continuum emission between 5 and 22 GHz that arises in close proximity to the molecular gas underlying the masers. Based on the analysis of the spectral-line and continuum maps, we conclude the following.

1. The largely north-south distribution of maser emission, aligned with a known

kpc-diameter molecular disk, and the segregation of blue- and red-shifted maser emisssion on the sky strongly support the model of Trotter et al. (1998) in which the masers trace a nearly edge-on molecular disk about 1 pc in radius.

2. The dynamical mass enclosed within a 0.4 pc radius is $2 \times 10^6 \, M_\odot$, and for a 40 to 160 km s^{-1} stellar bulge velocity dispersion is consistent with correlations between central mass and dispersion reported for broad samples of galaxies (Gebhardt et al. 2000a, 2000b; Ferrarese & Merritt 2000; Ferrarese et al. 2001). The ratio of bolometric to Eddington luminosity is $0.08 - 0.8$, consistent with accretion efficiencies of $0.01 - 1$ for Seyfert 1 systems.

3. The disk rotation curve is relatively flat, which is consistent with a mass of $\lesssim 7 \times 10^6 \, M_\odot$ between radii of 0.4 and 1.3 pc.

4. The angular distribution of maser emission is not as well ordered in NGC 3079 as in other "maser galaxies" (e.g., NGC 4258). The velocities of adjacent clumps of maser emission can differ by tens of km s^{-1} on scales of ~ 0.1 pc. As a result, we suggest the disk is relatively thick ($h/r \sim 0.1$ to 0.5) and may be flared.

5. Based on stability, cooling, and timescale arguments, we argue that the disk is self-gravitating, clumpy, and appears to meet the necessary conditions for star-formation. The maser emission most likely occurs due to clumps irradiated by X-rays from the central engine and overlapping on the sky, yielding long gain paths and narrow beam angles.

6. We report detection of a very steep spectrum synchrotron component (E) that is not collinear with the previously claimed compact jet. The spectrum

is consistent with an aging electron energy distribution. The observation of a "relic" favors the hypothesis that the jet in NGC 3079 has changed direction. In addition to the jet, we observe molecular gas that is dense enough to support maser emission at high latitudes above the disk. From this, we infer that the jet coexists with a wide angle outflow originating at parsec or smaller scales.

The proposed model can be tested through further VLBI study of the 3079 AGN. More sensitive images and proper motion studies of the continuum components, with a longer time baseline, may help to determine the nature of components E and F. If they are shocks in a wide angle outflow rather than remnants of jet emission, then new continuum components are expected to appear within the arc subtended by the superbubble. The presence of star-formation in the inner parsec can be confirmed with an ultra sensitive search for M82-like radio supernova remnants. A proper motion and monitoring study of the maser emission would be challenging (i.e., motions $< 2\,\mu\mathrm{as}\,\mathrm{yr}^{-1}$), but could be used to corroborate the proposed geometry for the inner parsec, although it might be difficult to disentangle motions due to kinematics from apparent motions due to local effects, such as clump alignments. Hosting a central engine, a jet, a thick and self-gravitating accretion disk, and possibly a wide-angle outflow, and star-formation, the nucleus of NGC 3079 constitutes a nearby laboratory for diverse astrophysical phenomena and is a strong candidate for the study of the starburst-AGN connection and of the complex interactions between gas, stars, and supermassive black holes.

referee for useful comments.

Chapter 6

Parsec-scale Accretion Disk in NGC 3393

Paul T. Kondratko, Lincoln J. Greenhill, James M. Moran

To be submitted to The Astrophysical Journal

Abstract

We present a Very Long Baseline Interferometry map of water maser emission in the nuclear region of NGC 3393. The maser emission occupies a linear distribution at P.A.$\sim -34°$, perpendicular to both the kpc-scale radio jet and the axis of the narrow line region. The position-velocity diagram displays a red-blue asymmetry about the systemic velocity and estimated dynamical center, and is thus consistent with rotation. Assuming Keplerian rotation and an edge-on disk, we obtain a mass of $(3.1 \pm 0.2) \times 10^7 \, M_\odot$ enclosed within $0.36 \pm 0.02 \, \mathrm{pc}$ ($1.48 \pm 0.06 \, \mathrm{mas}$), which

corresponds to a mean mass density of $\sim 10^{8.2}\,M_\odot\,\mathrm{pc}^{-3}$ (the mass and the inner radius might be as high as $[3.5\pm0.2]\times10^7\,M_\odot$ and $0.41\pm0.02\,\mathrm{pc}$, respectively, due to systematic errors). We also report the measurement with the Green Bank Telescope of velocity drift — a manifestation of centripetal acceleration within the disk — of $5\pm1\,\mathrm{km\,s^{-1}\,yr^{-1}}$ in the $\sim 3880\,\mathrm{km\,s^{-1}}$ maser feature, which is most likely located along the line of sight to the dynamical center. For this feature, we estimate a disk radius of $0.17\pm0.02\,\mathrm{pc}$, which is smaller than the inner disk radius ($0.36\pm0.02\,\mathrm{pc}$) of emission that occurs along the midline (i.e., the line of nodes). The emission along the line of sight to the dynamical center evidently occurs much closer to the center than the emission from the disk midline, contrary to the situation in the two archetypal maser systems NGC 4258 and NGC 1068.

6.1 Introduction

NGC 3393 is a face-on early spiral (Sa) galaxy classified optically as Seyfert 2 (Véron-Cetty & Véron 2003). It displays a prominent ring and interacts weakly with a companion 60 kpc away (Schmitt et al. 2001a). There is compelling evidence that the galaxy contains an active galactic nucleus (AGN). The X-ray spectra of the source exhibit a 6.4 keV Fe Kα line — an unambiguous indicator of nuclear activity (Maiolino et al. 1998b; Guainazzi et al. 2005). Compton-thick, cold reflection model applied to the BeppoSax X-ray data yields an observed $2-10\,\mathrm{keV}$ flux of $3.9\times10^{-13}\,\mathrm{erg\,cm^{-2}\,s^{-1}}$ absorbed by a column density of $>10^{25}\,\mathrm{cm^{-2}}$ (Maiolino et al. 1998b). If we assume, following Comastri (2004), that the observed $2-10\,\mathrm{keV}$ flux is $1-10\%$ of the unabsorbed $2-10\,\mathrm{keV}$ flux due to reflection and scattering, then the

intrinsic $2 - 10$ keV luminosity is $10^{8.5-9.5} L_\odot$. Based on XMM and BeppoSax data, Guainazzi et al. (2005) report absorbing column density of $\left(4.4^{+2.5}_{-1.1}\right) \times 10^{24}$ cm^{-2}, a spectral index of $2.8^{+1.2}_{-0.7}$, and an observed flux of $\left(9^{+6}_{-4}\right) \times 10^{-14}$ erg cm^{-2} s^{-1}, which corresponds to an intrinsic $2 - 10$ keV luminosity of $10^{10.2^{+2.0}_{-1.1}} L_\odot$ (as computed by Portable Interactive Multi-Mission Simulator[1]). In the context of the AGN unified model, such a high column density is indicative of an almost edge-on obscuring structure along the line of sight to the nucleus (Lawrence & Elvis 1982; Antonucci 1993). Furthermore, images of the inner-kpc reveal outflows from the nucleus, consistent with the presence of an AGN. The Narrow Line Region (NLR) as traced by [O III] emission has an S-shaped morphology with an opening angle of $\sim 90°$ and extends ~ 400 pc on either side of the nucleus along position angle (P.A.) of $\sim 55°$ (Schmitt & Kinney 1996; Cooke et al. 2000). Very Large Array (VLA) and Australia Telescope Compact Array (ATCA) observations reveal a double-sided jet with a total extent of ~ 700 pc along P.A.$= 56°$ (Schmitt et al. 2001b) or P.A.$\sim 45°$ (Morganti et al. 1999). The existence of an AGN in the nucleus of NGC 3393 is thus well established by the available data.

NGC 3393 does not show evidence of significant nuclear star formation. The IRAS fluxes measured on ~ 30 kpc scale (assuming IRAS beam of $\sim 2'$; Moshir, M., et al. 1990) are consistent with a total infrared luminosity of $10^{10} L_\odot$, a dust mass of $\sim 5 \times 10^5 M_\odot$, and two relatively cool dust components at 30 and 130 K (Diaz et al. 1988). Under the assumption that star formation alone contributes to the infrared flux, the IRAS luminosity yields a star formation rate of ~ 4 $M_\odot$ yr^{-1} on kpc

---

[1]http://heasarc.gsfc.nasa.gov/Tools/w3pimms.html

scales (Veilleux et al. 1994), which is not consistent with a high level of star-forming activity. Detailed stellar population synthesis work by Cid Fernandes et al. (2004) confirms that the blue optical spectrum of the central $\sim 200\,\text{pc}$ is dominated by an old stellar population ($> 2.5 \times 10^9\,\text{yrs}$) with a small contribution (14%) to the featureless continuum from an AGN. A starburst therefore most likely does not play a significant role in the nucleus of NGC 3393.

The NGC 3393 nucleus is also a source of water maser emission, which is currently the only resolvable tracer of warm dense molecular gas in the inner parsec of AGN beyond $\sim 1\,\text{Mpc}$. The maser spectrum of NGC 3393 shows a characteristic spectral signature of rotation in an edge-on disk: two complexes ($\sim 70\,\text{mJy}$) symmetrically offset by $\sim 600\,\text{km\,s}^{-1}$ from the systemic velocity (henceforth, high-velocity emission) and a single spectral complex ($\sim 28\,\text{mJy}$) within $130\,\text{km\,s}^{-1}$ of the systemic velocity (henceforth, low-velocity emission; Kondratko et al. 2006). Very Long Baseline Interferometry (VLBI) maps of seven water maser sources that show similar spectral signatures have been interpreted in a context of a model in which the maser emission traces a nearly edge-on disk of molecular material 0.1 to 1 pc from a supermassive black hole: NGC 4258 (Miyoshi et al. 1995; Herrnstein et al. 2005), NGC 1386 (Braatz et al. 1997a), NGC 4945 (Greenhill et al. 1997b), NGC 1068 (Greenhill & Gwinn 1997), NGC 3079 (Trotter et al. 1998; Yamauchi et al. 2004; Kondratko et al. 2005), IC 2560 (Ishihara et al. 2001), Circinus (Greenhill et al. 2003). The maser spectrum of NGC 3393 thus provides indirect evidence for an edge-on pc-scale molecular disk orbiting a supermassive black hole.

VLBI maps of nuclear water maser emission have been used to accurately estimate black hole masses and pc-scale accretion disk geometries. In three water

maser systems mapped with VLBI — NGC 4258 (Miyoshi et al. 1995), NGC 1068 (Greenhill & Gwinn 1997), and the Circinus Galaxy (Greenhill et al. 2003) — position and line-of-sight velocity data provided evidence for differential rotation and enabled accurate estimation of black hole mass and pc-scale molecular disk structure. In another system, NGC 3079, the rotation curve traced by the maser emission appears flat and was interpreted in the context of a pc-scale, thick, edge-on, self-gravitating, and possibly star forming molecular disk (Kondratko et al. 2005). In addition to mapping pc-scale molecular disk structure and accurately weighing supermassive black holes, nuclear water maser emission has also been used as a distance indicator. Distance determination is possible for systems where a detailed knowledge of the structure of the disk from VLBI is combined with a measurement of either maser proper motions or drifts in line-of-sight velocity of spectral features (i.e., centripetal acceleration). The distance to NGC 4258 obtained in this manner is the most accurate extragalactic distance thus far, is independent of standard candle calibrators such as Cepheids (Herrnstein et al. 1999), and has contributed to the analysis of the Cepheid period-luminosity relation (Freedman et al. 2001; Newman et al. 2001; Macri et al. 2006).

In this work, we present a VLBI map of the pc-scale accretion disk as traced by water maser emission and the determination of black hole mass in NGC 3393. Data calibration and reduction techniques are discussed in Section 6.2. Spectral-line images of the inner-pc region are presented in Section 6.3. In Section 6.4 we interpret the observed kinematics of the maser in terms of a nearly edge-on pc-scale molecular accretion disk that orbits a central mass. In this work, we adopt NGC 3393 systemic velocity from 21 cm line measurements of $3750 \pm 5\,\mathrm{km\,s^{-1}}$ (Theureau et al. 1998),

which yields a distance of 50 Mpc for a Hubble constant of $75\,\mathrm{km\,s^{-1}\,Mpc^{-1}}$. With this adopted distance, 1 mas corresponds to 0.24 pc.

6.2   Observations and Calibration

NGC 3393 was observed in spectral-line mode with the Very Long Baseline Array (VLBA) of the NRAO[2], augmented by the phased VLA and the Green Bank Telescope (GBT), for approximately 5 hours on 2004 April 26/27. The source was observed with $8 \times 16\,\mathrm{MHz}$ intermediate-frequency (IF) bands that covered continuously a velocity range of 3048 to $4430\,\mathrm{km\,s^{-1}}$. Limits on the VLBA correlator data rate necessitated two correlator passes (with 256 channels per IF) and resulted in two separate data sets that do not overlap in velocity: one in left-circular polarization covering the velocity range from 3048 to $3737\,\mathrm{km\,s^{-1}}$, the other in right-circular polarization extending from 3737 to $4430\,\mathrm{km\,s^{-1}}$. The data were reduced using Astronomical Image Processing System. The amplitude calibration included corrections for atmospheric opacity. Antenna gain curves and measurements of system temperature were used to calibrate amplitude data for each of the VLBA stations. Amplitude calibration for the VLA was based on the measurements with the VLA of flux densities for VLBI calibrators with respect to 3C 286, for which we adopted a 22 GHz flux density of 2.56 Jy. To minimize systematic errors due to atmospheric opacity effects, we used in this calibration only VLA scans of VLBI calibrators with elevations closest to the elevation of 3C 286 ($e = 28°$, $28 - 29°$, $54°$,

---

[2]The National Radio Astronomy Observatory is operated by Associated Universities, Inc., under cooperative agreement with the National Science Foundation

43°, 64° for 3C 286, 1055-248, 4C 39.25, 0727-115, 0748+126, respectively).

The data in each polarization were corrected for the effect of source parallactic angle on fringe phase. The zenith path delay over each antenna was estimated via observations of ~ 10 strong (> 0.5 Jy) calibrators with sub-mas positions for ~ 1 hour before and ~ 1 hour after the main imaging experiment. The residual multiband delays after applying this calibration were < 0.2 ns, which corresponds to a phase error of at most 1° for a 16 MHz IF band (Table 6.1). Time variation in delays and fringe rates due to the troposphere and clock uncertainties as well as electronic phase difference among bands were removed via ~ 4 min observations of strong ($3 - 7$ Jy) calibrators (0727-115, 0748+126, 4C 39.25) approximately every hour. We estimate that this calibration is accurate to within 0.2 ns and 1 mHz for delays and rates, respectively; we note that a residual rate of 1 mHz results in a phase error of 0.5° if not corrected over a 1 hour time span, an approximate time separation between the calibrator scans (Table 6.1). The complex bandpass shapes of each antenna were corrected using the data on 0727-115, 0748+126, and 4C 39.25. Phase and amplitude fluctuations due to the troposphere and clock uncertainties were removed via observations every ~ 100 s of 1055-248, located 2.4° away from NGC 3393, self-calibrating the data on 1055-248, and applying the resulting phase and amplitude solutions to the target source. As a result of this process, the position of the maser on the sky can be determined relative to 1055-248. Based on VLA data obtained at two epochs in B and BnA configuration, we estimate the 22 GHz flux of 1055-248 to be 0.38 ± 0.03 Jy. This measurement as well as the photometric data from the NASA extragalactic database (NED) and from NRAO VLA Sky Survey (0.33 Jy at 1.4 GHz; Condon et al. 1998) suggest that 1055-248 is a flat spectrum

Table 6.1. Sources of phase error in the VLBI experiment.

Name	Equation[a]	$\Delta\phi$[b] (degrees)
Uncertainty in group delay estimate	$(2\pi\Delta\nu)\left[\sqrt{\dfrac{3}{2\pi^2}}\left(\dfrac{T_S}{T_A}\right)\dfrac{1}{\sqrt{\Delta\nu^3 t_{\mathrm{cal}}}}\right]$	$0.5-1$
Residual delay error due to calibrator position error	$(2\pi\Delta\nu)\left[0.4\times10^{-9}\,\dfrac{B}{5000\,\mathrm{km}}\,\dfrac{\Delta\theta_c}{5\,\mathrm{mas}}\right]$	$0.07-0.2$
Residuals in atmospheric delay	$(2\pi\Delta\nu)\Delta\sigma_{\mathrm{atm}}$	<0.6
Uncertainty in fringe rate estimate	$(2\pi\Delta\nu)\dfrac{\Delta\omega}{\omega_o}t$	<0.5
Residual fringe rate from imperfect astrometry	$(2\pi\Delta\nu)\left[0.13\times10^{-3}\,\dfrac{B}{5000\,\mathrm{km}}\,\dfrac{\Delta\theta_c}{1\,\mathrm{mas}}\right]\dfrac{t}{\omega_o}$	$0.3-1$
Errors in baseline length	$(2\pi\Delta\nu)\dfrac{\Delta B}{c}$	0.2
Errors due to imperfect calibrator astrometry	$(2\pi\Delta\nu)\dfrac{B\Delta\theta_p}{c}$	0.2
Phase calibrator-target angular separation	$\dfrac{K}{\lambda_{\mathrm{mm}}}b_{km}^{\alpha}\ \mathrm{deg};\qquad b_{km}=\left[\dfrac{h}{\sin e}\,\Delta\theta+\dfrac{v_a t_{\mathrm{cyc}}}{2}\right]$ where $\alpha=\frac{5}{6}$ for $b_{\mathrm{km}}<1.2$	<40

[a] Adopted from Herrnstein (1997) except for the last entry which is based on Carilli & Holdaway (1999). $\Delta\nu = 8\,\mathrm{MHz}$ is the video bandwidth (i.e., the bandwidth across which various calibrations are applied and over which the resulting errors are propagated), $T_S \sim 1000\,\mathrm{Jy}$ is a representative system equivalent flux density of VLBI antennas, $T_A = 3-7\,\mathrm{Jy}$ is the flux density of delay/rate calibrators (i.e., 0727-115, 0748+126, 4C 39.25), $t_{\mathrm{cal}} \sim 3.5\,\mathrm{min}$ is the delay/rate calibrator scan duration, $\Delta\theta_c = 0.3-1\,\mathrm{mas}$ is the uncertainty in the delay/rate calibrator position (Ma et al. 1998), $B \sim 5000\,\mathrm{km}$ is an approximate baseline length, $\Delta\sigma_{\mathrm{atm}} < 0.2\,\mathrm{nsec}$ is the residual multiband delay after correcting for the zenith path delay over each antenna, $\Delta\omega < 1\,\mathrm{mHz}$ is the residual rate after correcting for time variation in delays and fringe rates due to the troposphere and clock uncertainties, $t = 1.5\,\mathrm{hrs}$ is an approximate time separation between the delay/rate calibrator scans, $\omega_o = 22\,\mathrm{GHz}$ is the observing frequency, $\Delta B \sim 2\,\mathrm{cm}$ is a representative uncertainty in baseline length, c is the speed of light, $\Delta\theta_p = 0.86\,\mathrm{mas}$ is the uncertainty in the phase calibrator (1055-248) position (Beasley et al. 2002), b_{km} is an effective baseline length in km, $K = 200-600$ is a constant that depends on weather conditions (values assumed here are for the VLA site), $v_a < 15\,\mathrm{m\,s^{-1}}$ is the tropospheric pattern speed, $h \sim 2\,\mathrm{km}$ is the water vapour scale height, $e \sim 25°$ is a representative antenna elevation, $\Delta\theta = 2.4°$ is the angular separation between the phase calibrator and the target source, $t_{\mathrm{cyc}} \sim 100\,\mathrm{s}$ is the time between successive phase calibrator observations, and $\lambda_{\mathrm{mm}} = 13$ is the observing wavelength in mm.

[b] Phase error.

source and is therefore expected to be unresolved on mas scales. In fact, using the source model obtained from self-calibration, we estimate that 90% of 1055-248 flux comes from a point source. The calibrator appears nearly point-like also in a narrow bandwidth ($250 \, \text{kHz} \sim 3.4 \, \text{km s}^{-1}$), which confirms the quality of bandpass calibration. Based on the consideration of the tropospheric structure function as predicted by the Kolmogorov turbulence theory (Carilli & Holdaway 1999), we estimate that the interferometer phase towards 1055-248 reproduces that towards NGC 3393 to within $\phi_{\text{rms}} < 40°$, which corresponds to a loss of signal on the target source of at most $1 - \exp[-\phi_{\text{rms}}^2/2] = 25\%$ (assuming water vapour scale height of $\sim 2 \, \text{km}$, a representative antenna elevation of $\sim 25°$, and a tropospheric pattern speed of $< 15 \, \text{km s}^{-1}$; Table 6.1). The uncertainty in phase due to calibrator-target angular separation is the most significant source of error in this experiment and depends sensitively on the assumed pattern speed, which is not well constrained for this experiment (Table 6.1).

After calibrating and imaging the spectral-line data set, the positions and the integrated fluxes of the maser features were obtained by fitting two-dimensional elliptical Gaussians to the distribution of the maser emission on the sky in each spectral channel. The resulting uncertainties in maser spot positions based on fits are consistent to within 60% with the theoretical expectations for a given signal-to-noise ratio and beam size. The synthesized beam dimensions were $3.5 \times 1 \, \text{mas}$ at P.A.$\sim -1°$ and the resulting noise level was $\sim 5 \, \text{mJy}$ in $\sim 3.4 \, \text{km s}^{-1}$ spectral channels, a spectral breadth comparable to the linewidth. To estimate the fraction of the power imaged by the interferometer and to monitor the maser with an aim to detect velocity drifts, we acquired with the GBT single-dish spectra of NGC 3393

using the configuration and calibration described in Kondratko et al. (2007). We note that all velocities have been computed in accordance with the optical definition of Doppler shift and in the heliocentric reference frame.

6.3 Results

The spectrum of imaged power agrees to within 2σ with the total power spectrum obtained with the GBT ~ 9 months after the VLBI observation (Fig. 6.1 and Table 6.2). Difference between the two spectra might be due to source variability, as single-dish monitoring of water maser sources has revealed substantial flux variability on timescales of months to years (this work for NGC 3393 and Baan & Haschick 1996 for other sources). The maser emission is distributed on the sky in a linear arrangement at P.A.$\sim -34°$ (Fig. 6.2 and Table 6.2), perpendicular to both the kpc-scale radio jet (P.A.$\sim 45°$ or $\sim 56°$ from Morganti et al. 1999 and Schmitt et al. 2001b, respectively) and the axis of the NLR (P.A.$\sim 55°$; Schmitt & Kinney 1996; Cooke et al. 2000). The distribution of maser emission on the sky is clearly segregated by velocity: emission red- and blue-shifted with respect to the systemic velocity is located in the north-western and south-eastern parts of the image, respectively. Although the two VLBA correlator passes do not overlap in velocity, we can nevertheless place a limit on their registration by aligning the mapped systemic maser spots in the two data sets. If we assume that the mapped low-velocity features arise at the same location on the sky, then the two correlator passes are registered to within 0.3 ± 0.1 mas and 0.9 ± 0.3 mas in RA and DEC, respectively. The systematic offset between the two correlator passes can also be estimated by

applying the calibration of one data set to the other. The transfer of phase and amplitude solutions from self-calibration on 1055-248 from one correlator pass to the other results in an offset of 1055-248 from map center of 0.30 ± 0.02 mas and 0.52 ± 0.06 mas in RA and DEC, respectively, which is consistent with the offsets based on the location of the low-velocity maser features. Radio maps of the inner-kpc are suggestive of a jet perpendicular to the distribution of maser emission on the sky. However, we find no evidence at a $4\sigma = 2.4$ mJy level for the 22 GHz continuum on ~ 50 pc scale.
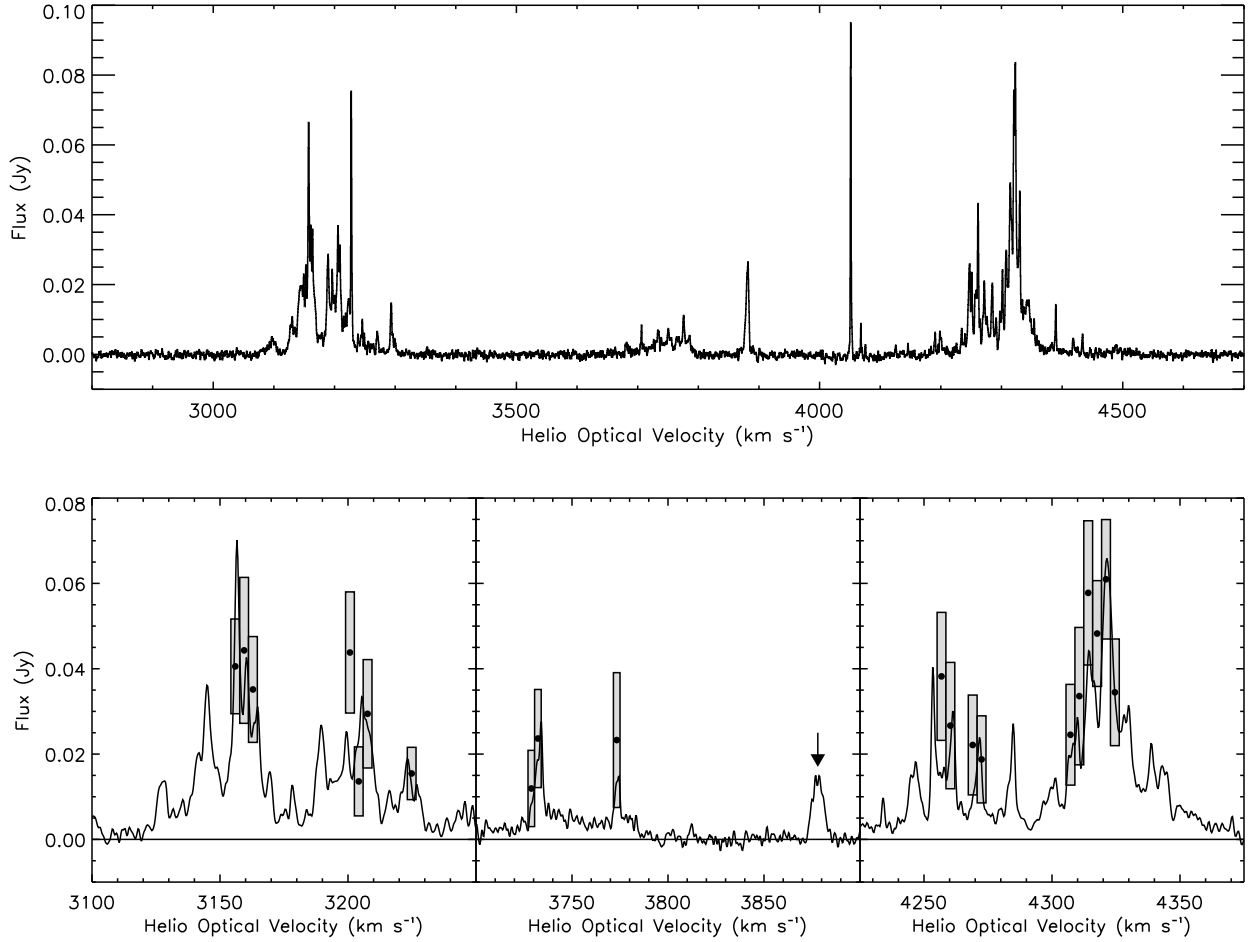
Figure 6.1.— *Top:* A weighted average of five total-power spectra of the maser in NGC 3393 obtained with the GBT on 2005 October 17, 2006 January 22, 2006 March 23, 2006 April 28, and 2006 May 23 with an effective resolution of 108 kHz ($\sim 1.5\,\mathrm{km\,s^{-1}}$) and $1\sigma = 0.6\,\mathrm{mJy}$. *Bottom:* Imaged-power (histograms and the corresponding filled circles) and total-power spectra (black trace) of the maser in NGC 3393. Total-power spectrum was obtained with the GBT on 2005 January 15 and has an effective resolution of 108 kHz ($\sim 1.5\,\mathrm{km\,s^{-1}}$). The spectrum of the imaged power is based on the VLBI observation conducted on 2004 April 26/27 and shows integrated flux (filled circles), integrated flux minus 1σ (grey histogram), and integrated flux plus 1σ (open histogram) from a fit of a two-dimensional elliptical Gaussian model to the distribution of the maser emission on the sky in each spectral channel. We note that the peak flux densities and the integrated fluxes of maser spots, both based on fits, are consistent to within 1σ. The low-velocity feature at $\sim 3880\,\mathrm{km\,s^{-1}}$ (vertical arrow), for which we report a velocity drift of $a = 5 \pm 1\,\mathrm{km\,s^{-1}\,yr^{-1}}$, was not detected in the VLBI experiment.

Table 6.2.   Velocities, positions, and integrated fluxes for mapped maser emission in NGC 3393.

Velocity[a] (km s^{-1})	RA[b] (mas)	DEC[b] (mas)	Flux[c] (Jy)
3154.3—3157.7	-0.3 ± 0.2	-0.9 ± 0.4	0.04 ± 0.01
3157.7—3161.1	-0.5 ± 0.3	-0.4 ± 0.7	0.04 ± 0.02
3161.1—3164.6	-0.3 ± 0.2	-0.4 ± 0.4	0.04 ± 0.01
3199.0—3202.5	-0.3 ± 0.2	-0.5 ± 0.5	0.04 ± 0.01
3202.5—3205.9	-0.1 ± 0.2	-1.7 ± 0.4	0.014 ± 0.008
3205.9—3209.4	0.0 ± 0.2	-2 ± 1	0.03 ± 0.01
3223.2—3226.6	0.1 ± 0.1	-1.5 ± 0.3	0.015 ± 0.006
3727.1—3730.5	-0.8 ± 0.2	1.0 ± 0.6	0.012 ± 0.009
3730.5—3734.0	-1.1 ± 0.3	0.3 ± 0.6	0.02 ± 0.01
3771.6—3775.0	-1.3 ± 0.2	-0.2 ± 0.3	0.02 ± 0.02
4255.1—4258.6	-2.5 ± 0.2	2.3 ± 0.7	0.04 ± 0.01
4258.6—4262.0	-2.1 ± 0.2	1.3 ± 0.5	0.03 ± 0.01
4267.3—4270.7	-2.5 ± 0.1	1.9 ± 0.6	0.02 ± 0.01
4270.8—4274.2	-2.5 ± 0.2	1.5 ± 0.3	0.02 ± 0.01
4305.5—4308.9	-2.3 ± 0.2	1.2 ± 0.5	0.02 ± 0.01
4308.9—4312.4	-2.0 ± 0.2	1.0 ± 0.6	0.03 ± 0.02
4312.4—4315.9	-2.0 ± 0.1	1.2 ± 0.4	0.06 ± 0.02
4315.9—4319.3	-2.13 ± 0.09	1.6 ± 0.2	0.05 ± 0.01
4319.4—4322.8	-2.20 ± 0.07	1.6 ± 0.2	0.06 ± 0.01
4322.8—4326.3	-1.9 ± 0.1	1.8 ± 0.4	0.03 ± 0.01

[a]Range of mapped optical heliocentric velocities.

[b]Right ascension and declination relative to α_{2000}=10:48:23.4660 and δ_{2000}=-25:09:43.478. A priori position for the maser was α_{2000}=10:48:23.45 and δ_{2000}=-25:09:43.6 with uncertainty of $\pm 0.''3$ from Kondratko et al. (2006).

[c]Integrated flux from a fit of a two-dimensional elliptical Gaussian model to the distribution of the maser emission on the sky in each spectral channel.
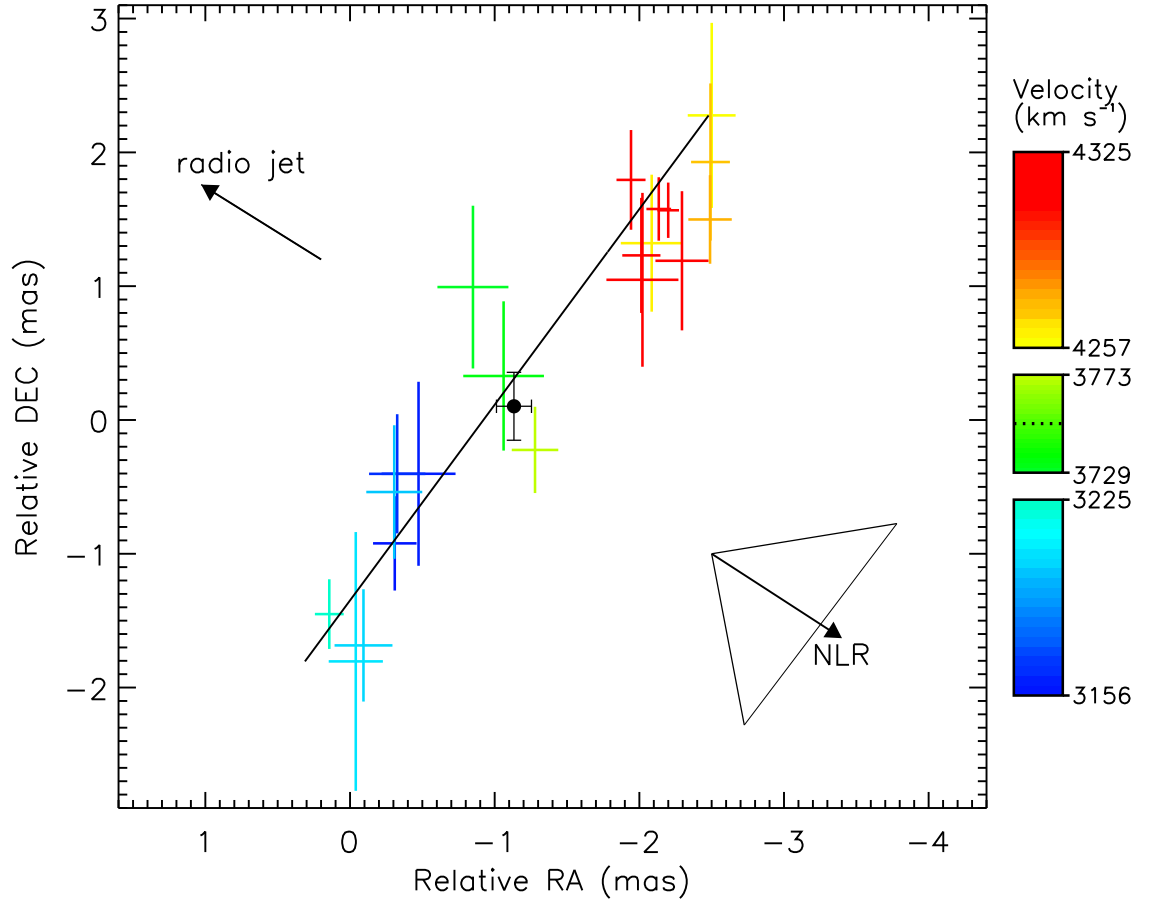
Figure 6.2.— Distribution of maser emission in the nuclear region of NGC 3393. Position uncertainties are 1σ and the color of the maser spots indicates heliocentric optical line-of-sight velocity in accordance with the bar on the right. The adopted location for the dynamical center (black circle) is computed from the positions of the low-velocity maser features. A line fitted to the distribution of maser emission on the sky (P.A.$\sim -34°$) is orthogonal to the kpc-scale radio jet (P.A.$\sim 45°$ or $\sim 56°$ from Morganti et al. 1999 and Schmitt et al. 2001b, respectively) and to the axis of the NLR (P.A.$\sim 55°$ with an opening angle of $\sim 90°$ Schmitt & Kinney 1996; Cooke et al. 2000). The horizontal dotted line shows the adopted systemic velocity of $3750\,\mathrm{km\,s^{-1}}$. The coordinates are relative to α_{2000}=10:48:23.4660 and δ_{2000}=-25:09:43.478.
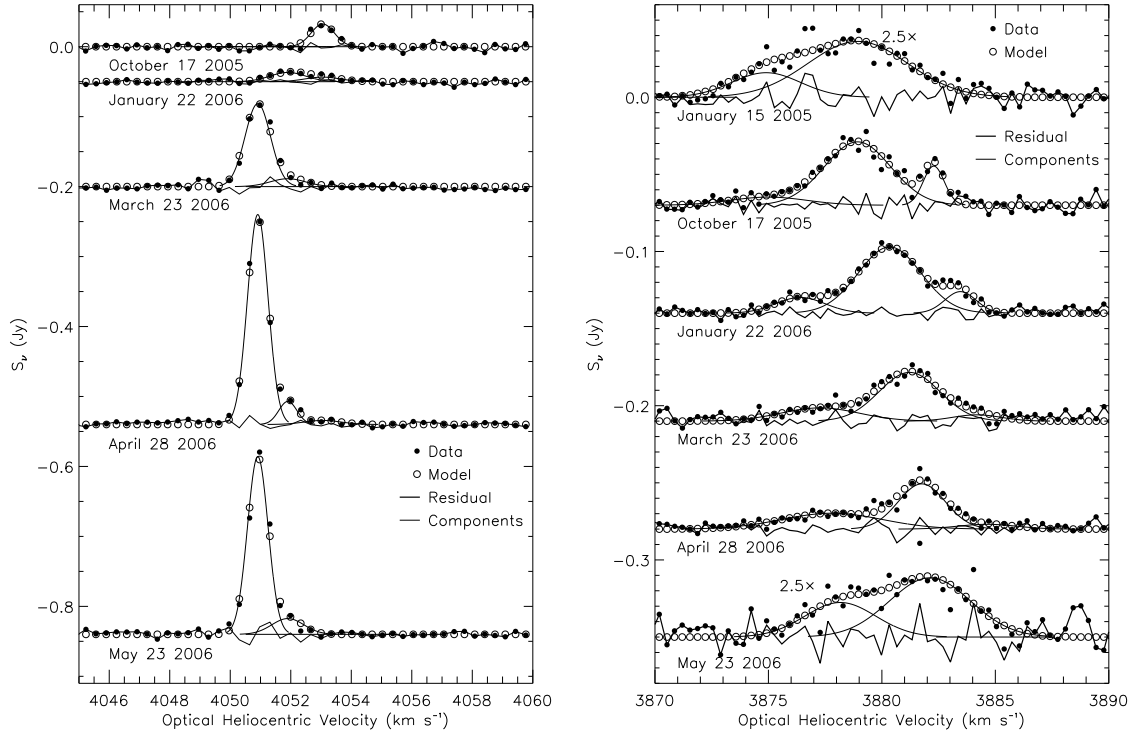
Figure 6.3.— Maser spectra of features at $\sim 3880\,\mathrm{km\,s^{-1}}$ and $\sim 4051\,\mathrm{km\,s^{-1}}$ obtained with the Green Bank Telescope and the results of Gaussian component decomposition. Emission in the immediate vicinity of the systemic velocity, $\sim 3750\,\mathrm{km\,s^{-1}}$, was too weak to allow Gaussian component decomposition and is not shown.

Table 6.3.   Results of Gaussian component decomposition of $\sim 3880\,\mathrm{km\,s^{-1}}$ and $\sim 4051\,\mathrm{km\,s^{-1}}$ spectral features in NGC 3393.

$\chi_R^{2\,(a)}$	Velocity[b] $(\mathrm{km\ s^{-1}})$	Drift[c] $(\mathrm{km\ s^{-1}\ yr^{-1}})$	Amplitude[d] (mJy)	FWHM[e] $(\mathrm{km\ s^{-1}})$	Date
1.2	3871.0 ± 0.9	5.3 ± 0.7	. . .	. . .	2005 Jan 15
			5 ± 2	4 ± 1	2005 Oct 17
			10 ± 2	2.6 ± 0.6	2006 Jan 22
			9 ± 2	4.1 ± 0.9	2006 Mar 23
			10 ± 1	5.2 ± 0.8	2006 Apr 28
			9 ± 2	3.7 ± 0.9	2006 May 23
	3874.9 ± 0.2	5.3 ± 0.2	6 ± 2	3.6 ± 0.7	2005 Jan 15
			41 ± 2	3.4 ± 0.3	2005 Oct 17
			43 ± 2	3.3 ± 0.2	2006 Jan 22
			32 ± 2	3.2 ± 0.3	2006 Mar 23
			29 ± 2	2.4 ± 0.2	2006 Apr 28
			15 ± 2	4.2 ± 0.6	2006 May 23
	3878.9 ± 0.2	4.4 ± 0.2	14.5 ± 0.9	5.2 ± 0.5	2005 Jan 15
			25 ± 5	1.1 ± 0.3	2005 Oct 17
			14 ± 2	1.6 ± 0.3	2006 Jan 22
			4 ± 2	2.5 ± 0.9	2006 Mar 23
			3 ± 1	3 ± 1	2006 Apr 28
			. . .	. . .	2006 May 23
2.0	4050.91 ± 0.01	0.003 ± 0.009	. . .	. . .	2005 Oct 17
			. . .	. . .	2006 Jan 22
			119 ± 5	0.99 ± 0.04	2006 Mar 23
			300 ± 5	0.80 ± 0.01	2006 Apr 28
			254 ± 8	0.80 ± 0.02	2006 May 23
	4051.9 ± 0.1	-0.05 ± 0.09	. . .	. . .	2005 Oct 17
			13 ± 3	1.4 ± 0.4	2006 Jan 22
			11 ± 4	1.4 ± 0.5	2006 Mar 23
			33 ± 6	0.7 ± 0.2	2006 Apr 28
			23 ± 4	1.2 ± 0.4	2006 May 23
	4053.06 ± 0.07	-0.7 ± 0.6	32 ± 5	0.9 ± 0.2	2005 Oct 17
			7 ± 3	1.4 ± 0.8	2006 Jan 22

Table 6.3—Continued

$\chi_R^{2\,(a)}$	Velocity[b]	Drift[c]	Amplitude[d]	FWHM[e]	Date
	(km s^{-1})	(km s^{-1} yr^{-1})	(mJy)	(km s^{-1})	
			. . .	. . .	2006 Mar 23
			6 ± 2	1.4 ± 0.7	2006 Apr 28
			. . .	. . .	2006 May 23

[a]Reduced chi-squared for a least squares solution that determines velocity drifts, amplitudes, peak centroids, and widths of all Gaussian components at all epochs simultaneously.

[b]Velocity of a Gaussian component at the reference epoch (2005 January 15 and 2005 October 17 for $\sim 3880\,\mathrm{km\,s^{-1}}$ and $\sim 4051\,\mathrm{km\,s^{-1}}$ features, respectively).

[c]Velocity drift of a Gaussian component.

[d]Amplitudes of a Gaussian component at the listed epochs.

[e]Full widths at half maxima of a Gaussian component at the listed epochs.

The low-velocity spectral features are expected to drift in velocity since they are located within the disk where the centripetal acceleration vector is along the line of sight. With an aim to detect these velocity drifts, we monitored NGC 3393 with the GBT and report the measurement of the centripetal acceleration in the low-velocity complex at $\sim 3880 \, \mathrm{km \, s^{-1}}$ (Fig. 6.3 and Table 6.3). Using the code described in Humphreys et al. 2007, we decomposed the complex at each epoch into three Gaussian components and used an iterative least squares technique to solve simultaneously for velocity drifts, amplitudes, peak centroids, and widths of all Gaussian components at all epochs. We obtain a reduced χ^2 of 1.2 and velocity drifts of 5.3 ± 0.7, 5.3 ± 0.2, and $4.4 \pm 0.2 \, \mathrm{km \, s^{-1} \, yr^{-1}}$ for components at 3871.0 ± 0.9, 3874.9 ± 0.2, and $3879 \pm 0.2 \, \mathrm{km \, s^{-1}}$, respectively, where the reference epoch for component velocities is 2005 January 15. In addition, spectra obtained since 2004 October 17 reveal a strong ($< 0.3 \, \mathrm{Jy}$) feature at $\sim 4051 \, \mathrm{km \, s^{-1}}$ that was present neither in earlier spectra of the source nor in the VLBI map (Fig. 6.3 and Table 6.3)). The first three epochs on this line were consistent with a negative centripetal acceleration, as would be expected for low-velocity emission that arises from behind the dynamical center. However, the line stopped drifting in recent spectra of the source. We note that such behavior can be reproduced by a variation in strength of multiple components that do not drift in velocity (i.e., stationary components). In fact, from a Gaussian decomposition of the five available epochs, we infer that the data on this complex are consistent (reduced χ^2 of 2.0) with three variable but stationary ($< 0.7 \, \mathrm{km \, s^{-1} \, yr^{-1}}$) Gaussian components at 4051, 4052, and $4053 \, \mathrm{km \, s^{-1}}$. High-velocity emission is not expected to drift in velocity since it is located along the disk midline where the centripetal acceleration vector is perpendicular to the line of

sight. We thus suggest that the newly detected complex at $\sim 4051\,\mathrm{km\,s^{-1}}$ may be high-velocity emission. We note that low-velocity emission that arises from behind the dynamical center has not been detected to date from known nuclear water maser sources. This non-detection can be explained if free free absorption by an intervening ionized gas is considerable (e.g., Herrnstein et al. 1996) or the presence of a background nuclear continuum source is necessary to generate via amplification low-velocity emission luminous enough for us to detect (e.g., Herrnstein et al. 1997).

6.4   Discussion

We interpret the linear distribution of the maser emission, perpendicular to the radio jet and to the axis of the NLR, as well as the segregation of the blue- and the red-shifted emission on the sky in the context of a pc-scale molecular disk. We assume that the disk is nearly edge-on and, based on the measured positive centripetal acceleration, we infer that the low-velocity emission lies in front of and along the line of sight to the dynamical center. The distribution of maser emission on the sky is consistent with a straight (i.e., unwarped) disk. We note that a 4th degree polynomial fit to the maser distribution yields a marginal (i.e., $\sim 10\%$) improvement in χ^2 over a straight line fit. Thus, the evidence for a warp is at most tentative with our signal-to-noise ratio (SNR).

We use the mean position of the low-velocity maser features to estimate the location of the dynamical center (Fig. 6.2) and $\sqrt{(RA_i - RA_{BH})^2 + (DEC_i - DEC_{BH})^2}$ to compute the impact parameter. The resulting position-velocity diagram displays a red-blue asymmetry about the adopted v_{sys} and estimated dynamical center and
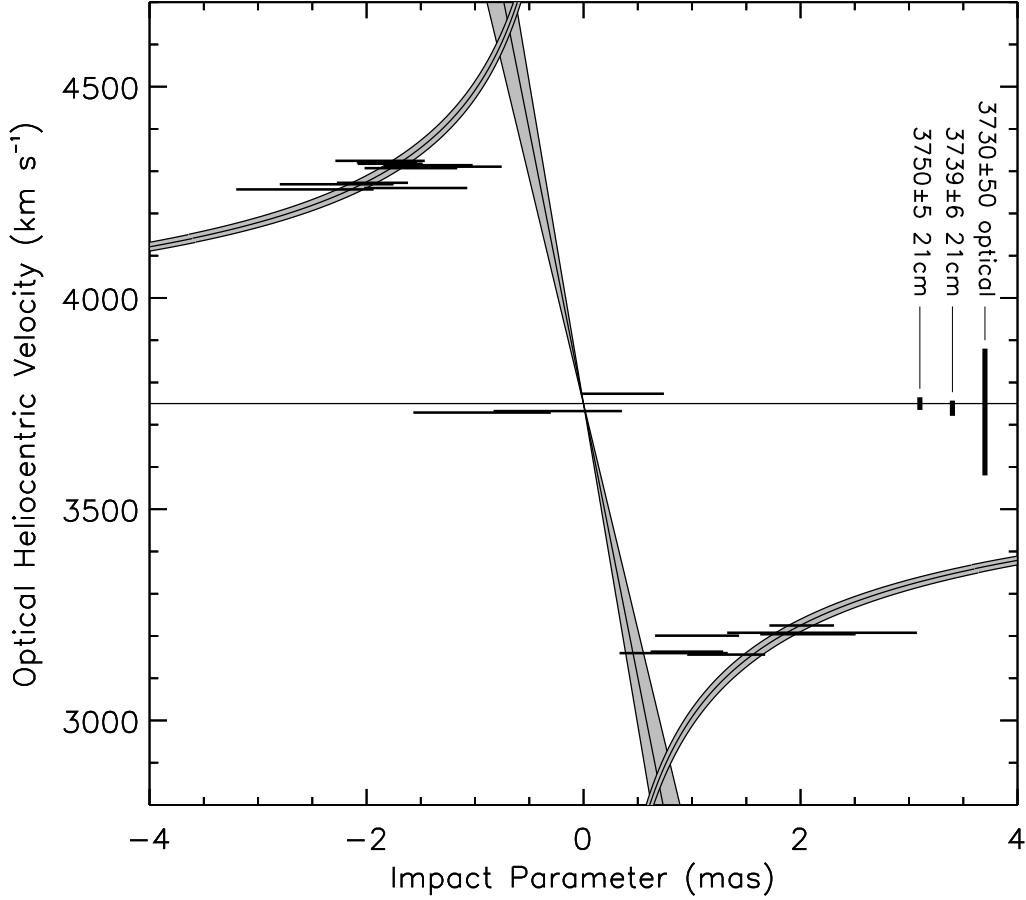
Figure 6.4.— Impact parameter-velocity diagram for the mapped maser emission in NGC 3393. A fit of the Keplerian rotation law to the high-velocity features (filled grey curves) yields a mass of $(3.1 \pm 0.2) \times 10^7 \, M_\odot$ enclosed within $0.36 \pm 0.02 \, \mathrm{pc}$ $(1.48 \pm 0.06 \, \mathrm{mas})$. From the measured velocity drift $(a = 5 \pm 1 \, \mathrm{km \, s^{-1} \, yr^{-1}})$, we infer the radius of the systemic feature at $\sim 3880 \, \mathrm{km \, s^{-1}}$ of $r_{sys} = \sqrt{GM_{BH}/a} = 0.17 \pm 0.02 \, \mathrm{pc}$, which corresponds to $\Omega_{sys} = \sqrt{GM_{BH}/r_{sys}^3} = a^{3/4}/(GM_{BH})^{1/4} = 0.005 \pm 0.001 \, \mathrm{rad \, yr^{-1}}$ (filled grey cone). The systemic velocity estimates are from the NED (1σ and 3σ uncertainties are quoted and plotted, respectively). In all the calculations, we adopted NGC 3393 systemic velocity from 21 cm line measurements of $3750 \pm 5 \, \mathrm{km \, s^{-1}}$ (Theureau et al. 1998).

is thus consistent with rotation (Fig. 6.4). From a fit of the Keplerian rotation to the high-velocity features ($\chi_R^2 = 0.6$), we obtain a mass of $(3.1 \pm 0.2) \times 10^7 \, M_\odot$

enclosed within 0.36 ± 0.01 pc (1.48 ± 0.06 mas; to estimate the minimum impact parameter from high-velocity data, we used the probability distribution function for a minimum of random variables following the Rice distribution). The fit to the blue- or the red-shifted emission alone yields $(3.0 \pm 0.3) \times 10^7 \, M_\odot$ or $(3.2 \pm 0.2) \times 10^7 \, M_\odot$, respectively. If one correlator pass is shifted 0.9 mas so that its single low-velocity maser feature overlaps the two low-velocity features in the other data set, then the mass becomes $(3.5 \pm 0.2) \times 10^7 \, M_\odot$ enclosed within 0.41 ± 0.02 pc (1.71 ± 0.07 mas), which reflects the sensitivity of our results to systematic errors. We note that, in addition to the Keplerian rotation, the data are also consistent (in the sense that $\chi_R^2 \lesssim 1$) with $v \propto r^\alpha$ for $-1 \leq \alpha \leq -0.1$. In particular, we obtain a minimum of $\chi_R^2 = 0.4$ at $\alpha = -0.2$, which suggests that uncertainties in the data are overestimated by a factor of ~ 1.6 and which corresponds to a mass of $2.6 \times 10^7 \, M_\odot$ enclosed within 0.36 pc (if we assume spherical symmetry). Under this model, the mass of the disk traced by the high-velocity maser emission ($0.36 - 1$ pc) is $1.9 \times 10^7 \, M_\odot$, which should be compared to disk masses (computed on similar scales) of $\sim 7 \times 10^6 \, M_\odot$ and $\sim 9 \times 10^6 \, M_\odot$ for NGC 3079 (Kondratko et al. 2005) and NGC 1068 (Lodato & Bertin 2003), respectively. A flat rotation curve model, which gives $1.1 \times 10^7 \, M_\odot$ enclosed within 0.16 pc, is excluded by the data ($\chi_R^2 \approx 20$), unless velocity dispersion on the order of $30 \, \mathrm{km \, s^{-1}}$ is included. Such a large velocity dispersion would most likely be indicative of macroscopic random motions among the molecular clumps responsible for the maser emission rather than turbulence within the clumps.

The mean mass density corresponding to $3.1 \times 10^7 \, M_\odot$ enclosed within 0.36 pc is $\sim 10^{8.2} \, M_\odot \, \mathrm{pc^{-3}}$. The relatively high mean mass density for NGC 3393 is suggestive

of a massive central black hole, which is consistent with the X-ray observations of the nucleus. The estimated enclosed mass of $(3.1 \pm 0.2) \times 10^7 \, M_\odot$ is in agreement with proposed correlations between bulge velocity dispersion and black hole mass (Gebhardt et al. 2000a, 2000b; Ferrarese & Merritt 2000; Ferrarese et al. 2001). If we adopt $M_{BH} = 1.2 \times 10^8 \, M_\odot \, [\sigma/(200 \text{ km s}^{-1})]^{3.75}$ (Gebhardt et al. 2000a, 2000b), then the velocity dispersion of the bulge, $184 \pm 18 \, \text{km s}^{-1}$ from the central $\sim 35 \, \text{kpc}$ (Terlevich et al. 1990) or $157 \pm 20 \, \text{km s}^{-1}$ from the central $\sim 200 \, \text{pc}$ (Cid Fernandes et al. 2004), is consistent with a black hole mass of $(9 \pm 4) \times 10^7 \, M_\odot$ or $(5 \pm 2) \times 10^7 \, M_\odot$, respectively.

Based on an average quasar spectral energy distribution (Fabian & Iwasawa 1999; Elvis et al. 2002), the $2 - 10 \, \text{keV}$ luminosity is $1 - 3\%$ of the AGN bolometric luminosity and we obtain a bolometric luminosity for NGC 3393 of $10^{10.0 - 12.2} \, L_\odot$ from the $2 - 10 \, \text{keV}$ X-ray data tabulated by Kondratko et al. (2006). We note that this estimate for the AGN bolometric luminosity is consistent with the total IRAS luminosity of the source of $\sim 10^{10} \, L_\odot$ (measured on $\sim 30 \, \text{kpc}$ scale; Moshir et al. 1990). The Eddington luminosity of a $3 \times 10^7 \, M_\odot$ object is $10^{12} \, L_\odot$. Assuming that all of the enclosed mass is concentrated in a supermassive black hole, the bolometric luminosity of the central engine yields an Eddington ratio of > 0.01, which is consistent with the $0.01 - 1$ range obtained for Seyfert 1 galaxies, representative supermassive black hole systems (e.g., Padovani 1989; Wandel et al. 1999), but larger than for advection dominated accretion flow systems (e.g., $10^{-3.6 \pm 1}$ Herrnstein et al. 1998; Yuan et al. 2002). Assuming a standard accretion efficiency of ~ 0.1 (Frank, King, & Raine 2002; see also Marconi et al. 2004), we estimate a mass accretion rate of $\dot{M} = 0.007 - 1 \, M_\odot \, \text{year}^{-1}$.

For a central mass of $(3.1 \pm 0.2) \times 10^7 \, M_\odot$ and the measured centripetal acceleration of $a = 5 \pm 1 \, \mathrm{km \, s^{-1} \, yr^{-1}}$, we estimate disk radius of the systemic maser feature at $\sim 3880 \, \mathrm{km \, s^{-1}}$ of $r_{sys} = \sqrt{GM_{BH}/a} = 0.17 \pm 0.02 \, \mathrm{pc}$, which becomes $0.18 \pm 0.02 \, \mathrm{pc}$ if the low-velocity emission in the two correlator passes is aligned and which is significantly smaller than the inner disk radius of the high-velocity emission $(0.36 \pm 0.02 \, \mathrm{pc})$. Evidently, the systemic emission in NGC 3393 arises much closer to the dynamical center than the high-velocity emission, which is in contrast to the situation in NGC 4258 (Herrnstein et al. 2005) and NGC 1068 (Greenhill et al. 1997b), where disk radii of low-velocity features are consistent with those occupied by high-velocity emission. It has been suggested that the systemic emission in NGC 4258 resides in a bowl that is a consequence of an inclination-warped disk (Herrnstein et al. 2005). Such a warp in the accretion disk structure might also determine the preferred radial location of the low-velocity features in NGC 3393. The resulting orbital velocity of the $\sim 3880 \, \mathrm{km \, s^{-1}}$ maser feature is $890 \pm 60 \, \mathrm{km \, s^{-1}}$ (which might be as high as $920 \pm 60 \, \mathrm{km \, s^{-1}}$ due to systematic errors). We note that the $130 \, \mathrm{km \, s^{-1}}$ offset of this feature from the adopted systemic velocity might be due its location within the disk at a non-zero azimuthal angle ϕ from the line of sight to the central engine. Using this velocity offset, we estimate $\phi = 8°$ and the resulting corrections to the derived radius and orbital velocity are much smaller than the corresponding uncertainties. The newly detected feature at $\sim 4051 \, \mathrm{km \, s^{-1}}$ that we postulate to be high-velocity emission was not detected in the VLBI experiment but would appear at a large disk radius and therefore can be used to constrain the disk size. From the computed enclosed mass and $r = GM_{BH}/v^2$, we estimate that the accretion disk extends from $0.17 \pm 0.02 \, \mathrm{pc}$ to $1.5 \pm 0.1 \, \mathrm{pc}$ (from $0.18 \pm 0.02 \, \mathrm{pc}$ to

1.7 ± 0.1 pc if the low-velocity emission in the two correlator passes is aligned).

6.5 Conclusion

We have mapped for the first time the maser emission in the nuclear region of NGC 3393. We interpret the linear distribution of the maser emission and the segregation of the blue- and the red-shifted emission on the sky in the context of a pc-scale nearly edge-on molecular disk that orbits a central mass of $(3.1 \pm 0.2) \times 10^7 \, M_\odot$ enclosed within 0.36 ± 0.02 pc (1.48 ± 0.06 mas). We also report the measurement of centripetal acceleration, $a = 5 \pm 1 \, \mathrm{km \, s^{-1} \, yr^{-1}}$, in the low-velocity maser feature at $\sim 3880 \, \mathrm{km \, s^{-1}}$, which yields disk radius of 0.17 ± 0.02 pc for the derived central mass. The low-velocity emission in NGC 3393 occurs much closer to the dynamical center than the high-velocity emission, contrary to the situation in NGC 4258 and NGC 1068, the two archetypal maser systems. An independent estimate for the disk radius of the low-velocity features would be provided by the measurement of their proper motions. For a distance D, a central mass $3.1 \, (D/50 \, \mathrm{Mpc}) \times 10^7 \, M_\odot$, and a radius $0.17 \, (D/50 \, \mathrm{Mpc})^{1/2}$ pc, we expect motions of $\sim 4 \, (D/50 \, \mathrm{Mpc})^{-3/4} \, \mu\mathrm{as \, yr^{-1}}$, which would be challenging to measure in light of the maser variability and weakness. Alternatively, a measurement of the position-velocity gradient in the low-velocity maser features would provide an independent estimate for their radial location within the disk ($r_{sys} = 0.17 \, [D/50 \, \mathrm{Mpc}] \, [\Delta/0.27 \, \mathrm{Mpc \, yr^{-1} \, rad^{-1}}]^{-2/3}$ pc, where D is the distance and $\Delta = v/\theta$ is the impact parameter-velocity gradient). We were precluded from making this measurement due to the low signal-to-noise ratio in our VLBI map. However, it is unclear what improvement in SNR would be necessary

to yield this measurement, as there is a dearth of low-velocity features even in the sensitive single-dish spectra of the source. An independent estimate for the disk radius of the low-velocity features either from proper motions or position-velocity gradient could be used to determine a distance to NGC 3393, a result of considerable value since the galaxy is within the Hubble flow ($v_{\mathrm{sys}} = 3750$ km s^{-1}) and thus might be used to establish a Hubble relation independent of standard candle calibrators such as Cepheids.

6.6   Acknowledgements

Chapter 7

Conclusion

This dissertation presents results of extensive surveys for water maser emission conducted with the two NASA Deep Space Network (DSN) 70-m antennas at Tidbinbilla, Australia and at Robledo, Spain and with the 100-m Green Bank Telescope (GBT) in Green Bank, West Virginia. We detected 23 new water maser sources, eight of which are high-velocity systems. The VLA positions of the newly discovered emission are consistent with the optical positions of the host nuclei, which corroborates the association of the detected emission with nuclear activity. The survey results reported here and in Greenhill et al. (2003) resulted in a 60% increase in the number of known nuclear water maser sources, from ~ 37 to ~ 60, the largest increase since the seminal work by Braatz et al. (1997b). This considerable growth has enabled us to consider or revisit statistical properties of the nuclear water maser sources. For the 30 sources with available hard X-ray data, we found a possible correlation between unabsorbed X-ray luminosity $(2 - 10\,\mathrm{keV})$ and total isotropic water maser luminosity of the form $L_{2-10} \propto L_{\mathrm{H_2O}}^{0.5 \pm 0.1}$. This relationship is consistent

with the model proposed by Neufeld et al. (1994) in which X-ray irradiation of
molecular accretion disk gas by the central engine excites the maser emission. Braatz
et al. (1997b) previously reported marginal predisposition for water maser emission
to occur in edge-on active galaxies. However, we find no evidence for this preference
based on the survey detection rates among highly inclined ($> 70°$) AGN and based
on the distribution of galactic plane inclinations for known water maser systems.
This null result is consistent with studies that have shown lack of correlation between
galactic plane orientation and nuclear jet or narrow line region direction.

In this work, we also report the first VLBI map of water maser emission in
NGC 3393. Emission in this system appears to follow Keplerian rotation and traces
a linear structure between disk radii of 0.36 and $\sim 1\,\mathrm{pc}$. The size of the maser disk
in NGC 3393 is thus comparable to that in NGC 1068 ($0.6 - 1.3$; Greenhill & Gwinn
1997; Lodato & Bertin 2003) but larger than that in NGC 4258 ($0.16 - 0.28\,\mathrm{pc}$;
Herrnstein et al. 2005) and Circinus ($0.11 - 0.40\,\mathrm{pc}$; Greenhill et al. 2003). Assuming
an edge-on disk and $v \propto r^{-0.5}$, the inferred central mass is $(3.1 \pm 0.2) \times 10^7\,M_\odot$
enclosed within $0.36 \pm 0.02\,\mathrm{pc}$, which should be compared to masses of $\sim 10^7\,M_\odot$
(within 0.6 pc), $(3.9 \pm 0.1) \times 10^7\,M_\odot$ (within 0.16 pc), and $(1.7 \pm 0.3) \times 10^6\,M_\odot$
(within 0.11 pc) for NGC 1068 (Greenhill & Gwinn 1997; Lodato & Bertin 2003),
NGC 4258 (Herrnstein et al. 2005), and Circinus (Greenhill et al. 2003), respectively.
An alternative model, $v \propto r^{-0.2}$, yields a marginally better fit to the positions
and line-of-sight velocities of maser emission, in which case, the central mass
(within 0.36 pc) and disk mass traced by the maser emission ($0.36 - 1\,\mathrm{pc}$) become
$2.6 \times 10^7\,M_\odot$ and $1.9 \times 10^7\,M_\odot$, respectively.

We also presented the first VLBI map of the red-shifted high-velocity emission

in NGC 3079. The newly mapped emission allowed us to reconsider the dynamics of the system. The largely north-south distribution of emission, aligned with a kpc-scale molecular disk, and the segregation of blue- and red-shifted emission on the sky are suggestive of a nearly edge-on molecular disk on pc-scales. Positions and line-of-sight velocities of maser emission are consistent with a central mass of $\sim 2 \times 10^6\ M_\odot$ enclosed within ~ 0.4 pc. Trotter et al. (1998) reported a similar enclosed mass, $\sim 10^6\ M_\odot$, from consideration of the blue-shifted emission only. In our case, however, both the blue- and the red-shifted emission provide independent and consistent estimates of the enclosed mass. Because the rotation curve traced by the maser emission is flat, the mass of the disk (within 1.3 pc) is significant and might be as large as $7 \times 10^6\ M_\odot$. Based on the kinematics of the system, we also proposed that the disk is geometrically-thick, subject to gravitational instabilities, and hence most likely clumpy and star-forming. The accretion disk in NGC 3079 is thus significantly different from the compact, thin, warped, differentially rotating disk in the archetypal maser galaxy NGC 4258.

VLBI studies of high-velocity systems like the two presented in this dissertation reveal the spectacular diversity of supermassive black masses and pc-scale nuclear structures. The inferred central masses range from 10^6 up to $10^8\ M_\odot$, while the maser emission appears to trace not only compact, thin, differentially-rotating accretion disks but also jets, wide-angle outflows, and disorganized geometrically-thick rotating structures. The two systems considered here contribute to this variety: the disk in NGC 3393 appears to be differentially-rotating, as also observed in the archetypical water maser system NGC 4258, while the disk in NGC 3079 has a flat rotation curve and is disorganized, thick, and flaring. NGC 3079 study has provided what might

be the first evidence of star-formation in a pc-scale accretion disk and the second example of clumps hydromagnetically uplifted from the surface of an accretion disk (first is Circinus; Greenhill et al. 2003). Estimates for the binding masses in these two systems are highly significant, since VLBI study of water maser emission is currently the most precise method of determining black hole masses, and hence Eddington luminosities. VLBI results presented here have elucidated the geometry and dynamics of pc-scale structures in these two AGN and the relationship of these structures to their host galaxies. In NGC 3393 study, we also reported the measurement of centripetal acceleration and demonstrated the feasibility of a VLBI experiment despite the source weakness; as a result, NGC 3393 now constitutes a good candidate for the determination of the maser distance. At the very least, further synthesis imaging efforts will reveal structures in the inner-pc of AGN and yield additional black hole mass estimates, which might result in an independent estimate for the slope of the $M - \sigma$ relationship and thus provide a stringent test of other techniques for the determination of black hole masses.

The NGC 3393 VLBI experiment suffered from low signal-to-noise-ratio (SNR) due to technical difficulties with the GBT and thus another imaging attempt is warranted. If the sensitivity of the GBT can be fully exploited, then an increase in SNR by a factor of roughly 2 is feasible. Two imaging tracks as opposed to one would yield another $\sqrt{2}$ increase, for a total improvement in SNR by a factor of nearly 3. These enhancements might enable the determination of the position-velocity gradient for the systemic maser features and hence yield an independent estimate for their disk radius. However, it is not clear what improvement in SNR would be necessary to yield this measurement, as there is a dearth of low-velocity features even

in the sensitive single-dish spectra of the source. Nevertheless, another attempt to make this measurement is certainly justified, as an independent estimate for the disk radius of the systemic emission could be used to determine a distance to NGC 3393, a result of considerable value since the galaxy is within the Hubble flow ($v_{\mathrm{sys}} = 3750$ km s^{-1}) and thus might be used to establish a Hubble relation independent of standard candle calibrators such as Cepheids. A proposal to re-observe NGC 3393 in two tracks with VLBA + GBT + VLA has been accepted and the data was acquired on January 31st 2007.

Synthesis imaging studies of other systems are continuing with an aim to determine black hole masses, disk geometries, and possibly maser distances. VLBI data on IC 2560, MRK 1419, NGC 1386, UGC 3789, NGC 6323, and NGC 4945 have already been acquired, and in some cases (UGC 3789, NGC 6323, IC 2560, NGC 4945) processed and modelled. Data on the three high-velocity systems discovered with the GBT (2MASX J08362280+3327383, NGC 6264, and UGC 09618 NED02) have already been obtained and correlated. Among these sources, NGC 6264, UGC 09618 NED02 (this work), IC 2560 (Ishihara et al. 2001), MRK 1419 (Henkel et al. 2002), and NGC 6323 (L. Greenhill 2007, private communication) are best candidates for the determination of distance, as there already exists an unambiguous detection of centripetal acceleration in these systems. Attempts to detect centripetal acceleration in other sources and efforts to improve the already existing measurements are continuing with the GBT. Five epochs of GBT data on MRK 0034 have already been acquired while another epoch on 2MASX J08362280+3327383, NGC 6264, and UGC 09618 NED02 will be obtained in Winter 2007. To confirm the centripetal acceleration measurement reported in this dissertation, the monitoring of NGC 3393

with the GBT will continue until early 2007. The additional single-dish data will extend the temporal baseline and possibly reduce the uncertainty in the velocity drift measurement by factors of ~ 2 and nearly 3, respectively (latter result is based on numerical simulations). These single-dish efforts when combined with robust models of accretion disks from synthesis imaging experiments might yield another anchor point in the extragalactic distance ladder.

Surveys for water maser emission are also ongoing. The GBT program to detect water maser emission in galaxies host to Cepheid and type Ia supernovae is coming to completion. A search for water maser emission among Sloan Digital Sky Survey AGN has recently yielded new detections (J. Braatz 2006, private communication). The discovery of water maser emission from a quasar at redshift $z = 0.66$ (Barvainis & Antonucci 2005) has proven a catalyst for surveys among more distant AGN, although no other high-z sources have been discovered to date. We continue deep integrations on known non-high-velocity systems with the GBT with an aim to detect weak high-velocity features, emission that might have been missed with less-sensitive apertures. These efforts will increase the number of known water maser sources and of high-velocity systems. Such a growth will not only yield a larger pool of candidates for the determination of black hole masses and maser distances but also allow for the evaluation of statistical properties of nuclear water maser sources. For instance, if verified using a larger sample of sources, the proposed correlation between X-ray and water maser luminosities would be valuable in the modelling of maser excitation, identification of maser-rich samples of AGN using hard X-ray sky surveys, and perhaps modelling of the hard X-ray background. Evidence for the preference of maser emission to occur in edge-on galaxies might emerge from a larger

sample of nuclear water maser sources, which would increase our understanding of the geometry of the inner parsec in AGN and its relationship to the kpc-scale stellar disk. The majority of individual data points that constitute the Henkel et al. (2005) luminosity function are computed from three or fewer number of sources. A larger sample of known sources would thus yield an improved maser luminosity function, which in turn could clarify not only the distinction between star-forming and nuclear water maser sources but also our prospects of detecting sources at cosmologically significant redshifts (Henkel et al. 2005). Both the luminosity function and the correlation between water and X-ray luminosities would also benefit from a proper treatment of maser variability, a source of significant systematic error. X-ray studies of galaxies host to water maser emission are currently ongoing and should continue concurrently with the survey work. The measurement of the X-ray spectra above $10\,\mathrm{keV}$ for additional water maser systems would contribute to the evaluation of the putative correlation between X-ray and water maser luminosities and of the correlation between maser luminosity and absorbing column density (Madejski et al. 2006; Zhang et al. 2006).

In the near term, synthesis imaging studies of water maser emission with VLBI will benefit from the fully operational Expanded Very Large Array (EVLA). The goal of the EVLA project is to improve most of the capabilities of the VLA by at least an order of magnitude. The most significant enhancement is the installation of a new digital correlator (commissioning planned for 2009), which will provide wide bandwidths ($\sim 2\,\mathrm{GHz}$) and up to $262,144$ spectral channels. In addition, the signal path of each antenna will be overhauled to allow for operation at any frequency between 1 and $50\,\mathrm{GHz}$ and for an instantaneous IF bandwidth

of up to 8 GHz at each polarization (from 50 MHz, currently). As a result, the continuum sensitivity between 10 and 50 GHz will improve by a factor of ~ 20. Currently, it is often not possible to cover the full extent of water maser emission because of either the relatively narrow 2×50 MHz bandwidth or the restrictions on where these 50 MHz bands can be placed (only discrete frequencies are permitted, $20.5 + [n \times 0.3] + [m \times 0.05] \pm 0.1 \pm 0.0101$ GHz, where n and m are integers). It is the increase in continuum sensitivity and frequency agility that will most substantively enhance the importance of the phased EVLA as an element in future VLBI experiments, as it will improve the array's frequency coverage and tuning flexibility and decrease the time required for phasing the array (either by decreasing the requisite integration time on stronger calibrators or by enabling the use of weaker calibrators closer to the target, thereby decreasing the slew time).

In the more distant future, both the survey work and the follow-up synthesis imaging studies will be advanced substantively by the operational Square Kilometer Array (SKA). If built to current specifications, SKA will be two orders of magnitude more sensitive than the present 100-m class telescopes, and therefore permit detection of water maser emission at cosmologically significant redshifts (Morganti et al. 2004). The most luminous high-velocity water maser known (IRAS F22265-1826; peak flux density of ~ 300 mJy) would be detectable out to $z \sim 0.4$ with the most sensitive telescopes currently in operation (Henkel et al. 2005). The SKA, however, would extend this limit to distances $10\times$ greater and might increase the number of known maser sources by three orders of magnitude (Morganti et al. 2004). Nearby targets could be surveyed with increased sensitivity which would have significant ramifications for survey completeness. One limitation of VLBI is

the absence of nearby ($< 1°$) calibrators for phase referencing. From a survey with the Ryle Telescope at $15\,\mathrm{GHz}$, Taylor et al. (2001) estimate a differential source count of $8 \left(\dfrac{S}{100\,\mathrm{mJy}}\right)^{-2} \mathrm{mJy}^{-1}\,\mathrm{str}^{-1}$, which yields $8 \times 10^4 \left(\dfrac{\mathrm{mJy}}{S}\right) \mathrm{str}^{-1}$ for the angular density of sources with strength greater than S. We thus expect to have one phase reference calibrator of strength $> 5\,\mathrm{mJy}$ at $15\,\mathrm{GHz}$ (or $> 3.8\,\mathrm{mJy}$ at $22\,\mathrm{GHz}$, assuming the standard -0.7 for the spectral index) within $0.25\,\mathrm{degrees}$ of an arbitrary target source. A continuum source of such a strength would be sufficient for the calibration of the interferometer phase in a VLBI experiment involving the SKA.[1] In principle then, any newly discovered high-velocity system would have a suitable nearby phase reference calibrator. The anticipated sensitivity of the array would thus significantly increase the number of potential calibrators and hence increase the number of targets suitable for mapping with VLBI. For follow-up imaging studies, SKA, when combined with other outrigger antennae, would provide an order of magnitude improvement in sensitivity, which would increase both the distance at which imaging is possible and the number of suitable targets by half an order of magnitude and approximately two orders of magnitude, respectively (Morganti et al. 2004). A VLBI experiment involving the SKA could resolve pc-scale accretion disks up to $z \sim 0.1$; thus, to map potential high-velocity discoveries at $z \sim 0.4$, an addition of an orbiting radio telescope such as VSOP2 or iARISE would be required. The resulting phenomenal growth in the number of targets would

---

[1]A continuum source of strength $> 3.8\,\mathrm{mJy}$ would be detected with a signal-to-noise ratio of at least 4 in a single atmospheric coherence time ($\sim 30\,\mathrm{s}$ at $22\,\mathrm{GHz}$) on a baseline between the SKA core and a 25-m antenna, where we assumed a $16\,\mathrm{MHz}$ observing bandwidth and system equivalent flux densities of 0.56 and $1100\,\mathrm{Jy}$ for the SKA and the 25-m dish, respectively (Morganti et al. 2004).

inevitably yield more black hole mass and distance estimations. Such measurements conducted for a large sample of water maser systems would produce multiple anchor points in the extragalactic distance ladder, provide stringent tests of other techniques for determination of black hole masses, yield an independent estimate for the slope of the $M - \sigma$ relation, and result in a census of pc-scale nuclear structures, with significant impact on cosmology and our understanding of the AGN environment.

Chapter 8

Appendix

8.1 Acquisition and Processing of Single-dish Spectral Data

The 70-m Deep Space Network (DSN) antennae at Tidbinbilla, Australia, and Robledo, Spain, are equipped with cooled HEMT receivers that cover a frequency range $18 - 26\,\mathrm{GHz}$ and deliver a single left-circular polarization channel. The signal is first limited by a $600\,\mathrm{MHz}$ bandpass filter and then downconverted to a band centered at $321.4\,\mathrm{MHz}$. The second downconversion results in a $400\,\mathrm{MHz}$ band centered at $200\,\mathrm{MHz}$ ($400\,\mathrm{MHz} \approx 5350\,\mathrm{km\,s^{-1}}$ at $1.3\,\mathrm{cm}$, assuming the radio definition of Doppler shift). The signal is then correlated using a $2\,\mathrm{bit}$, 4096-lag, four-level digital spectrometer. To obtain total power spectra of each source, the telescope is moved repeatedly between the target source and the reference position on the sky (separated by $\sim 0.125°$). The correlator integrates at each position of

the telescope for approximately 30 s and the overhead due to antenna slew is $\sim 20\,\mathrm{s}$ ($\sim 67\%$ inefficiency). Thus, every $\sim 50\,\mathrm{s}$, an autocorrelation (AC) array of size 4096 is written in a Flexible Image Transfer System (FITS) format and contains $\sim 30\,\mathrm{s}$ of either on-source or off-source data.

The GBT receiver delivers four independent signals: two beams, each with two polarizations. The spectra in this case are obtained with two 200 MHz IFs configured to overlap by 50 MHz. The center of the resulting 350 MHz instantaneous bandwidth is tuned to the systemic velocity of each target source ($350\,\mathrm{MHz} \approx 4880\,\mathrm{km\,s^{-1}}$ for a representative recessional velocity of $5000\,\mathrm{km\,s^{-1}}$, assuming the optical definition of Doppler shift). The correlator is configured to yield channel spacing of 24.4 kHz and 16384 channels for each 200 MHz window. To obtain total-power spectra of each source, the antenna is moved by $3'$ every 2 min between two positions on the sky so that a target is always present in one of the two GBT beams. The overhead due to antenna slew in this case is only $\sim 20\,\mathrm{s}$ ($\sim 17\%$ inefficiency). Every 2 min and for each independent signal path, a new FITs file is created and contains an autocorrelation (AC) array of size 16384.

In what follows, we describe the data processing approach adopted for the DSN data. In the case of the GBT, the processing is analogous but requires additional data bookkeeping due to the presence of the four independent signals. The script, written in the Interactive Data Language (IDL), first obtains a list of all FITS files that satisfy a selection criterion (i.e., files that either correspond to a user-specified source name or are located in a specified directory). The script then continues through the list, and, for each two adjacent elements in the list, obtains the AC functions for the neighboring on-source and off-source scans (see Fig. 8.1 for a

graphical demonstration). Quantization correction is first applied to both on-source and off-source AC functions (Fig. 8.1). The two functions are then separately prepared for the Fast Fourier Transform (FFT) in accordance with the standard convention: lag 0 is placed into the 0th array element, lag 1 is loaded into array elements 1 and $N - 1$, etc., where N is double the size of the AC array ($N = 8192$ and $N = 32768$ for the DSN and the GBT, respectively). The following IDL code accomplishes the loading process:

```
N=8192

actemp=dblarr(N)

chan=dindgen(N/2+1)

actemp(chan)=ac_off(chan)

actemp(N-chan(1:N-1))=ac_off(chan(1:N-1))

actemp(N/2)=actemp(N/2-1)
```

Note that the coefficient corresponding to the Nyquist frequency (i.e., array element $N/2$) is effectively equated to the AC bias, which can be accomplished by setting that coefficient equal either to the $(N/2 - 1)$th AC element (as shown here for the DSN data) or to an average of the AC function over higher lags (as for the GBT). We found no noticeable difference between these two approaches.

Before the actual transformation, Hanning window is also applied to the data. To obtain an exact expression for the Hanning window in lag space, we first define the window in the frequency domain using the weights $[0.25, 0.5, 0.25]$ and then Fourier transform back:

```
window=dblarr(N)

window(0)=0.5

window(1)=0.25

window(N-1)=0.25

window=FFT(window,1,/double)
```

The resulting spectral window (at array elements $0, \ldots, N-1$) is effectively the cosine function shifted upward (Fig. 8.1). We maintain both the original and the smoothed data throughout data processing. The actual Fourier transform is accomplished in the following manner:

```
spec_off=(double(FFT(actemp,-1)))(0:N/2)

spec_off_s=(double(FFT(actemp*window,-1)))(0:N/2)
```

for the off-source scan for instance. To apply the Hanning window k times, we would use `window^k` in the above. The FFT results in four data products: on-source spectrum S_{on}, off-source spectrum S_{off}, and their two Hanning-smoothed counterparts. The total power spectrum is then computed using $S = \dfrac{S_{on} - S_{off}}{S_{off}}$, and similarly for the smoothed data.

At this stage, the system temperature and gain calibration is applied. The multiplicative calibration factor (from raw "correlator" units to Jy) is given by

```
factor = exp(tau/sin(e*!pi/180.))*(Tsyson+Tsysoff)/2.*$
         ( 2.*k/(7000.^2*!pi/4.* gain(e) )/1.E-23 )
```

where k is the Stefan-Boltzmann constant in cgs units, e is the antenna elevation averaged across the two scans under consideration, the function `gain(e)` returns antenna gain at an elevation e, 7000 is the diameter of the DSN telescopes in cm, `tau` is the opacity (obtained separately using a tipping scan), and `Tsyson` and `Tsysoff` are average system temperatures (in K) across the on-source integration and off-source integration, respectively. For the GBT (Fig. 8.2), the gain polynomial is given by

```
gain = -0.018644534+0.071262825*e-0.0032179002*e^2+8.0399697d-005*e^3+
          -1.2328783d-006*e^4+1.0759349d-008*e^5-3.9829447d-011*e^6.
```

For the DSN antennae in Tidbinbilla, Australia, and Robledo, Spain, the gain is given by

```
gain = 0.174012+0.0139313*e-0.000156126*e^2
```

and

```
gain=0.43*(-1.1737563+0.12943496*e-0.0023824174*e^2+1.2627183e-005*e^3),
```

respectively (Figs. 8.3-8.4). A fully calibrated total power spectrum in Jy units is then obtained simply by multiplying the raw total power by factor. The resulting spectrum (thereafter, an individual total power spectrum) corresponds to $\sim 60\,\mathrm{s}$ and $4\,\mathrm{min}$ of data for the DSN and the GBT, respectively. As the script continues through the list of all FITS files that satisfy a specified criterion, the procedure just described is repeated for every pair of adjacent on-source and off-source scans.

The weakness of extragalactic maser emission typically requires hours of integration on a target source and it is therefore necessary to appropriately combine the individual total power spectra into a composite product. For this purpose, we compute the noise level in the individual total power spectrum in four distinct ways:

- Simple sample variance: $\frac{1}{n-1}\sum_k (S_k - \langle S \rangle)^2$, where n is the number of spectral channels used in the average

- Sample variance of the spectrum with the running mean removed: $\frac{1}{n-1}\sum_k (S_k - Avg_k)^2$, where Avg_k gives the value of the running mean at spectral channel k

- Fit of a Gaussian model to a histogram (number versus flux)

- Fit of a Gaussian model to a histogram after the removal of the running mean

To reduce the impact of band-edge irregularities, we typically use the inner 75% of the spectrum in the above calculations. The running mean is computed using a boxcar of width 256 channels, which corresponds to a spectral width ($\sim 340\,\mathrm{km\,s^{-1}}$) that is larger than the broadest maser feature currently known.

Following the noise level calculation, the script performs automatic flagging of data. An individual total power spectrum is not included in the composite average if any of the four computed noise levels either exceed the expected noise level by a factor of ~ 1.5 (which signifies noisy data) or is below the expectation (which signifies algorithm failure). Here, the expected noise level is computed from the radiometer equation: $\sqrt{\frac{2}{\tau_{on}\Delta\nu}} \times \texttt{factor}$, where $\Delta\nu$ is the channel width in Hz (97.6 kHz and 24.4 kHz for the DSN and the GBT, respectively), τ_{on} is the time

antenna is on-source ($\sim 30\,\mathrm{s}$ and $2\,\mathrm{min}$ for the DSN and the GBT, respectively), and a factor of 2 accounts for the division in the calculation of the individual total power spectra, i.e., $S = \dfrac{S_{on} - S_{off}}{S_{off}}$. If an individual total power spectrum passes the noise level test, it is included in the composite spectrum with weight $1/\sigma^2$. Based on empirical tests, we have determined that the fourth method is the most reliable in estimating σ.

8.2   Iterative Hanning Smoothing

Total-power spectra presented in this work have been smoothed by an application of a Hanning window. In the case of the DSN data, the spectra have been smoothed only once, which has an effect of improving the rms noise level by a factor of $\sqrt{3/8}$. In the case of the GBT spectra, however, the Hanning window has been applied four times and it is important to understand the dependence of the resulting noise level on the number of the applications of the Hanning window. In what follows, we derive an expression for the noise level in a spectrum Hanning smoothed multiple times. We first express the smoothed spectrum in terms of the original spectrum, i.e., in term of a spectrum for which the neighboring channels are independent. Using the recursive definition of the Hanning window, we obtain for the jth spectral channel:

$$S_{j,n} = \left(\frac{1}{4}\right)^n \sum_{k=0}^{2n} \begin{pmatrix} 2n \\ k \end{pmatrix} S_{j-n+k}$$

where n is the number of applications of the Hanning window, S_k is kth spectral

channel in the original spectrum, and the function $\begin{pmatrix} 2n \\ k \end{pmatrix}$ gives the Binomial

coefficient "k choose $2n$". Taking the variance of both sides and simplifying, we

arrive at:

$$\sigma_n^2 = \sigma_o^2 \, \frac{1}{\sqrt{\pi}} \, \frac{\Gamma\left[\frac{1}{2} + 2n\right]}{\Gamma\left[1 + 2n\right]}$$

where $\Gamma(x)$ is the complete gamma function and σ_o and σ_n are the noise levels (i.e.,

standard deviations) in the original and the smoothed n times spectra, respectively.

The expression above is the exact expression for the variance of a spectrum Hanning

smoothed n times. Figure 8.5 compares this theoretical result to the calculations

based on actual spectral data.
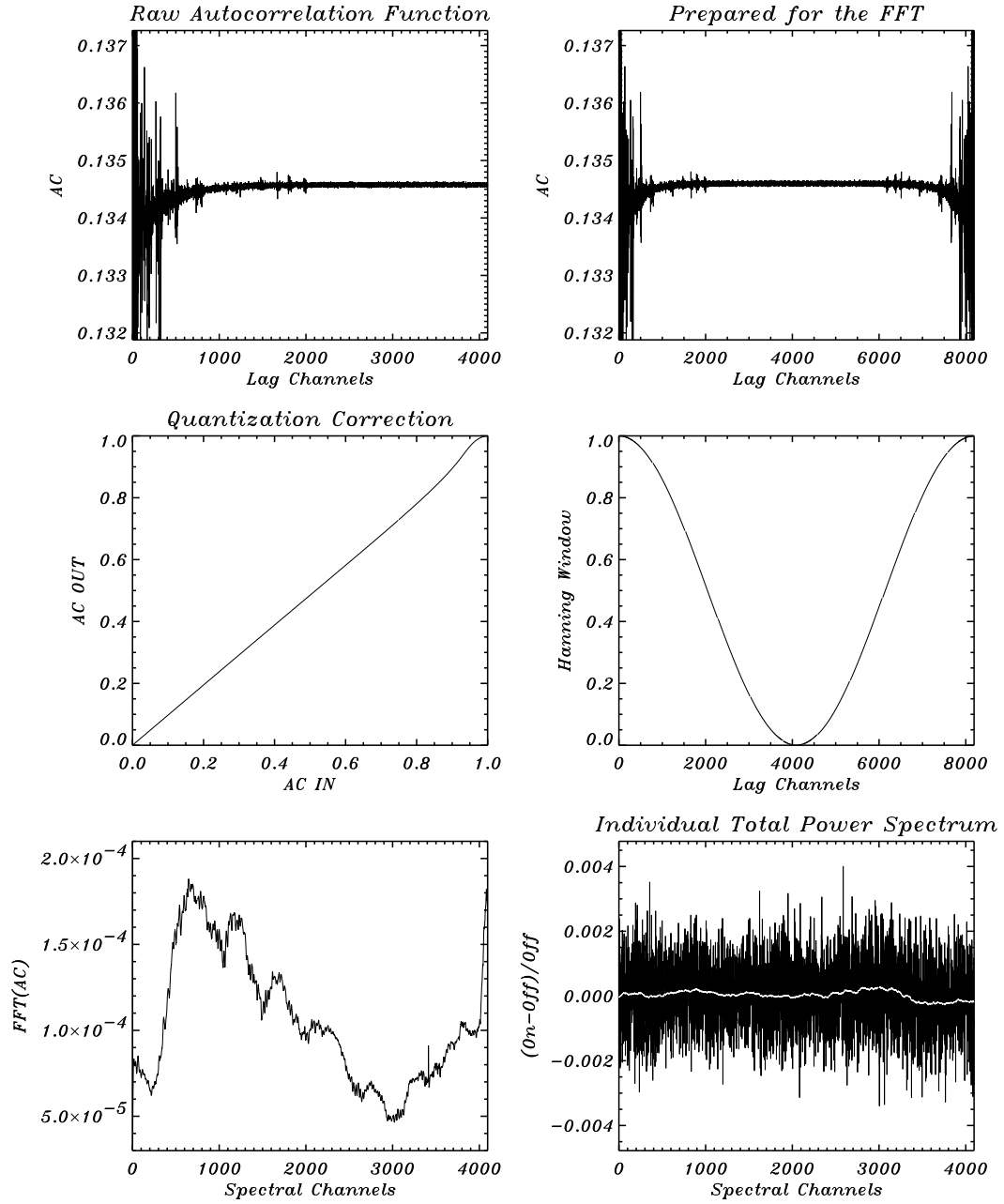
Figure 8.1.— Graphical summary of the data processing approach adopted for the Deep Space Network data: an autocorrelation (AC) function that is returned by the digital correlator and stored in the online FITS files (top, left), the same function but prepared for the Fast Fourier Transform (FFT; top, right), the quantization correction applied to the AC data (middle, left), the Hanning window as it appears in the lag domain (middle, right), FFT of the AC function (in this particular case, an on-source spectrum, S_{on}; bottom, left), and an individual total power spectrum, $(S_{on} - S_{off})/S_{off}$, before the application of gain and T_{sys} calibration and with the running mean shown (bottom, right).
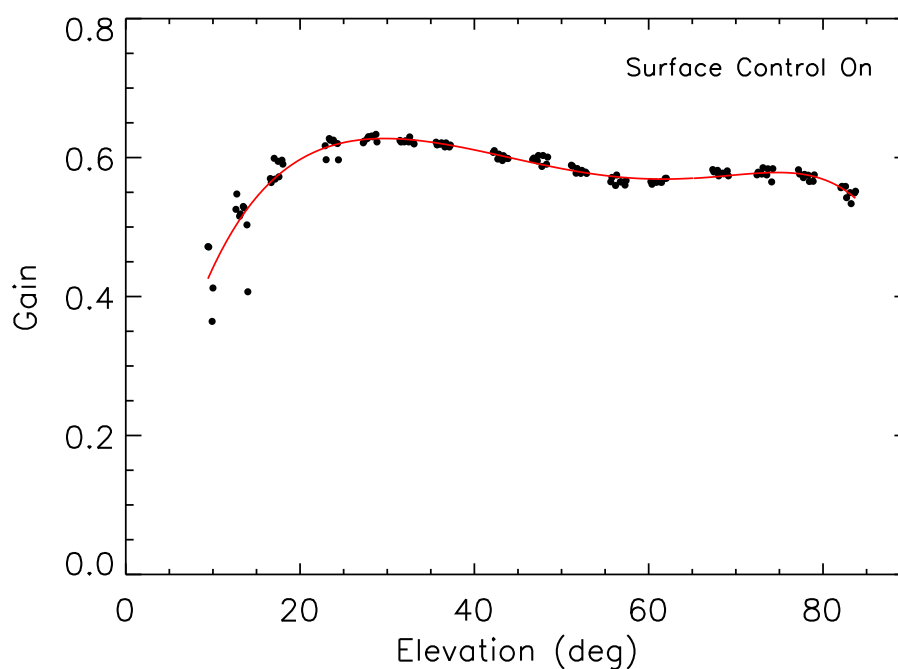
Figure 8.2.— Gain curve for the 100-m Green Bank Telescope based on measurements of opacity corrected antenna temperature for NGC 7027 at $\sim 1.4\,\mathrm{cm}$ (R. Maddalena 2003, private communication). Throughout these measurements, the surface actuators — mounted beneath the aperture paraboloid — dynamically adjusted the surface of the antenna to correct for thermal and gravitational deformations. The gain curve indicates an efficiency of 0.63 at 30°.
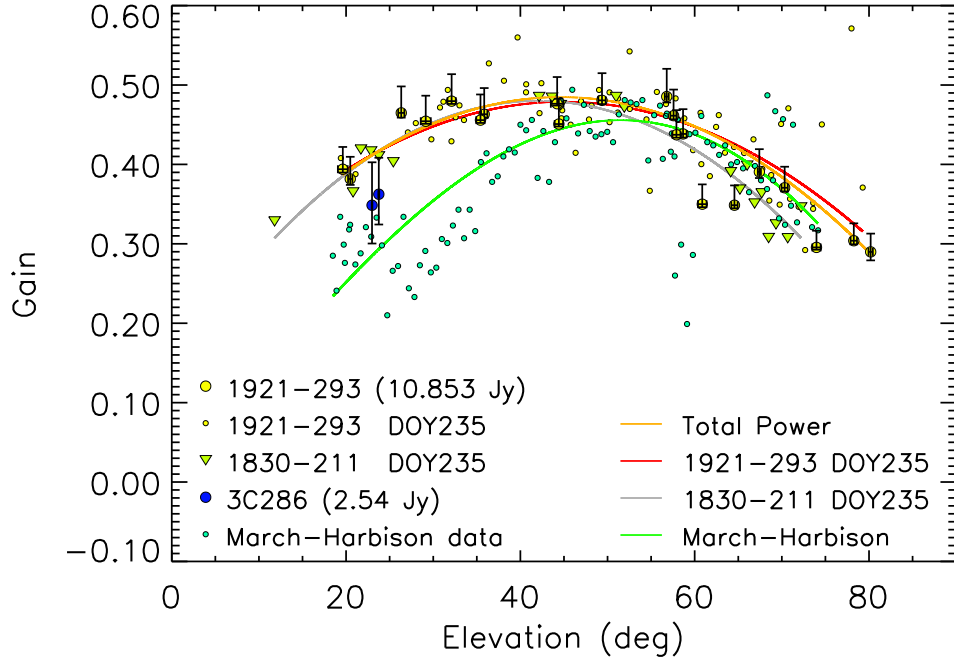
Figure 8.3.— Multiple estimates for the gain curve of the 70-m Deep Space Network antenna in Tidbinbilla, Australia. To calibrate the survey data, we estimated the gain curve from measurements of opacity corrected antenna temperature for PKS 1921-293 and PKS 1830-211, whose fluxes were calibrated against 3C 286 (2.54 Jy at 21.8 GHz). The resulting peak aperture efficiency is 0.48 ± 0.05 at $45° \pm 5°$. A gain curve in use prior to this calibration (March-Harbison) is shown for comparison.
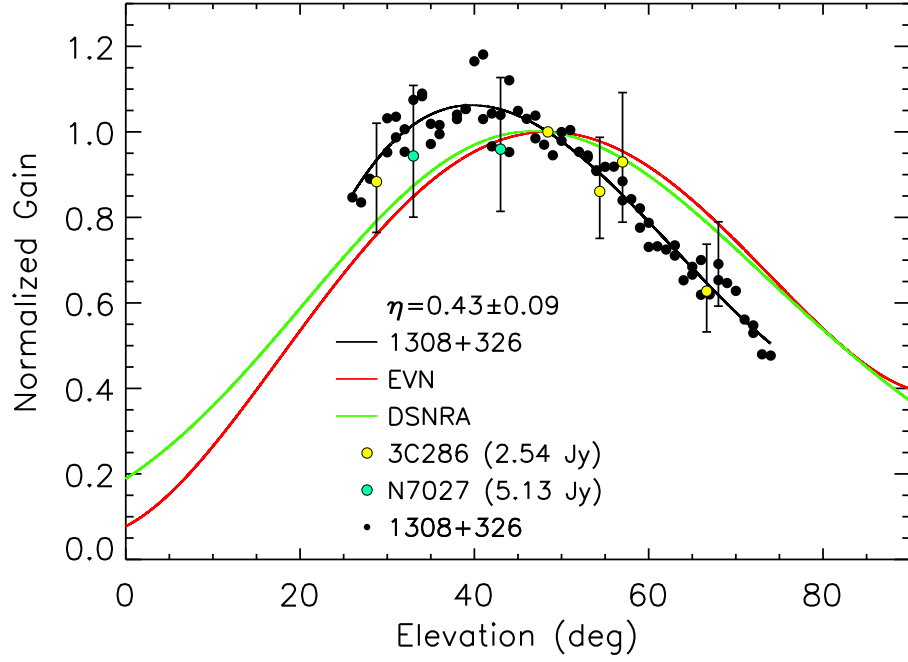
Figure 8.4.— Gain curve for the 70-m Deep Space Network antenna in Robledo, Spain. We estimated the gain curve and aperture efficiency through measurement of opacity corrected antenna temperature of 3C 147 (1308+326), for which we adopted a flux density of $1.82\,\mathrm{Jy}$ at $22.175\,\mathrm{GHz}$. The resulting peak efficiency is 0.43 ± 0.09 at $43° \pm 5°$ elevation, which yields a sensitivity of $1.7 \pm 0.3\,\mathrm{Jy\,K^{-1}}$. Gain curves in use prior to our calibration (DSNRA and EVN) are shown for comparison.
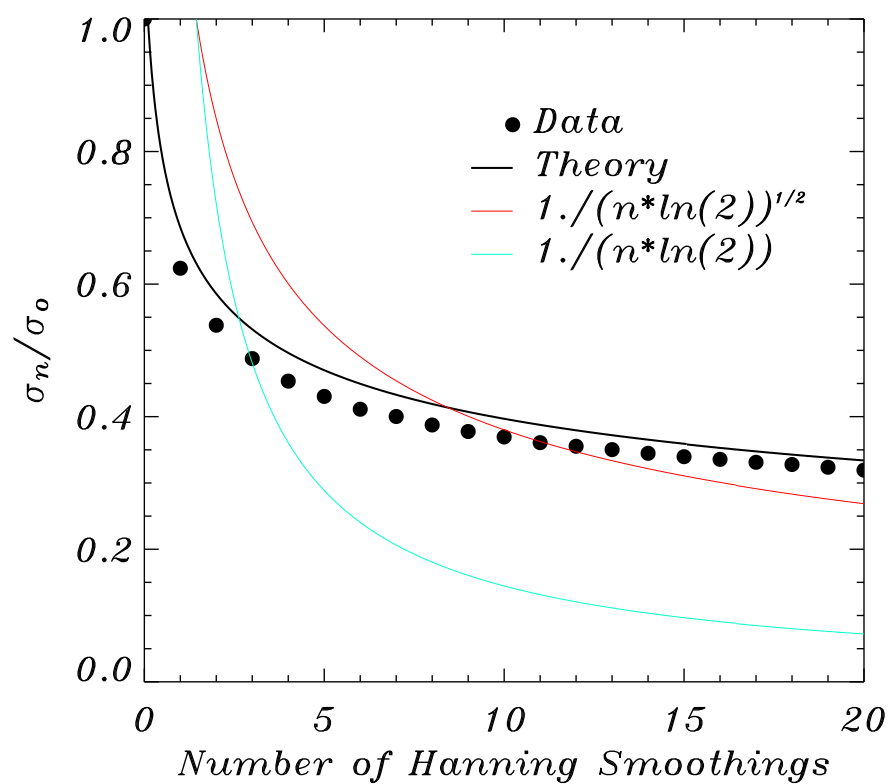
Figure 8.5.— Improvement in the noise level from multiple applications of the Hanning window for actual spectral data (circles) and as expected from theoretical considerations (black line). Note the small but systematic discrepancy between the data and the model.

References

Akylas, A., Georgantopoulos, I., & Comastri, A. 2001, MNRAS, 324, 521

Akylas, A., Georgantopoulos, I., Griffiths, R. G., Papadakis, I. E., Mastichiadis, A., Warwick, R. S., Nandra, K., & Smith, D. A. 2002, MNRAS, 332, L23

Allen, M. L. & Kronberg, P. P. 1998, ApJ, 502, 218

Alves, D. R. & Nelson, C. A. 2000, ApJ, 542, 789

Antonucci, R. 1993, ARA&A, 31, 473

Antonucci, R. R. J. & Miller, J. S. 1985, ApJ, 297, 621

Armus, L., et al. 2004, ApJS, 154, 178

Aurass, H., Vršnak, B., & Mann, G. 2002, A&A, 384, 273

Baan, W. A. & Haschick, A. 1996, ApJ, 473, 269

Baan, W. A. & Irwin, J. A. 1995, ApJ, 446, 602

Baars, J. W. M., Genzel, R., Pauliny-Toth, I. I. K., & Witzel, A. 1977, A&A, 61, 99

Ball, G. H., Greenhill, L. J., Moran, J. M., Zaw, I., & Henkel, C. 2005, in ASP Conf. Ser. 340: Future Directions in High Resolution Astronomy, ed. J. Romney & M. Reid, 235

Ballo, L., Braito, V., Della Ceca, R., Maraschi, L., Tavecchio, F., & Dadina, M. 2004, ApJ, 600, 634

Bardeen, J. M. & Petterson, J. A. 1975, ApJ, 195, L65

Bartel, N., et al. 2002, ApJ, 581, 404

Barth, A. J., Filippenko, A. V., & Moran, E. C. 1999a, ApJ, 515, L61

—. 1999b, ApJ, 525, 673

Barvainis, R. & Antonucci, R. 2005, ApJ, 628, L89

Bassani, L., Dadina, M., Maiolino, R., Salvati, M., Risaliti, G., della Ceca, R., Matt, G., & Zamorani, G. 1999, ApJS, 121, 473

Baudry, A., Brouillet, N., & Henkel, C. 1994, A&A, 287, 20

Beasley, A. J., Gordon, D., Peck, A. B., Petrov, L., MacMillan, D. S., Fomalont, E. B., & Ma, C. 2002, ApJS, 141, 13

Bianchi, S., Balestra, I., Matt, G., Guainazzi, M., & Perola, G. C. 2003, A&A, 402, 141

Bicknell, G. V., Dopita, M. A., & O'Dea, C. P. O. 1997, ApJ, 485, 112

Blandford, R. D. & Payne, D. G. 1982, MNRAS, 199, 883

Blitz, L. & Thaddeus, P. 1980, ApJ, 241, 676

Bottinelli, L., et al. 1993, VizieR Online Data Catalog, 410, 20057

Braatz, J., Greenhill, L., Moran, J., Wilson, A., & Herrnstein, J. 1997a, BAAS, 29, 1374

Braatz, J. A., Henkel, C., Greenhill, L. J., Moran, J. M., & Wilson, A. S. 2004, ApJ, 617, L29

Braatz, J. A., Wilson, A. S., & Henkel, C. 1994, ApJ, 437, L99

—. 1996, ApJS, 106, 51

—. 1997b, ApJS, 110, 321

Braatz, J. A., Wilson, A. S., Henkel, C., Gough, R., & Sinclair, M. 2003, ApJS, 146, 249

Braine, J., Guelin, M., Dumke, M., Brouillet, N., Herpin, F., & Wielebinski, R. 1997, A&A, 326, 963

Brandl, B., et al. 1996, ApJ, 466, 254

Brindle, C., Hough, J. H., Bailey, J. A., Axon, D. J., Ward, M. J., Sparks, W. B., & McLean, I. S. 1990, MNRAS, 244, 577

Buchanan, C. L., Gallimore, J. F., O'Dea, C. P., Baum, S. A., Axon, D. J., Robinson, A., Elitzur, M., & Elvis, M. 2006, AJ, 132, 401

Campbell, B., et al. 1992, AJ, 104, 1721

Cappi, M., et al. 1999, A&A, 344, 857

Carilli, C. L. & Holdaway, M. A. 1999, Tropospheric Phase Calibration in Millimeter Interferometry

Cecil, G., Bland-Hawthorn, J., & Veilleux, S. 2002, ApJ, 576, 745

Cecil, G., Bland-Hawthorn, J., Veilleux, S., & Filippenko, A. V. 2001, ApJ, 555, 338

Cecil, G., et al. 2000, ApJ, 536, 675

Cheung, A. C., Rank, D. M., Townes, C. H., Thornton, D. D., & Welch, W. J. 1969, Nature, 221, 626

Churchwell, E., Witzel, A., Huchtmeier, W., Pauliny-Toth, I., Roland, J., & Sieber, W. 1977, A&A, 54, 969

Cid Fernandes, R., Gu, Q., Melnick, J., Terlevich, E., Terlevich, R., Kunth, D., Rodrigues Lacerda, R., & Joguet, B. 2004, MNRAS, 355, 273

Cid Fernandes, R., Heckman, T., Schmitt, H., Delgado, R. M. G., & Storchi-Bergmann, T. 2001, ApJ, 558, 81

Clarke, C. J., Kinney, A. L., & Pringle, J. E. 1998, ApJ, 495, 189

Claussen, M. J., Diamond, P. J., Braatz, J. A., Wilson, A. S., & Henkel, C. 1998, ApJ, 500, L129

Claussen, M. J., Heiligman, G. M., & Lo, K. Y. 1984, Nature, 310, 298

Claussen, M. J. & Lo, K.-Y. 1986, ApJ, 308, 592

Colbert, E. J. M., Baum, S. A., Gallimore, J. F., O'Dea, C. P., & Christensen, J. A. 1996a, ApJ, 467, 551

Colbert, E. J. M., Baum, S. A., Gallimore, J. F., O'Dea, C. P., Lehnert, M. D., Tsvetanov, Z. I., Mulchaey, J. S., & Caganoff, S. 1996b, ApJS, 105, 75

Colbert, E. J. M., Baum, S. A., O'Dea, C. P., & Veilleux, S. 1998, ApJ, 496, 786

Colbert, E. J. M., Weaver, K. A., Krolik, J. H., Mulchaey, J. S., & Mushotzky, R. F. 2002, ApJ, 581, 182

Collison, A. J. & Watson, W. D. 1995, ApJ, 452, L103

Comastri, A. 2004, Compton-Thick AGN: The Dark Side of the X-Ray Background (ASSL Vol. 308: Supermassive Black Holes in the Distant Universe), 245

Condon, J. J. 2003, GBT PTCS Project Notes, 26

Condon, J. J., Cotton, W. D., Greisen, E. W., Yin, Q. F., Perley, R. A., Taylor, G. B., & Broderick, J. J. 1998, AJ, 115, 1693

Cooke, A. J., Baldwin, J. A., Ferland, G. J., Netzer, H., & Wilson, A. S. 2000, ApJS, 129, 517

Corbett, E. A., Robinson, A., Axon, D. J., Young, S., & Hough, J. H. 1998, MNRAS, 296, 721

Curran, S. J. 2000, A&AS, 144, 271

da Costa, L. N., Pellegrini, P. S., Davis, M., Meiksin, A., Sargent, W. L. W., & Tonry, J. L. 1991, ApJS, 75, 935

da Costa, L. N., et al. 1998, AJ, 116, 1

Dale, D. A., Giovanelli, R., Haynes, M. P., Campusano, L. E., & Hardy, E. 1999, AJ, 118, 1489

Davoust, E. & Contini, T. 2004, A&A, 416, 515

de Vaucouleurs, G., de Vaucouleurs, A., Corwin, Jr., H. G., Buta, R. J., Paturel, G., & Fouque, P. 1991, Third Reference Catalogue of Bright Galaxies (Volume 1-3, XII, 2069 pp. 7 figs.. Springer-Verlag Berlin Heidelberg New York)

De Villiers, J.-P., Hawley, J. F., & Krolik, J. H. 2003, ApJ, 599, 1238

Deguchi, S. & Watson, W. D. 1989, ApJ, 340, L17

Della Ceca, R., et al. 2002, ApJ, 581, L9

Desch, S. J., Wallin, B. K., & Watson, W. D. 1998, ApJ, 496, 775

Devereux, N. 1987, ApJ, 323, 91

di Nella, H., Garcia, A. M., Garnier, R., & Paturel, G. 1995, A&AS, 113, 151

Diaz, A. I., Prieto, M. A., & Wamsteker, W. 1988, A&A, 195, 53

Done, C., Madejski, G. M., Życki, P. T., & Greenhill, L. J. 2003, ApJ, 588, 763

Dos Santos, P. M. & Lepine, J. R. D. 1979, Nature, 278, 34

Duric, N. & Seaquist, E. R. 1988, ApJ, 326, 574

Elitzur, M., Hollenbach, D. J., & McKee, C. F. 1989, ApJ, 346, 983

Elitzur, M. & Shlosman, I. 2006, ApJ, 648, L101

Elvis, M., Risaliti, G., Nicastro, F., Miller, J. M., Fiore, F., & Puccetti, S. 2004, ApJ, 615, L25

Elvis, M., Risaliti, G., & Zamorani, G. 2002, ApJ, 565, L75

Elvis, M., et al. 1994, ApJS, 95, 1

Emmering, R. T., Blandford, R. D., & Shlosman, I. 1992, ApJ, 385, 460

Fabian, A. C. & Iwasawa, K. 1999, MNRAS, 303, L34

Falcke, H. & Biermann, P. L. 1999, A&A, 342, 49

Falcke, H., Nagar, N. M., Wilson, A. S., & Ulvestad, J. S. 2000, ApJ, 542, 197

Falco, E. E., et al. 1999, PASP, 111, 438

Ferrarese, L. & Merritt, D. 2000, ApJ, 539, L9

Ferrarese, L., Pogge, R. W., Peterson, B. M., Merritt, D., Wandel, A., & Joseph, C. L. 2001, ApJ, 555, L79

Fisher, K. B., et al. 1995, ApJS, 100, 69

Ford, H. C., Dahari, O., Jacoby, G. H., Crane, P. C., & Ciardullo, R. 1986, ApJ, 311, L7

Franceschini, A., et al. 2005, AJ, 129, 2074

Frank, J., King, A., & Raine, D. J. 2002, Accretion Power in Astrophysics: Third Edition (Accretion Power in Astrophysics: Third Edition, by Juhan Frank, Andrew King, and Derek J. Raine. Cambridge University Press, 2002, 398 pp.)

Freedman, W. L., et al. 2001, ApJ, 553, 47

Fruscione, A., Greenhill, L. J., Filippenko, A. V., Moran, J. M., Herrnstein, J. R., & Galle, E. 2005, ApJ, 624, 103

Fukazawa, Y., Iyomoto, N., Kubota, A., Matsumoto, Y., & Makishima, K. 2001, A&A, 374, 73

Gallimore, J. F., Baum, S. A., & O'Dea, C. P. 2004, ApJ, 613, 794

Gallimore, J. F., Henkel, C., Baum, S. A., Glass, I. S., Claussen, M. J., Prieto, M. A., & Von Kap-herr, A. 2001, ApJ, 556, 694

Gammie, C. F. 2001, ApJ, 553, 174

Gardner, F. F. & Whiteoak, J. B. 1982, MNRAS, 201, 13

Gebhardt, K., et al. 2000a, ApJ, 539, L13

—. 2000b, ApJ, 543, L5

Genzel, R., Thatte, N., Krabbe, A., Kroker, H., & Tacconi-Garman, L. E. 1996, ApJ, 472, 153

Genzel, R., et al. 2003, ApJ, 594, 812

Georgantopoulos, I., Papadakis, I., Warwick, R. S., Smith, D. A., Stewart, G. C., & Griffiths, R. G. 1999, MNRAS, 307, 815

Georgantopoulos, I. & Papadakis, I. E. 2001, MNRAS, 322, 218

Gimeno, G. N., Díaz, R. J., & Carranza, G. J. 2004, AJ, 128, 62

Goodman, J. 2003, MNRAS, 339, 937

Greenhill, L. J. 2004, New Astronomy Reviews, 48, 1079

Greenhill, L. J. & Gwinn, C. R. 1997, Ap&SS, 248, 261

Greenhill, L. J., Herrnstein, J. R., Moran, J. M., Menten, K. M., & Velusamy, T. 1997a, ApJ, 486, L15

Greenhill, L. J., Kondratko, P. T., Lovell, J. E. J., Kuiper, T. B. H., Moran, J. M., Jauncey, D. L., & Baines, G. P. 2003, ApJ, 582, L11

Greenhill, L. J., Moran, J. M., & Herrnstein, J. R. 1997b, ApJ, 481, L23

Greenhill, L. J., Moran, J. M., Reid, M. J., Gwinn, C. R., Menten, K. M., Eckart, A., & Hirabayashi, H. 1990, ApJ, 364, 513

Greenhill, L. J., et al. 2002, ApJ, 565, 836

—. 2003, ApJ, 590, 162

Guainazzi, M. 2002, MNRAS, 329, L13

Guainazzi, M. & Antonelli, L. A. 1999, MNRAS, 304, L15

Guainazzi, M., Fabian, A. C., Iwasawa, K., Matt, G., & Fiore, F. 2005, MNRAS, 356, 295

Guainazzi, M., Matt, G., Brandt, W. N., Antonelli, L. A., Barr, P., & Bassani, L. 2000a, A&A, 356, 463

Guainazzi, M., Oosterbroek, T., Antonelli, L. A., & Matt, G. 2000b, A&A, 364, L80

Guainazzi, M., Rodriguez-Pascual, P., Fabian, A. C., Iwasawa, K., & Matt, G. 2004, MNRAS, 355, 297

Guainazzi, M., et al. 1999, MNRAS, 310, 10

Gwinn, C. R. 1994, ApJ, 429, 253

Hagiwara, Y., Diamond, P. J., & Miyoshi, M. 2003a, A&A, 400, 457

Hagiwara, Y., Diamond, P. J., Miyoshi, M., Rovilos, E., & Baan, W. 2003b, MNRAS, 344, L53

Hagiwara, Y., Diamond, P. J., Nakai, N., & Kawabe, R. 2001a, ApJ, 560, 119

Hagiwara, Y., Henkel, C., Menten, K. M., & Nakai, N. 2001b, ApJ, 560, L37

Hagiwara, Y., Henkel, C., Sherwood, W. A., & Baan, W. A. 2002, A&A, 387, L29

Hagiwara, Y., Kloeckner, H. R., & Baan, W. 2004, astro-ph/0404347

Haschick, A. D. & Baan, W. A. 1985, Nature, 314, 144

Hawarden, T. G., Israel, F. P., Geballe, T. R., & Wade, R. 1995, MNRAS, 276, 1197

Hawarden, T. G., Mountain, C. M., Leggett, S. K., & Puxley, P. J. 1986, MNRAS, 221, 41P

Heckman, T. M. 1980, A&A, 87, 152

Henkel, C., Braatz, J. A., Greenhill, L. J., & Wilson, A. S. 2002, A&A, 394, L23

Henkel, C., Güsten, R., Downes, D., Thum, C., Wilson, T. L., & Biermann, P. 1984, A&A, 141, L1

Henkel, C., Peck, A. B., Tarchi, A., Nagar, N. M., Braatz, J. A., Castangia, P., & Moscadelli, L. 2005, A&A, 436, 75

Henkel, C., Wang, Y. P., Falcke, H., Wilson, A. S., & Braatz, J. A. 1998, A&A, 335, 463

Herrnstein, J. R. 1997, Ph.D. Thesis

Herrnstein, J. R., Greenhill, L. J., & Moran, J. M. 1996, ApJ, 468, L17

Herrnstein, J. R., Greenhill, L. J., Moran, J. M., Diamond, P. J., Inoue, M., Nakai, N., & Miyoshi, M. 1998, ApJ, 497, L69

Herrnstein, J. R., Moran, J. M., Greenhill, L. J., Diamond, P. J., Miyoshi, M., Nakai, N., & Inoue, M. 1997, ApJ, 475, L17

Herrnstein, J. R., Moran, J. M., Greenhill, L. J., & Trotter, A. S. 2005, ApJ, 629, 719

Herrnstein, J. R., et al. 1999, Nature, 400, 539

Hirotani, K. 2005, ApJ, 619, 73

Ho, L. C. 1999a, Advances in Space Research, 23, 813

—. 1999b, ApJ, 516, 672

Ho, L. C., Filippenko, A. V., & Sargent, W. L. W. 1997a, ApJS, 112, 315

—. 1997b, ApJ, 487, 568

—. 2003, ApJ, 583, 159

Ho, L. C., Filippenko, A. V., Sargent, W. L. W., & Peng, C. Y. 1997c, ApJS, 112, 391

Ho, P. T. P., Martin, R. N., Henkel, C., & Turner, J. L. 1987, ApJ, 320, 663

Hollenbach, D. & McKee, C. F. 1989, ApJ, 342, 306

Hubble, E. P. 1926, ApJ, 64, 321

Huchra, J., Latham, D. W., da Costa, L. N., Pellegrini, P. S., & Willmer, C. N. A. 1993, AJ, 105, 1637

Huchra, J. P., Vogeley, M. S., & Geller, M. J. 1999, ApJS, 121, 287

Humason, M. L., Mayall, N. U., & Sandage, A. R. 1956, AJ, 61, 97

Humphreys, E. M. L., et al. 2007, ApJ, submitted

Hunt, L. K., Malkan, M. A., Rush, B., Bicay, M. D., Nelson, B. O., Stanga, R. M., & Webb, W. 1999, ApJS, 125, 349

Huré, J.-M. 2000, A&A, 358, 378

Ikebe, Y., Leighly, K., Tanaka, Y., Nakagawa, T., Terashima, Y., & Komossa, S. 2000, MNRAS, 316, 433

Irwin, J. A. & Saikia, D. J. 2003, MNRAS, 346, 977

Irwin, J. A. & Seaquist, E. R. 1988, ApJ, 335, 658

Ishihara, Y., Nakai, N., Iyomoto, N., Makishima, K., Diamond, P., & Hall, P. 2001, PASJ, 53, 215

Israel, F. P., van der Werf, P. P., Hawarden, T. G., & Aspin, C. 1998, A&A, 336, 433

Iwasawa, K., Maloney, P. R., & Fabian, A. C. 2002, MNRAS, 336, L71

Iyomoto, N., Fukazawa, Y., Nakai, N., & Ishihara, Y. 2001, ApJ, 561, L69

Jaffe, W., et al. 2004, Nature, 429, 47

Jogee, S. 2001, in IAU Symposium, 228

Jungwiert, B., Combes, F., & Axon, D. J. 1997, A&AS, 125, 479

Kadler, M., Kerp, J., Ros, E., Falcke, H., Pogge, R. W., & Zensus, J. A. 2004, A&A, 420, 467

Kameno, S., Nakai, N., Sawada-Satoh, S., Sato, N., & Haba, A. 2005, ApJ, 620, 145

Kardashev, N. S. 1962, Soviet Astronomy, 6, 317

Kartje, J. F., Königl, A., & Elitzur, M. 1999, ApJ, 513, 180

Keel, W. C. 1996, ApJS, 106, 27

Kellermann, K. I. & Verschuur, G. L., eds. 1988, Galactic and extragalactic radio astronomy (2nd edition)

Kellermann, K. I., et al. 2004, ApJ, 609, 539

Kewley, L. J., Groves, B., Kauffmann, G., & Heckman, T. 2006, MNRAS, 372, 961

Kinney, A. L., Schmitt, H. R., Clarke, C. J., Pringle, J. E., Ulvestad, J. S., & Antonucci, R. R. J. 2000, ApJ, 537, 152

Kirhakos, S. D. & Steiner, J. E. 1990a, AJ, 99, 1435

—. 1990b, AJ, 99, 1722

Klaas, U. & Walker, H. J. 2002, A&A, 391, 911

Koda, J., Sofue, Y., Kohno, K., Nakanishi, H., Onodera, S., Okumura, S. K., & Irwin, J. A. 2002, ApJ, 573, 105

Koekemoer, A. M., Henkel, C., Greenhill, L. J., Dey, A., van Breugel, W., Codella, C., & Antonucci, R. 1995, Nature, 378, 697

Kohno, K., Matsushita, S., Vila-Vilaró, B., Okumura, S. K., Shibatsuka, T., Okiura, M., Ishizuki, S., & Kawabe, R. 2001, in ASP Conf. Ser. 249: The Central Kiloparsec of Starbursts and AGN: The La Palma Connection, 672

Kondratko, P. K., Greenhill, L. J., & Moran, J. M. 2000, Bulletin of the American Astronomical Society, 32, 1586

Kondratko, P. T., Greenhill, L. J., & Moran, J. M. 2005, ApJ, 618, 618

—. 2006, ApJ, 652, 136

Kondratko, P. T., Greenhill, L. J., Moran, J. M., & Reid, M. J. 2007, in preparation

Kondratko, P. T., et al. 2006, ApJ, 638, 100

Königl, A. & Kartje, J. F. 1994, ApJ, 434, 446

Kraft, R. P., Hardcastle, M. J., Worrall, D. M., & Murray, S. S. 2005, ApJ, 622, 149

Krolik, J. H. 2001, New Astronomy Review, 45, 625

Krolik, J. H. & Begelman, M. C. 1988, ApJ, 329, 702

Krolik, J. H. & Kriss, G. A. 2001, ApJ, 561, 684

Kumar, P. 1999, ApJ, 519, 599

Kuraszkiewicz, J. K., et al. 2003, ApJ, 590, 128

Lamer, G., Uttley, P., & McHardy, I. M. 2000, MNRAS, 319, 949

Larson, R. B. 1982, MNRAS, 200, 159

Lawrence, A. & Elvis, M. 1982, ApJ, 256, 410

Lawrence, A., Ward, M., Elvis, M., Fabbiano, G., Willner, S. P., Carleton, N. P., & Longmore, A. 1985, ApJ, 291, 117

Leighly, K. M., Halpern, J. P., Awaki, H., Cappi, M., Ueno, S., & Siebert, J. 1999, ApJ, 522, 209

Levenson, N. A., Weaver, K. A., & Heckman, T. M. 2001, ApJS, 133, 269

Lin, D. N. C. & Pringle, J. E. 1987, MNRAS, 225, 607

Lira, P., Ward, M. J., Zezas, A., & Murray, S. S. 2002, MNRAS, 333, 709

Lodato, G. & Bertin, G. 2003, A&A, 398, 517

Lutz, D., Maiolino, R., Spoon, H. W. W., & Moorwood, A. F. M. 2004, A&A, 418, 465

Lynden-Bell, D. 1969, Nature, 223, 690

—. 1996, MNRAS, 279, 389

Ma, C., et al. 1998, AJ, 116, 516

Macri, L. M., Stanek, K. Z., Bersier, D., Greenhill, L., & Reid, M. 2006, A new Cepheid distance to the maser-host galaxy NGC 4258 and its implications for the Hubble Constant

Maddox, L. A., Leighly, K. M., Nava, A., Matsumoto, C., & Grupe, D. 2002, BAAS, 34, 1183

Madejski, G., Done, C., Życki, P. T., & Greenhill, L. 2006, ApJ, 636, 75

Maia, M. A. G., da Costa, L. N., Willmer, C., Pellegrini, P. S., & Rite, C. 1987, AJ, 93, 546

Maiolino, R., Krabbe, A., Thatte, N., & Genzel, R. 1998a, ApJ, 493, 650

Maiolino, R., Salvati, M., Bassani, L., Dadina, M., della Ceca, R., Matt, G., Risaliti, G., & Zamorani, G. 1998b, A&A, 338, 781

Makishima, K., Ohashi, T., Kondo, H., Palumbo, G. G. C., & Trinchieri, G. 1990, ApJ, 365, 159

Malizia, A., Bassani, L., Stephen, J. B., Malaguti, G., & Palumbo, G. G. C. 1997, ApJS, 113, 311

Malkan, M. A., Gorjian, V., & Tam, R. 1998, ApJS, 117, 25

Maloney, P. R., Hollenbach, D. J., & Tielens, A. G. G. M. 1996, ApJ, 466, 561

Maoz, D., Nagar, N. M., Falcke, H., & Wilson, A. S. 2005, ApJ, 625, 699

Maoz, E. 1995a, ApJ, 447, L91

—. 1995b, ApJ, 455, L131

Maoz, E. & McKee, C. F. 1998, ApJ, 494, 218

Marconi, A., Risaliti, G., Gilli, R., Hunt, L. K., Maiolino, R., & Salvati, M. 2004, MNRAS, 351, 169

Martel, A. R., Turner, N. J., Sparks, W. B., & Baum, S. A. 2000, ApJS, 130, 267

Mas-Hesse, J. M., Rodriguez-Pascual, P. M., de Cordoba, L. S. F., & Mirabel, I. F. 1994, ApJS, 92, 599

Mas-Hesse, J. M., Rodriguez-Pascual, P. M., Sanz Fernandez de Cordoba, L., Mirabel, I. F., Wamsteker, W., Makino, F., & Otani, C. 1995, A&A, 298, 22

Massey, P. & Hunter, D. A. 1998, ApJ, 493, 180

Matsumoto, C., Nava, A., Maddox, L. A., Leighly, K. M., Grupe, D., Awaki, H., & Ueno, S. 2004, ApJ, 617, 930

Matt, G., Fabian, A. C., Guainazzi, M., Iwasawa, K., Bassani, L., & Malaguti, G. 2000, MNRAS, 318, 173

Matt, G., Guainazzi, M., Perola, G. C., Fiore, F., Nicastro, F., Cappi, M., & Piro, L. 2001, A&A, 377, L31

Matt, G., et al. 1999, A&A, 341, L39

Mazzarella, J. M. & Boroson, T. A. 1993, ApJS, 85, 27

McDonald, A. R., Muxlow, T. W. B., Pedlar, A., Garrett, M. A., Wills, K. A., Garrington, S. T., Diamond, P. J., & Wilkinson, P. N. 2001, MNRAS, 322, 100

McDonald, A. R., Muxlow, T. W. B., Wills, K. A., Pedlar, A., & Beswick, R. J. 2002, MNRAS, 334, 912

McHardy, I. M., Papadakis, I. E., Uttley, P., Page, M. J., & Mason, K. O. 2004, MNRAS, 348, 783

Mezger, P. G. & Henderson, A. P. 1967, ApJ, 147, 471

Middelberg, E., Krichbaum, T. P., Roy, A. L., Witzel, A., & Zensus, J. A. 2003, astro-ph/0309382

Middelberg, E., et al. 2004, A&A, 417, 925

Milosavljević, M. & Loeb, A. 2004, ApJ, 604, L45

Miyoshi, M., Moran, J., Herrnstein, J., Greenhill, L., Nakai, N., Diamond, P., & Inoue, M. 1995, Nature, 373, 127

Modjaz, M., Moran, J. M., Kondratko, P. T., & Greenhill, L. J. 2005, ApJ, 626, 104

Monaghan, J. J. & Lattanzio, J. C. 1991, ApJ, 375, 177

Monk, A. S., Penston, M. V., Pettini, M., & Blades, J. C. 1986, MNRAS, 222, 787

Morganti, R., Greenhill, L. J., Peck, A. B., Jones, D. L., & Henkel, C. 2004, New Astronomy Review, 48, 1195

Morganti, R., Tsvetanov, Z. I., Gallimore, J., & Allen, M. G. 1999, A&AS, 137, 457

Moshir, M., et al. 1990, in IRAS Faint Source Catalogue, version 2.0 (1990), 0

Murray, N., Chiang, J., Grossman, S. A., & Voit, G. M. 1995, ApJ, 451, 498

Muxlow, T. W. B., Pedlar, A., Holloway, A. J., Gallimore, J. F., & Antonucci, R. R. J. 1996, MNRAS, 278, 854

Myers, P. C. 1985, in Protostars and Planets II, 81–103

Nagar, N. M., Falcke, H., Wilson, A. S., & Ho, L. C. 2000, ApJ, 542, 186

Nagar, N. M., Falcke, H., Wilson, A. S., & Ulvestad, J. S. 2002a, A&A, 392, 53

Nagar, N. M., Oliva, E., Marconi, A., & Maiolino, R. 2002b, A&A, 391, L21

Nagar, N. M. & Wilson, A. S. 1999, ApJ, 516, 97

Nakai, N., Inoue, M., Miyazawa, K., Miyoski, M., & Hall, P. 1995, PASJ, 47, 771

Nandra, K. & Pounds, K. A. 1994, MNRAS, 268, 405

Neufeld, D. A., Lepp, S., & Melnick, G. J. 1995, ApJS, 100, 132

Neufeld, D. A. & Maloney, P. R. 1995, ApJ, 447, L17

Neufeld, D. A., Maloney, P. R., & Conger, S. 1994, ApJ, 436, L127

Newman, J. A., Ferrarese, L., Stetson, P. B., Maoz, E., Zepf, S. E., Davis, M., Freedman, W. L., & Madore, B. F. 2001, ApJ, 553, 562

Nordgren, T. E., Chengalur, J. N., Salpeter, E. E., & Terzian, Y. 1997, AJ, 114, 77

O'Dea, C. P., Baum, S. A., & Stanghellini, C. 1991, ApJ, 380, 66

Ohno, M., Fukazawa, Y., & Iyomoto, N. 2004, PASJ, 56, 425

O'Neill, P. M., Nandra, K., Papadakis, I. E., & Turner, T. J. 2005, MNRAS, 358, 1405

Osterbrock, D. E. 1977, ApJ, 215, 733

—. 1981, ApJ, 249, 462

Padovani, P. 1989, A&A, 209, 27

Peck, A. B., Henkel, C., Ulvestad, J. S., Brunthaler, A., Falcke, H., Elitzur, M., Menten, K. M., & Gallimore, J. F. 2003, ApJ, 590, 149

Perola, G. C., Matt, G., Cappi, M., Fiore, F., Guainazzi, M., Maraschi, L., Petrucci, P. O., & Piro, L. 2002, A&A, 389, 802

Phillips, R. B. & Mutel, R. L. 1982, A&A, 106, 21

Planesas, P., Colina, L., & Perez-Olea, D. 1997, A&A, 325, 81

Pounds, K. A., Reeves, J. N., King, A. R., & Page, K. L. 2004, MNRAS, 350, 10

Pringle, J. 1997, MNRAS, 292, 136

Pringle, J. E. 1996, MNRAS, 281, 357

Ptak, A., Heckman, T., Levenson, N. A., Weaver, K., & Strickland, D. 2003, ApJ, 592, 782

Reynolds, C. S., Fabian, A. C., Celotti, A., & Rees, M. J. 1996, MNRAS, 283, 873

Rines, K., Geller, M. J., Diaferio, A., Mahdavi, A., Mohr, J. J., & Wegner, G. 2002, AJ, 124, 1266

Risaliti, G. 2002, A&A, 386, 379

Risaliti, G., Gilli, R., Maiolino, R., & Salvati, M. 2000, A&A, 357, 13

Risaliti, G., Maiolino, R., & Salvati, M. 1999, ApJ, 522, 157

Rothberg, B. & Joseph, R. D. 2006, AJ, 131, 185

Sakamoto, K., Okumura, S. K., Ishizuki, S., & Scoville, N. Z. 1999, ApJ, 525, 691

Sako, M., Kahn, S. M., Paerels, F., & Liedahl, D. A. 2000, ApJ, 543, L115

Salvati, M., Bassani, L., della Ceca, R., Maiolino, R., Matt, G., & Zamorani, G. 1997, A&A, 323, L1

Satyapal, S., Dudik, R. P., O'Halloran, B., & Gliozzi, M. 2005, ApJ, 633, 86

Satyapal, S., Sambruna, R. M., & Dudik, R. P. 2004, A&A, 414, 825

Sawada-Satoh, S., Inoue, M., Shibata, K. M., Kameno, S., Migenes, V., Nakai, N., & Diamond, P. J. 2000, PASJ, 52, 421

Sawada-Satoh, S., Inoue, M., Shibata, K. M., Kameno, S., Nakai, N., Migenes, V., & Diamond, P. J. 2002, in IAU Symposium, 404

Schmitt, H. R., Antonucci, R. R. J., Ulvestad, J. S., Kinney, A. L., Clarke, C. J., & Pringle, J. E. 2001a, ApJ, 555, 663

Schmitt, H. R., Donley, J. L., Antonucci, R. R. J., Hutchings, J. B., Kinney, A. L., & Pringle, J. E. 2003, ApJ, 597, 768

Schmitt, H. R. & Kinney, A. L. 1996, ApJ, 463, 498

Schmitt, H. R., Kinney, A. L., Storchi-Bergmann, T., & Antonucci, R. 1997, ApJ, 477, 623

Schmitt, H. R., Pringle, J. E., Clarke, C. J., & Kinney, A. L. 2002, ApJ, 575, 150

Schmitt, H. R., Ulvestad, J. S., Antonucci, R. R. J., & Kinney, A. L. 2001b, ApJS, 132, 199

Serabyn, E., Güsten, R., & Schulz, A. 1993, ApJ, 413, 571

Shakura, N. I. & Sunyaev, R. A. 1973, A&A, 24, 337

Shaw, M., Wilkinson, A., & Carter, D. 1993, A&A, 268, 511

Shlosman, I. & Begelman, M. C. 1989, ApJ, 341, 685

Silk, J. 1985, ApJ, 292, L71

Silk, J. 1987, in IAU Symp. 115: Star Forming Regions, 663–689

Simcoe, R., McLeod, K. K., Schachter, J., & Elvis, M. 1997, ApJ, 489, 615

Skrutskie, M. F., et al. 2006, AJ, 131, 1163

Smith, D. A. & Done, C. 1996, MNRAS, 280, 355

Smith, D. A. & Wilson, A. S. 2001, ApJ, 557, 180

Soifer, B. T., Boehmer, L., Neugebauer, G., & Sanders, D. B. 1989, AJ, 98, 766

Soifer, B. T., Sanders, D. B., Madore, B. F., Neugebauer, G., Danielson, G. E., Elias, J. H., Lonsdale, C. J., & Rice, W. L. 1987, ApJ, 320, 238

Strauss, M. A., Huchra, J. P., Davis, M., Yahil, A., Fisher, K. B., & Tonry, J. 1992, ApJS, 83, 29

Strickland, D. K., Heckman, T. M., Colbert, E. J. M., Hoopes, C. G., & Weaver, K. A. 2004a, ApJS, 151, 193

—. 2004b, ApJ, 606, 829

Tarchi, A., Henkel, C., Chiaberge, M., & Menten, K. M. 2003, A&A, 407, L33

Taylor, A. C., Grainge, K., Jones, M. E., Pooley, G. G., Saunders, R. D. E., & Waldram, E. M. 2001, MNRAS, 327, L1

Terashima, Y., Ho, L. C., & Ptak, A. F. 2000, ApJ, 539, 161

Terashima, Y., Iyomoto, N., Ho, L. C., & Ptak, A. F. 2002, ApJS, 139, 1

Terashima, Y. & Wilson, A. S. 2003, ApJ, 583, 145

Terlevich, E., Diaz, A. I., & Terlevich, R. 1990, MNRAS, 242, 271

Terlevich, R. 1996, Vistas in Astronomy, 40, 17

Theureau, G., Bottinelli, L., Coudreau-Durand, N., Gouguenheim, L., Hallet, N., Loulergue, M., Paturel, G., & Teerikorpi, P. 1998, A&AS, 130, 333

Thompson, I. B. & Martin, P. G. 1988, ApJ, 330, 121

Tingay, S. J. & Murphy, D. W. 2001, ApJ, 546, 210

Totani, T., Sumi, T., Kosugi, G., Yasuda, N., Doi, M., & Oda, T. 2005, ApJ, 621, L9

Tran, H. D. 1995, ApJ, 440, 565

Trotter, A. S., Greenhill, L. J., Moran, J. M., Reid, M. J., Irwin, J. A., & Lo, K. 1998, ApJ, 495, 740

Tully, R. B. 1988, Nearby galaxies catalog (Cambridge and New York, Cambridge University Press, 1988, 221 p.)

Tully, R. B., Shaya, E. J., & Pierce, M. J. 1992, ApJS, 80, 479

Ueda, Y., Ishisaki, Y., Takahashi, T., Makishima, K., & Ohashi, T. 2001, ApJS, 133, 1

Ulvestad, J. S. & Wilson, A. S. 1984, ApJ, 285, 439

Uttley, P., Fruscione, A., McHardy, I., & Lamer, G. 2003, ApJ, 595, 656

Uttley, P., McHardy, I. M., Papadakis, I. E., Guainazzi, M., & Fruscione, A. 1999, MNRAS, 307, L6

Uttley, P., Taylor, R. D., McHardy, I. M., Page, M. J., Mason, K. O., Lamer, G., & Fruscione, A. 2004, MNRAS, 347, 1345

Véron-Cetty, M.-P. & Véron, P. 2003, A&A, 412, 399

Veilleux, S., Cecil, G., Bland-Hawthorn, J., Tully, R. B., Filippenko, A. V., & Sargent, W. L. W. 1994, ApJ, 433, 48

Veron-Cetty, M.-P. & Veron, P. 1986, A&AS, 66, 335

Vignati, P., et al. 1999, A&A, 349, L57

Vollmer, B., Beckert, T., & Duschl, W. J. 2004, A&A, 413, 949

Vorontsov-Vel'Yaminov, B. A. 1977, A&AS, 28, 1

Wainscoat, R. J., Freeman, K. C., & Hyland, A. R. 1989, ApJ, 337, 163

Wall, J. V. & Jenkins, C. R. 2003, Practical Statistics for Astronomers (Princeton Series in Astrophysics)

Wallin, B. K., Watson, W. D., & Wyld, H. W. 1998, ApJ, 495, 774

Wandel, A. 1999, in ASP Conf. Ser. 175: Structure and Kinematics of Quasar Broad Line Regions, 285

Wandel, A., Peterson, B. M., & Malkan, M. A. 1999, ApJ, 526, 579

Wang, J., Heckman, T. M., Weaver, K. A., & Armus, L. 1997, ApJ, 474, 659

Wang, T., Mihara, T., Otani, C., Matsuoka, M., & Awaki, H. 1999, ApJ, 515, 567

Wardle, J. F. C., Homan, D. C., Ojha, R., & Roberts, D. H. 1998, Nature, 395, 457

Warwick, R. S., Koyama, K., Inoue, H., Takano, S., Awaki, H., & Hoshi, R. 1989, PASJ, 41, 739

Weaver, K. A., Wilson, A. S., Henkel, C., & Braatz, J. A. 1999, ApJ, 520, 130

Webb, W., Malkan, M., Schmidt, G., & Impey, C. 1993, ApJ, 419, 494

Weiler, K. W., Panagia, N., & Sramek, R. A. 1990, ApJ, 364, 611

Weiler, K. W., Sramek, R. A., Panagia, N., van der Hulst, J. M., & Salvati, M. 1986, ApJ, 301, 790

Wilkes, B. J., Mathur, S., Fiore, F., Antonelli, A., & Nicastro, F. 2001, ApJ, 549, 248

Wilking, B. A. & Lada, C. J. 1983, ApJ, 274, 698

Wilson, A. S., Yang, Y., & Cecil, G. 2001, ApJ, 560, 689

Wilson, A. S., et al. 1998, ApJ, 505, 587

Winkler, H. 1992, MNRAS, 257, 677

Yamauchi, A., Nakai, N., Sato, N., & Diamond, P. 2004, PASJ, 56, 605

Yamauchi, A., Sato, N., Hirota, A., & Nakai, N. 2005, PASJ, 57, 861

Young, J. S., Schloerb, F. P., Kenney, J. D., & Lord, S. D. 1986, ApJ, 304, 443

Yuan, F., Markoff, S., Falcke, H., & Biermann, P. L. 2002, A&A, 391, 139

Zezas, A., Ward, M. J., & Murray, S. S. 2003, ApJ, 594, L31

Zhang, J. S., Henkel, C., Kadler, M., Greenhill, L. J., Nagar, N., Wilson, A. S., & Braatz, J. A. 2006, A&A, 450, 933